A COMBINED LOW ENERGY ELECTRON DIFFRACTION AND AUGER ELECTRON SPECTROSCOPY STUDY OF OXYGEN ADSORPTION ON COPPER

by

L.McDonnell, B.Sc.

A Thesis

Submitted for the Degree of

of

Doctor of Philosophy

of the

University of Warwick

October,1974.

When all that story's finished, what's the news?
In luck or out the toil has left its mark:
That old perplexity an empty purse
Or the day's vanity, the night's remorse.

William Butler Yeats

MEMORANDUM

The work reported in this Thesis was performed by myself, except where specifically acknowledged as otherwise in the text, in the Department of Physics of the University of Warwick under the supervision of Dr.D.P.Woodruff. Parts of this Thesis have been published while other parts are in the course of publication and details are given overleaf. For convenience, the references cited in each chapter have been listed at the end of each chapter rather than at the end of the Thesis.

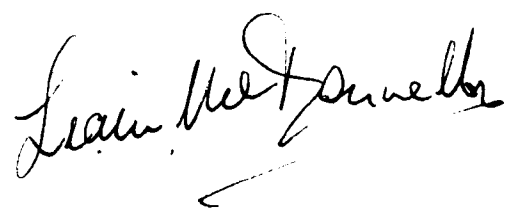

Liam McDonnell

PUBLICATIONS

CHAPTER FOUR — L.McDonnell, B.D.Powell & D.P.Woodruff, *Surface Sci.* 40 (1973) 669.

D.P.Woodruff & L.McDonnell, *Surface Sci.* 40 (1973) 200.

CHAPTER FIVE — L.McDonnell & D.P.Woodruff, accepted by *Surface Sci.*

CHAPTER SIX — L.McDonnell, D.P.Woodruff & K.A.R.Mitchell, *Surface Sci.* 45 (1974) 1.

CHAPTER SEVEN — L.McDonnell & D.P.Woodruff, *Vacuum* 22 (1972) 477.

B.W.Holland, L.McDonnell & D.P.Woodruff, *Solid State Comm.* 11 (1972) 991.

ACKNOWLEDGEMENTS

I wish to express my sincere thanks to my supervisor Dr.D.P. Woodruff for his enthusiastic support during the course of this work and his continual encouragement and to Professor A.J.Forty for the provision of facilities within the Department of Physics and his interest in this work.

I would also like to thank the numerous members of the Department of Physics who have assisted me in many ways while this work was in progress, in particular Drs.B.D.Powell, B.W. Holland and K.A.R.Mitchell* with whom it has been an honour to collaborate. Also, I wish to thank all the members of the Surface Physics group, past and present, with whom it has been a great pleasure to be associated. I am particularly grateful for the excellent technical support provided by Mr.O.S.Simpson. My sincere thanks are due to Dr.J.E.Demuth, IBM Thomas J.Watson Research Centre, New York, for permission to include his data prior to publication.

The financial support of the Science Research Council during the course of this work is gratefully acknowledged. In addition I am indebted to Reverend C.S.Cassidy, St.Austin, Stafford and Mr.& Mrs.R.Rudge, Coventry Printers Ltd., for their very generous provision of typing facilities.

Finally, I would like to thank my parents and wife for their wonderful support during the course of this work.

---

* On leave from the Department of Chemistry, University of British Columbia, Vancouver, Canada.

SUMMARY

The adsorption of oxygen at room temperature onto clean (100) and (111) surfaces of copper has been studied using low energy electron diffraction (LEED) and Auger electron spectroscopy (AES). By combining an energy-analysing Faraday cup with a commercial LEED display a versatile LEED experimental system has been obtained. Detailed intensity-energy spectra for several diffraction beams have been obtained from clean, ordered (100) and (111) copper surfaces and compare favourably with previous experimental studies and also with current dynamical calculations. Certain features existing in secondary electron spectra from copper surfaces have been identified by their unique temperature dependence as diffraction effects rather than Auger features.

Although no ordered oxygen structures were observed on the copper (111) surface, two ordered structures were observed on the (100) surface: a $(\sqrt{2}\times\sqrt{2})R45^{o}$ structure following oxygen exposures of 1×10^{-5} torr-minutes and a (2x2) structure following oxygen exposures of 1×10^{-4} torr-minutes. The latter structure has not been reported by other workers. Detailed intensity-energy spectra have been obtained from these surfaces, particularly from the $(\sqrt{2}\times\sqrt{2})R45^{o}$ structure which has been preliminarily interpreted by dynamical calculations as a reconstructed surface. A new Auger peak at 79 eV, associated with low oxygen coverages, has been observed on the copper (111) surface and attributed to a copper-oxygen cross-transition.

The constant momentum averaging scheme has been applied to both the clean and oxygen adsorbed (100) and (111) surfaces of copper and the differences between the clean and adsorbate averages has been interpreted using pseudo-kinematical calculations. The results of the analysis of three adsorbate structures, which are the first structural analyses performed on unknown surface structures using this technique, have all been physically reasonable solutions.

The energy-analysing facility of the Faraday cup has enabled the first observation of anisotropies in the angular distribution of Auger electron emission from a single crystal surface. Crystallographically associated anisotropies have been observed in the 62 eV copper Auger emission from both the (100) and (111) copper surfaces. The effect of adsorbates has been briefly examined.

*****

TABLE OF CONTENTS

CHAPTER ONE. INTRODUCTION

Since the first demonstration of the wave-like nature of the electron by Davisson and Germer[1] in 1927 low energy electron diffraction (LEED) has been recognised as a powerful technique for investigating surface order. Many aspects of present technology are related specifically to surface dominated microscopic processes, for example corrosion and catalysis, and as such, an accurate description of the surface in both atomic and electronic terms is essential to their understanding. Consequently, attention has been focussed for many years on LEED in an effort to extract the structural information relevant to such processes.

While LEED has indeed been very successful in demonstrating that specific surface phenomena exist, for example the reconstruction of certain clean surfaces and the ordered adsorption of particular gases on certain substrates, the exploitation of the LEED technique has been limited for a considerable period by both technical and theoretical complexities. The essential experimental requirement is an environment in which surfaces can be initially cleaned and then maintained in that state for considerable periods. Technical advances in vacuum engineering have overcome this particular problem and since the mid-1960's the routine achievement of ultra high vacuum (better than 10^{-9} torr) has been relatively straightforward. Even so the time scale of experiments often exceeds the period for which specific surface conditions can be maintained. Fortunately Auger electron spectroscopy, a technique that is physically compatible with the LEED experiment, allows the *in situ* identification of the elemental composition of the surface region and has rapidly superceded the indirect criteria for cleanliness of a surface that have often been employed.

The major impediment encountered in surface structural studies has been the lack of a simple theory to allow the interpretation of the intensities in LEED. The strength of the interaction of low energy electrons with solid surfaces is such that multiple scattering dominates intensities and the simple

kinematical theory which has been so successful in bulk structure determination using X-ray diffraction, where the interaction with the solid is weak, can not be employed. However, dynamical calculations have in recent years been developed to a stage where very good agreement has been achieved in describing LEED behaviour from certain clean metal surfaces; a particularly good example being the low index surfaces of nickel.[2] More recently, several attempts at determining unknown surface structures, produced by simple adsorption onto metallic surfaces, have been made using LEED.[3-7] Although major differences existed in the initial interpretations of the same adsorbate structure (Ni(100)-($\sqrt{2}$x$\sqrt{2}$)R45^{o}-O surface) by three independent theoretical groups, agreement does appear to have been achieved at the present time.

The accuracy of any proposed surface structure depends on the degree of correlation obtained between experiment and theory. In the limit of satisfactory correlation being obtained, confidence in the solution will depend on the quality of the experimental data used in the analysis. Correlation is often sought using only one intensity-energy spectrum for each diffracted beam for one particular scattering condition[3,4] which may put undue emphasis on the quality of the data. Such restrictions may not be deliberate; although the adsorption of gases onto metal substrates, for example, has been extensively studied in LEED, nearly all these studies have been limited to recording the changes induced in the LEED pattern by adsorption, with only occasional intensity-energy spectra recorded. Detailed experimental and theoretical intensity-energy spectra for a wide range of scattering geometries are very infrequent in the literature.

In the LEED study reported here of oxygen adsorption on the (100) and (111) surfaces of copper, an attempt was made to obtain a data base that was reliable (using Auger electron spectroscopy to characterise the surface) and also sufficiently extensive as to provide a rigorous test of the available dynamical calculations. In order to acquire intensity data from well-characterised surfaces for as wide a range of scattering geometries as possible, a new experimental system was specifically commissioned. This study was restricted

to room temperature adsorption, although limited post-adsorption annealing was performed. The main aim of the study was to obtain sufficiently extensive intensity data from well characterised surfaces as a firm basis for structural analysis,rather than to completely characterise this particular chemisorption system in terms of the exposures and temperatures at which oxygen surface structures are formed. Determination of the atomic positions for oxygen structures produced at room temperature will allow the identification of the initial adsorption sites, a matter which is fundamental to an understanding of oxidation.

Following a brief resumé of LEED and Auger electron spectroscopy and a description of the experimental system in chapters two and three respectively, the results of the general study are presented separately for the clean and oxygen adsorbed surfaces in chapters four and five respectively. In chapter six a new data reduction technique that circumvents the complexities of structural analyses that are based on dynamical theory by extracting the kinematical contributions to LEED intensities[8] is applied to both clean and oxygen adsorbate data. Finally in chapter seven the results of a study of the angular dependences of Auger electron emission from both clean and adsorbate covered copper surfaces are presented.

*****

REFERENCES

(1) C.J.Davisson & L.H.Germer, *Phys.Rev.* 30 (1927) 705.

(2) J.E.Demuth,D.W.Jepsen & P.M.Marcus, to be published.

(3) S.Andersson & J.B.Pendry, *J.Phys.C.* 6 (1973) 601.

(4) F.Forstmann,W.Berndt & P.Buttner, *Phys.Rev.Lett.* 30 (1973) 17.

(5) S.Andersson,B.Kasemo,J.B.Pendry & M.A.Van Hove, *Phys.Rev.Lett.* 31 (1973) 595.

(6) C.B.Duke,N.O.Lipari,G.E.Laramore & J.B.Theeten, *Solid State Commun.* 13 (1973) 579.

(7) J.E.Demuth,D.W.Jepsen & P.M.Marcus, *Solid State Commun.* 13 (1973) 1313.

(8) M.G.Lagally,T.C.Ngoc & M.B.Webb, *Phys.Rev.Lett.* 26 (1971) 1557.

CHAPTER TWO. LOW ENERGY ELECTRON DIFFRACTION AND AUGER ELECTRON SPECTROSCOPY

Recently, several authors have extensively reviewed the experimental and theoretical aspects of LEED[1-4] and AES[5,6] and consequently similarly detailed accounts are not duplicated here. Instead, a resumé of the physical and theoretical features that are directly relevant to the general content of this thesis is presented in this chapter.

When a monoenergetic electron beam of energy E_p is directed at a solid the energy distribution $N(E)$ of the *secondary* electrons back-scattered from the surface is typically of the form shown in figure 2.1. $N(E)$ spectra have three distinct features:

(a) A broad maximum near zero energy, often termed the *slow peak*, consisting of true secondary electrons thought to be produced by cascade processes within the solid.

(b) An intermediate region characterised by a slowly varying background superimposed with weak features mainly due to plasmon excitations, interband transitions and Auger emitted electrons. As a result this particular region contains valuable information relating to the surface and consequently it is extensively studied using a variety of techniques that include Auger electron spectroscopy (AES) and inelastic low energy electron diffraction (ILEED).

(c) At E_p a single narrow peak, the *elastic peak*, is observed and comprises both elastically scattered (*primary*) electrons and *pseudoelastic* electrons that are not generally separately resolved as they have only undergone low energy losses (of the order of 0.01 eV) due to electron-phonon interactions. It is the spatial distribution of the electron intensity within this peak and, more particularly, the variation of this distribution with electron energy which are of interest in LEED.

The useful energy range in LEED and AES is determined by the mean

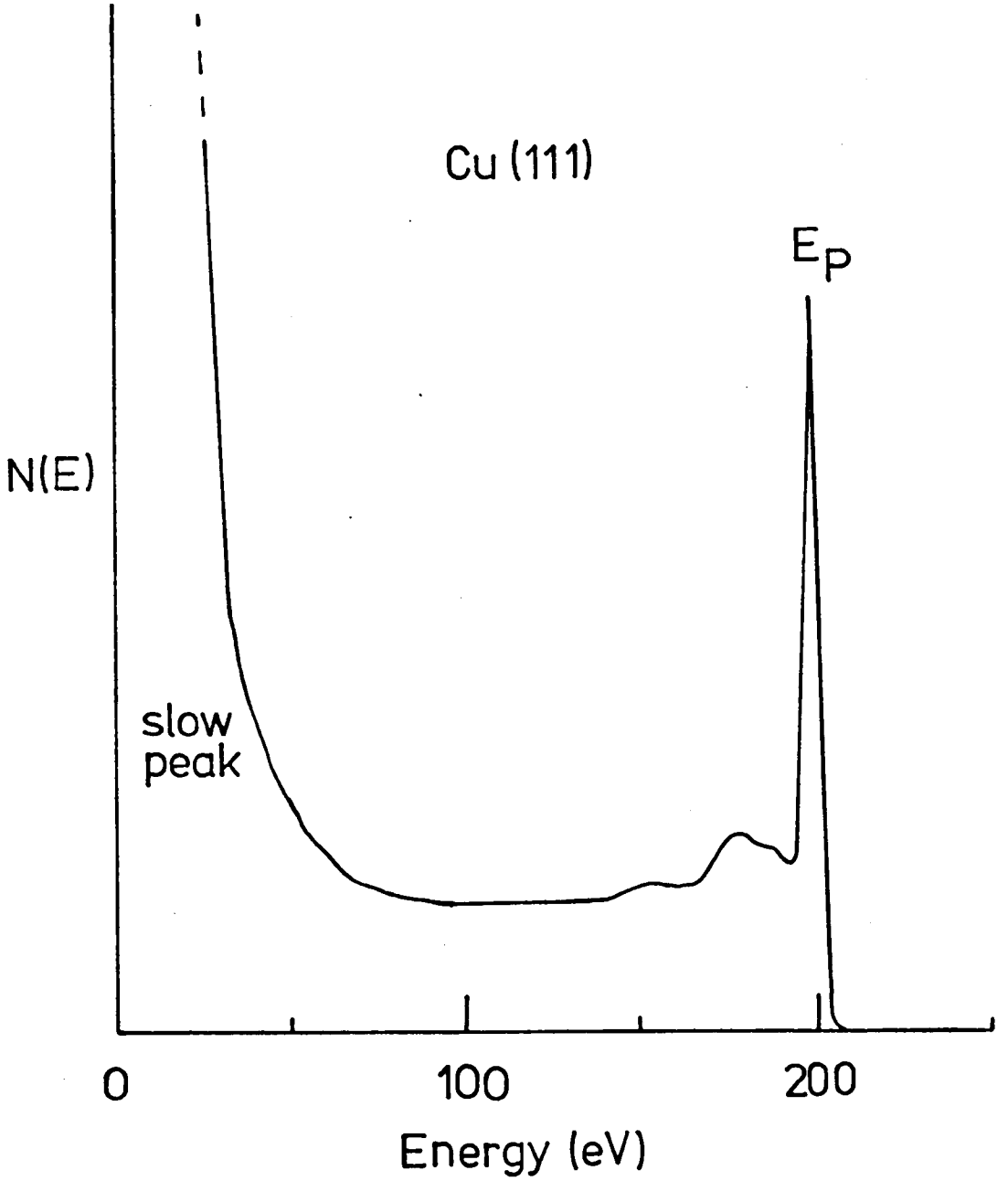

Figure 2.1 Typical *N(E)* spectrum obtained when a monoenergetic electron beam of energy E_P is directed at a solid.

escape depth for elastic electrons which is often described in terms of a mean free path λ_{ee}. Figure 2.2 shows the variation of the mean escape depth with electron energy derived from the experimental data recently collated by Rivière[6]. Although these data specifically relate to measurements on Auger emitted electrons and photoelectrons, the resultant trend is also applicable to LEED as identical loss mechanisms operate. The broad minimum in this curve between 15 and 300 eV defines the region of maximum surface sensitivity and hence the most useful energy region for LEED and AES.

In this energy region both the elastic and inelastic scattering cross-sections are large and the relative weakness of elastic scattering in the backward direction coupled with the strong inelastic scattering results in low LEED yields. For example, at electron energies of about 100 eV only about 1% of the incident electrons are back-scattered elastically from copper[7]. At energies below the plasmon threshold (typically about 10 eV) inelastic scattering is necessarily very weak and at these energies elastic yields of 10 to 50% are typical. Unfortunately, these high yields can not be utilised because at these particular energies the elastic scattering is dominated by the electronic band structure rather than by the structural periodicities of the surface.

2.1 Auger Electron Spectroscopy

The Auger emitted electrons observed in the *N(E)* distributions are particularly valuable in LEED experiments as they allow the identification of the chemical species of the surface region. The Auger process is a two stage radiationless transfer of energy to an electron following the ionisation of a core electron level (figure 2.3). Except for hydrogen and helium, an electron from a higher energy level is able to fill the core vacancy and the surplus energy is released either as a photon in the form of X-ray fluorescence or used to eject an Auger electron from the atom. For primary energies below 2 KeV, and also for light elements, the probability of Auger

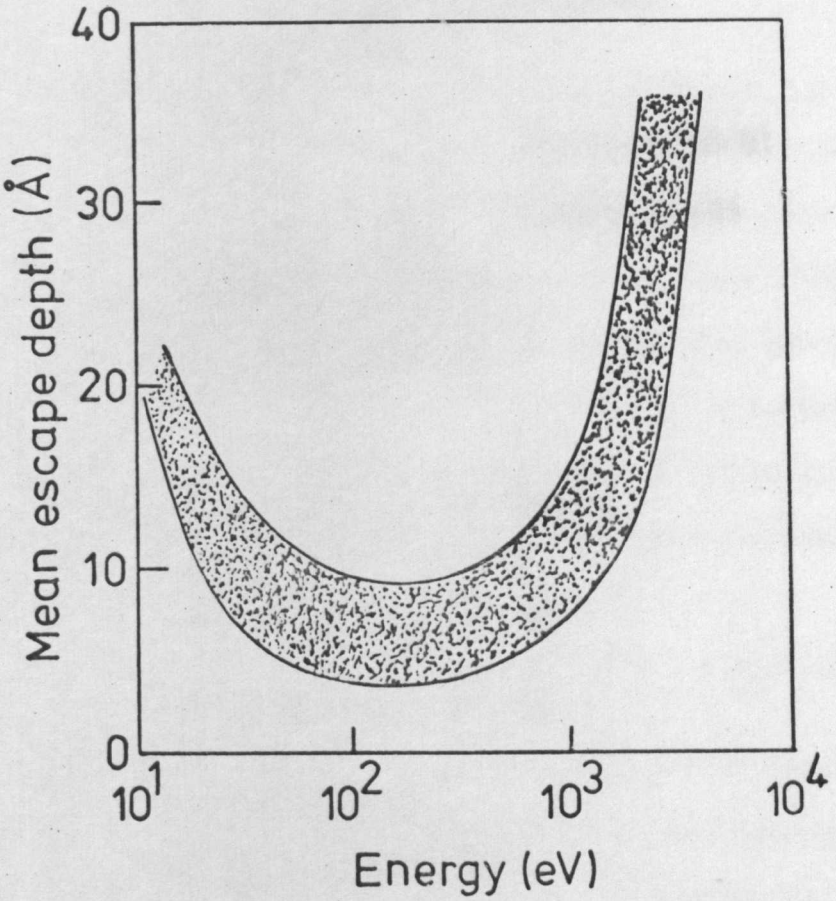

Figure 2.2 The variation of mean escape depth with electron energy for a wide range of elements (after Rivière[6])

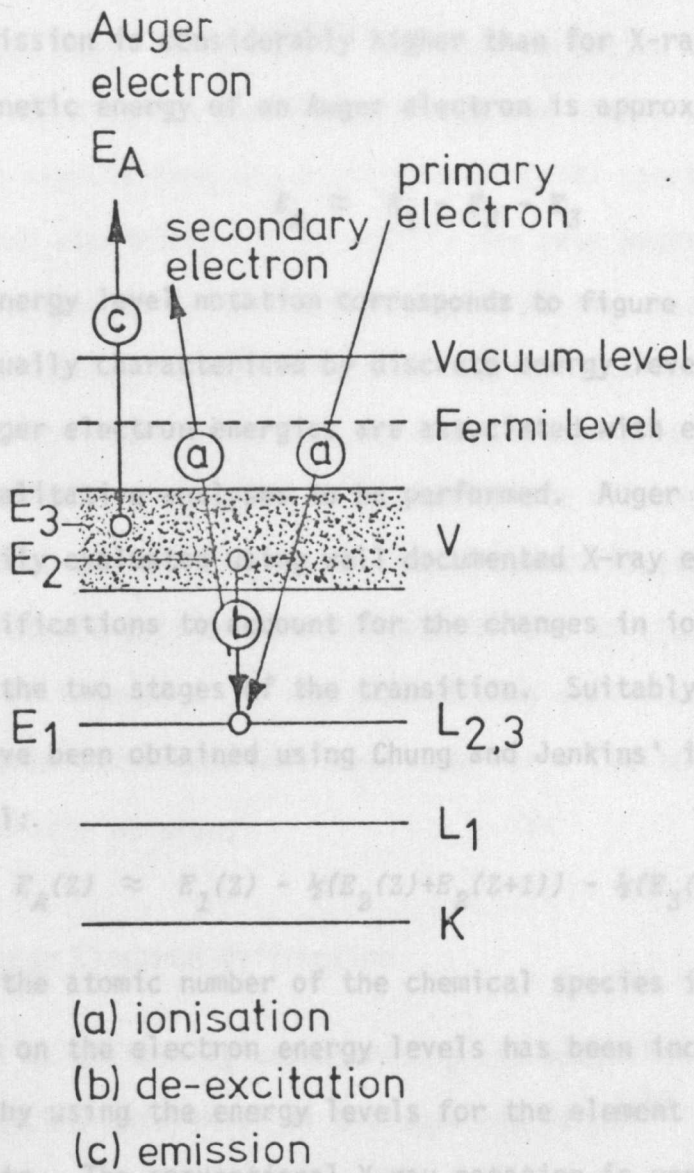

Figure 2.3 Schematic representation of the $L_{2,3}VV$ Auger transition.

electron emission is considerably higher than for X-ray fluorescence.[8]

The kinetic energy of an Auger electron is approximately given by:

$$E_A \simeq E_1 - E_2 - E_3 \qquad \ldots 2.1,$$

where the energy level notation corresponds to figure 2.3. Atomic species are individually characterised by discrete energy levels and consequently specific Auger electron energies are associated with each element, thereby enabling qualitative analyses to be performed. Auger electron energies can be readily evaluated using well documented X-ray energy levels[9] but require modifications to account for the changes in ionicity of the emitting ion during the two stages of the transition. Suitably accurate Auger electron energies have been obtained using Chung and Jenkins' interpretation[10] of equation 2.1:

$$E_A(Z) \simeq E_1(Z) - \tfrac{1}{2}(E_2(Z)+E_2(Z+1)) - \tfrac{1}{2}(E_3(Z)+E_3(Z+1)) \qquad \ldots 2.2,$$

where Z is the atomic number of the chemical species involved. The effect of ionicity on the electron energy levels has been incorporated into the transition by using the energy levels for the element $Z+1$ to describe the ionised state. The conventional X-ray notation is used to classify each Auger emission by referring in strict transitional sequence to the three energy levels involved. For example, the Auger process shown schematically in figure 2.3 is a $L_{2,3}VV$ transition where the $L_{2,3}$ notation indicates that the discrete energy levels L_2 and L_3 of the isolated atom are broadened into a band in the solid. For many solids where the valence electron density is high Auger transitions involving the valence band V, either once or twice, are particularly intense. Although the observation of only a few intense Auger emissions from most chemical species implies that selection rules for the transitions must be in operation, they have not been identified as yet. However, a reasonable guide to the relative intensities of Auger emissions from specific elements can be obtained from the electron multiplicity for the particular combination of energy levels involved.[11]

Tabulated Auger energies[12,13] and representative Auger spectra[14] for the majority of elements are now available and enable the surface researcher to establish rapidly from his $N'(E)$ spectra ($N(E)$ spectra are usually differentiated electronically to amplify the weak Auger features) the identity of the atomic species in the surface region of his specimen. Unfortunately, quantitative assessments can not be so readily obtained and with the intensity of impurity atom Auger emissions, for example, governed by such factors as the back-scattering properties of the substrate element(s), the in-depth distribution of the emitting atoms, etc., quantification requires independent calibration experiments to be performed for the particular elemental combination of interest. At the present time quantitative assessments using AES calibration techniques have been made for a limited number of systems[15-17] with considerable accuracy.

2.2 Low Energy Electron Diffraction

As well as profoundly demonstrating the wave-like nature of the electron, the original LEED experiment of Davisson and Germer[18] in 1927 established a technique for experimentally probing surface order that has yet to be fully exploited. Davisson and Germer's observations provided experimental support to de Broglie's hypothesis that a wavelength λ is related to an electron's energy E (in eV) such that:

$$\lambda = \left(\frac{150.4}{E}\right)^{\frac{1}{2}} \text{ Å} \qquad \ldots 2.3$$

At sufficiently low energies where the electron wavelength is comparable to atomic spacings, for example at 150 eV the wavelength is nearly 1 Å, the electrons are scattered into individual beams by the atomic periodicities of the crystal surface. The geometry of the spatial distribution of these discrete beams, termed the *LEED pattern*, is a representation in reciprocal space of the real net of the surface.

Because of the strong inelastic scattering at LEED energies, incident electrons do not experience the full three-dimensional periodicity of the bulk crystal. Instead the scattering potential experienced has essentially perfect periodicity only in the two dimensions parallel to the surface. This two-dimensional periodicity ensures that electrons are scattered elastically into particular discrete beams. If the incident electron beam is represented by a plane wave $e^{-i\underline{K}_{in}\cdot\underline{r}}$ where the magnitude of the propagation vector $\underline{K}_{in}$ is:

$$\underline{K}_{in} = \frac{2\pi}{\lambda} \qquad \ldots 2.4,$$

then the diffracted beams $\underline{K}_{out}$ are subject to the constraints of a conservation of parallel momentum:

$$\underline{K}^{//}_{out} = \underline{K}^{//}_{in} + \underline{G}^{//}_{hk} \qquad \ldots 2.5,$$

where $\underline{G}^{//}_{hk}$ is some reciprocal net vector parallel to the surface, and also a conservation of energy:

$$\left|\underline{K}_{out}\right|^2 = \left|\underline{K}_{in}\right|^2 \qquad \ldots 2.6.$$

A convenient method of determining the directions of diffracted beams $\underline{K}_{out}$ is the *Ewald sphere construction* in reciprocal space. If, for example, we consider the (100) surface of a simple cubic crystal of lattice parameter a, then a reciprocal lattice (also simple cubic) will be associated with it but with lattice parameter a^* ($=1/a$). Increasing the (100) interplanar spacing reduces a^* so that for a single layer the reciprocal lattice points of the bulk geometry merge into reciprocal lattice rods passing through the lattice points of the reciprocal net. The intersection of the Ewald sphere, drawn such that its radius is $1/\lambda$ (i.e. with $(1/2\pi)\underline{K}_{in}$ as a radius vector terminating at the origin of the reciprocal net), with these rods defines the allowed beams. This is illustrated in figure 2.4 for normal incidence onto the (100) surface of a f.c.c. crystal.

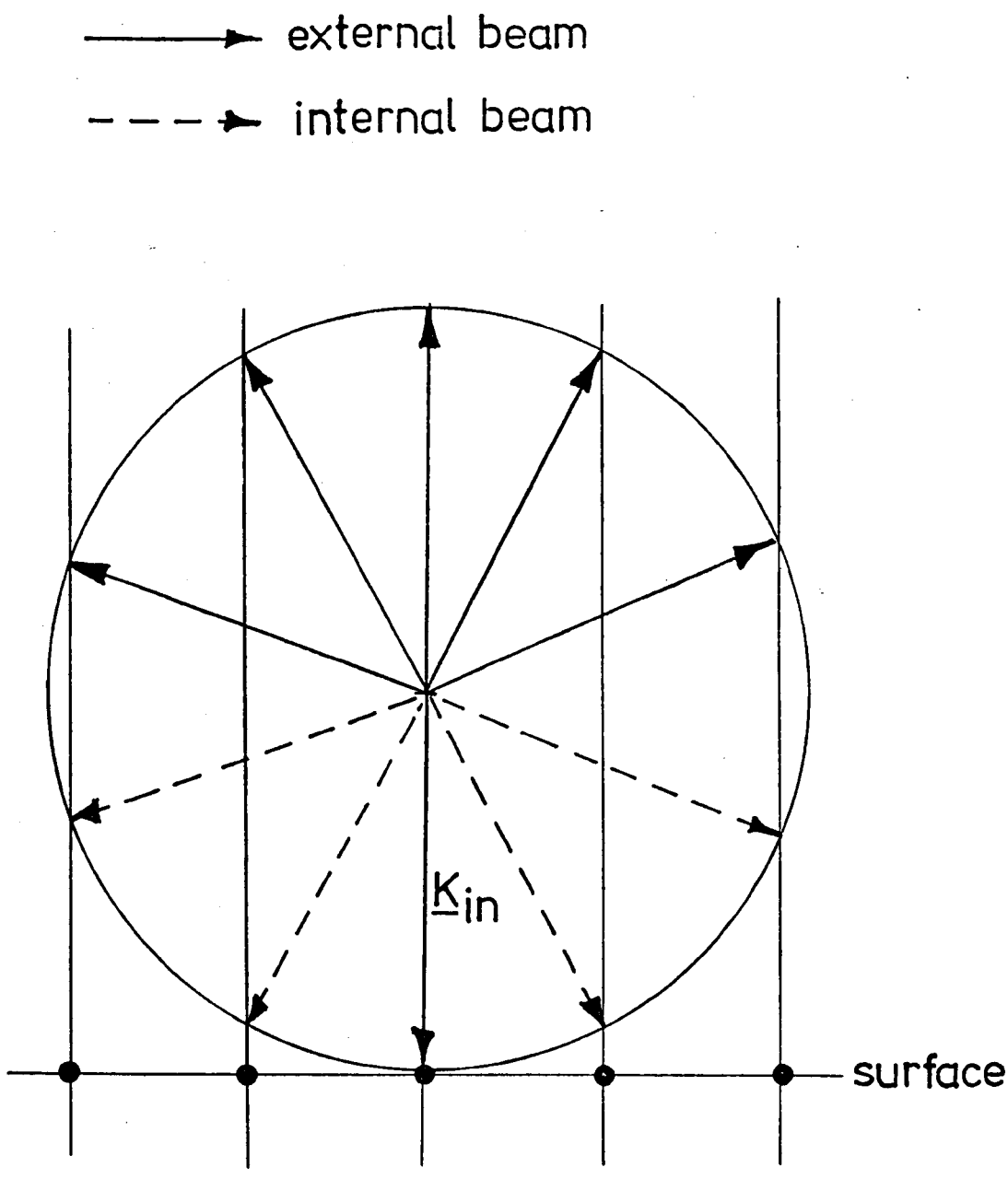

Figure 2.4 The Ewald sphere construction for normal incidence onto the (100) surface of a f.c.c. crystal. The intersection of the Ewald sphere with the reciprocal lattice rods defines the allowed beams.

2.2.1 Surface Crystallography

A crystal may be described by reference to a regular array of points in three-dimensional space, termed a *lattice*, such that the arrangement of atoms around any lattice point is identical to that around every other lattice point. The arrangement of atoms around the lattice points is termed the *basis* or *unit cell*. Lattice points are related by the following translation operations:

$$\underline{T}_b = n_a\underline{a} + n_b\underline{b} + n_c\underline{c} \qquad \ldots 2.7$$

where n_a, n_b and n_c are integers and $\underline{a}$, $\underline{b}$ and $\underline{c}$ are translation vectors with dimensions equal to the sides of the unit cell and directions parallel to the sides of the unit cell.

For a crystal surface, although the full three-dimensional symmetry of the bulk is lost, translational symmetry within the surface plane is retained and is characterised by the following two-dimensional translation operations:

$$\underline{T}_s = n_a\underline{a} + n_b\underline{b} \qquad \ldots 2.8$$

It can be shown that perfect two-dimensional symmetry only allows a finite number of different types of rotation with only those rotations through an angle of $2\pi/N$ where N = 1, 2, 3, 4 or 6 being allowed. These five rotations allow the types of primitive translations to be classified; for example, rotations through $2\pi/3$ and $2\pi/6$ must be associated with hexagonal lattices. Mirror operations also restrict the types of primitive translations and consequently only five two-dimensional Bravais lattices are possible and these are shown in figure 2.5. The symmetry of the surface is not fully described by its Bravais lattice alone; the basis will remain invariant under certain symmetry operations and the collection of symmetry operations that leave the basis and the lattice invariant is termed a *crystallographic point group* for which there are ten in two dimensions. The total symmetry of a crystal surface is then described by the combination of the Bravais lattice and the crystallographic point group of the basis and the lattice

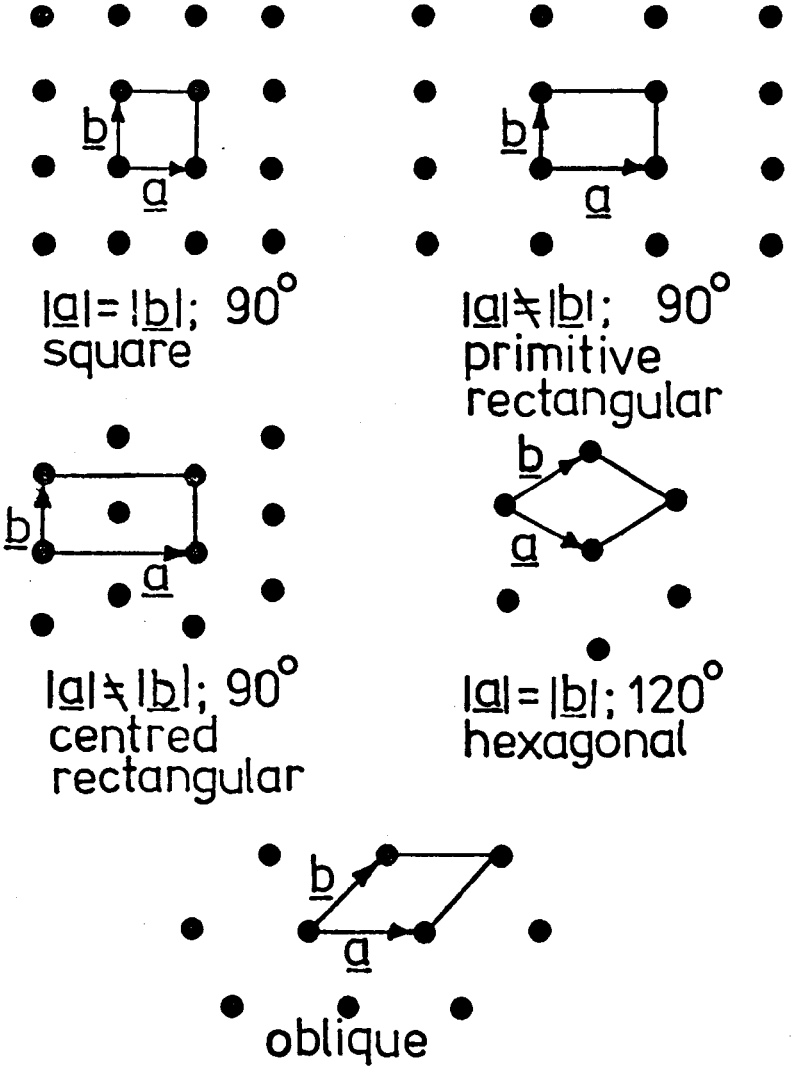

Figure 2.5 The five two-dimensional Bravais lattices.

to provide one of the seventeen two-dimensional *space groups*. These space groups have been considered in detail by Wood.[19]

2.2.2 LEED Nomenclature

The parameters used to define the scattering geometry of LEED are defined in figure 2.6. The angle of incidence θ was taken as the angle between the direction of the incident electron beam and the outgoing surface normal $\underline{n}$. The angle of azimuth ϕ was defined as the angle between an arbitrarily chosen direction within the crystal surface and the plane containing both the incident beam direction and the surface normal. Throughout this work the convention adopted to define $\phi = 0^0$ was that particular direction in the crystal surface corresponding to the shortest vector in the real surface net.

The reciprocal net vector $\underline{G}_{hk}$ provides a useful parameter for indexing diffraction beams in LEED. For a given two-dimensional Bravais lattice with primitive translation vectors $\underline{a}$ and $\underline{b}$ the corresponding reciprocal net vectors $\underline{G}_a$ and $\underline{G}_b$ are given by:

$$\underline{G}_a = 2\pi \frac{\underline{b} \times \underline{n}}{\underline{a} \cdot \underline{b} \times \underline{n}} \qquad ...2.9$$

and

$$\underline{G}_b = 2\pi \frac{\underline{a} \times \underline{n}}{\underline{b} \cdot \underline{a} \times \underline{n}} \qquad ...2.10$$

where

$$\underline{a} \cdot \underline{G}_a = \underline{b} \cdot \underline{G}_b = 2\pi \qquad ...2.11$$

and

$$\underline{a} \cdot \underline{G}_b = \underline{b} \cdot \underline{G}_a = 0 \qquad ...2.12$$

A reciprocal net vector can then be constructed:

$$\underline{G}_{hk} = h\underline{G}_a + k\underline{G}_b \qquad ...2.13$$

where h and k are integers. $\underline{G}_{hk}$ is perpendicular to the two-dimensional planes with *(hk)* indices and its length is $2\pi / d_{hk}$ where d_{hk} is the corresponding interplanar spacing.

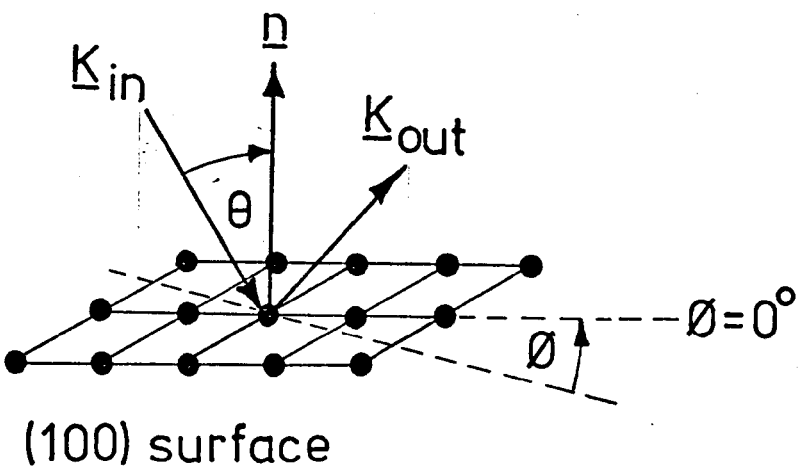

Figure 2.6 Definition of the scattering geometry of LEED.

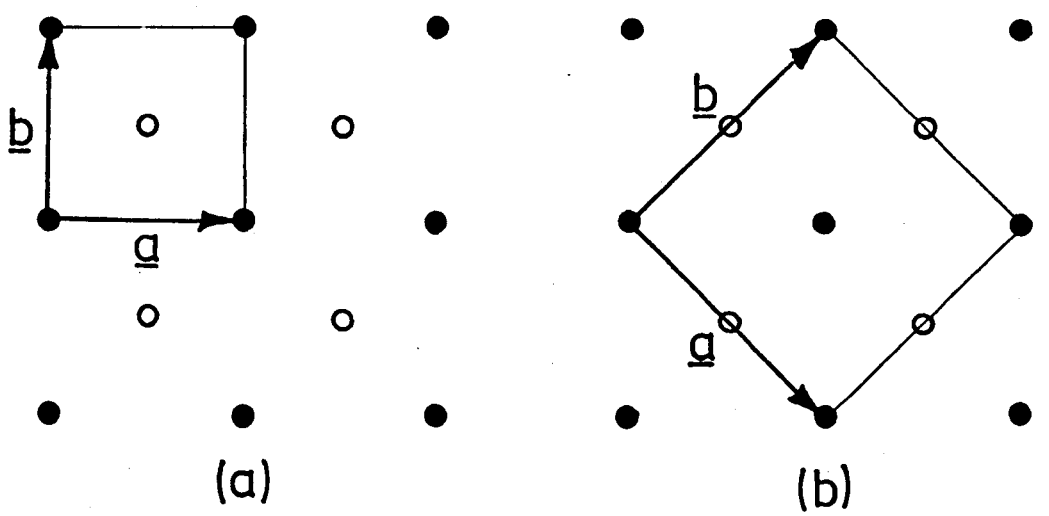

Figure 2.7 The primitive two-dimensional unit cell (a) and the three-dimensional (or X-ray) unit cell projection (b). Atoms in the top layer are denoted ● while atoms in the second layer are denoted O .

LEED patterns can then be indexed using (hk) indices commencing with the designation of the specular beam as (00). The current LEED literature has become extremely confused due to the use of two indexing systems that are based on two different unit cells. For example, the first diffraction beams to emerge from the (100) surface of f.c.c. crystals can be indexed as either (10) or (11) depending on whether the primitive two-dimensional net or the three-dimensional unit cell is used (figure 2.7). The notation that has been used here is the former one which allows a self-consistent indexing of an isolated surface layer, whereas the latter is artificial in requiring the indexing of a surface to be consistent with the bulk structure in a situation where the three-dimensional periodicity does not exist. LEED beams are normally indexed with respect to the clean or unreconstructed surface in the case of an adsorbate or a reconstructed surface respectively, using a fractional order notation for the extra beams produced.

A useful method of determining the real space lattice of an unknown surface structure from the indices of its LEED pattern has been suggested by Park and Madden.[20] From equation 2.11 two matrices $\underline{A}$ and $\underline{G}$ can be constructed such that:

$$\underline{A} = \underline{G}^{-1} \qquad \ldots 2.14$$

If the components of $\underline{G}$ are taken as the indices of the fractional order beams and expressed in terms of the clean, or unreconstructed,surface then its inverse $\underline{A}$ will provide the coordinates of the basis vectors of the real net in terms of the primitive net vectors of the primary surface structure.

Where a surface structure is known to be associated with a particular adsorbate the chemical symbol or formula for the adsorbate and also the substrate are generally incorporated into the description of the surface structure. For example, for a copper (100) surface on which oxygen has adsorbed in a structure that has the same unit mesh as the substrate the description would be Cu(100)-(1x1)-O. This notation will be used throughout this thesis.

2.3 Theory of LEED

2.3.1 The Electron-Solid Interaction

On entering a crystal an electron is scattered in several ways: by the surface barrier produced by the step in potential at the crystal surface, by interactions with the conduction or valence electrons and by interactions with the ion-cores.

Inadequacies existing in the present treatment of a realistically dense inhomogeneous electron gas have been overcome by the use of simple models in which the valence electron gas is considered to be uniform as far as a boundary plane situated adjacent to the top layer of ion-cores. In practice an electron would see a smoothly varying potential, due to the valence electrons, that scatters weakly on comparison with the ion-cores. LEED theories however usually adopt an unrealistic sharp potential step at the surface and then circumvent its strong scattering characteristic by neglecting any scattering from the boundary of the electron gas, although refraction at the boundary is generally included in order to obtain correct emergence angles for the diffracted beams.

The incident electron undergoes two types of interaction with the electron gas; virtual excitations that produce a correlation hole around the incident electron with a lowering of its energy while real excitations, mainly surface and volume plasmon losses and interband transitions, result in inelastic scattering. These interactions are incorporated into the *self-energy* of the electron which is given as:

$$\Gamma(E) = Vo_r(E) - iVo_i(E) \qquad \ldots 2.15$$

where

$$Vo_i(E) = \hbar(2(E + Vo_r(E))/m)^{\frac{1}{2}}/\lambda_{ee} \qquad \ldots 2.16$$

The real part of the self-energy $Vo_r(E)$ is known as the *inner potential* and accounts for that extra energy acquired by the electron on entering the crystal while the imaginary part of the self-energy $Vo_i(E)$ represents the electron

intensity absorbed from the elastic flux by inelastic and incoherent processes.

Although Pendry[21] has performed reasonably accurate calculations of the inner potential for nickel and niobium, the more usual approach has been to ignore the energy dependence of the inner potential and to use:

$$Vo_r \simeq E_F + \phi_f \qquad \ldots 2.17,$$

where E_F is the *Fermi energy* and ϕ_f is the *work function*. A particularly unfortunate feature of such an approximation is that the value of inner potential that correctly locates the energies of major LEED intensity features for one particular crystal surface may fail to do so on another surface to an extent that is often greater than the respective difference in work function; this is particularly noticeable for tungsten.[22]

At the ion-cores a non-uniform potential produces strong scattering of electrons in a highly energy-dependent manner. There are three contributions to this potential: the potential of the nucleus, the potential due to the core electron density and an exchange potential between the incident electrons and those core electrons with parallel spin. Screening of the ion-core potential is only important at low energies where the ion-core scattering is considerably weakened by the cancellation effects of the core states. At higher energies this cancellation effect is much weaker and Pendry[23] has shown that the scattering power of the potential for copper increases by a factor of ten between 10 and 100 eV.

An accurate construction of the ion-core potential is of paramount importance in an exact description of elastic scattering. Several approximations however are involved in such a construction and these limit the intrinsic accuracy of LEED calculations. The first approximation occurs in the calculation of the charge densities at the atoms. There are two basic approaches which involve either a linear superposition of charge densities, while allowing charge overlap, or a renormalised approach where

charge overlap is not allowed. A comparison of these two approximations with the arduous, but exact, self-consistent calculations by Wakoh[24] for nickel has shown that the linear superposition approach is by far the best approximation,[25] at least for this particular case. The second approximation occurs in the incorporation of exchange and correlation effects using either the Slater or Hartree-Fock terms. Neither of these corrections are a function of energy and both fail to include rigorous correlation effects; for example, the potential due to imaging of the incident electron is neglected. However, despite these shortcomings the ion-core potential has proved fairly insensitive to exchange effects by comparison with the effect of varying the charge densities.[25] The final approximation exists in the muffin-tin model used to describe the crystal, but in the absence of any rigorous description of the bulk crystal the effect of such an approximation can not be assessed.

Obviously, a detailed description of the scattering depends on the scattering properties of the particular ion-cores involved and also on the energy of the electrons. Whatever model is chosen for the scattering potential, its scattering characteristics are usually described in terms of phase shifts δ_l which are related to the atomic scattering factor $f(\theta)$ by the following equation:

$$f(\theta) = (2ik(E))^{-1} \Sigma_l (2l+1)(e^{2i\delta_l}-1)P_l \cos\theta \qquad \ldots 2.18$$

for the lth partial wave and where $k(E)$ is given by:

$$k(E) = (2m(E + \Gamma(E))/h^2)^{\frac{1}{2}} \qquad \ldots 2.19.$$

The differential cross-section for elastic scattering is then obtained from:

$$\frac{d\sigma}{d\Omega} = |f(\theta)|^2 \qquad \ldots 2.20$$

2.3.2 Kinematical Theory

The simplest description of electron-solid scattering uses the *Born approximation* of electron scattering from a rigid array of ion-core scatterers and forms the basis of the single scattering or *kinematical* theory. With the ion-cores taken as the basic scattering units and the effective wave-field incident on each scatterer taken to be the primary wave, the diffraction amplitude M is obtained as the sum of the atomic scattering factors f_j, each modified by a phase factor describing the propagation of a wave to the jth atom and back to the point of observation (defined relative to the jth atom by $\underline{r}_j$). Thus:

$$M = \Sigma_j f_j(K_{in}K_{out}) e^{i\underline{S}.\underline{r}_j} \qquad ...2.21$$

where $\underline{S}$ is the scattering vector defined by:

$$\underline{S} = \underline{K}_{out} - \underline{K}_{in} \qquad ...2.22$$

The summation in equation 2.21 is performed over all the atoms within the unit mesh of the surface and to infinite depth into the crystal.

It was appreciated as early as the original LEED experiments of Davisson and Germer that a kinematical description was completely inadequate in predicting the experimental behaviour of LEED intensities. Equation 2.21 predicts a series of delta functions located at the Bragg conditions that are too intense, too narrow and incorrectly located in energy when experimental intensity-energy spectra are examined. Even if the most kinematical peaks are selected in experimental spectra (see for example figure 2.8), i.e. the narrow single peaks located near the Bragg energies, their behaviour with changes in angle of incidence θ is not kinematical (the solid lines in figure 2.8 represent the variation predicted by kinematical theory). More particularly, experimental LEED intensities display a variation with angle of azimuth ϕ (figure 2.9) that, although less marked than the variation with θ, is significant in that kinematical

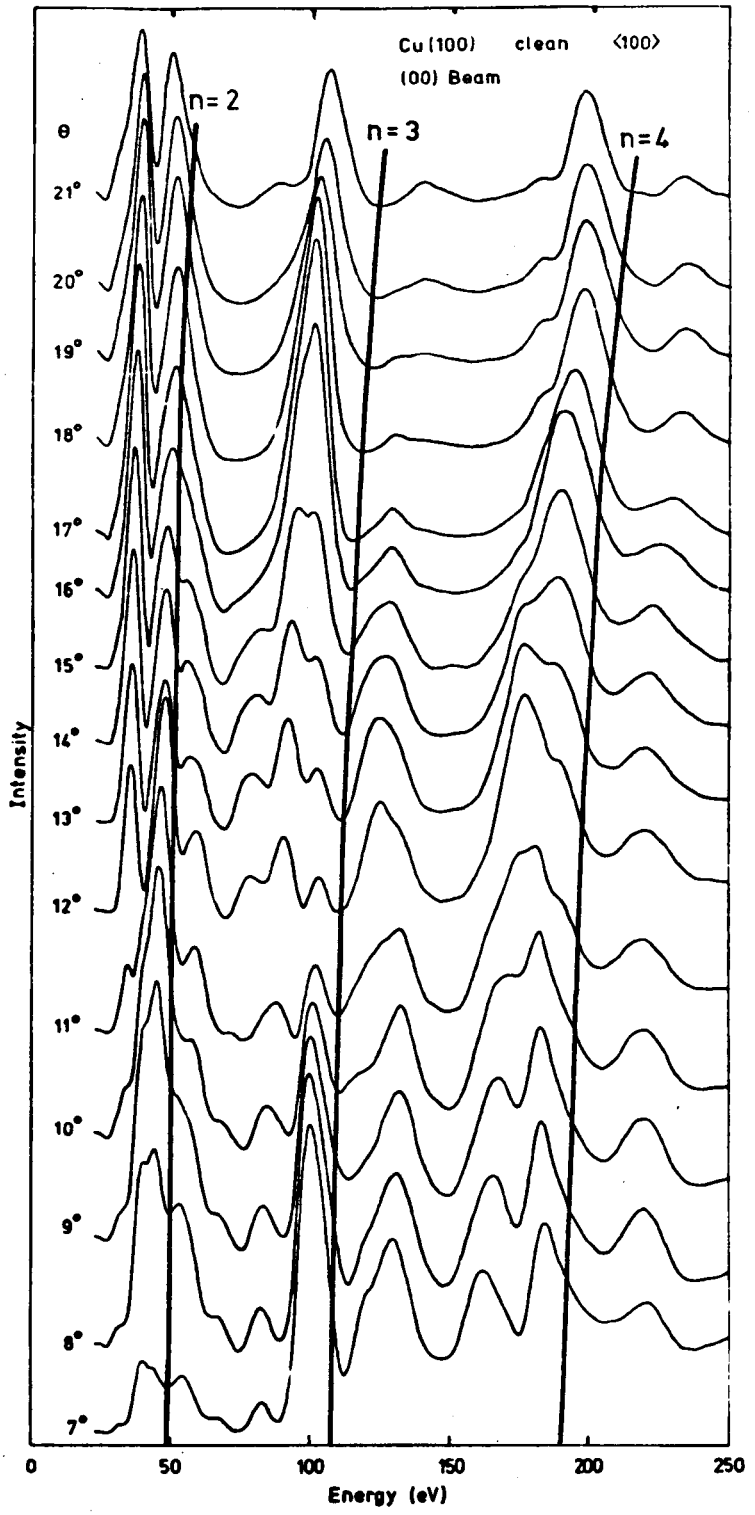

Figure 2.8 (00) beam intensity-energy spectra from clean copper (100) as a function of angle of incidence θ. The dependence predicted by kinematical theory is represented by the solid lines.

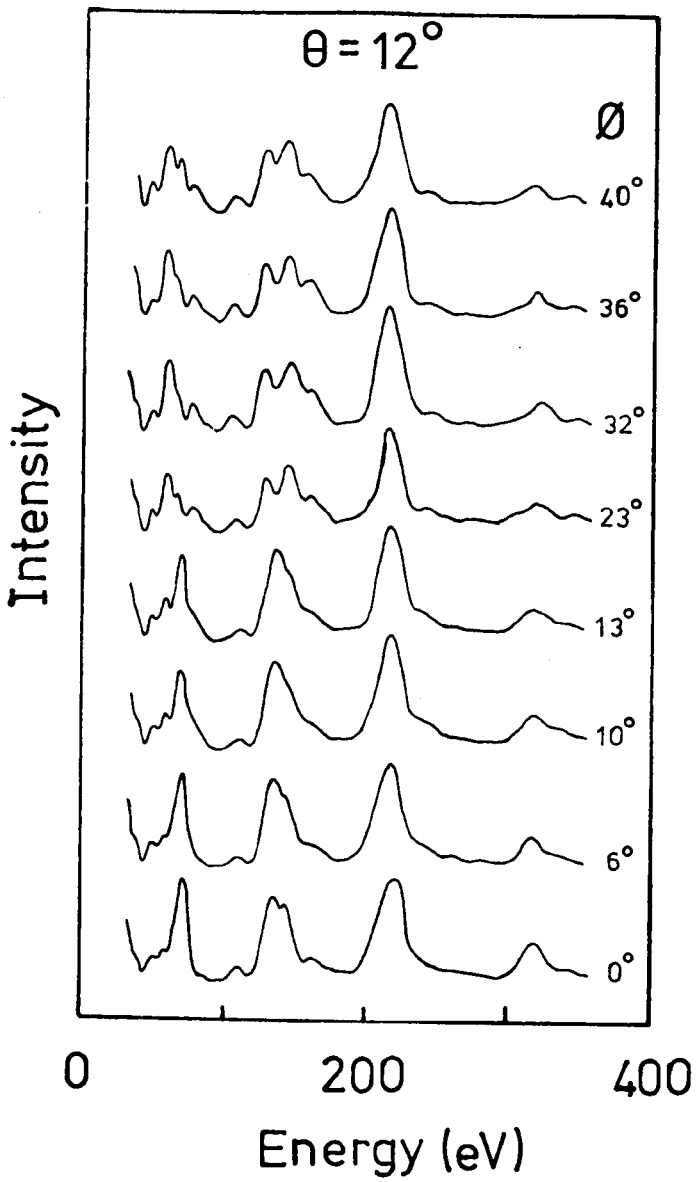

Figure 2.9 (00) beam intensity-energy spectra from clean copper (111) as a function of angle of azimuth ø. Kinematical theory does not predict an azimuthal variation.

theory does not predict a dependence on azimuth.

The most obvious flaw in equation 2.21 is the inclusion of scattering to infinite depth in the crystal. Although this paradox can be simply overcome by introducing a complex depth-dependent attenuation factor, such a modification fails to introduce the further structure required despite its promising effects of providing inner potential corrections to peak positions and also some peak broadening.

In an alternative formalism of kinematical theory, the atomic layers parallel to the surface of the crystal are taken as the basic scattering units. The diffraction amplitudes of the individual layers are then summed to obtain the diffraction amplitude of the crystal which is expressed in terms of the amplitude transmission coefficients $t_n(\underline{K}_{in})$ and the amplitude reflection coefficients $r_n(\underline{K}_{out}, \underline{K}_{in})$ for the individual layers where n is the layer index. For the specular beam from a crystal of identical and equally spaced layers of spacing d, the diffracted amplitude is:

$$M(\underline{K}_{out}, \underline{K}_{in}) = \frac{r(\underline{K}_{out}, \underline{K}_{in})}{1 - (t(\underline{K}_{in}) \exp(iK_{in}d)^2} \qquad \ldots 2.23$$

In an effort to produce the further structure required in the theoretical spectra double- and triple-diffraction schemes using the latter formalism have been proposed.[26,27] The double-diffraction model[26] involves a single back-scattering event and a single forward-scattering event and predicts secondary Bragg peaks. The extension of this approach to higher orders of inter-layer scattering is limited by the relative weakness of backscattering and the limited number of layers that can be considered to a triple-diffraction sequence[27] involving one back-scattering event and two forward-scattering events; the alternative sequence of three back-scattering events would produce negligible intensities. Although inadequate in themselves, models of this nature clearly demonstrated that realistic theories of LEED should incorporate all orders of multiple scattering.

2.3.3 Dynamical Theory

Models of low energy electron scattering that include all orders of multiple scattering are termed dynamical theories. Present LEED theories are based on formalisms that clearly reflect the historical development of LEED theory. Although the basis of the two approaches will be discussed separately in the following two sections a particular feature of current LEED theories is their growing similarity to one another. Regardless of the formalism of the LEED problem certain basic assumptions are common to both approaches. Firstly, the incident or primary beam of electrons is considered to be a plane wave. Thus:

$$\Psi_{in}(\underline{r},\underline{K}) = e^{i\underline{K}_{in}\cdot\underline{r}} \qquad \ldots 2.24$$

Secondly, the crystal model chosen is that of rigid static potentials located on a periodic lattice and is defined by the Hamiltonian:

$$H_o = \frac{h^2\nabla}{2m} + V \qquad \ldots 2.25$$

where H_o is the kinetic energy of the electron and V is the interaction energy of the electron with the ion cores.

2.3.3.1 The Wave-Function Matching Approach

In this model the differential form of the Schrodinger equation:

$$(\nabla^2+K^2)\Psi(\underline{r},\underline{K}) = u(\underline{r})\Psi(\underline{r},\underline{K}) \qquad \ldots 2.26$$

is solved to give the reflection coefficients by a smooth matching of the crystal wave-function with the vacuum wave-function at a sharp crystal/vacuum boundary. $u(\underline{r})$ in equation 2.26 is $2m/\hbar^2$ times the potential V. Here the crystal wave-function is described by a linear combination of Bloch waves while the vacuum wave-function is represented as a linear combination of plane waves.

Although the early calculations[28-30] based on this method involved a

very crude ion core potential, the resultant intensity-energy spectra and, more particularly their behaviour were much more representative of their contemporary experiments than the kinematical approach despite the generally poor agreement obtained.

Pendry[31] and Capart[32] for example have shown that when this approach is refined by using carefully constructed ion-core potentials the LEED spectra obtained possess a profusion of fine structure in excess of that required by experiment. Indeed, this rather ironic situation was entirely due to the absence of inelastic scattering from the calculations. Further calculations by Pendry[33] and others, that included inelastic scattering in the manner suggested by Hirabayashi[34] by introducing an imaginary component of V, yielded spectra with more subdued fine structure that were in better agreement with experiment.

2.3.3.2 Multiple Scattering Theory

The alternative approach commences with the integral form of the Schrodinger equation:

$$\Psi(\underline{r},\underline{K}) = \Psi_{in}(\underline{r},\underline{K}) - 1/4\pi \int_{\underline{r}'} G(\underline{r},\underline{r}')u(\underline{r}')\Psi(\underline{r}',\underline{K})\, d^3r' \qquad \ldots 2.27$$

where $\Psi_{in}(\underline{r},\underline{K})$ is the incident beam, $G(\underline{r},\underline{r}')$ is a Green function and $u(\underline{r}')$ is the potential. In the multiple scattering formalism the effective wave-field incident on any given atom is the sum of the primary wave-field and all the fields emitted by all the other atoms. Consequently the field emitted by any atom is a function of all fields emitted by all the other atoms and for sufficiently large scattering cross-sections multiple scattering of all orders will result.

Although originally formulated by Lax[35] in 1951, the first application of the multiple scattering concept to LEED was made by McRae[36] in 1966 and subsequently developed more rigorously by Kambe[37] and Beeby.[38] An important feature of the latter developments was the separate treatment of inter- and

intra-layer scattering processes. Good agreement with experiment was not achieved until inelastic damping was included following the suggestion of Duke and Tucker.[39]

The inelastic-collision model of Duke and Tucker has been developed from an approximate treatment involving isotropic scatterers[40] to the exact microscopic model in present use where detailed ion-core scattering is incorporated.[41] Inelastic scattering is included by considering the wave-function of the incident electron to be distorted by the inelastic processes before, during and after multiple elastic scattering by the ion cores.

2.3.4 Data Reduction Methods

Although kinematical theory fails to predict observed intensities in LEED kinematical effects can be discerned in experimental spectra. For example, although LEED spectra are dominated by complex fine (multiple scattering) structure, intensities are generally largest near to the primary Bragg conditions. Indeed multiple scattering calculations show that the centroid in energy of groups of multiple scattering features display the dependence on scattering geometry predicted for kinematical Bragg peaks. Although implicit in calculations by Morse[29], its significance was only recently established by Duke and Tucker[39] who conceived individual LEED spectra as dense arrays of randomly (sic) located individual multiple-scattering peaks modulated by a kinematical "Bragg envelope". This type of behaviour is illustrated in figure 2.10 where the LEED spectra of figure 2.8 have been displayed (after correction for an inner potential of 14 eV) as a $\underline{K}$-space polar diagram of the type proposed by Seah[42] where peaks in the original spectra are now represented as dots whose magnitude indicates the relative intensity. From figure 2.10 it can be seen that the peaks are distributed in both size and position about the primary Bragg conditions,

An immediate implication of the apparent validity of the "Bragg envelope concept" is the consideration as to whether the kinematical information retained by LEED intensity-energy spectra can be satisfactorily extracted

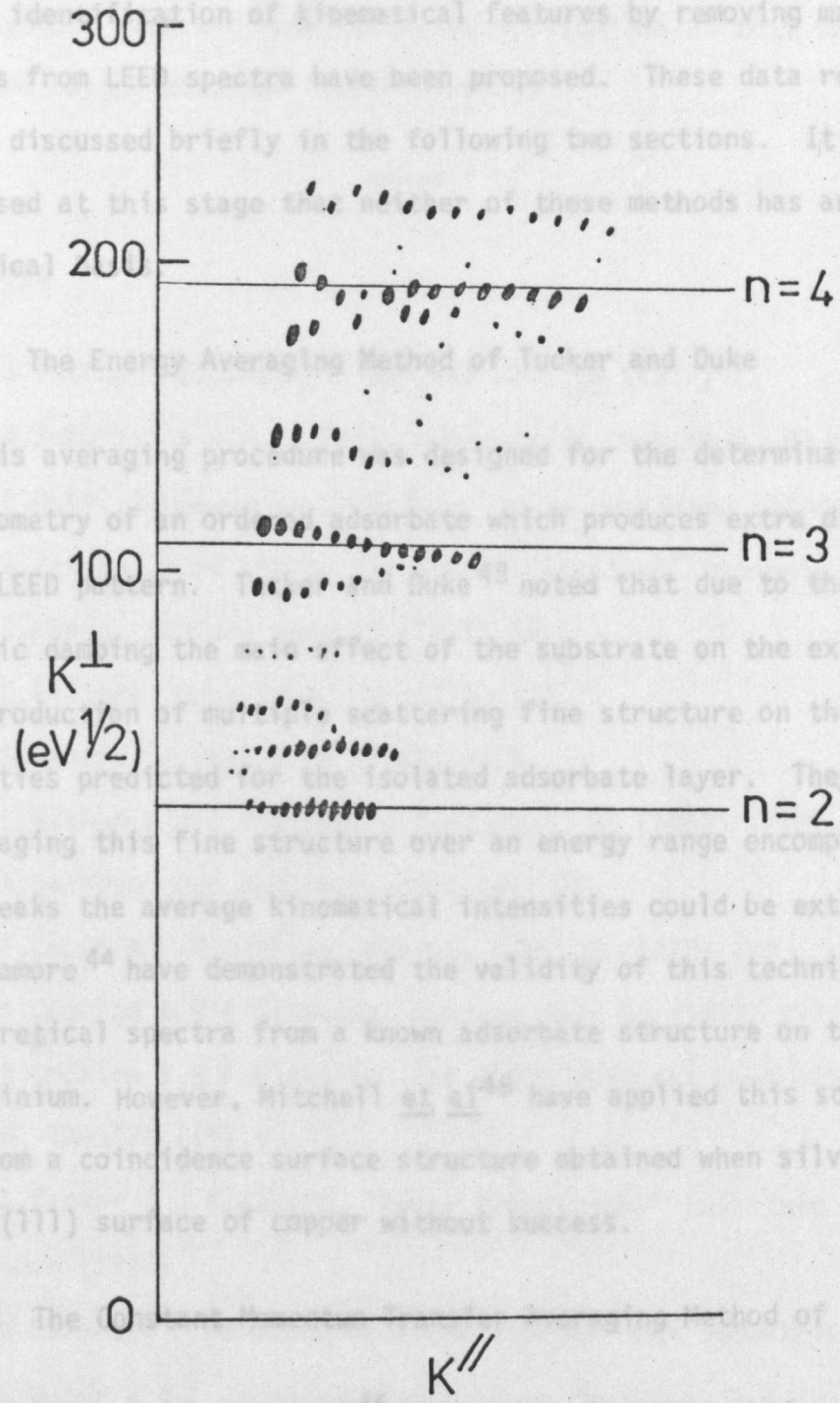

Figure 2.10 *K*-space polar diagram of the intensity-energy spectra shown in figure 2.8. Peaks in the original spectra are now represented by dots whose magnitude indicates the intensity. An inner potential of 14 eV has been included and the horizontal lines represent the kinematic predictions.

and interpreted in terms of surface structure. To this end two techniques for the identification of kinematical features by removing multiple scattering features from LEED spectra have been proposed. These data reduction methods will be discussed briefly in the following two sections. It should be emphasised at this stage that neither of these methods has any firm theoretical basis.

2.3.4.1 The Energy Averaging Method of Tucker and Duke

This averaging procedure was designed for the determination of the unit cell geometry of an ordered adsorbate which produces extra diffraction beams in the LEED pattern. Tucker and Duke[43] noted that due to the strength of inelastic damping the main effect of the substrate on the extra beams was the introduction of multiple scattering fine structure on the kinematical intensities predicted for the isolated adsorbate layer. They proposed that by averaging this fine structure over an energy range encompassing several Bragg peaks the average kinematical intensities could be extracted. Duke and Laramore[44] have demonstrated the validity of this technique when applied to theoretical spectra from a known adsorbate structure on the (100) surface of aluminium. However, Mitchell et al[45] have applied this scheme to "real" data from a coincidence surface structure obtained when silver is deposited on the (111) surface of copper without success.

2.3.4.2 The Constant Momentum Transfer Averaging Method of Lagally et al.

Lagally et al's proposal[46] is based on the observation that whereas multiple scattering depends explicitly on the propagation vectors of the incident, diffracted and intermediate diffraction beams,single scattering depends only on the scattering vector $\underline{S}$ where $\underline{S}$ is defined in equation 2.22. The assumption then is that if intensities are averaged such that $\underline{S}$ is kept constant, i.e. for constant momentum transfer, then the multiple scattering contributions to the intensity-energy spectra might average out to a constant background, thereby revealing the kinematic contribution to the intensities.

This data reduction method will be discussed in greater detail in chapter six together with the results of the application of this technique to both clean and oxygen adsorbed copper surfaces.

*****

REFERENCES

(1) P.J.Estrup & E.G.McRae. *Surface Sci.* 25 (1971) 1.

(2) G.A.Somorjai & H.H.Farrell. *Advances in Chem.Phys.* 20 (1971) 215.

(3) C.B.Duke. *Advances in Chem.Phys.* to be published (1974).

(4) J.B.Pendry. "Low Energy Electron Diffraction" Academic Press (1974)

(5) C.C.Chang. *Surface Sci.* 25 (1971) 53.

(6) J.C.Riviere. *Cont.Phys.* 14 (1973) 513.

(7) J.B.Pendry. *J.Phys.C.* 2 (1969) 2273.

(8) H.E.Bishop & J.C.Rivière. *J.Appl.Phys.* 40 (1969) 1740.

(9) J.A.Bearden. *Rev.Mod.Phys.* 39 (1967) 78.

(10) M.F.Chung & L.H.Jenkins. *Surface Sci.* 22 (1970) 172.

(11) W.A.Coghlan & R.E.Clausing. *Surface Sci.* 33 (1972) 411.

(12) W.A.Coghlan & R.F.Clausing. Oak Ridge National Laboratory Report ORNL-TM-3576 (1971).

(13) M.E.Packer & J.M.Wilson. "Auger Transitions" Institute of Physics London (1973).

(14) P.W.Palmberg. "Handbook of Auger Spectra" Phi Industries Inc.

(15) R.E.Weber & A.L.Johnson, *J.Appl.Phys.* 40 (1969) 314.

(16) M.Perdereau, *Surface Sci.* 24 (1971) 239.

(17) M.P.Seah, *Surface Sci.* 32 (1972) 703.

(18) C.J.Davisson & L.H.Germer. *Phys.Rev.* 30 (1927) 705.

(19) E.A.Wood. *J.Appl.Phys.* 35 (1964) 1306.

(20) R.L.Park & H.H.Madden,Jr. *Surface Sci.* 11 (1968) 188.

(21) J.B.Pendry. *J.Phys.C.* 2 (1969) 1215.

(22) R.M.Stern & A.Gervais, *Surface Sci.* 17, (1969) 273.

(23) J.B.Pendry, *J.Phys.C.* 4 (1971) 2501.

(24) S.Wakoh, *J.Phys.Soc.Japan.* 20 (1965) 1984.

(25) J.B.Pendry, Institute of Physics Meeting,Imperial College,May(1974).

(26) E.G.McRae, *Surface Sci.* 11 (1968) 492.

(27) C.M.K.Watts, *J.Phys.C.* 1 (1968) 1237.

(28) H.Bethe, *Ann.d.Physik.* 87 (1928) 55.

(29) P.M.Morse, *Phys.Rev.* 35 (1930) 1310.

(30) D.S.Boudreaux & V.Heine, *Surface Sci.* 8 (1967) 426.

(31) J.B.Pendry, *J.Phys.C.* 2 (1969) 2273.

(32) G.Capart, *Surface Sci.* 26 (1971) 429.

(33) J.B.Pendry, *J.Phys.C.* 2 (1969) 2283.

(34) K.Hirabayashi, *J.Phys.Soc.Japan.* 24 (1968) 846.

(35) M.Lax, *Rev.Mod.Phys.* 23 (1951) 287.

(36) E.G.McRae, *Surface Sci.* 8 (1967)14.

E.G.McRae, *J.Chem.Phys.* 45 (1968) 3258.

(37) K.Kambe, *Z.Naturforsch.* 22a (1967) 322.

(38) J.L.Beeby, *J.Phys.C.* 1 (1968) 82.

(39) C.B.Duke & C.W.Tucker,Jr., *Surface Sci.* 15 (1969) 231.

(40) C.W.Tucker,Jr. & C.B.Duke, *Surface Sci.* 24 (1971) 31.

(41) G.E.Laramore & C.B.Duke, *Phys.Rev.B.* 5 (1972) 267.

(42) M.P.Seah, Ph.D.Thesis, University of Warwick (1969)

(43) C.W.Tucker,Jr. & C.B.Duke, *Surface Sci.* 23 (1970) 411; 29 (1972) 237.

(44) C.B.Duke & G.E.Laramore. *Surface Sci.* 30 (1972) 659.

(45) K.A.R.Mitchell,D.P.Woodruff & G.W.Vernon. submitted to *Surface Sci.*

(46) M.G.Lagally,T.C.Ngoc & M.B.Webb. *Phys.Rev.Lett.* 26 (1971) 1557.

CHAPTER THREE. THE COMBINED FARADAY CUP AND LEED DISPLAY SYSTEM

A schematic diagram of the original LEED experiment of Davisson and Germer is shown in figure 3.1 and can be seen to have consisted of a Faraday cup that could be moved in a fixed plane about the specimen. This arrangement was also adopted by Farnsworth for his initial LEED work.[1] The main disadvantage of this method was the difficulty encountered in determining the LEED pattern: the crystal had to be rotated around the axis of the normally incident electron beam while the Faraday cup had to be traversed through the range of emergence angles available in order to intercept all the non-specular beams defining the reciprocal net.

Ehrenberg[2] overcame this severe difficulty by developing a post-retardation acceleration display which allowed the instantaneous observation of the LEED pattern on a fluorescent screen. His method, the forerunner of the present two- and three-grid LEED optics, is shown schematically in figure 3.2. Fine metal grids were used to filter out the inelastic electrons electrostatically after which the elastic electrons were accelerated onto a phosphor coated screen where their fluorescence could be readily observed. This arrangement was later adapted by Scheibner *et al*[3] who dispensed with Ehrenberg's cylindrical geometry and adopted a purely planar arrangement. Both of the latter arrangements produced a distorted LEED pattern which was considerably inconvenient. A hemi-spherically geometric display system was eventually developed by Lander *et al*[4] and this produced undistorted LEED patterns.

With the advent of commercially available versions of Lander *et al*'s LEED display system this method was rapidly adopted by the majority of workers entering the field of LEED. A notable exception to this trend was Farnsworth (*et al*) who continued to use a Faraday cup system which soon acquired a high degree of sophistication.

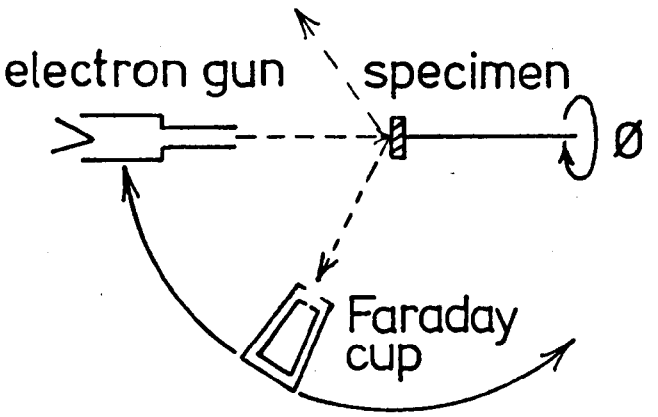

Figure 3.1 Schematic diagram of the experimental arrangement for LEED as used by Davisson and Germer.

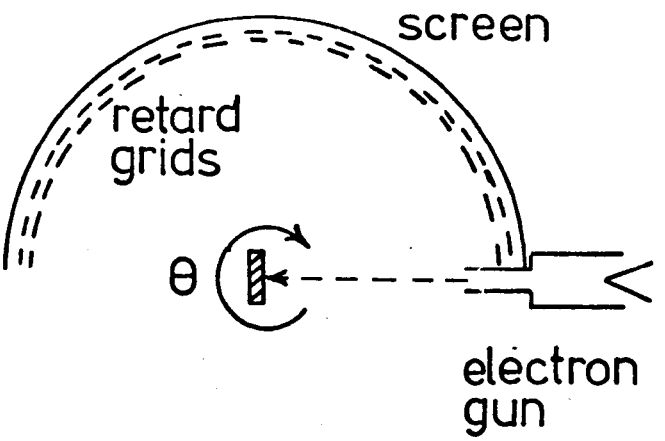

Figure 3.2 The post-retardation acceleration display system developed for LEED by Ehrenberg.

3.1 Intensity Measurements in LEED

3.1.1 The LEED Pattern

As the majority of experimental LEED systems in present use are of the fluorescent display type the LEED pattern can be readily observed and recorded using conventional photographic techniques. An alternative approach has been developed by Farnsworth *et al*[5] in which an automatically scanning Faraday cup intercepts the diffraction beams from a rapidly rotating specimen, thereby enabling the LEED pattern to be displayed electronically. The complexity of this technique in comparison with the direct display method has discouraged any adoption of this technique by other workers.

3.1.2 Intensity-Energy Spectra

Three methods of recording intensity-energy spectra are currently employed in LEED:

(a) Photographic recording from the fluorescent display.

(b) Photometric techniques using narrow angle spot-photometers focussed on the fluorescent screen.

(c) Direct diffracted beam current measurement using a Faraday cup.

Although the inherent simplicity of the photographic method and the ability to record the intensities of several diffracted beams simultaneously are particularly attractive features, this method is subject to several uncertainties in the calibration steps from film density to diffracted beam current. Experimental reproducibility requires a rigorous control over film processing while the non-linear responses of both the fluorescent screen phosphor and the photographic film emulsion present further difficulties. For large energy ranges this method has often to be limited for convenience to fairly coarse energy increments which prove unsatisfactory in comparisons with theory. Selection of this technique then is usually dictated by absolute necessity rather than by preference.

The most widely used method is the photometric technique in which a narrow acceptance angle spot photometer is focussed on the fluorescence emitted by the LEED display screen. This arrangement has several disadvantages:

(a) Difficulties arise with the alignment of the externally mounted spot photometer making it cumbersome to use. The extreme difficulty of reliably tracking non-specular beams, which converge onto the specular beam with increasing electron energy, often restricts measurements to the stationary specular beam.

(b) The non-linear responses of the LEED screen phosphor and the spot photometer photocell severely limit the accuracy of this method.

(c) The signal to noise ratio of the ancillary electronics is usually poor and consequently requires the use of long time constants in the detection system which severely limits the sweep speed at which the intensity-energy spectra can be acquired.

(d) Low energies and high angles of incidence are limited by the edge of the LEED screen while high energies and low angles of incidence are often limited by the physical dimensions of the specimen holder.

The restriction imposed on the experimental sweep speed by (c) is particularly disadvantageous as the range of data that can be acquired under specifically characterised surface conditions is often severely limited.

All of these difficulties can be overcome by using a Faraday cup to measure directly the electron current in the individual LEED beams. LEED systems that incorporate only a Faraday cup lose the advantage offered by a fluorescent display of a rapid visual assessment of surface order and thus the ideal arrangement for LEED is a combination of a fluorescent display for observing the LEED pattern and a Faraday cup to measure the intensity-energy spectra. This concept was successfully developed by Seah and Forty[6] using a rather unusual geometric arrangement in which the two measurements were physically separated within the experimental chamber. The arrangement adopted for the work reported here extends this approach by combining an

energy-analysing Faraday cup with a commercial LEED display in a more satisfactory manner which allows the simultaneous use of both monitoring techniques. The utilisation of standard components would allow the ready adaptation of most existing LEED systems to this technique.

3.2 Ultra High Vacuum System

The experimental system used throughout this study consisted of a purpose built stainless steel experimental chamber, constructed in the engineering workshops of the Department of Physics to a design by Woodruff, mounted on a commercial ultra high vacuum (UHV) pumping station.

3.2.1 Experimental Chamber

Two general views of the experimental chamber are shown in figures 3.3(a) and (b). The demountable flanges have machined knife-edges of the "Conflat" type and are vacuum sealed using oxygen free high conductivity (OFHC) copper gaskets. During commissioning of the experimental system some difficulty was experienced initially with leaking welds but once this was overcome pressures of 2×10^{-10} torr were routinely achieved following typical bakeout schedules of 24 hours at $220^{o}C$.

The ports available on this experimental chamber have been labelled in figures 3.3(a),(b) and their uses listed in table 3.1. The basic configuration consisted of three ports A, B and C arranged on the mutually perpendicular axes AD and BC whose intersection defined the specimen position for the electron scattering experiments. The experimental chamber was connected via a six inch diameter pumping line to the pumping station described in the following section.

3.2.2 UHV Pumping Station

Two separate pumping assemblies were available on the Vacuum Generators Ltd. UHV pumping station. UHV pumping was provided by a 120 l s^{-1} Ferranti

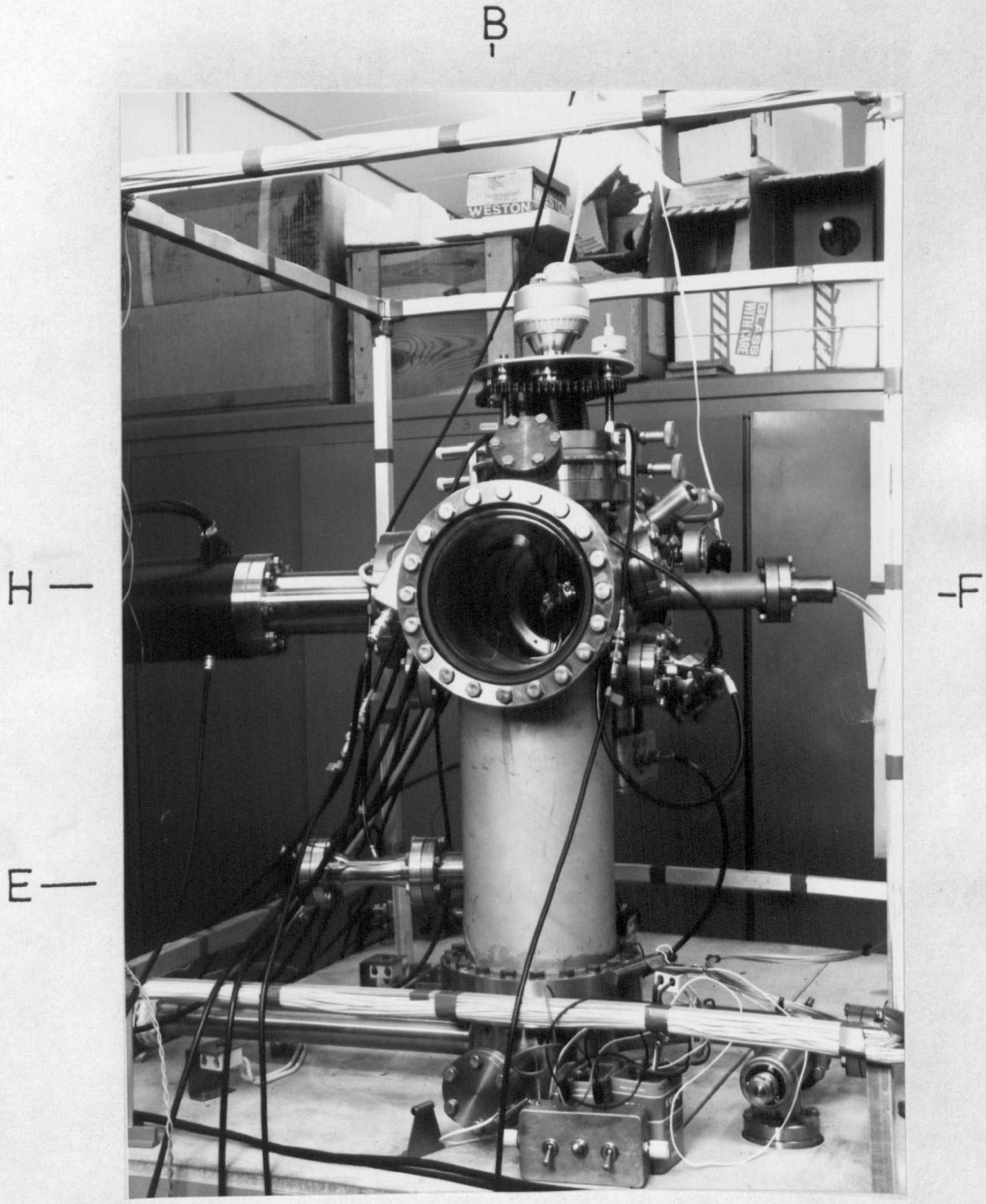

Figure 3.3(a) Front view of the combined Faraday cup/LEED display system.

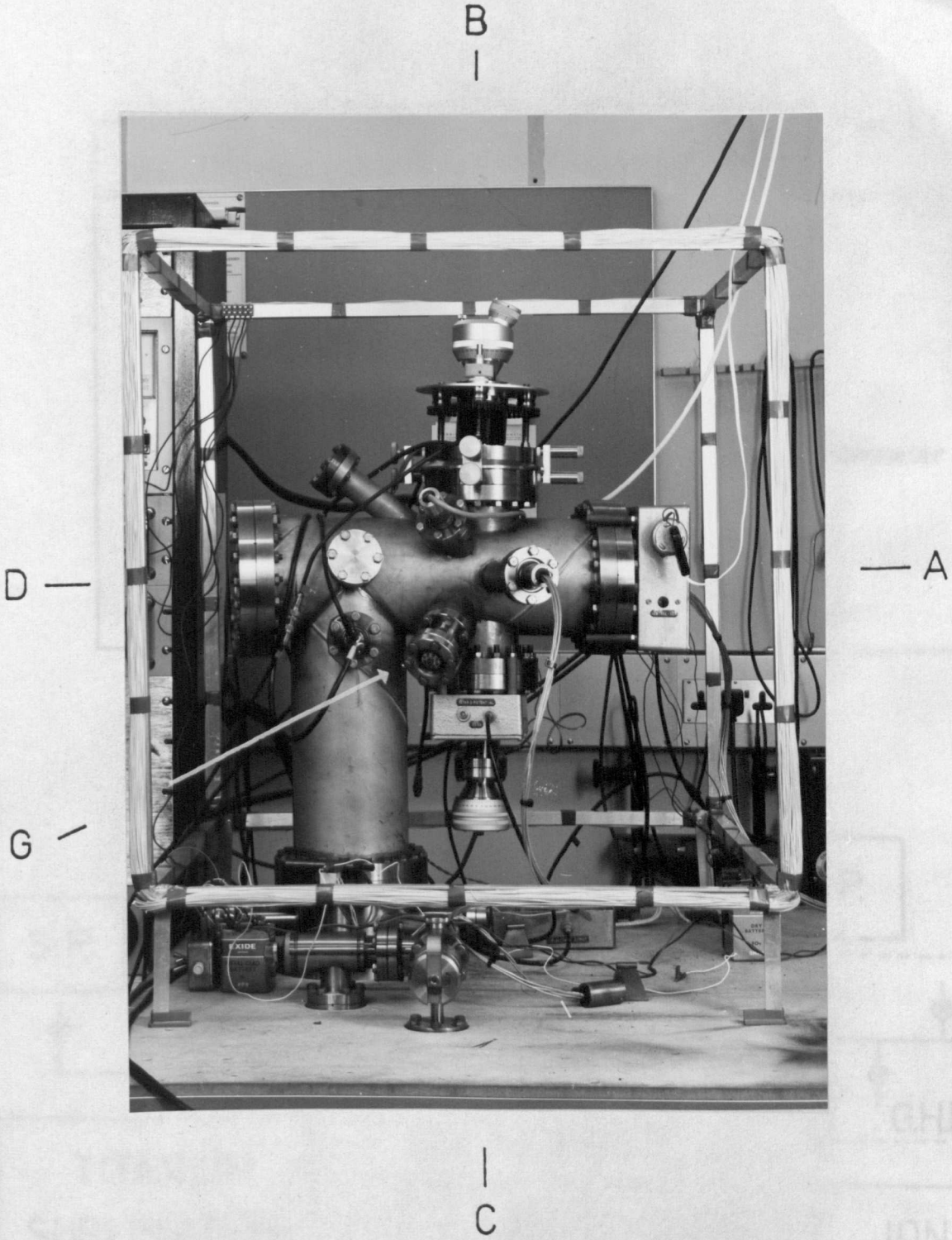

Figure 3.3(b) Side view of the combined Faraday cup/LEED display system.

TABLE 3.1

Port	Usage
A	LEED optics
B	Specimen manipulator
C	Faraday cup
D	Window
E	Micromass 2 magnetic mass spectrometer
F	SE3K/5U electron gun
G	Ion gun
H	Q7 quadrupole mass spectrometer

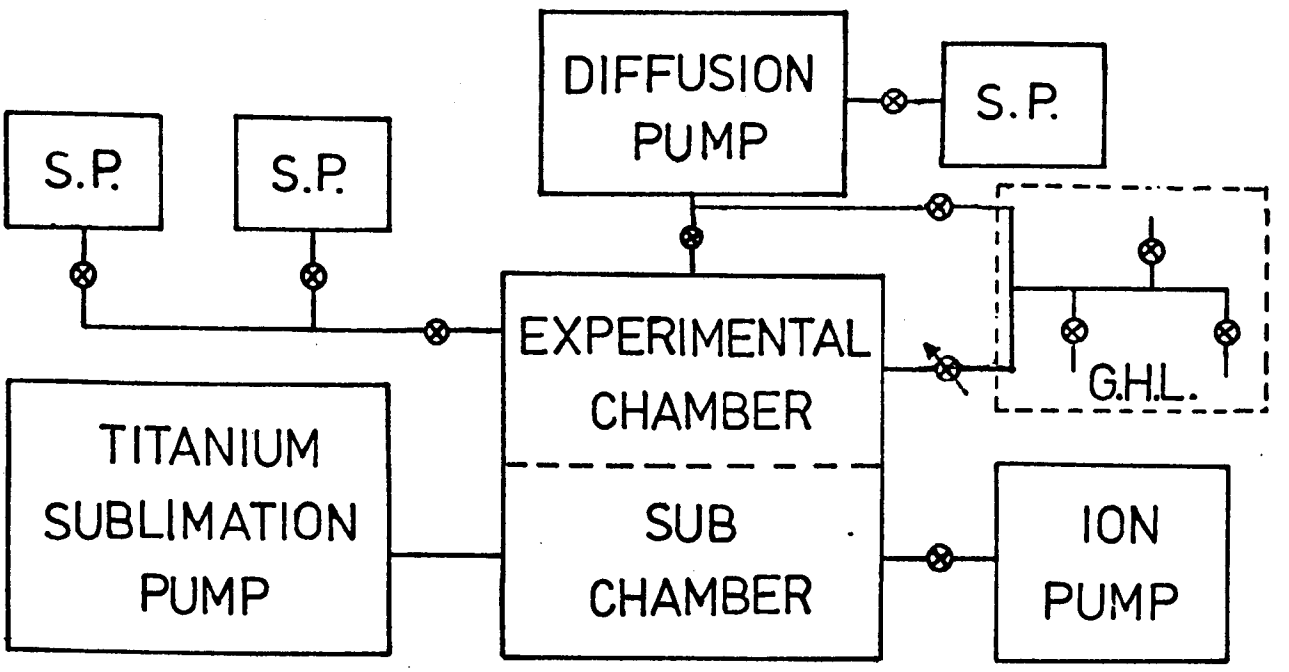

Figure 3.4 Schematic diagram of pumping system. where S.P. and G.H.L. represent a sorption pump and the gas-handling line respectively.

ion pump and an intermittently operated titanium sublimation pump, with provision for either water or liquid nitrogen cooling. As shown in the schematic diagram of the pumping system (figure 3.4) a valve enabled the ion pump to be isolated from the experimental chamber whenever it was required.

The secondary pumping facility provided was a four inch diameter mercury diffusion pump with integral cold trap which was used to evacuate either the experimental chamber or the gas handling line. An oil- and vibration-free system was obtained by using liquid nitrogen cooled sorption pumps to "back" the diffusion pump and also to "rough down" the entire system from atmospheric pressure.

With the ion pump isolated under UHV conditions and the experimental and sub chambers at atmosphere a typical UHV pumping schedule was as follows:

(a) Two sorption pumps were used in sequence to "rough down" the system from atmosphere to 10^{-3} torr.

(b) The diffusion pump was used to reduce the pressure to 10^{-6} torr.

(c) The experimental and sub chambers were than baked at 220^{0}C into the diffusion pump for about eight hours to give a pressure of 10^{-8} torr when cool.

(d) With the diffusion pump isolated, a further bake into the ion-pump was then performed for sixteen hours. While cooling the titanium sublimation pump filaments were outgassed and this pump was then operated on short cycles until pressures of the order of $5x10^{-10}$ torr were obtained.

(e) When cool all ion gun, electron gun and pressure gauge filaments were progressively outgassed to finally give a pressure of $2x10^{-10}$ torr.

3.2.3 Residual Gas Analysis

In order to allow the analysis of residual gas species two mass spectrometers were mounted on the experimental chamber: a Micromass 2 magnetic instrument on port E and a Q7 quadrupole mass spectrometer on port H (both instuments from VG Micromass Ltd.). The Micromass 2 was primarily used as a trouble-shooting instrument for leak detection and non-UHV partial

pressure analysis; its high magnetic field rendering it totally unsuitable for operation during electron scattering experiments. However, the non-magnetic Q7 with its high sensitivity of 10^{-13} torr enabled partial pressure analyses to be readily performed at total pressures of $2x10^{-10}$ torr. The Q7 spectrum shown in figure 3.5 was obtained at a base pressure of $5x10^{-10}$ torr and is typical of a baked UHV system of this type (the mass numbers of the major peaks are marked on the figure).

3.2.4 Gas Handling Facility

The gas handling facility (figure 3.4) enabled up to three different high purity gases to be introduced into the experimental chamber at carefully controlled rates via a needle leak valve. Only occasional baking of this line was necessary as pressures of about $5x10^{-7}$ torr were typically obtained using the diffusion pump. Usually it was sufficient to flush the gas-handling line with the required gas after an initial evacuation, re-evacuate and then backfill to about 1 torr. The provision of a Pirani gauge and a VIG 20 ion gauge on the gas-handling line enabled a wide range of pressures to be measured.

3.2.5 Specimen Heating Stage

The ability to heat the copper specimens to temperatures of the order of about $600^{o}C$ was necessary because of the usual cleaning procedure for copper and also because of the desire to study temperature dependences of LEED processes. The provision of a wide range of specimen rotation about two independent axes while allowing satisfactory heating was the major constraint on the design of a suitable heating stage. A further consideration was that of aligning the specimen surface as closely as possible to the axis of rotation that defined the angle of incidence θ of the electron beam. Displacement from this axis has two effects as the angle of incidence is altered: the source to specimen distance and also the electron beam position on the specimen vary.

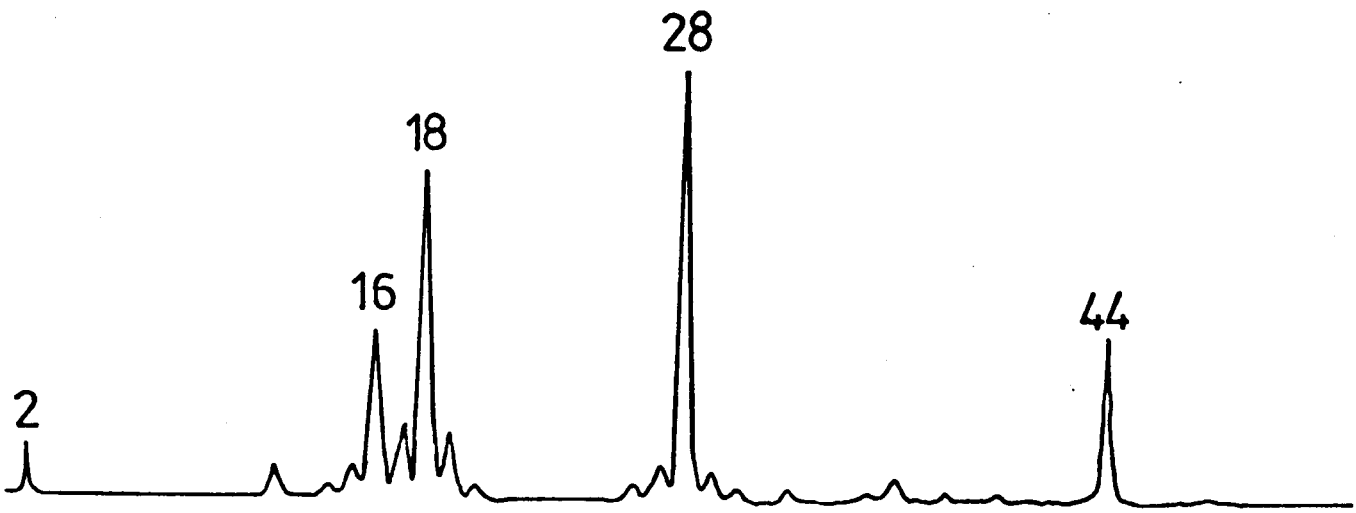

Figure 3.5 Quadrupole mass spectrum for typical UHV conditions. This spectrum was obtained at a total pressure of 5×10^{-10} torr and the major peaks have been identified by their mass number.

The design adopted is shown in figure 3.6 Two specimens were mounted in a recess on the stainless steel front plate and were positively located by a molybdenum mask with an 8 mm diameter hole that exposed the front surfaces of the specimens. A chromel-alumel thermocouple, held in contact with the specimen surface, was used to monitor the temperature of the specimens which was displayed on a calibrated digital voltmeter (Ether Ltd.). The specimens were heated by electron bombardment from a lanthanum hexaboride coated rhenium filament mounted behind the specimens on a ceramic support ring. Both the bombardment filament and the specimens were electrically isolated from each other and also from ground potential; during heating the filament was earthed while a positive potential was applied to the specimen as this arrangement minimised heating of the rest of the specimen manipulator. With 20 mA electron emission and a 1 KV accelerating potential available temperatures up to $800^{o}C$ were readily achieved.

The heating stage was mounted on a commercial double-motion rotary drive (RD2:Vacuum Generators Ltd.) that allowed a 350^{o} rotation about the vertical axis (to establish the angle of incidence θ) as well as a 180^{o} rotation about a horizontal axis normal to the specimen surface (to establish the angle of azimuth ϕ). A universal manipulator attached to the rotary drive allowed a tilt of $\pm 5^{o}$, a vertical translation of $\pm$ 1 inch and two mutually perpendicular horizontal translations of $\pm$ 0.5 inch with respect to the mean specimen position.

Although the heating stage was kept as compact as possible the specimen surfaces were several millimetres off the vertical axis of rotation of the manipulator. In order to ensure that the movement of the electron beam on the specimen that ocurred as θ varied did not affect the intensity-energy spectra acquired, normal incidence (00) beam spectra were obtained for different positions on the specimen and found to be identical.

Figure 3.6 Side view of specimen heating stage showing the electron bombardment filament assembly.

3.2.6 Specimen Preparation

Single crystal slices of about 1 mm thickness were spark-machined from a 12 mm diameter bar of 5N purity copper single crystal of random orientation (Metals Research Ltd.). The rod was oriented by X-ray Laue back-reflection to within 1^{o} of the desired orientation prior to spark machining. (100) and (111) orientation specimens were prepared and suitably sectioned, prior to polishing and cleaning, ready for mounting in the specimen stage.

The crystal region damaged by spark-machining was removed by acid-polishing using a solution of concentrated hydrochloric acid saturated with cuprous chloride and a polishing wheel of the type described by Young and Wilson.[7] Final polishing was performed using the same solution but with a flat-bed polisher. After a satisfactory finish was obtained the specimens were vapour degreased using trichloroethylene, mounted on the heating stage and then installed into the experimental chamber.

3.3 Electronic Configuration

The primary consideration in the design and commissioning of the electrical power supplies and the electronic detection system for LEED was the achievement of fast sweep rates for the acquisition of intensity-energy spectra without corrupting the data. Spot-photometer systems typically take at least 5 minutes to sweep an energy range of 300 eV which is clearly undesirable when large blocks of data are required for well characterised surfaces. Indeed slow sweep rates are particularly unsuitable for non-specular beams where repetitive sweeping is required in order to build up the individual spectra.

3.3.1 Three Grid LEED Optics

The commercial three grid LEED display, or optics, used in this work (Vacuum Generators Ltd.) can be seen, together with the Faraday cup, in figure 3.7 and a schematic diagram of the experimental configuration for LEED

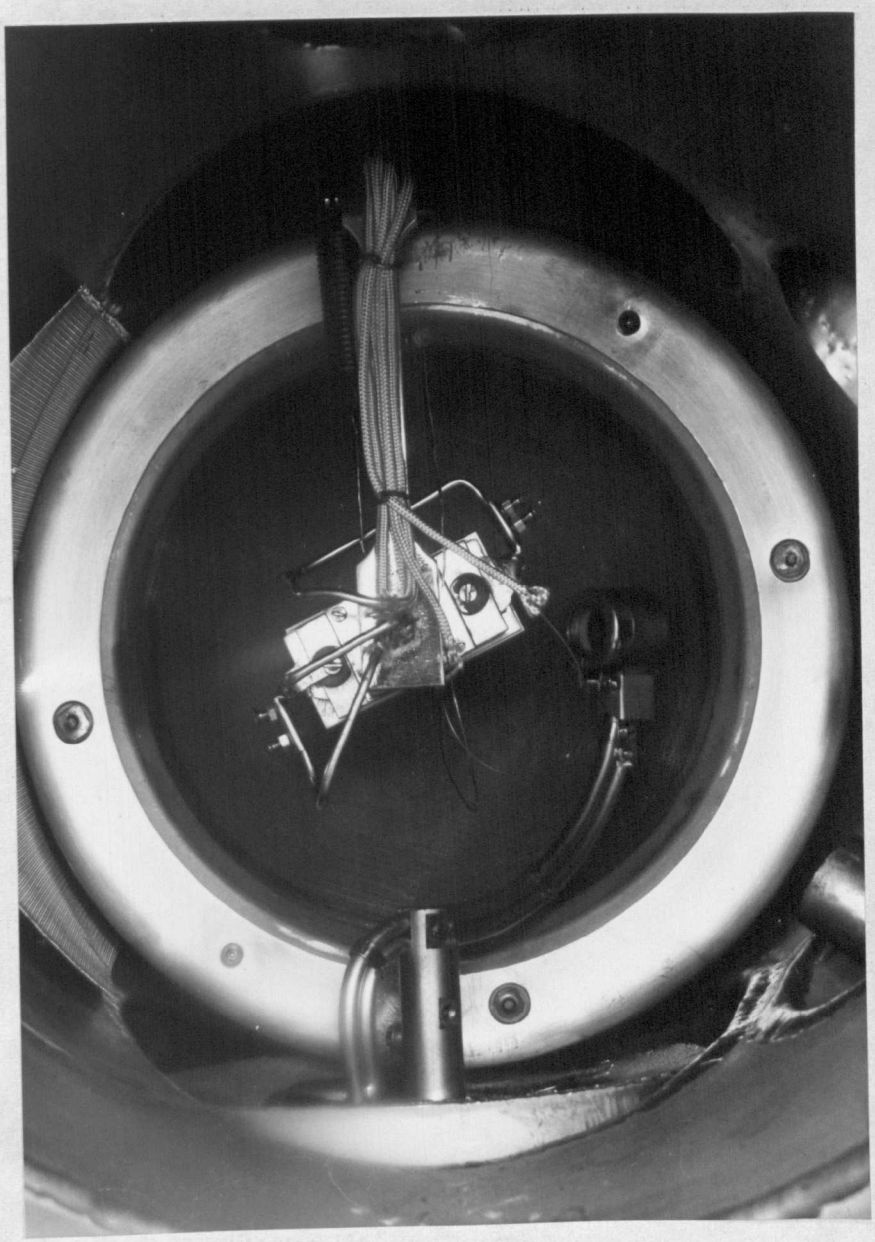

Figure 3.7 Internal view of experimental chamber showing the LEED optics at the rear and the Faraday cup to the right of the specimen manipulator.

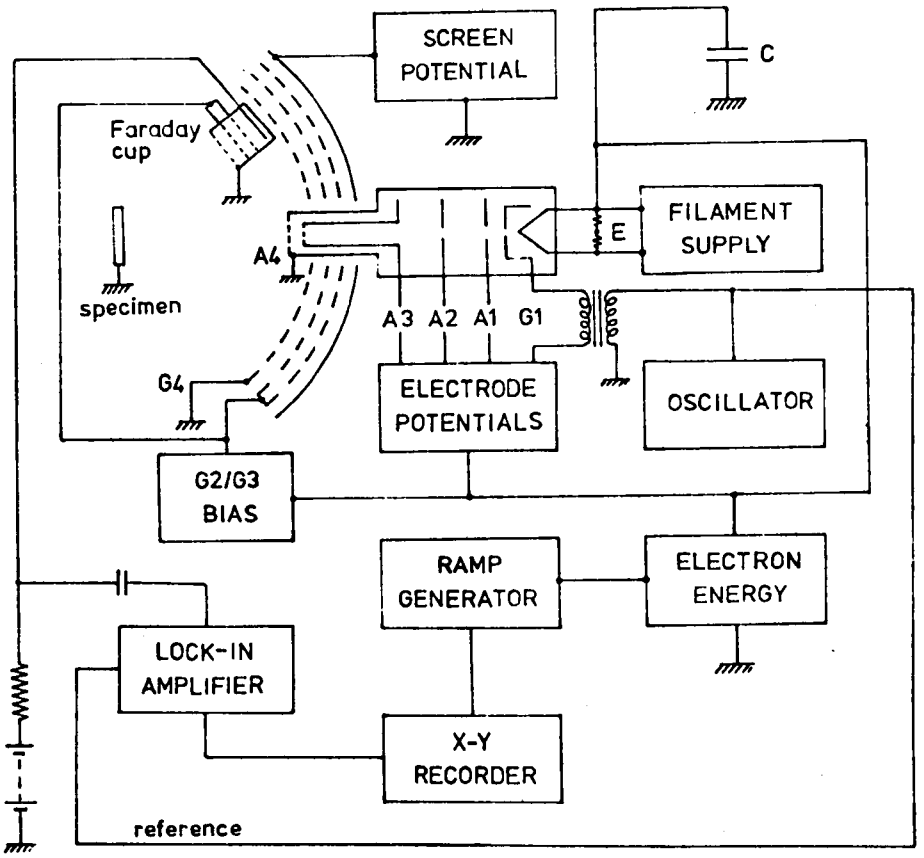

Figure 3.8 Schematic diagram of the experimental configuration for LEED. The capacitance C was optimised for maximum sweep speed and minimum ripple to be 0.1 uF.

is shown in figure 3.8 The LEED optics and integral LEG2 electron gun were mounted on port B of the experimental chamber. In order to obtain electrostatic field free conditions in the electron scattering region the inner grid G4, the final anode A4 of the electron gun and the specimen were all maintained at earth potential while magnetic field free conditions were established using three orthogonal sets of Helmholtz coils (section 3.3.4).

By maintaining the retard grids G2 and G3 at a potential close to the primary beam energy, actually $-(E_P - \delta)$ where δ is a suitable applied bias, elastically back-scattered electrons and electrons that have not undergone significant energy loss are able to pass through to be accelerated onto a phosphor coated screen where visible fluorescence is produced on impact. The LEED optics was operated with the two retard grids connected together in order to reduce electrostatic field penetration through the mesh apertures by the screen potential of + 5 KV. This arrangement optimised the energy resolution of the grids and although this improved LEED pattern contrast the main purpose was to improve the quality of AES spectra obtained when using the LEED optics as a retarding-field energy analyser.

The LEG2 electron gun was fitted with a lanthanum hexaboride coated rhenium filament and produced focussed beams of 1 to 2 mm diameter at the specimen and beam currents from 1 to 3 uA as measured into the Faraday cup. Details of the power supplies for this electron gun are given in the next section.

3.3.2 LEED Electrical Power Supplies

The prime requirement of obtaining fast sweep speeds while maintaining the quality of intensity-energy spectra necessitated careful consideration of the response times of the electrical power supplies and the electronic detection system. The presence of excessively long time constants in "swept" power supplies corrupts intensity-energy spectra in three ways:

(a) Features are moved to higher energies (for positive going ramps).

(b) Overall intensities are reduced to below their true value.

(c) Full widths at half maximum (FWHM) are increased.

Indeed the only feature of the intensity-energy spectra that remains unmodified is the total area under the spectra which would only allow integral cross-sections to be reliably extracted from distorted spectra. In general the shorter the time constant of the "swept"systen then the more accurate is the reproduction of the spectra. Typically, sufficient accuracy is obtained if the time constant is less than one-fifth of the FWHM of the narrowest feature of interest in the spectra.[8] For a typical design requirement for LEED of a sweep speed of 10 eV s^{-1} and a minimum FWHM of 1 eV the overall time constant of the detection system would have to be less than 20 ms to satisfy the above criterion.

Unfortunately, the need for short time constants can not be readily reconciled with the design of ripple free power supplies that are also fully floating with respect to earth (for AES the electron gun power supplies are biased with respect to earth by up to 3 KV and for LEED by up to 500 V). Power supplies with an output isolated from earth usually have high mains (50 Hz) ripple levels superimposed on the output and require the introduction of smoothing capacitances to ground. Ripple is particularly undesirable as its effect on the intensity-energy spectra may not, unlike noise, be readily apparent. For example, the presence of ripple on the beam energy smears out fine structure in the spectra while the presence of ripple on the gun focus potentials produces a time-varying spot diameter at the specimen.

The filament power supply used was a specially built fully floating stabilised unit (KSM Ltd.) with a fully variable 0 to 12 V and 0 to 10 A d.c. output. All electron gun electrode and LEED optics potentials were derived using multi-turn potentiometers from two series connected 300 V d.c. supplies and a 30-0-30 V d.c. supply (all APT Ltd.). A programmable 0 to 3 KV d.c. supply (NM230:J&P Ltd.) provided the stabilised (to within 0.1%) beam energy. Although this particular unit was designed for sweep speeds up to 1 KV s^{-1}, linear sweep speeds above 1 V s^{-1} could only be obtained by

commencing the sweep from a base voltage of 100 V. In order to obtain linear sweeps from zero energy the 100 V base of the EHT unit was backed off by a series battery to provide zero volts at the electron gun. With A4 maintained at earth potential the beam energy was established by applying a negative accelerating potential to the filament and referring all other gun potentials to that point. The beam energy was measured at the midpoint E of two 1Kilohm resistors connected across the electron gun filament using a calibrated digital voltmeter.

However, despite the use of the special filament power supply excessive ripple was evident on the power supplies and a smoothing capacitance C was introduced between one side of the filament power supply and ground. It was possible to optimise empirically the maximum sweep speed and the residual ripple level such that undistorted spectra could be obtained at sweep speeds up to 10 eV s^{-1} with a mains ripple level of 200 mV peak to peak.

3.3.3 Electrical Configuration for AES

The arrangement of the LEED optics and ancillary electronics as a retarding-field energy analyser for AES is shown schematically in figure 3.9 A modulation $k\sin\omega t$ was applied to the retarding energy via an isolating transformer and with the Brookdeal lock-in amplifier tuned to either ω or 2ω $N(E)$ and $N'(E)$ spectra were obtained respectively using the LEED screen as the secondary electron collector. With the LEED optics subtending an angle of 100° to the specimen the total solid angle of collection was π steradians. A particularly simple method of neutralising the capacitative coupling between the retard grid and the collector was used. Bridge networks were dispensed with and instead a suitable capacitance was introduced between the low side of the oscillator coupling transformer and the lock-in detector input in order to cancel out the fundamental component in the signal. Using this method the level of modulation breakthrough was reduced to 20 mV peak to peak and although a further reduction was possible by incorporating a phase-shifting RC network this refinement proved to be of value only for $N(E)$ measurements.

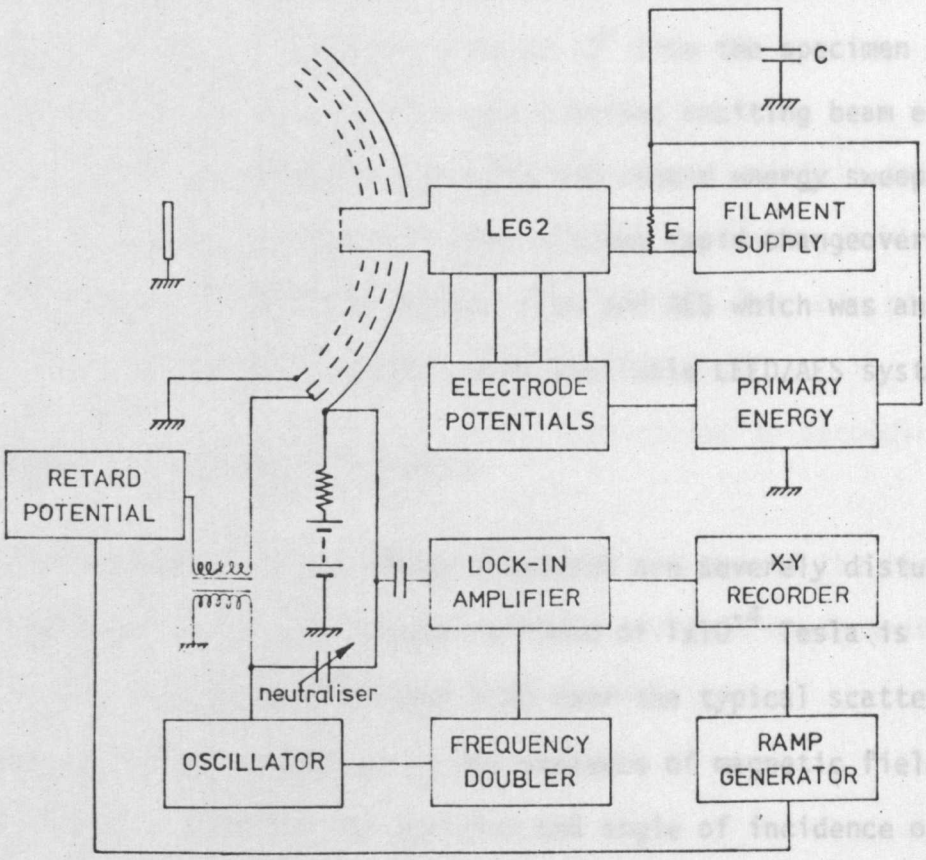

Figure 3.9 Schematic diagram of the experimental configuration of the LEED optics and ancillary electronics for AES.

The primary electron beam for AES was obtained either from the LEG2 electron gun at normal incidence or by a higher current electron gun (SE3K/5U:Superior Electronics Inc.;identical to the LEG3:Vacuum Generators Ltd.) at a glancing angle of incidence of about 15^{o} from the specimen surface. A second EHT unit was used to provide the constant exciting beam energy while the other unit was programmed to provide the retard energy sweep. Automated switching of the ancillary electronics allowed rapid changeovers of the LEED optic's mode of operation between LEED and AES which was an extremely valuable facility lacked by commercially available LEED/AES systems.

3.3.4 Magnetic Field Neutralisation

The trajectories of low energy electrons are severely disturbed by ambient magnetic fields; for example a field of $1x10^{-4}$ Tesla is sufficient to delect 100 eV electrons by about 8 mm over the typical scattering distances encountered in LEED. Consequently the presence of magnetic fields distorts the LEED pattern, modifies the position and angle of incidence of the electron beam on the specimen and degrades the energy resolution of the retarding-field arrangement by producing non-radial trajectories.

Fortunately, the net ambient magnetic field that arose from the earth's magnetic field (for which the horizontal component is $1.8x10^{-5}$ Tesla) and neighbouring magnetic equipment, in this case an imperfectly shielded ion-pump, could be effectively neutralised using three mutually perpendicular sets of square Helmholtz coils. Although it did not satisfy the optimum Helmholtz condition the coils were arranged for convenience in a cubic configuration with cube side dimensions of 0.75 m. Sixty turns of 1.5 mm diameter double cotton covered copper wire were used in each coil and each pair of coils were powered by a stabilised d.c. supply (Farnell Instruments Ltd.).

Satisfactory neutralisation was determined using the criterion that the specular beam should remain stationary for all incident energies if field free space was established over all electron trajectories for all incident energies. The effectiveness of this cancellation was determined by examining intensity-

energy spectra for symmetrically equivalent beams; for example, the (00) beam at equivalent angles of incidence on either side of the surface normal or non-specular beams of the same order at normal incidence.

3.4 Energy-Analysing Faraday Cup

The retarding-field energy analyser acts as a high pass filter for which the ideal cut-off characteristic is shown in figure 3.10 together with the characteristic typically obtained in practice. Two main effects are evident:

(a) The intensities at low energies are reduced due to secondary electron emission at the collector.

(b) The departure from the ideal step cut-off is due to the limited energy resolution of the real high pass filter and is a measure of the actual energy resolution as shown in figure 3.10.

3.4.1 Faraday Cup Design

The design of the Faraday cup used in the majority of the work described here is shown in figure 3.11 In the original design only one retard grid was used but this was soon modified to the present double grid arrangement to improve the energy resolution ($\Delta E/E$) from 8% to 0.8% as determined by FWHM measurements on elastic peaks.

As well as requiring 100% efficiency in collecting the electrons that enter it, absolute measurement of electron current with a Faraday cup requires that its acceptance aperture is sufficiently large to accommodate the entire diffracted beam diameter over the entire energy range of operation. Here it must be remembered that typical LEED electron guns require different focus conditions over their working range in order to maintain constant incident and hence diffracted beam diameters. Indeed the LEG2 electron gun requires three focussing regimes over the 15 to 300 eV energy range[9] and consequently for convenience and speed in measuring intensities over this range the LEG2 electron gun was operated in a condition of best overall focus.

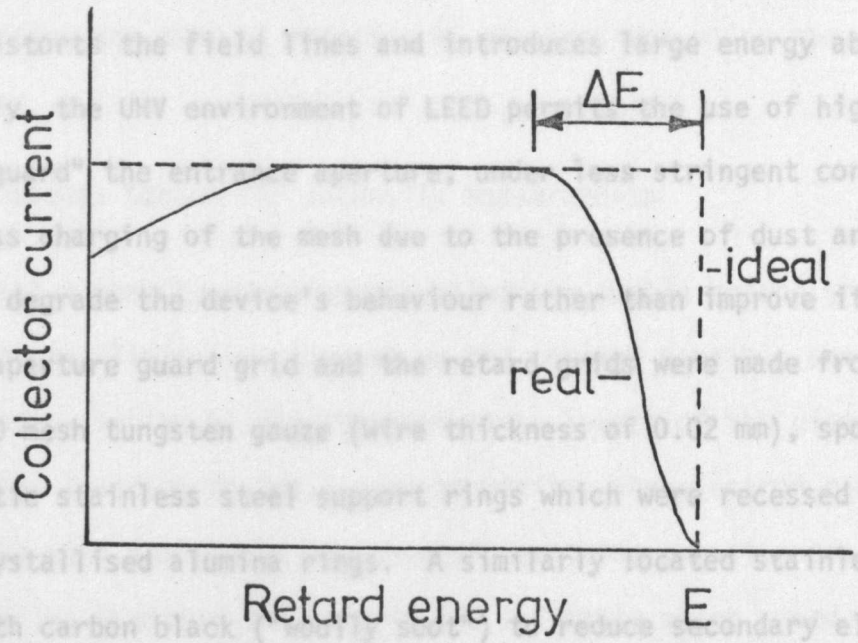

Figure 3.10 The ideal and real cut-off characteristics for the retarding-field energy analyser. The energy resolution of the real device is given as $\Delta E/E$.

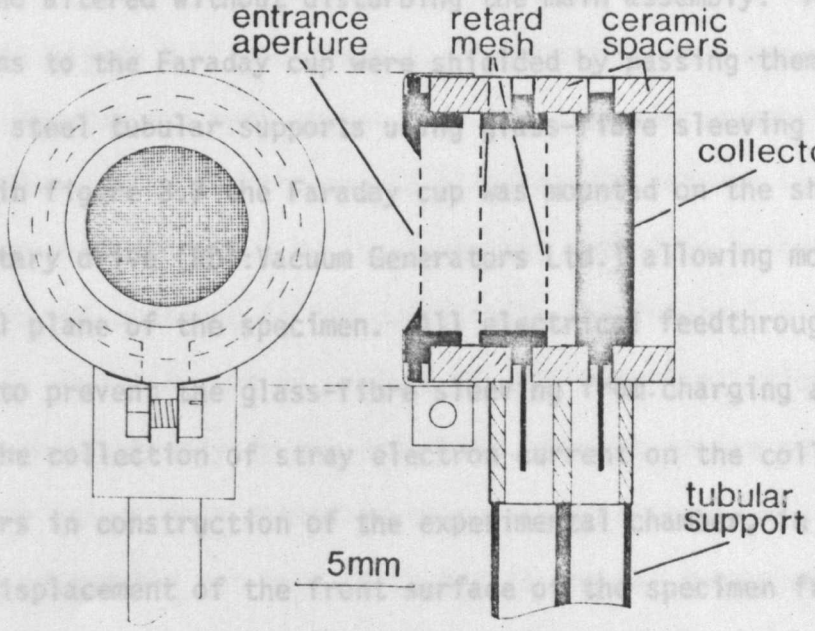

Figure 3.11 Design of the double-retard grid Faraday cup

The use of a wide single entrance aperture is unsatisfactory as the opening distorts the field lines and introduces large energy aberrations.[10] Fortunately, the UHV environment of LEED permits the use of high transparency mesh to "guard" the entrance aperture; under less stringent conditions of cleanliness charging of the mesh due to the presence of dust and grease would seriously degrade the device's behaviour rather than improve it.

The aperture guard grid and the retard grids were made from 96% transparent 100 mesh tungsten gauze (wire thickness of 0.02 mm), spot-welded to non-magnetic stainless steel support rings which were recessed to locate onto recrystallised alumina rings. A similarly located stainless steel disc, coated with carbon black ("woolly soot") to reduce secondary electron emission[11], was used as the electron collector. The retard grids and the collector were mounted in an earthed nichrome cylinder that was formerly a Wehnelt can from a standard electron gun. The acceptance aperture of the Faraday cup subtended a cone of collection with a 3^{o} half-angle relative to the specimen providing a total solid angle of collection of 0.03 steradians The design of the Faraday cup enabled the entrance aperture to be readily removed and altered without disturbing the main assembly. All the electrical connections to the Faraday cup were shielded by passing them through the stainless steel tubular supports using glass-fibre sleeving for insulation. As shown in figure 3.? the Faraday cup was mounted on the shaft of a single motion rotary drive (RD1:Vacuum Generators Ltd.) allowing movement within the equatorial plane of the specimen. All electrical feedthroughs were carefully screened to prevent the glass-fibre sleeving from charging and also to prevent the collection of stray electron current on the collector terminal.

Errors in construction of the experimental chamber, in the rotary drives and the displacement of the front surface of the specimen from the axis of rotation resulted in a slight misalignment of the axes of the specimen manipulator and the Faraday cup. The misalignment was determined by measuring the angle between two non-specular beams in the same azimuth at a particular

energy. This angle could then be simply corrected to the calculated value by translating the axis of rotation of the specimen using the universal manipulator.

3.4.2 Detection Scheme for Intensity Measurements

Initial intensity measurements using the double retard grid Faraday cup showed that the limitation imposed on the maximum possible sweep speed of the LEED detection system by the inherent noise levels of the picoammeter (Model 417:Keithley Instruments Inc.) used to monitor the electron current was more severe than that due to the presence of smoothing capacitances in the LEED power supplies (section 3.3.2). As the available sweep speed compatible with an acceptable signal to noise ratio in the output was found to be unsatisfactory, d.c. measurements were discontinued and instead an a.c. detection scheme was employed.

The lock-in amplifier, described for use in AES in section 3.3.3, was used as a conventional a.c. detector with the primary beam modulated by a 1 KHz signal superimposed on the G1 bias via an isolating transformer (figure 3.8). The beam current / G1 bias characteristic for the LEG2 electron gun is shown in figure 3.12 and for d.c. measurements this gun was operated with G1 set at the current peak shown. For the a.c. measurements the modulation amplitude was chosen to vary the G1 bias voltage between total beam cut-off and maximum beam current. By adopting this technique an excellent signal to noise ratio was obtained in the output with the internal time constant of the lock-in amplifier set to minimum (1 ms). The limitation on the sweep speed was then set only by the smoothing required in the power supplies. In order to ensure that intensity-energy spectra obtained using the a.c. detection scheme had not been corrupted in any way measurements were performed consecutively using the two techniques and compared. Figure 3.13 shows the results of such a comparison. Both spectra are identical. The effect of increasing the sweep rate is clearly illustrated in figure 3.14 where the spectrum shows evidence of distortion at rates greater than about 10 eV s^{-1}.

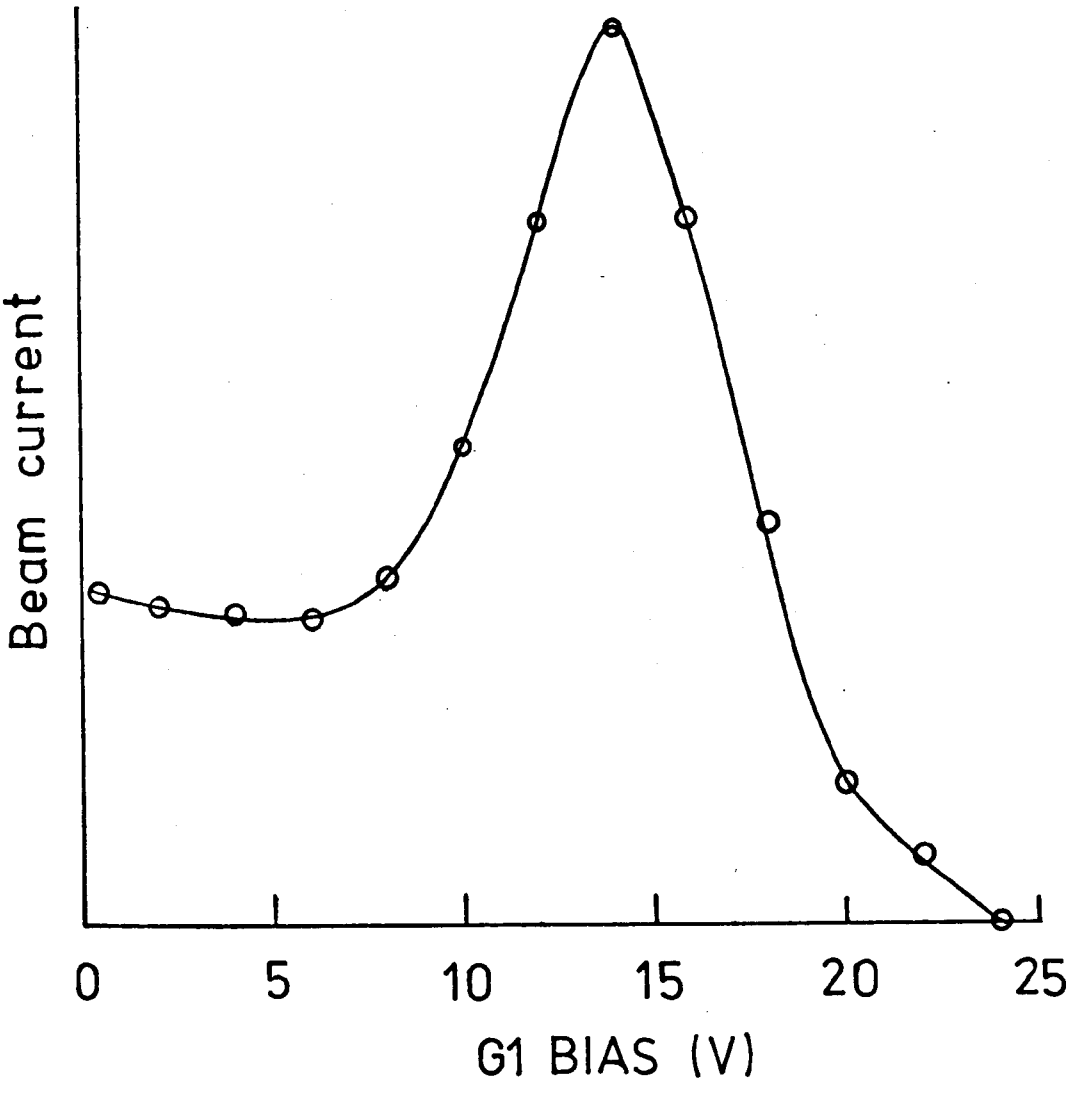

Figure 3.12 The beam current/G1 bias characteristic for the LEG2 electron gun. For d.c. measurements this gun was operated at the current peak shown whereas for a.c. measurements the modulation amplitude was chosen to vary the G1 bias voltage between beam cut-off and maximum beam current.

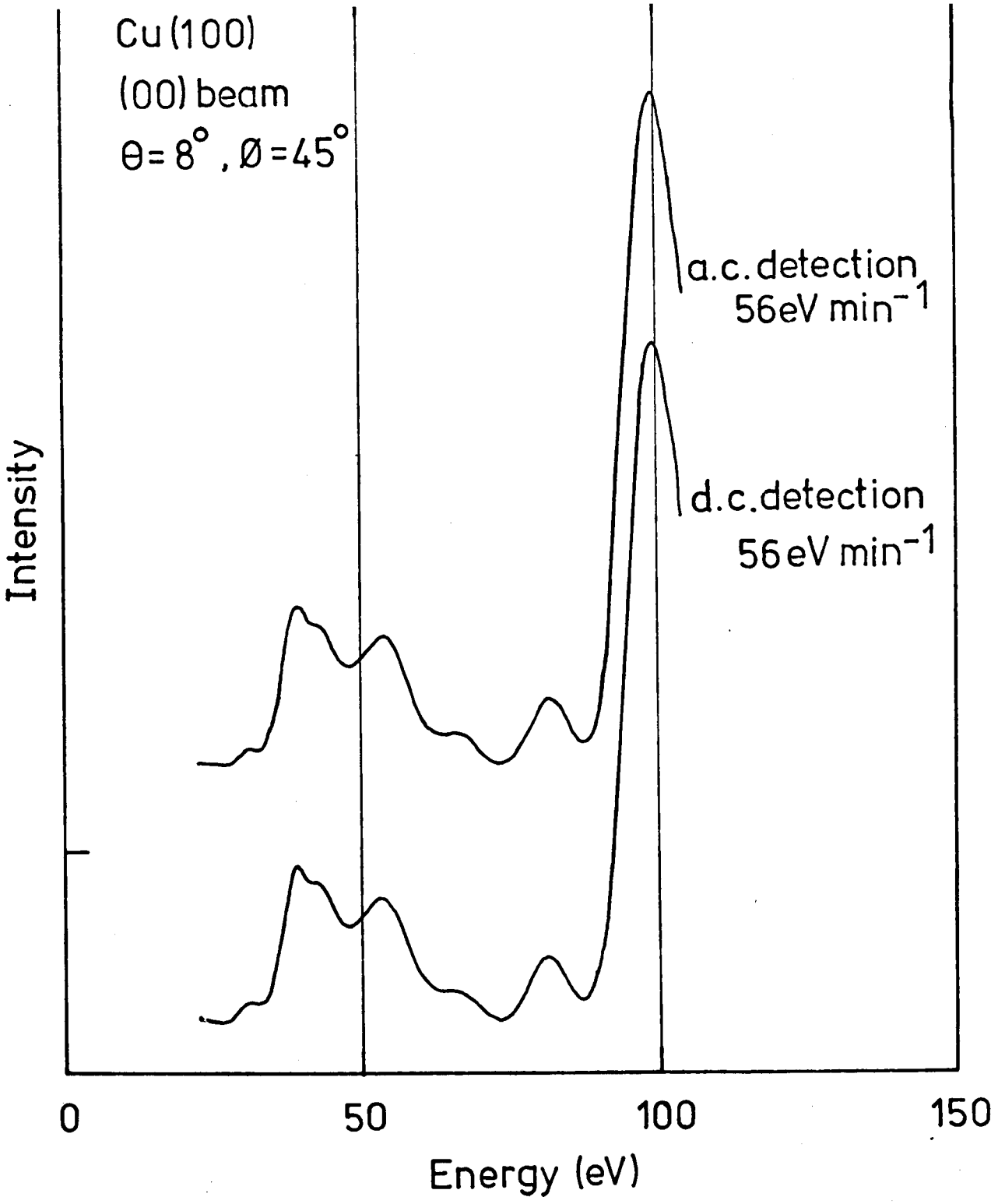

Figure 3.13 A comparison of (00) beam spectra acquired using the d.c. and a.c. measurement techniques.

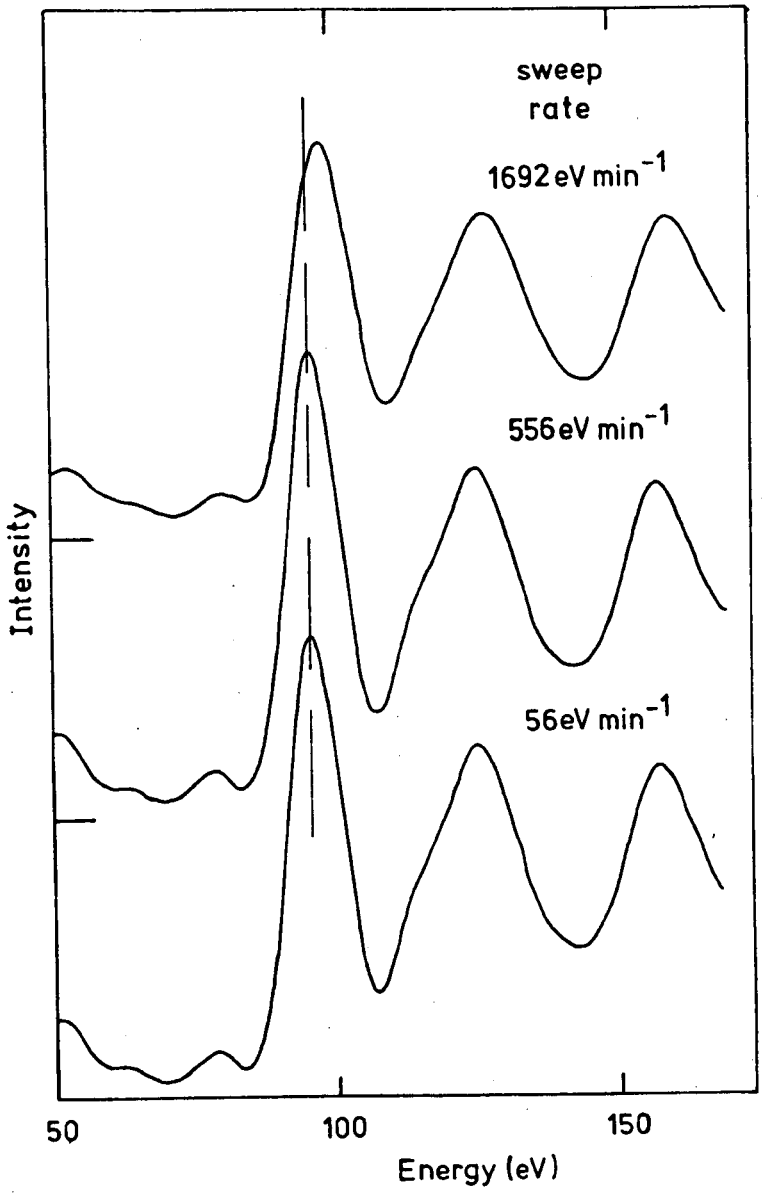

Figure 3.14 The effect of increasing the sweep speed using the a.c. measurement technique.

3.4.3 Normalisation of Intensity-Energy Spectra

In the more sophisticated comparisons of theoretical and experimental LEED intensity-energy spectra, some emphasis has been placed on correlating lineshapes and absolute intensities.[12] "Raw" intensities are not usually normalised; LEED electron guns do not in general exhibit constant beam current / energy characteristics and consequently experimental spectra have to be corrected for this and also for any variations in the efficiency of the collection system with energy if normalised intensities are required.

The normalising function for the LEG2 electron gun and the double retard grid Faraday cup was measured for the best overall focus over the energy range 0 to 300 eV and is shown in figure 3.15 This measurement was performed with the electron beam directed into the Faraday cup which was positioned in direct line of sight of the electron gun with the specimen displaced vertically out of the beam. In this position the angular divergence of the electron beam is identical to that in LEED and an identical collection efficiency should apply for both cases at all energies. It can be seen from the curve in figure 3.15 that the major variation in current occurs below 50 eV with the variation leveling off substantially after that point. The ease with which the normalising function can be acquired with a Faraday cup detection system contrasts sharply with the indirect techniques. Prutton[13] has shown that several corrections have to be applied before spot-photometer derived intensities can be reliably normalised. In the absence of an electronic means of *in situ* normalisation[14] the only alternative was manual normalisation. In view of the large quantity of data involved and the limited benefit to be obtained (above about 50 eV intensities vary by only about 10%) the intensity-energy spectra presented in the following chapters have not been normalised.

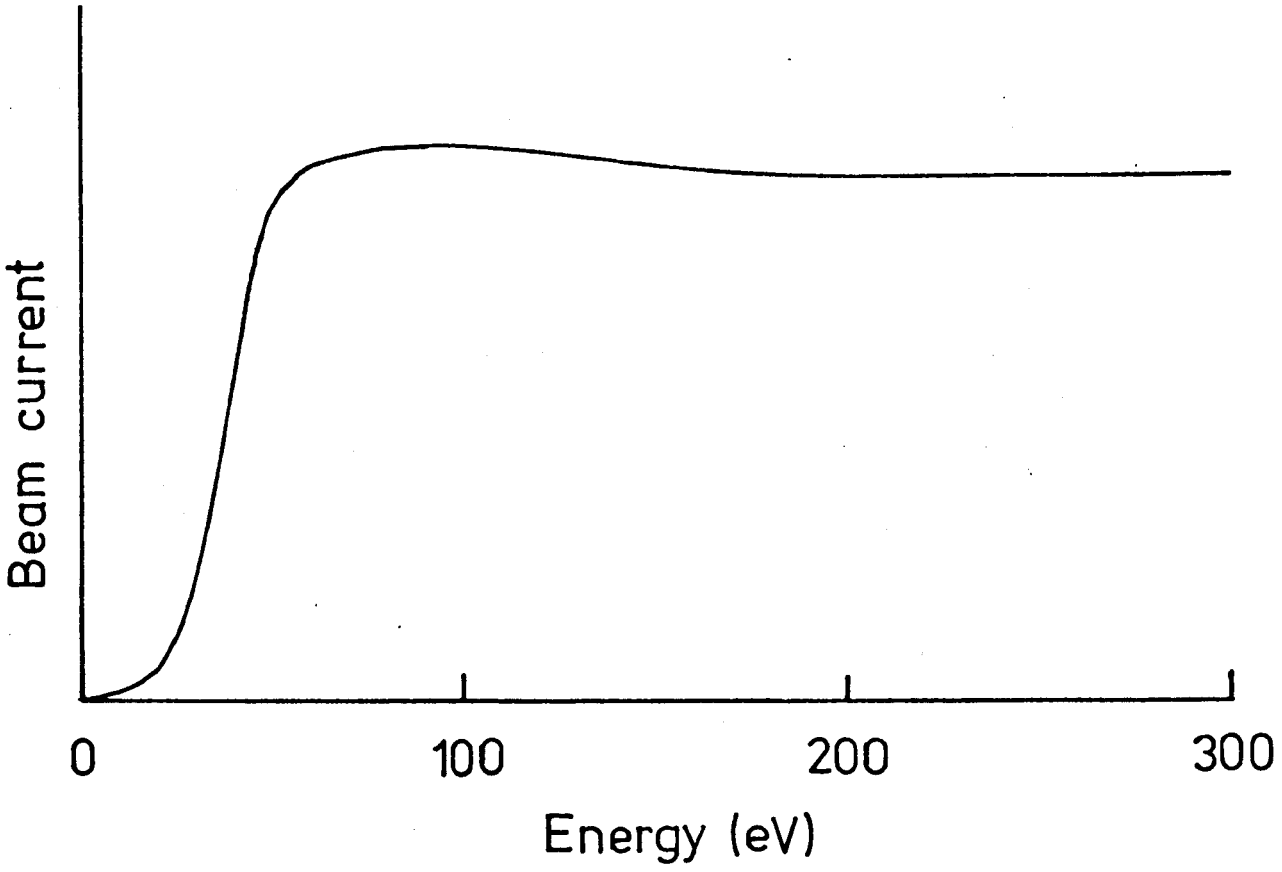

Figure 3.15 The normalising function for the LEG2 electron gun as measured using the double-retard grid Faraday cup.

3.4.4 Specular Beam Intensity-Energy Spectra

Providing that the ambient magnetic field is effectively neutralised, the specular beam does not move with varying electron energy and consequently the acquisition of intensity-energy spectra for this particular beam is a relatively straightforward matter. Once the required scattering geometry had been established and the position of the Faraday cup optimised to produce maximum diffracted beam current at a fixed arbitrary energy, the intensity-energy spectra were rapidly displayed on a X-Y recorder (Bryans Southern Instruments Ltd.). At the maximum sweep speed of 10 eV s^{-1} (00) beam spectra were typically obtained in about 30 seconds.

Although the azimuthal angle ϕ could be easily determined to within $1/2^{o}$ from photographs of the LEED pattern, definition of the angle of incidence θ was not as simple. Although relative values of θ could be accurately determined directly from the graduations on the rotary drive absolute angles required an independent establishment of normal incidence. Fortunately, reciprocity,[15] which ensures that the intensity of the (00) beam in any azimuth is the same for equivalent angles of incidence on either side of the surface normal, could be employed to establish normal incidence to better than $\pm 1/2^{o}$. Once normal incidence had been defined, absolute angles of incidence could then be reliably established using the rotary drive calibration although great care had to be taken to minimise back-lash in the rotary drive by always making the θ measurements without reversing the sense of rotation.

3.4.5 Non-Specular Beam Intensity-Energy Spectra

The acquisition of intensity-energy spectra for non-specular beams is considerably more complicated due to the convergence of these beams towards the specular beam with increasing electron energy. With the particular experimental geometry employed here only one azimuthal angle of collection, in which the incident and diffracted beams are coplanar at all angles of incidence, is available for the non-specular beams. Alignment of this

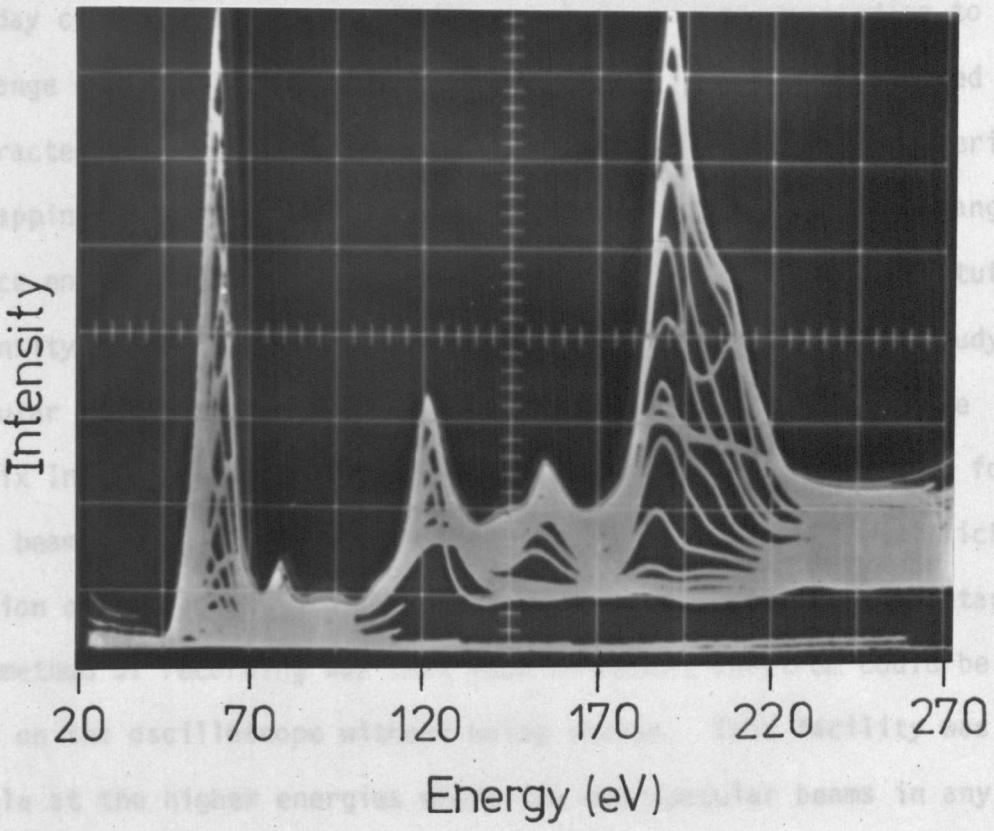

Figure 3.16 A typical (11) beam spectrum from clean copper (100) as recorded on the storage oscilloscope. The composition of the spectrum is clearly evident.

azimuth was achieved by varying the azimuthal angle ϕ at a fixed arbitrary energy until the maximum collected current was obtained. Normal incidence was then established in the manner described in the previous section.

As there were no facilities available to enable the Faraday cup to automatically track the non-specular beam as the energy was varied, the method employed by Park and Farnsworth[5] was adopted. In this technique the Faraday cup is stepped through the angular range corresponding to the energy range of interest and at each position the current is recorded as the diffracted beam sweeps across the Faraday cup. In this way a series of overlapping peaks, each corresponding to a different collection angle (and hence energy) are recorded, the outer envelope of which constitutes the intensity-energy spectra for the non-specular beam. In this study the non-specular beam spectra were compiled using a Storage Oscilloscope (Tektronix Inc.) and recorded photographically. A typical spectrum for the (11) beam from clean copper (100) is shown in figure 3.16 in which the composition of the spectrum is clearly evident. A particular advantage of this method of recording was that each component spectrum could be observed on the oscilloscope without being stored. This facility was invaluable at the higher energies where the non-specular beams in any particular azimuth get quite close together and there is a danger of recording the contributions from neighbouring beams.

*****

REFERENCES

(1) H.E.Farnsworth, *Phys.Rev.* 34 (1929) 679.

(2) W.Ehrenberg, *Phil.Mag.* 18 (1934) 878.

(3) E.J.Scheibner,L.H.Germer & C.D.Hartman, *Rev.Sci.Instr.* 31 (1960) 112.

(4) J.J.Lander,J.Morrison & F.Unterwald, *Rev.Sci.Instr.* 33 (1962) 782.

(5) R.L.Park & H.E.Farnsworth, *Rev.Sci.Instr.* 35 (1964) 1592.

(6) M.P.Seah & A.J.Forty, *J.Phys.E.* 3 (1970) 833.

(7) F.W.Young,Jr. & T.R.Wilson, *Rev.Sci.Instr.* 32 (1961) 559.

(8) K.D.Sevier, "Low Energy Electron Spectrometry",Wiley-Interscience (1972)

(9) R.J.Reid, Ph.D.Thesis. University of Warwick. (1971).

(10) J.A.Simpson, *Rev.Sci.Instr.* 32 (1961) 1283.

(11) M.P.Seah, Ph.D.Thesis. University of Warwick. (1969).

(12) J.E.Demuth,D.W.Jepsen & P.M.Marcus, *Phys.Rev.Lett.* 31 (1973) 540.

(13) M.P.Prutton, Institute of Physics Meeting,Imperial College, May (1974).

(14) R.R.Green, cited in J.E.Demuth's Ph.D.Thesis, Cornell (1973).

(15) D.P.Woodruff & B.W.Holland, *Phys.Lett.* 31a (1970) 207.

CHAPTER FOUR. CLEAN (100) AND (111) SURFACES OF COPPER

Following the successful commissioning of the combined Faraday cup / display LEED system, a study of LEED and AES behaviour from clean copper surfaces was undertaken. This served two purposes: it allowed a rigorous test of the experimental system and also provided an opportunity to compare previous experimental data[1,2], acquired with a spot-photometer system without AES facilities, thereby ensuring that a reliable reference existed for comparison with subsequent oxygen adsorbate data.

4.1 *In Situ* Cleaning of Copper

The AES spectrum of an "as loaded" copper (100) specimen that has been baked but not subjected to any other *in situ* treatment is shown in figure 4.1. The surface contaminants identified by AES were sulphur, carbon, chlorine, nitrogen and oxygen with the suppression (relative to figure 4.2) of the copper Auger transitions shown indicating the degree of contamination. Annealing at temperatures up to 650^{o}C increased the sulphur concentration primarily, although the carbon concentration also increased to a much lesser extent, while the chlorine, nitrogen and oxygen concentrations remained unaltered. The increased sulphur concentration was thought to be due to segregation from the bulk as residual gas analysis with the Q7 mass spectrometer did not show any evidence of gaseous sulphur compounds. As both carbon monoxide and carbon dioxide were present in appreciable concentrations in the ambient atmosphere the occurence of carbon segregation from the bulk can not be positively established although the shape of the carbon Auger peak resembles that of graphite rather than that of a carbide or carbon monoxide[3]. No diffraction features were observed on either the (100) or (111) surfaces before or after this treatment.

Both surfaces were successfully cleaned by bombardment with medium energy argon ions which sputtered off the contaminated surface. A simple

Figure 4.1 AES spectrum of an "as loaded" copper (100) specimen obtained using the LEG2 electron gun at normal incidence with a beam energy of 1.5 KeV is shown overleaf.

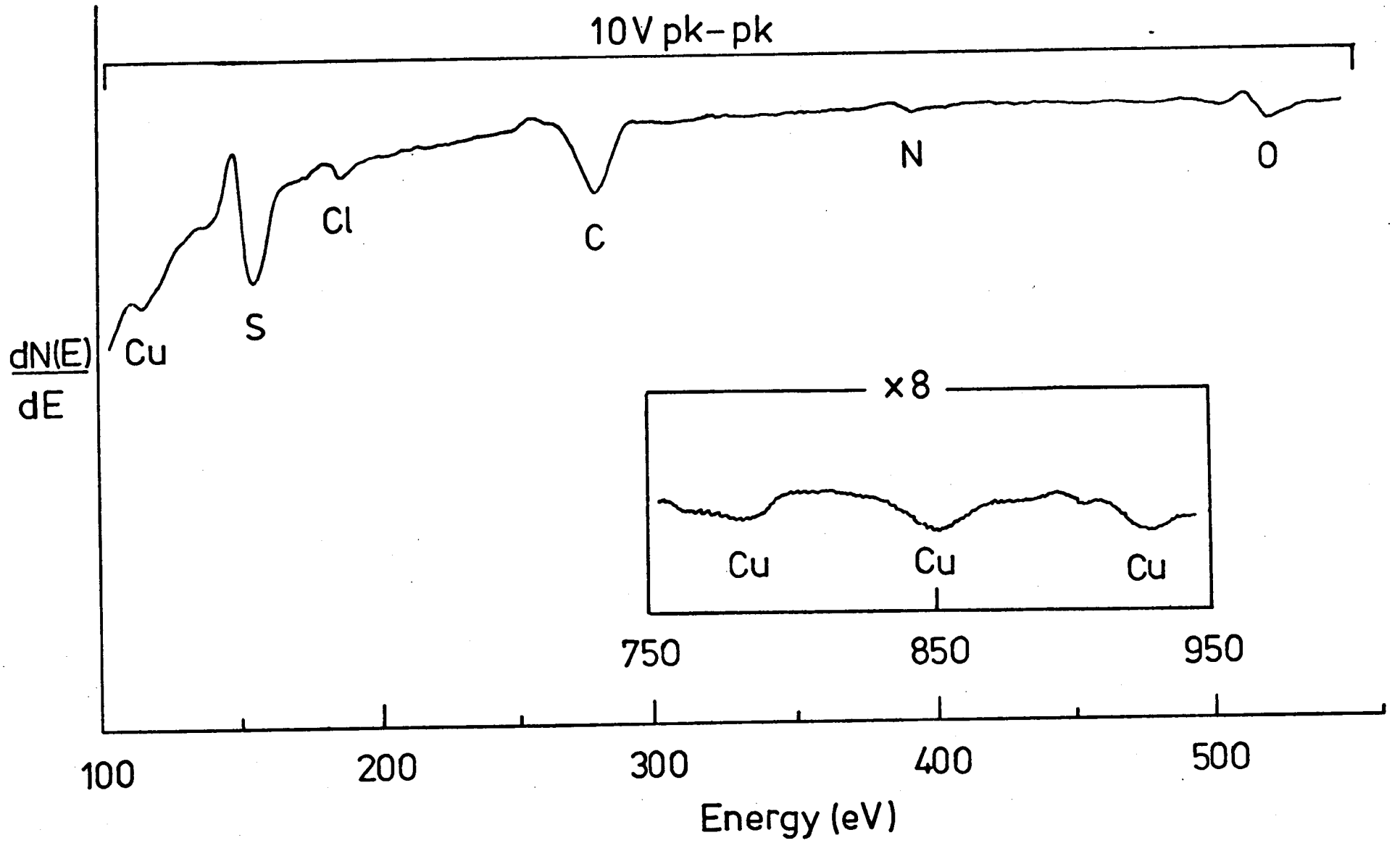
10V pk-pk
Cu
S
Cl
C
N
O
dN(E)
dE
x8
Cu
Cu
Cu
750
850
950
100
200
300
400
500
Energy (eV)

ion gun based on a conventional ion gauge design and incorporating two filaments produced 500 eV ions with a beam density of approximately 1 uA cm^{-2} at an argon pressure of 10^{-4} torr. Before use the ion gun was carefully outgassed to minimise cross-contamination of the surface and prior to the introduction of the high purity argon (Grade X:B.O.C.Ltd.) the titanium sublimation pump was operated to remove active gaseous species during the bombardment. The ion pump was isolated throughout the bombardment and on completion of the bombardment the argon was removed by the diffusion pump. Pressures less than 10^{-9} torr were quickly established with AES being typically performed at $2x10^{-10}$ torr within two minutes of the end of the bombardment.

Although clean, the "as bombarded" surfaces were shown by LEED to be considerably disordered and annealing was required to remove occluded argon and also to thermally re-order the surface. Due to the rapid segregation of sulphur from the bulk to the surface, annealing temperatures less than 500°C were found to be essential in producing well-ordered, clean surfaces. This observation has been confirmed by Jenkins and Chung [4] (and others) who also showed that an upper limit to the segregation of sulphur existed at 900°C. Such extreme temperatures were considered to be undesirable due to the considerable evaporation of copper that occurs. Several cleaning cycles, each consisting of 30 minutes bombardment and 30 minutes annealing at 450°C, were required to completely remove the contamination from the "as loaded" specimens. Once clean subsequent contamination could usually be removed by a single cleaning cycle.

4.2 The AES Spectrum of Clean Copper

Typical AES spectra from clean, ordered (100) and (111) surfaces of copper are shown in figure 4.2 from which it is clearly evident that no contamination was detected within the limits of the available sensitivity. Indeed, an upper limit to the possible sulphur contamination has been established from the specific AES calibration experiments of Perdereau [5] and Argile and Rhead [6] as approximately 0.05% (see Appendix 1).

Figure 4.2 AES spectra from clean, ordered (100) and (111) surfaces of copper obtained using the LEG2 electron gun at normal incidence with a beam energy of 1.5 KeV are presented overleaf in (a) and (b) respectively.

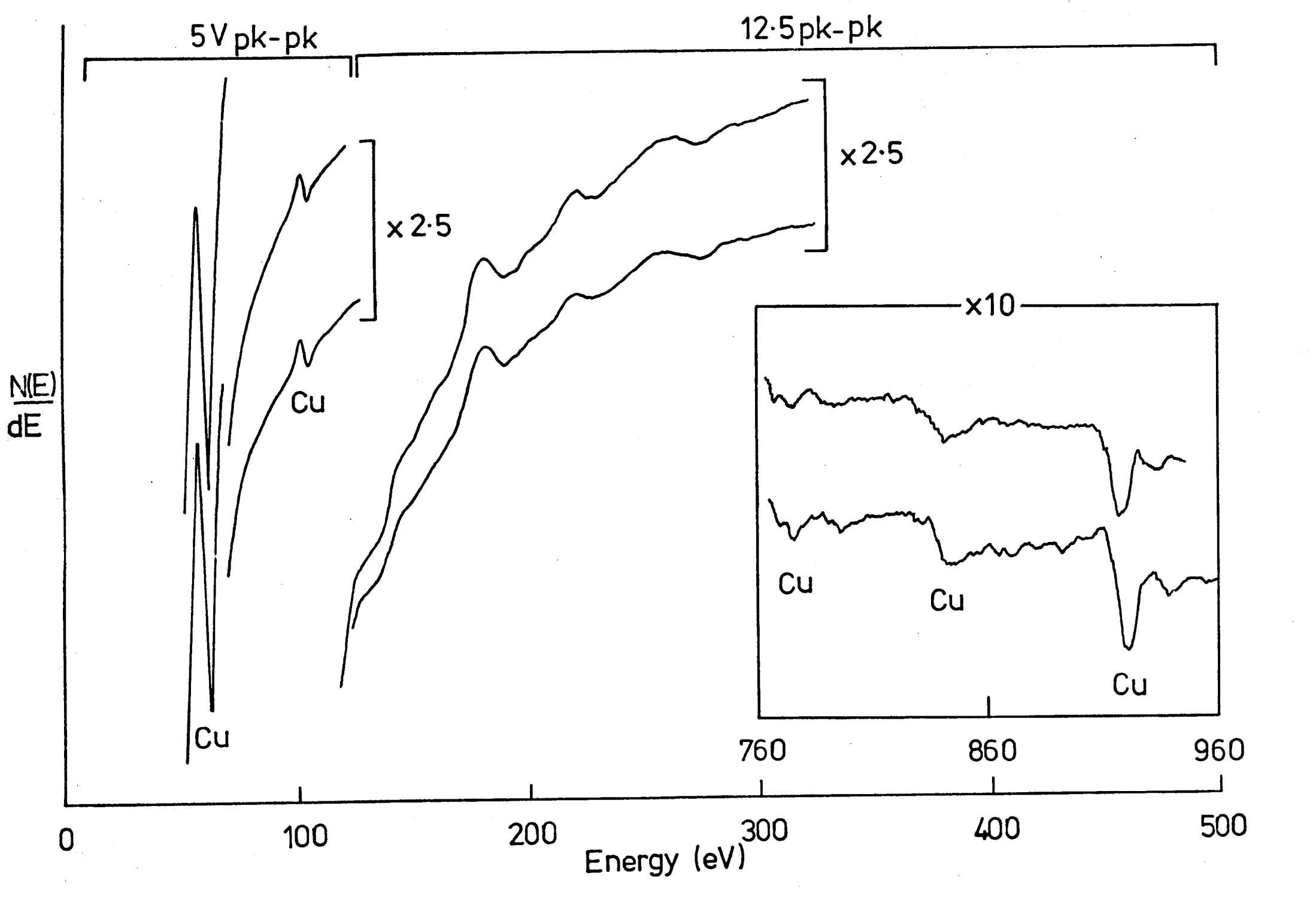
5 V pk-pk
12·5 pk-pk
x 2·5
x 2·5
x10
Cu
Cu
Cu
Cu
Cu
Cu
N(E)
dE
0
100
200
300
400
500
760
860
960
Energy (eV)

TABLE 4.1

Energy (eV)	Transition
62	$M_{2,3}M_{4,5}M_{4,5}$
108	$M_1M_{4,5}M_{4,5}$
774	$L_3M_2M_3$
844	$L_3M_2M_{4,5}$
920	$L_3M_{4,5}M_{4,5}$

The positions of the copper Auger peaks are shown in table 4.1 where the standard notation of describing peaks in $N'(E)$ spectra in terms of the position of the maximum negative excursion has been used. The peak positions (and relative intensities) are all in excellent agreement with the results of Jenkins and Chung on copper (111) with identical results being obtained on both the (111) and (100) surfaces. The 62 eV peak is actually a doublet, $M_2M_{4,5}M_{4,5}$-$M_3M_{4,5}M_{4,5}$, that has not been resolved due to the relatively large modulation amplitude used.

4.3 Temperature Dependent Peaks in Secondary Electron Spectra

As well as the reported Auger peaks, several extra features were evident in the secondary electron spectra from both clean (100) and (111) surfaces of copper, which could not be explained in terms of the normal Auger process. The initial confusion that arose from the erroneous assignment of these features as impurity Auger peaks prompted a detailed study of these features in order to establish their origin. During the course of this study it was established that although other workers had observed similar effects on various materials, reference to these features in the literature was at that stage restricted to a brief comment by Pritchard et al[7] who indicated that although the existence of these features in spectra from copper (100) might have been due to the presence of impurities, their work function measurements and also their results on copper (111) rendered this unlikely.

4.3.1 Experimental Observations

Figure 4.3 shows $N'(E)$ spectra from clean, ordered (100) and (111) surfaces of copper obtained using the three grid LEED optics in the retarding-field energy analysis mode with both retard grids strapped together to optimise the energy resolution. Unless specifically stated as otherwise, all measurements referred to in the following two sections were obtained in this manner. As well as the copper Auger transitions discussed

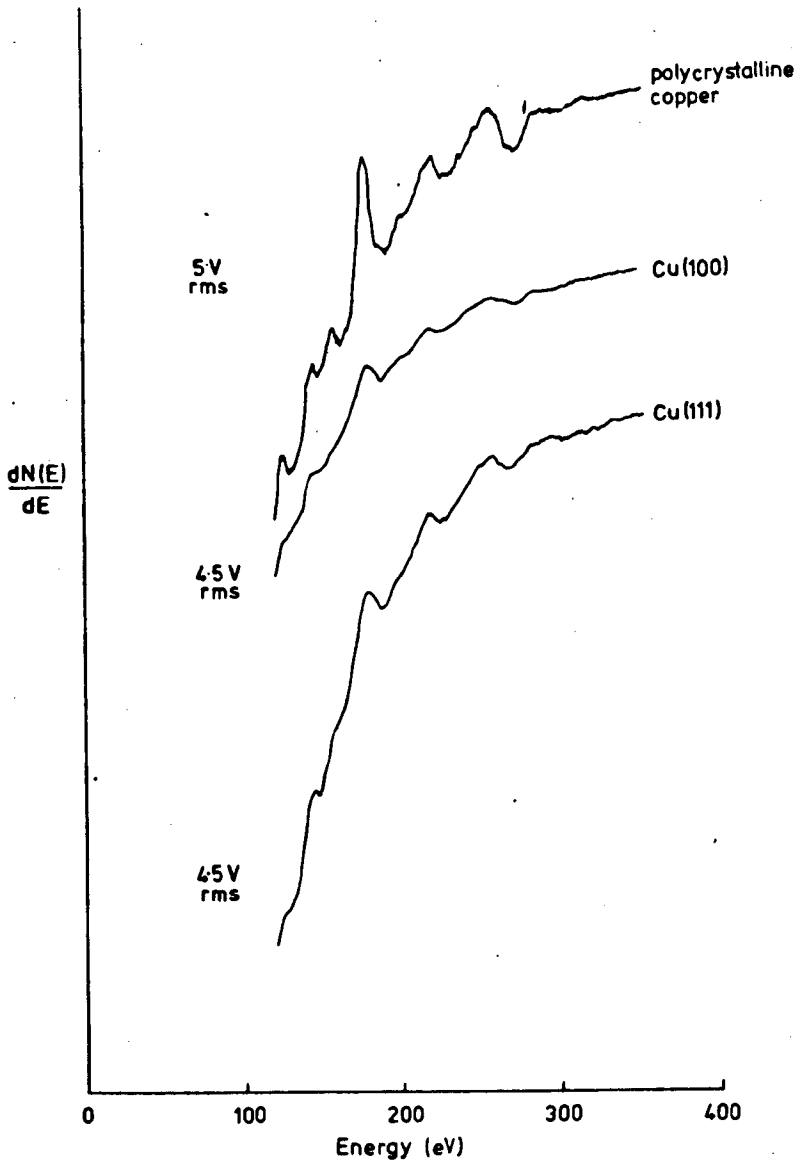

Figure 4.3 *N'(E)* spectra from clean, ordered (100) and (111) surfaces of copper obtained at room temperature with a primary beam energy of 1.5 KeV. Also included is a room temperature *N'(E)* spectrum from polycrystalline copper obtained by Powell[8] using a primary beam energy of 2.0 KeV.

in the previous section, extra peaks were observed at approximately 130, 147, 162, 190, 226 and 270 eV. Also included in figure 4.3 is a spectrum obtained by Powell[8] from a polycrystalline copper surface in which very similar features to those seen in the single crystal spectra are clearly evident.

As well as demonstrating the invariance of these features with surface crystallography, the spectra in figure 4.3 also demonstrate their invariance with the direction of the incident electron beam: the polycrystalline spectrum was obtained at glancing incidence (about 75^{o} from the surface normal) while the single crystal spectra were obtained at normal incidence.

In addition to the above observations, these features have also been observed on copper by Dobson[9] while other features of this type have been seen on a range of different materials: namely, on silver by Pritchard et al[7]; on nickel (100) by Becker and Hagstrum[10], on nickel (110) by Falconer and Madix[11], on nickel oxide (100) by Netzer and Prutton[12], on cobalt by Powell[8] and probably on iron and aluminium by Powell[8].

The features observed by Becker and Hagstrum on the (100) surface of nickel are remarkably similar in shape and relative intensities to those observed on copper, but with a systematic shift to higher energies (see table 4.2). It will be shown in the next section that the most striking aspect of the behaviour of these features is their marked temperature dependence and for convenience they will be referred to as TDP's (Temperature Dependent Peaks) in the following.

4.3.2 Behaviour of TDP's

The effect of increasing the temperature of the specimen is clearly shown in figure 4.4. Comparison of the upper and lower $N'(E)$ spectra obtained at $25^{o}C$ and $220^{o}C$ respectively reveals an almost complete suppression of the amplitudes of all the TDP's whereas the copper Auger peak intensities remain unaltered. Detailed observation of this temperature dependence showed that this effect was fully reversible, without any noticeable hysteresis.

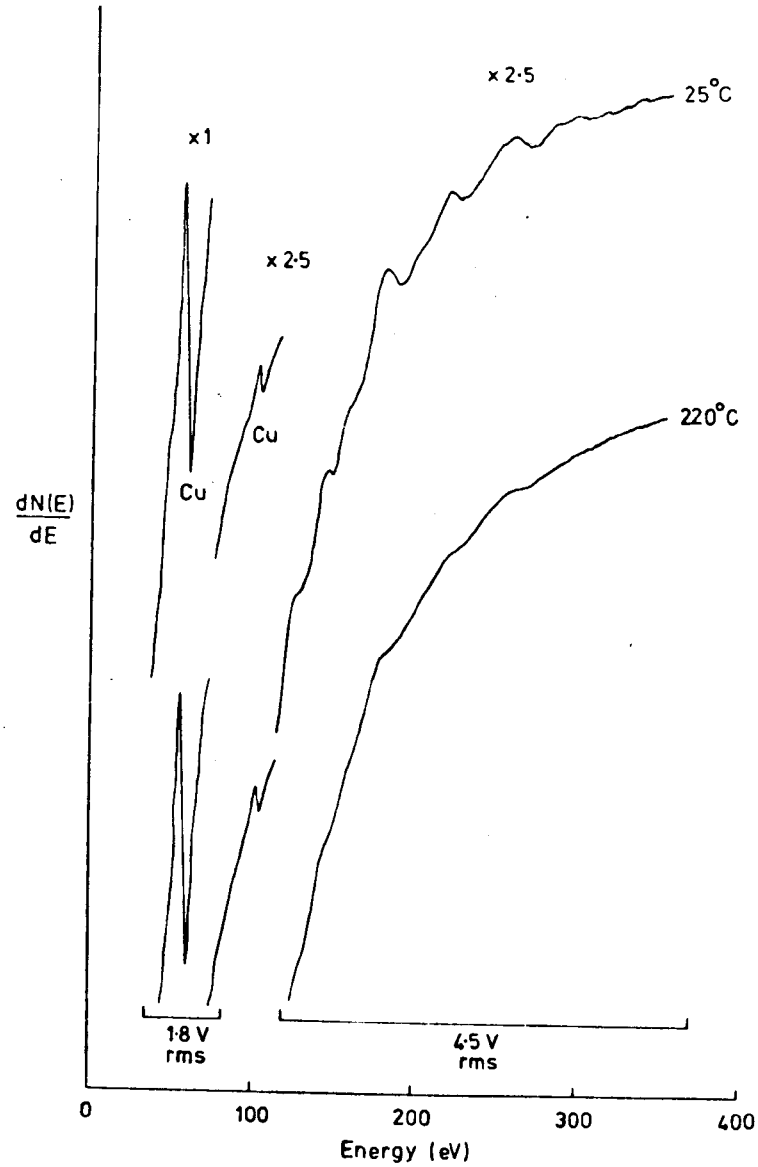

Figure 4.4 *N'(E)* spectra from copper (111) at room temperature and 220°C including the normal low energy copper peaks. Primary beam energy of 1.5 KeV.

Pritchard et al have shown that for low temperature measurements, down to liquid nitrogen temperatures, the TDP amplitudes continue to increase with decreasing temperature.

A further property of the TDP's is their sensitivity to surface order and contamination. As first indicated by Becker and Hagstrom, TDP's are weaker on a surface that has been bombarded with inert gas ions but not annealed, than on a clean and ordered surface. Similarly, although the peaks are normally suppressed when significant impurities are detected by AES, they are particularly insensitive to the presence of well-ordered adsorbates. In figure 4.5 spectrum (a) was obtained from a copper (100) surface that was contaminated with oxygen and sulphur and exhibited a well-ordered ($\sqrt{2}$x $\sqrt{2}$)R45^{o} LEED pattern while exhibiting strong TDP's. Comparison of spectrum (a) with spectrum (b), also obtained from a copper (100) surface but with a similar degree of disordered contamination, reveals a significant relative suppression of the strength of the TDP's due solely to the disorder of the contamination.

The amplitude of the TDP's on copper was found to increase with decreasing primary beam energy: the dependence of the amplitude of the most intense TDP on the copper (111) surface (190 eV) is shown in figure 4.6. The 190 eV TDP amplitudes were measured down to incident energies of 300 eV where difficulties were encountered due to the superposition of the TDP on a rapidly sloping background produced by the plasmon loss peak associated with the primary beam energy. Measurements by Powell[8] on cobalt showed a completely different behaviour with incident energy with the TDP amplitudes increasing slowly with increasing energy. A similar effect was observed on nickel (100) by Becker and Hagstrom; indeed, over the energy range from 0.6 to 1.5 KeV the behaviour of their most intense TDP at 204 eV was identical, to within 4%, to that of the 152 eV sulphur Auger transition. In order to ensure that the variation of the 190 eV copper TDP amplitude was not an artefact of the electron gun, the beam current / energy characteristic of the LEG2 electron gun was measured using the Faraday cup over the energy range in question and is shown in figure 4.6 to be relatively insignificant.

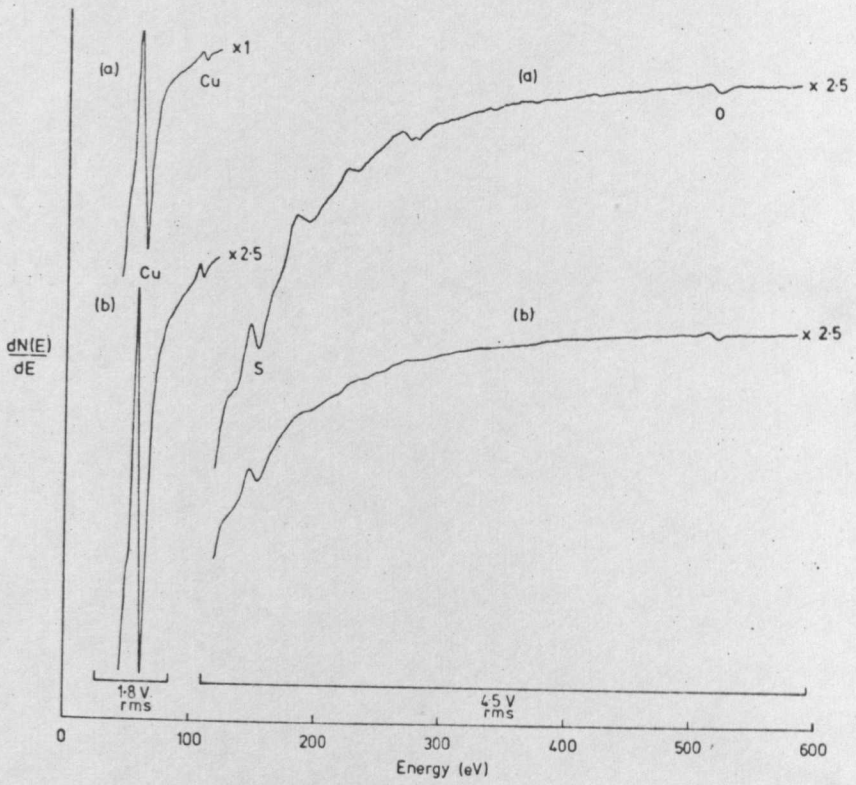

Figure 4.5 *N'(E)* spectra from copper (100) contaminated with oxygen and sulphur. In spectrum (a), an ordered structure, $(\sqrt{2}x\sqrt{2})R45^{o}$, was associated with the adsorbate whereas in (b) the adsorbate appeared to be disordered.

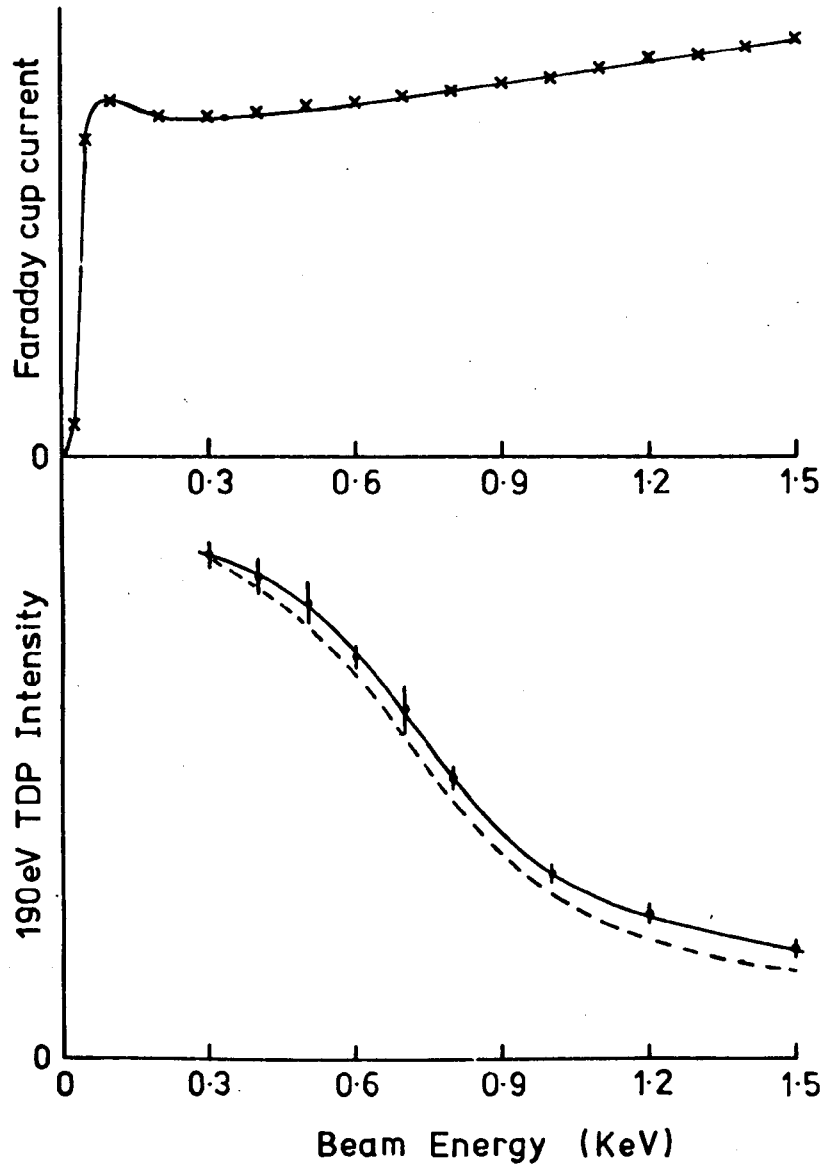

Figure 4.6 Amplitude (peak to peak value from $N'(E)$ spectrum) of the 190 eV TDP from a copper (111) surface against primary beam energy. Solid line represents the observed values while the dashed line represents the normalised value derived using the SE3K/5U electron gun characteristic shown in the upper curve.

4.3.3 Origin of TDP's: The Auger Process

Although the TDP's observed on copper, for example, cannot be ascribed to copper Auger processes (there are no transitions between 117 and 674 eV[13]), it is relatively easy to relate one or more TDP's to a variety of impurity elements. However, it is difficult to reconcile such an interpretation with the observed temperature dependence of the TDP's as this would involve the introduction of temperature dependent contamination, either by requiring the alternate adsorption and desorption of an ambient gas species or by requiring the segregation of a bulk impurity to and from the surface. Both proposals seem unlikely in view of the time scale of the experiments (minutes), the base pressure of 2×10^{-10} torr and the persistence of the temperature dependence down to 77 K without any noticeable hysterisis. The Auger process itself is insensitive to temperature and any Auger type transition, involving states that have not been identified as yet, would be unlikely to be temperature dependent in the range 77 to 500 K in view of the large binding energies involved (hundreds of eV).

The possibility of the TDP's originating from the Auger process is rendered even more unlikely by:

(a) The observed shape of the TDP's which appear in $N'(E)$ spectra as purely positive excursions, i.e. corresponding to steps in electron current rather than true peaks. While true Auger peaks may have their low energy sides broadened by energy loss processes, even to the extent of producing purely negative excursions (e.g. the 270 eV carbon Auger peak), there is no evidence of Auger peaks existing as purely positive excursions in $N'(E)$ spectra.

(b) For copper, the observed dependence on incident electron energy is totally inconsistent with the Auger process, for which intensities are normally greatest for primary energies of the order of three times the ionisation energy of the relevant core state.[14]

4.3.4 Origin of TDP's: Diffraction

An alternative proposal for the origin of TDP's is diffraction of the outgoing electrons within the crystal. Diffraction processes depend upon the long range order within a crystal which is reduced when the crystal is heated, when the surface becomes disordered or when a disordered overlayer is present. All of the latter effects have been shown in the preceding sections to be characteristic of TDP's. A further implication of a diffraction model is that the TDP energies for materials with the same crystal structure, for example copper and nickel are both f.c.c., should be characterised by their respective lattice parameters. The experimental TDP energies for both copper and nickel are shown in table 4.2 together with the ratios of the TDP energies for the two elements. A diffraction mechanism would require that these ratios should be equal to the ratio of the square of the lattice parameters. Before dividing,the TDP energies should strictly have been converted into "internal" energies by correcting with the inner potential. However, the difference in inner potential for copper and nickel is small and will be relatively insignificant at the energies being considered here.

The diffraction hypothesis also predicts that the TDP's should be characterised by a direction within the crystal as well as by a discrete energy. Consequently, the marked similarity of the TDP profiles from the (100), (111) and polycrystalline copper surfaces must be an artefact of the large angle of integration involved (π steradians). Indeed, although spectra obtained by Powell[8], using a hemicylindrical mirror AES analyser with a solid angle of collection of $\pi/12$ steradians, yielded TDP profiles very similar to those in figure 4.3 for the polycrystalline copper surface, the spectrum from the (111) surface showed only the 190 eV TDP for the particular collection geometry used. The LEED optics used in this study subtends a collection cone with a 50^{0} half angle with respect to the specimen. When this large acceptance angle is drawn onto the stereographic projection for a cubic solid (as shown in figure 4.7 for the (100) projection) it encompasses

TABLE 4.2

Copper TDP (ev)	Nickel[10] TDP (eV)	E(Copper) / E(Nickel)	a^2(Nickel) / a^2(Copper)
-	119	-	
130	136	0.96	
147	-	-	
162	169	0.96	= 0.955
190	196	0.97	
226	236	0.96	
270	280	0.97	

COMPARISON OF TDP ENERGIES ON COPPER AND NICKEL

most of several unit triangles and consequently the LEED optics averages out most symmetrically non-equivalent directions, thereby ensuring that the spectra are similar with this collector for the different crystallographic surfaces. Inspection of figure 4.7 reveals that the possible emission angles of the TDP's must exclude the <111> and <100> directions which are excluded by this collection geometry in normal incidence experiments on (100) and (111) surface respectively.

The temperature dependence of diffraction processes is well known and consequently it might be expected that the temperature dependence of the TDP's might be characterised by a Debye-Waller factor. A semi-logarithmic plot of the temperature dependence of the amplitude of the 190 eV copper TDP obtained during the (slow) free cooling of the specimen from an elevated temperature, is shown in figure 4.8. The Debye temperature θ_D was calculated from the slope of this plot x (i.e. where $x = (\Delta \ln I)/(\Delta T)$) using:

$$\theta_D^2 = \frac{152.84\ E \cos^2\theta}{M\ x} \qquad \ldots 4.1$$

where M is the molecular weight of the vibrating species and E and θ are the energy and angle of incidence respectively inside the crystal. It has been assumed that the scattering vector here is for the case of total back-scattering, i.e. for the LEED (00) beam at normal incidence. The usual approximations applicable to the use of this type of analysis in LEED have also been made: namely, the harmonic approximation, kinematical diffraction and the high temperature approximation. The Debye temperature derived from figure 4.8 using equation 4.1 was 190 K; although this value is much lower than the value for bulk copper, LEED peaks from copper surfaces have been observed with this value of θ_D.[1]

Similar measurements by Powell on cobalt gave θ_D values of 260 and 265 K for the 130 and 201 eV TDP's respectively as shown in figure 4.8. Comparison of these values with the bulk values yields ($\theta_D$effective/$\theta_D$bulk) ratios of 0.56, 0.58 and 0.59 respectively. Although the approximations involved in

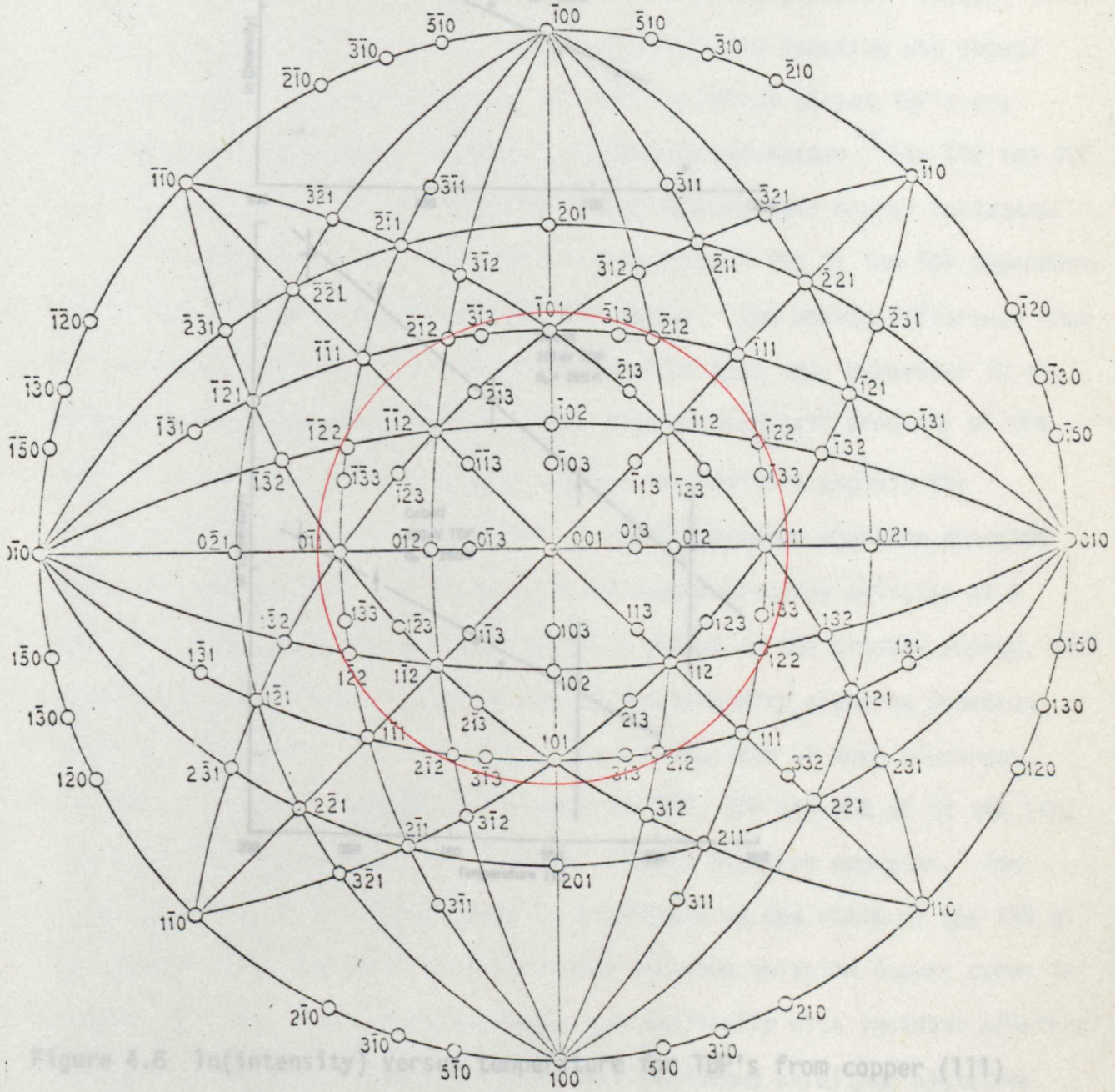

Figure 4.7 Stereographic projection for a cubic solid ((100) projection) with the angle subtended by the LEED optics for a normal incidence experiment on a (100) surface superimposed.

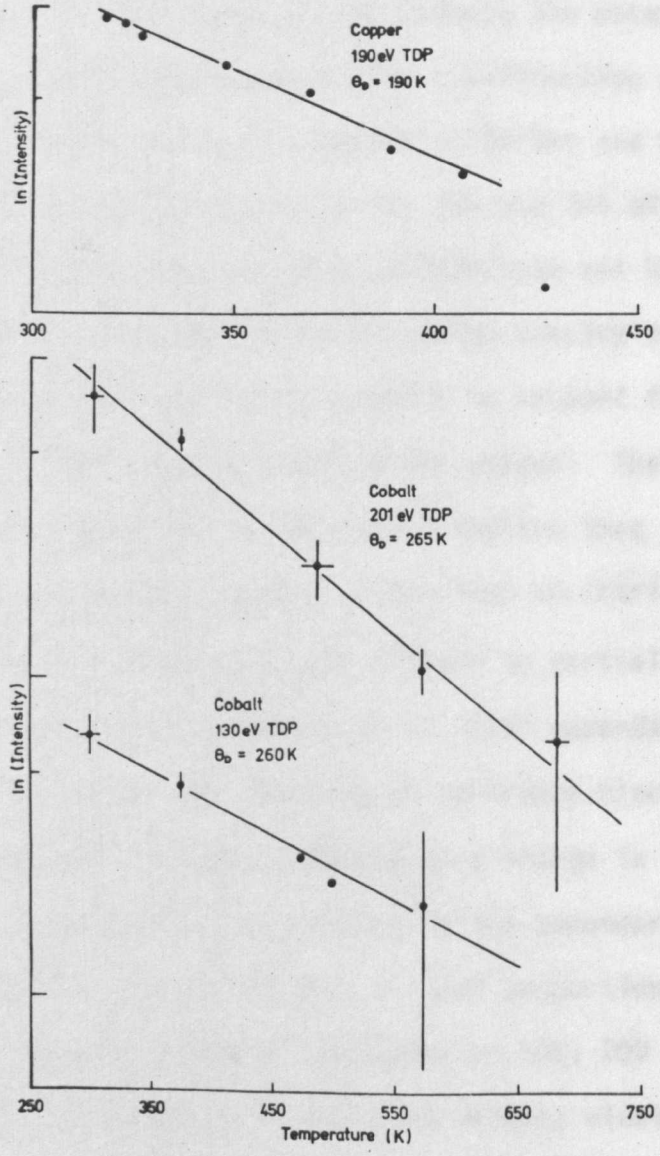

Figure 4.8 ln(intensity) versus temperature for TDP's from copper (111) and polycrystalline cobalt (cobalt data due to Powell[8]).

this analysis must render such good agreement as this as rather fortuitous, there does seem to be a relationship between the observed temperature dependence and that to be expected for a diffraction process. Indeed, this conclusion is supported by the results of Becker and Hagstrum who showed that the temperature dependence of the 204 and 241 eV nickel TDP's was extremely similar to that observed by Andersson and Kasemo [15] for 192 and 300 eV LEED peaks in (00) beam intensity-energy spectra near normal incidence.

The particularly difficult property to account for is the TDP dependence on incident electron energy observed for copper. The marked difference from the behaviour of both nickel and cobalt implies that this behaviour is an artefact of the material studied rather than an intrinsic property of the TDP's. A detailed study on copper appears to partially explain the observations in terms of a variation in total secondary electron emission with incident energy. Any increase in secondary electron emission at a particular secondary energy, produced by a change in the primary energy, will increase the amplitude of any feature in the secondary electron spectrum whose mechanism is associated with a fixed proportion of such electrons. Figure 4.9 shows the number of electrons at 100, 200 and 300 eV in the $N(E)$ spectrum from copper (111) at different primary electron energies. The observed trend, while encouraging, is inadequate as the ratio of the 190 eV TDP amplitude to the equivalent secondary electron emission (upper curve in figure 4.9) is a function that changes systematically with incident electron energy. Similar experiments have not been performed on either nickel or cobalt and consequently the above results do not offer any explanation for the observed differences in behaviour.

An alternative mechanism for the energy dependence of copper has been suggested by Powell.[16] In this mechanism the observed energy dependence is attributed to an increasing specimen temperature (and hence from figure 4.8 a decreasing amplitude is observed) produced by an increase in Joule heating of the surface by the electron beam. Over this energy range, the LEG2 electron gun exhibits approximately constant beam currents (upper curve in

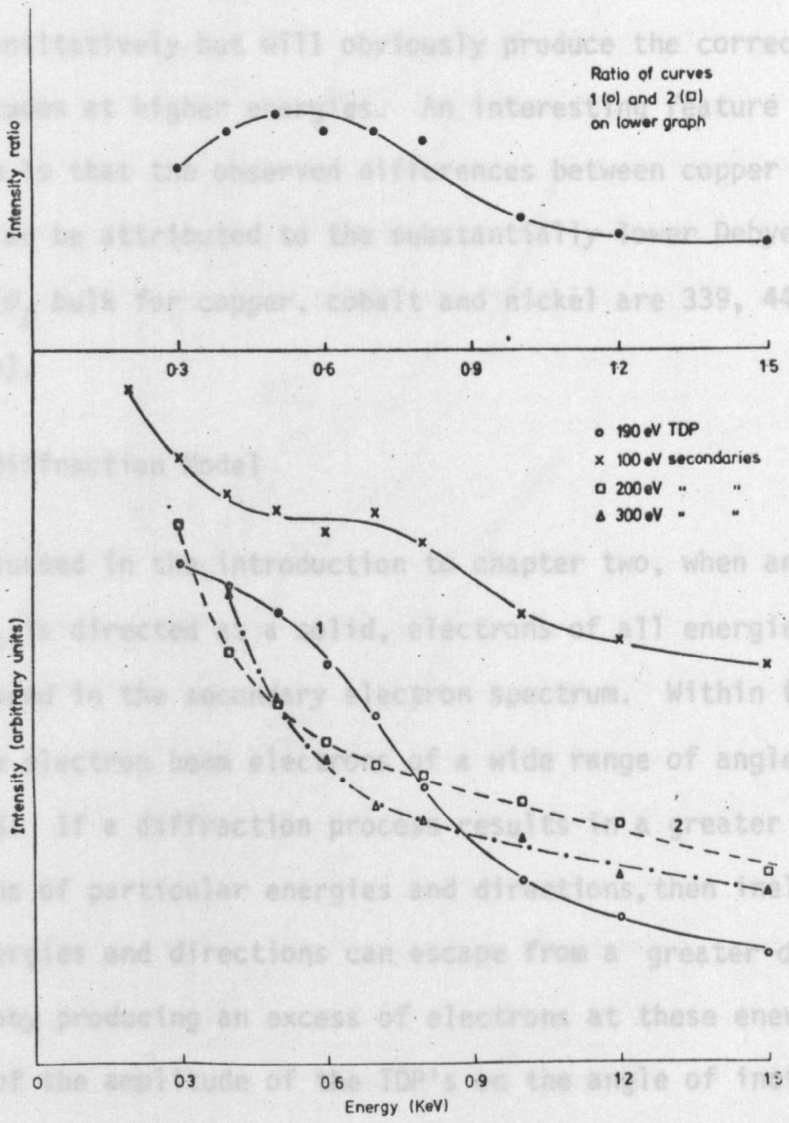

Figure 4.9 Curves demonstrating the relationship of TDP intensity to total number of secondaries at specific energies as a function of primary beam energy. The top curve shows the ratio of the 190 eV TDP intensity to the total number of secondary electrons near this energy.

figure 4.6) and beam diameters and consequently the power density at the specimen increases approximately linearly with incident energy. The accompanying increase in temperature of the surface region can not be assessed quantitatively but will obviously produce the correct trend to lower amplitudes at higher energies. An interesting feature of this type of mechanism is that the observed differences between copper and both cobalt and nickel can be attributed to the substantially lower Debye temperature for copper (θ_D bulk for copper, cobalt and nickel are 339, 445 and 456 K respectively).

4.3.5 The Diffraction Model

As discussed in the introduction to chapter two, when an electron beam of energy E_P is directed at a solid, electrons of all energies from zero to E_P are produced in the secondary electron spectrum. Within the penetration depth of the electron beam electrons of a wide range of angles and directions are produced. If a diffraction process results in a greater mean free path for electrons of particular energies and directions, then inelastic electrons of these energies and directions can escape from a greater depth within the solid, thereby producing an excess of electrons at these energies. The weak dependence of the amplitude of the TDP's on the angle of incidence of the electron beam is strong evidence that the electrons comprising these peaks must originate from an average depth that is greater than that of Auger electrons from surface atoms which approximately show a $\sec\theta$ dependence on the angle of incidence θ of the electron beam.[17]

In the absence of a simple theoretical model the diffraction hypothesis was examined by a further experiment. The total elastic electron current collected by the LEED optics was measured as a function of primary energy for a copper (111) surface at normal incidence. As shown in figure 4.10 the resultant curve contains considerable structure (compared with the results of Farnsworth[18]) which is suppressed on heating to 225°C. A further experiment in which the results of twelve of the above experiments, performed

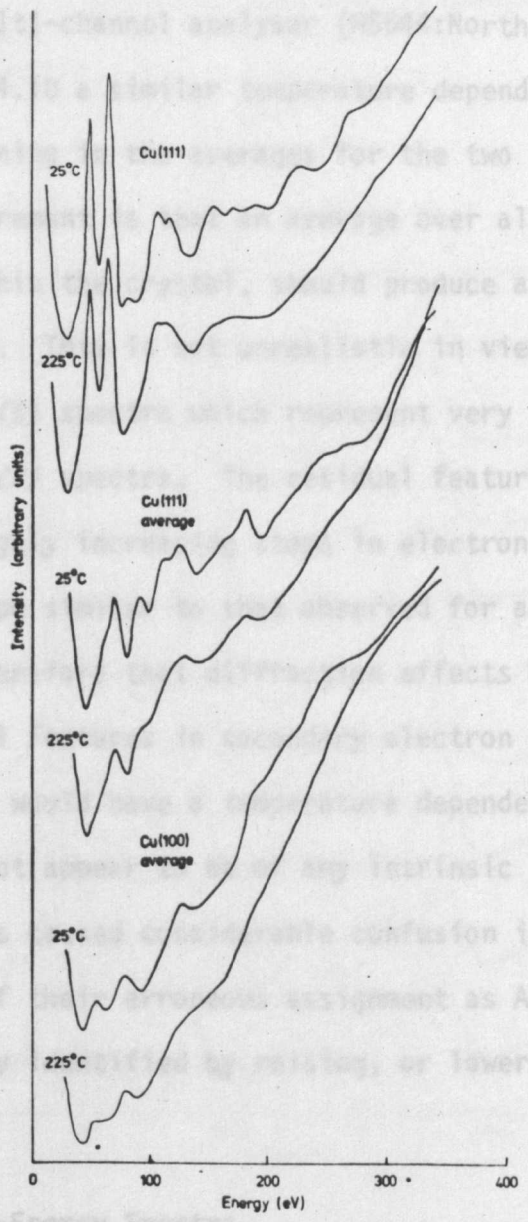

Figure 4.10 Plots of elastically scattered electrons collected by the entire LEED optics from copper surfaces versus electron energy. The upper curves correspond to a normal incidence experiment at two different temperatures whereas the middle and lower curves correspond to an average over twelve different angles of incidence.

at different angles of incidence and hence of collection, were averaged together using a multi-channel analyser (NS544:Northern Scientific Inc.). As shown in figure 4.10 a similar temperature dependence was observed for the structure remaining in the averages for the two surfaces.

Thus the requirement is that an average over all angles of incidence, including those within the crystal, should produce a spectrum containing some peaks or steps. This is not unrealistic in view of the magnitude of the TDP's in the $N'(E)$ spectra which represent very small inflections on the corresponding $N(E)$ spectra. The residual features in the averages in figure 4.10 are largely increasing steps in electron current which would generate a line shape similar to that observed for all the TDP's.

It is clear therefore that diffraction effects might be expected to produce rather small features in secondary electron emission spectra and that these features would have a temperature dependence of the form observed. Although TDP's do not appear to be of any intrinsic interest their presence in $N'(E)$ spectra has caused considerable confusion in their interpretation, primarily because of their erroneous assignment as Auger peaks. Fortunately TDP's can be readily identified by raising, or lowering, the temperature of the specimen.

4.4 LEED Intensity-Energy Spectra

LEED intensities were obtained for both the (100) and (111) surfaces of clean copper using the measurement techniques described in section 3.4.4 for the specular beam and in section 3.4.5 for the non-specular beams. Clean, ordered surfaces were defined as those exhibiting sharp LEED patterns, with no evidence of streaking or extra diffraction beams, and displaying AES spectra with no detectable contamination but several TDP's.

4.4.1 Copper (100) Surface

Intensity-energy spectra for the (00), (10) and (11) beams from clean, ordered copper (100) are shown in figures 4.11, 4.12 and 4.13 respectively.

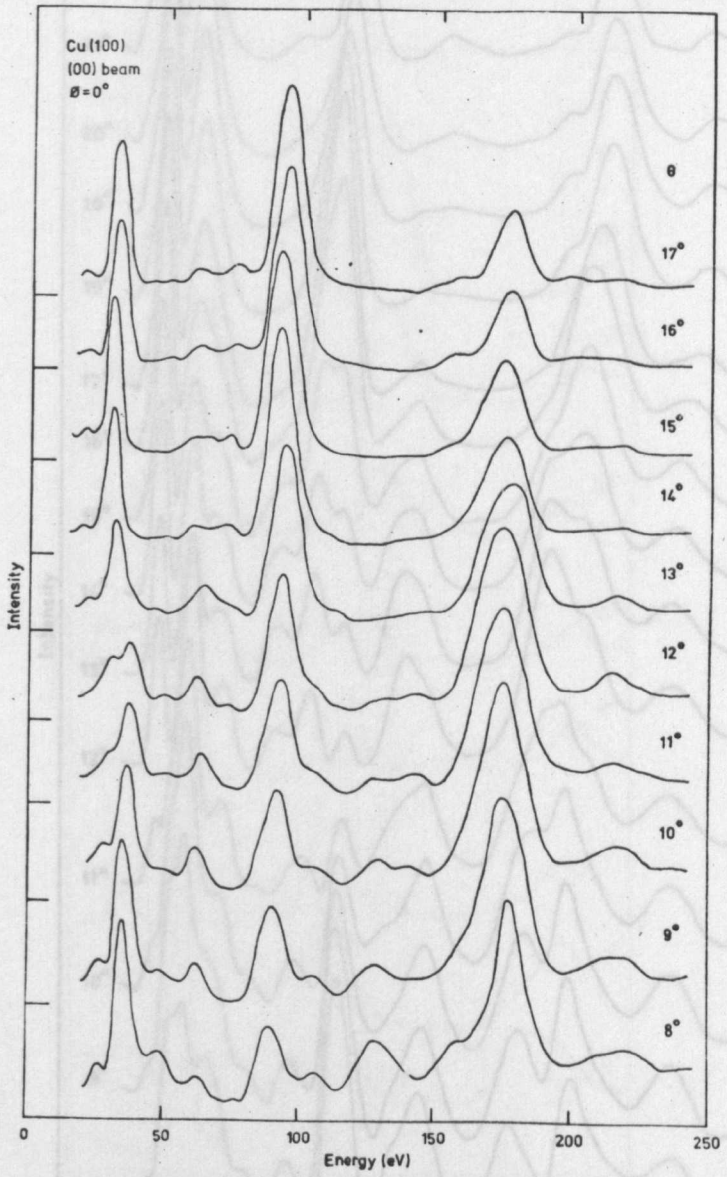

Figure 4.11a Intensity-energy spectra for the (00) beam from clean, ordered copper (100) for a range of θ and for $\phi = 0^{o}$.

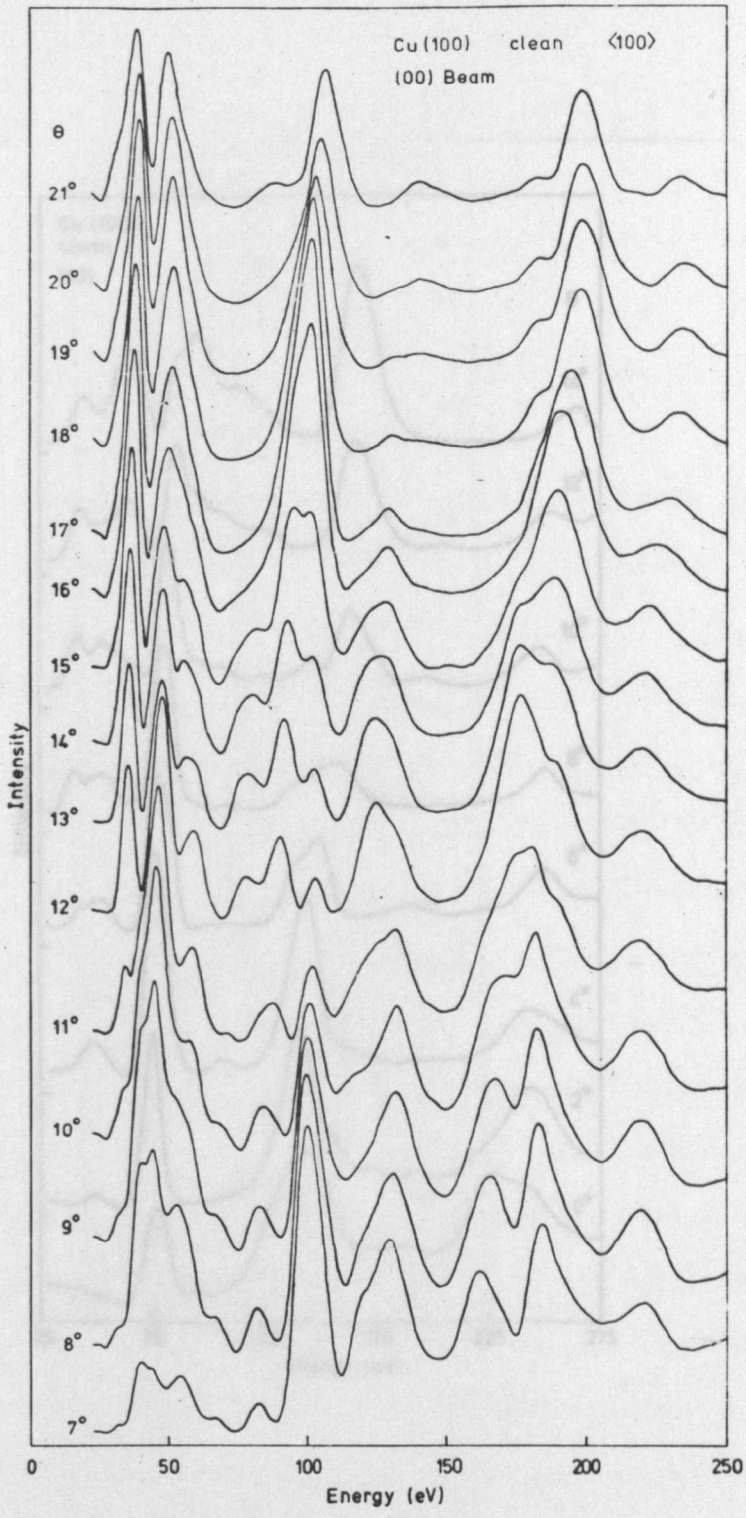

Figure 4.11b Intensity-energy spectra for the (00) beam from clean,ordered copper (100) for a range of θ and for $\phi = 45^{o}$.

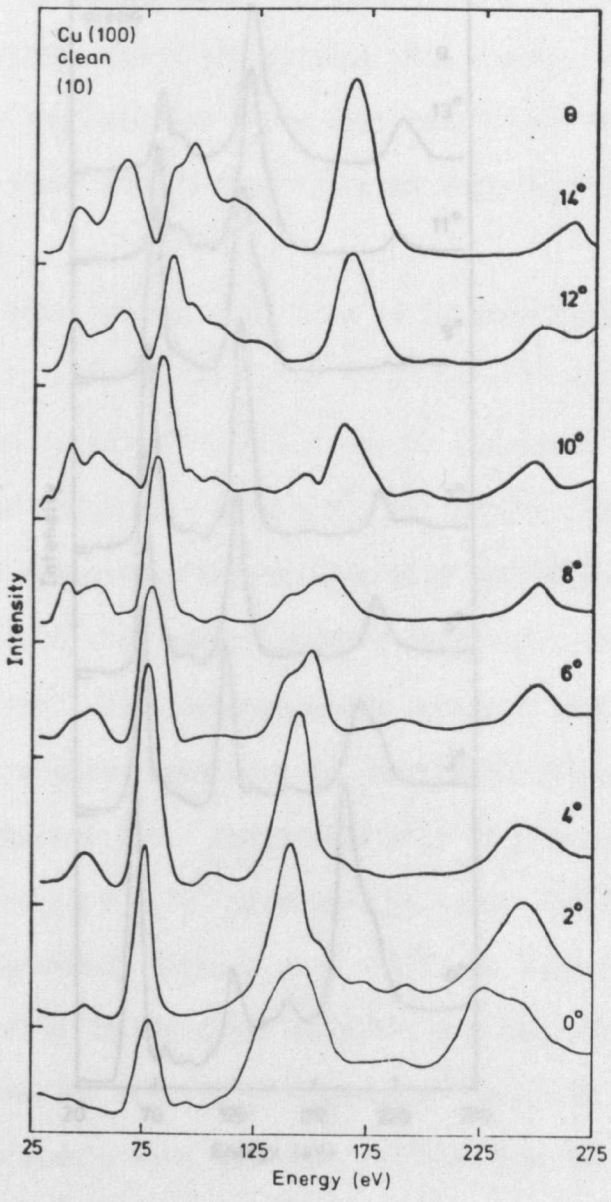

Figure 4.12 Intensity-energy spectra for the (10) beam from clean,ordered copper (100) for a range of θ.

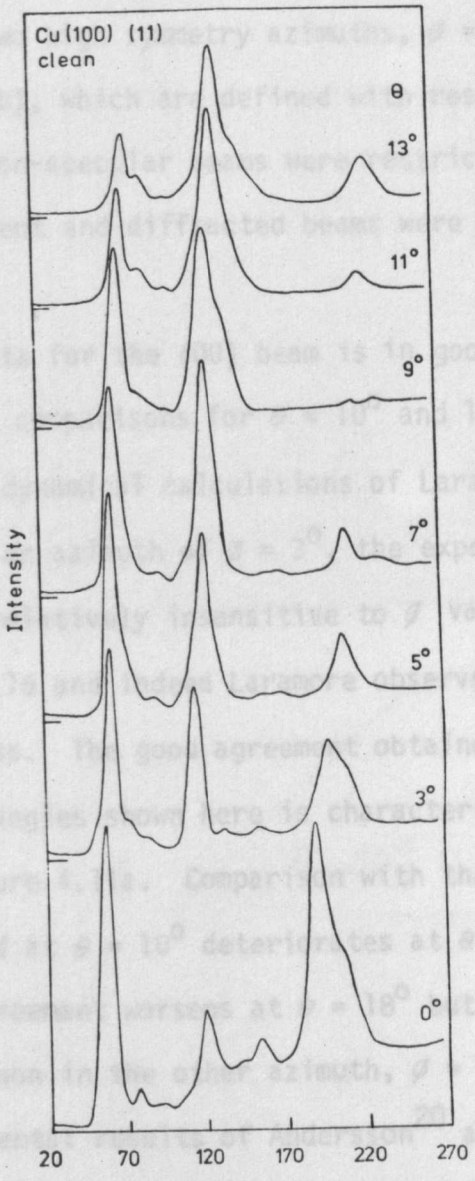

Figure 4.13 Intensity-energy spectra for the (11) beam from clean, ordered copper (100) for a range of θ.

for a range in angle of incidence θ. While the (00) beam spectra were obtained for the two high symmetry azimuths, $\phi = 0^{o}$ (figure 4.11a) and $\phi = 45^{o}$ (figure 4.11b), which are defined with respect to the LEED pattern in figure 4.14, the non-specular beams were restricted to the single azimuth in which the incident and diffracted beams were coplanar at all angles of incidence.

The $\phi = 0^{o}$ data for the (00) beam is in good agreement with that of Reid[1] and specific comparisons for $\theta = 10^{o}$ and 14^{o} are shown in figure 4.15 together with the dynamical calculations of Laramore.[19] Although Reid's data were acquired for an azimuth of $\phi = 3^{o}$, the experimental (00) beam spectra were found to be relatively insensitive to ϕ variations of this magnitude as shown in figure 4.16 and indeed Laramore observed a similar insensitivity in his calculations. The good agreement obtained with Reid's experimental data for the two angles shown here is characteristic of the entire range of data shown in figure 4.11a. Comparison with theory shows that the good agreement obtained at $\theta = 10^{o}$ deteriorates at $\theta = 14^{o}$ while Laramore has shown that the agreement worsens at $\theta = 18^{o}$ but then improves at $\theta = 22^{o}$. A similar comparison in the other azimuth, $\phi = 45^{o}$, is shown in figure 4.17 using the experimental results of Andersson[20] and the calculations of Laramore for $\theta = 8^{o}$. Andersson's data has been shifted from its published values by removing the 3 eV work function correction that he applied to his "raw" data; this procedure was considered reasonable and it gave better agreement with the present results. As before, agreement with the theory is quite reasonable.

The (10) and (11) beam spectra acquired at normal incidence ($\theta = 0^{o}$) are compared in figures 4.18 and 4.19 respectively with the experimental data of Andersson and the calculations of Laramore and also Duke and Lipari.[21] While both sets of calculations are based on the inelastic collision model of LEED and use full T-matrix inversion schemes, Laramore has used five phase shifts and a realistic temperature of 300 K compared to Duke and Lipari's choice of four phase shifts and a temperature of 10 K. Quite reasonable agreement exists between the experimental and theoretical spectra

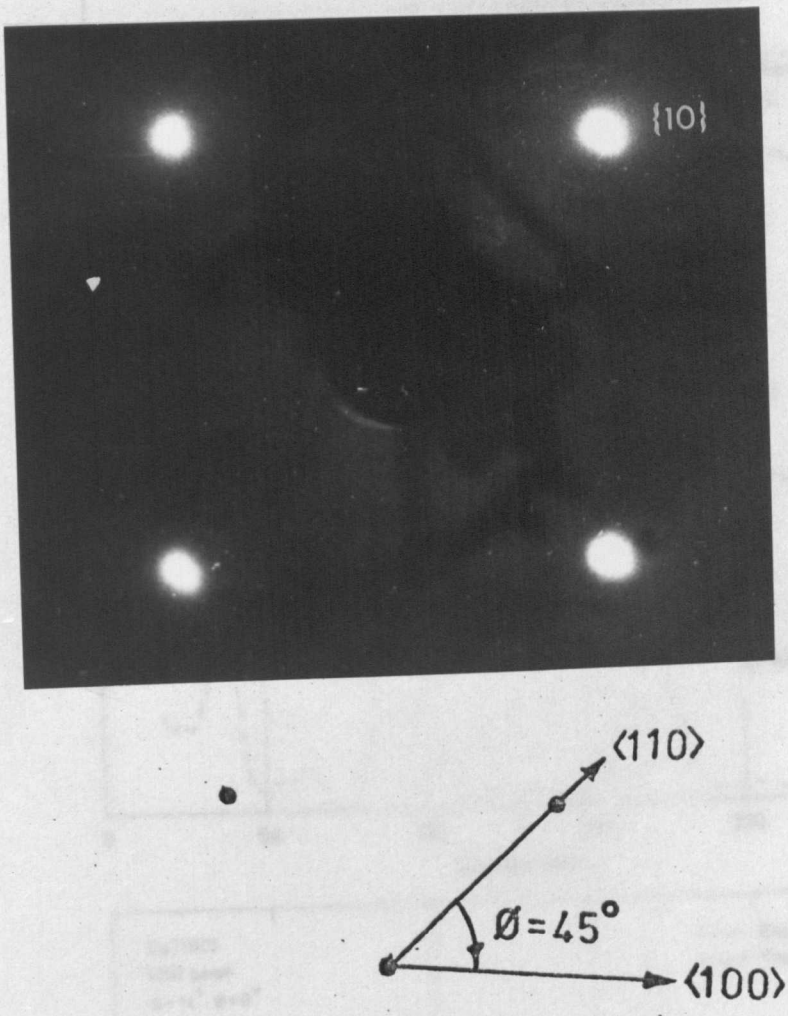

Figure 4.14 61 eV LEED pattern from clean, ordered copper (100).

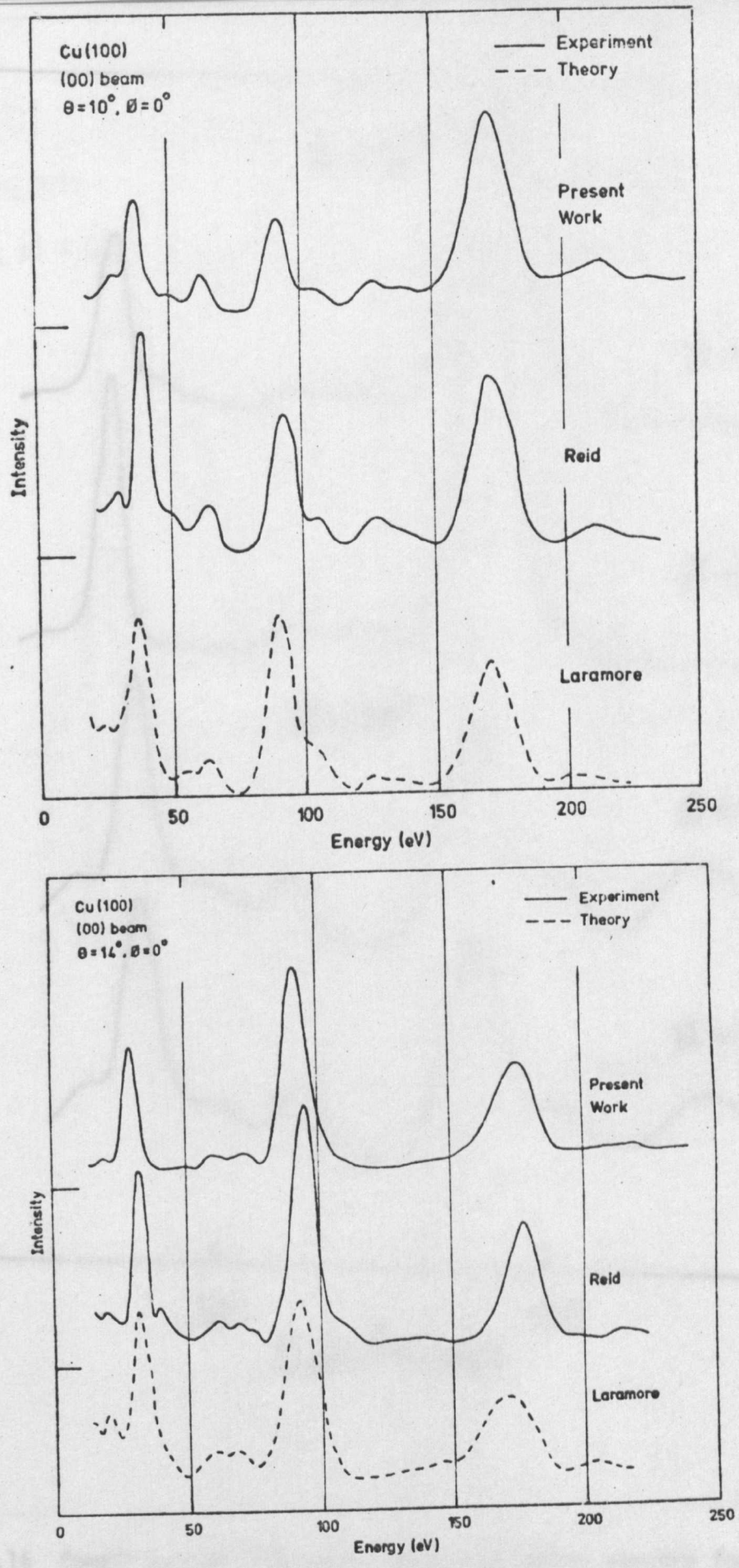

Figure 4.15 A comparison of the (00) beam intensity-energy spectra for clean copper (100). Spectra for θ = 10^{0} and 14^{0} are shown for the ϕ = 0^{0} azimuth.

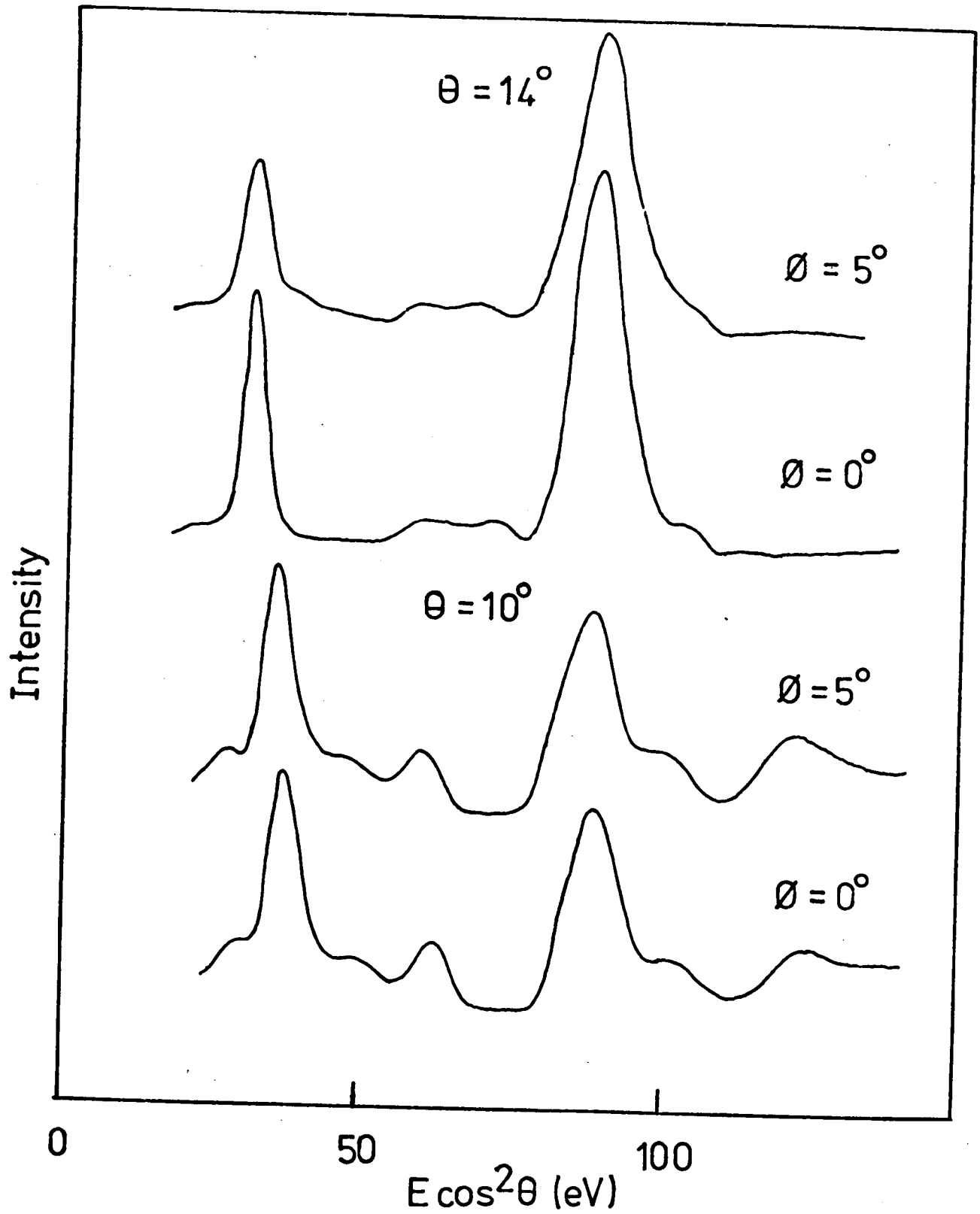

Figure 4.16 Comparison of (00) beam intensity-energy spectra for θ = 10° and 14° for the azimuths ϕ_c = 0° and 5° for the clean copper (100) surface.

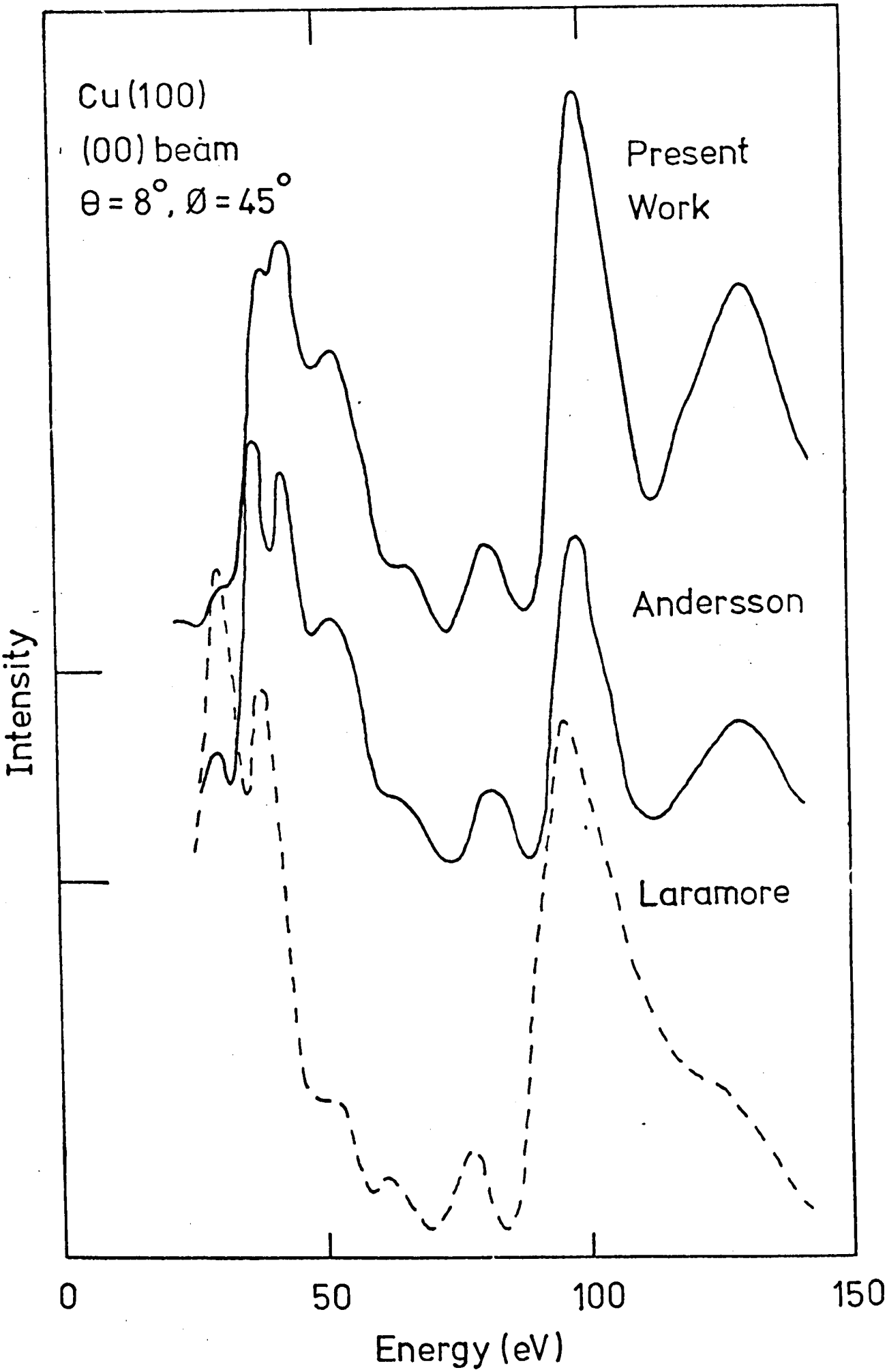

Figure 4.17 A comparison of (00) beam intensity-energy spectra for clean copper (100) at $\theta = 8^{o}$ and $\phi = 45^{o}$

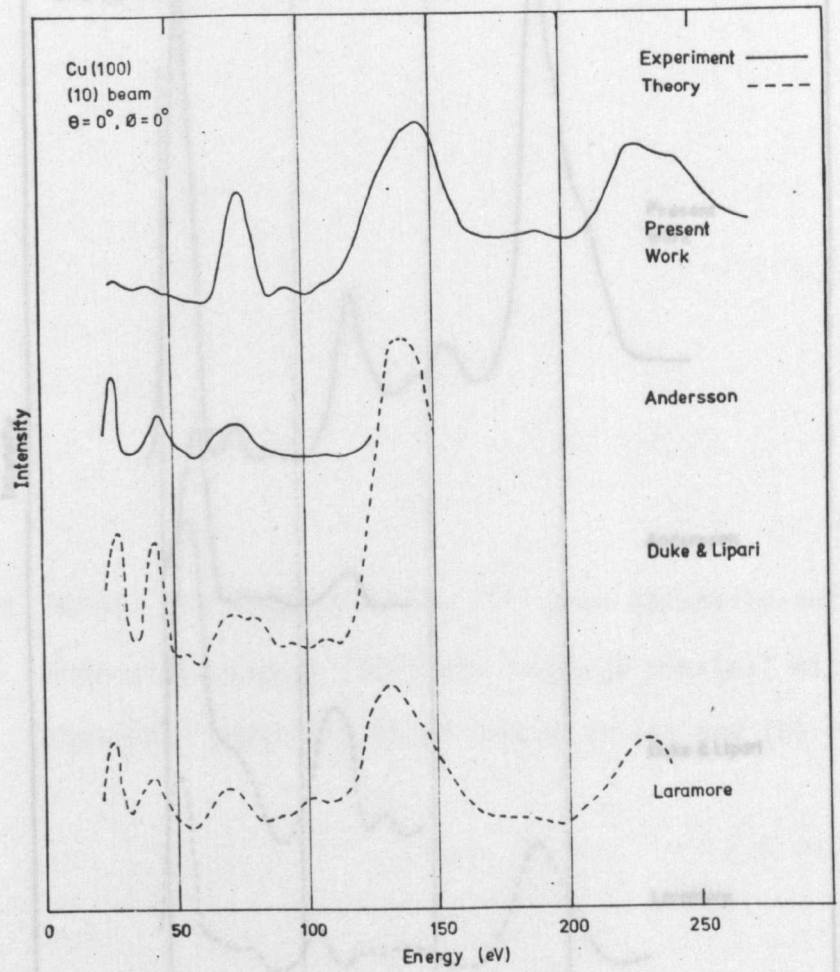

Figure 4.18 Comparison of (10) beam spectra from clean copper (100) at normal incidence.

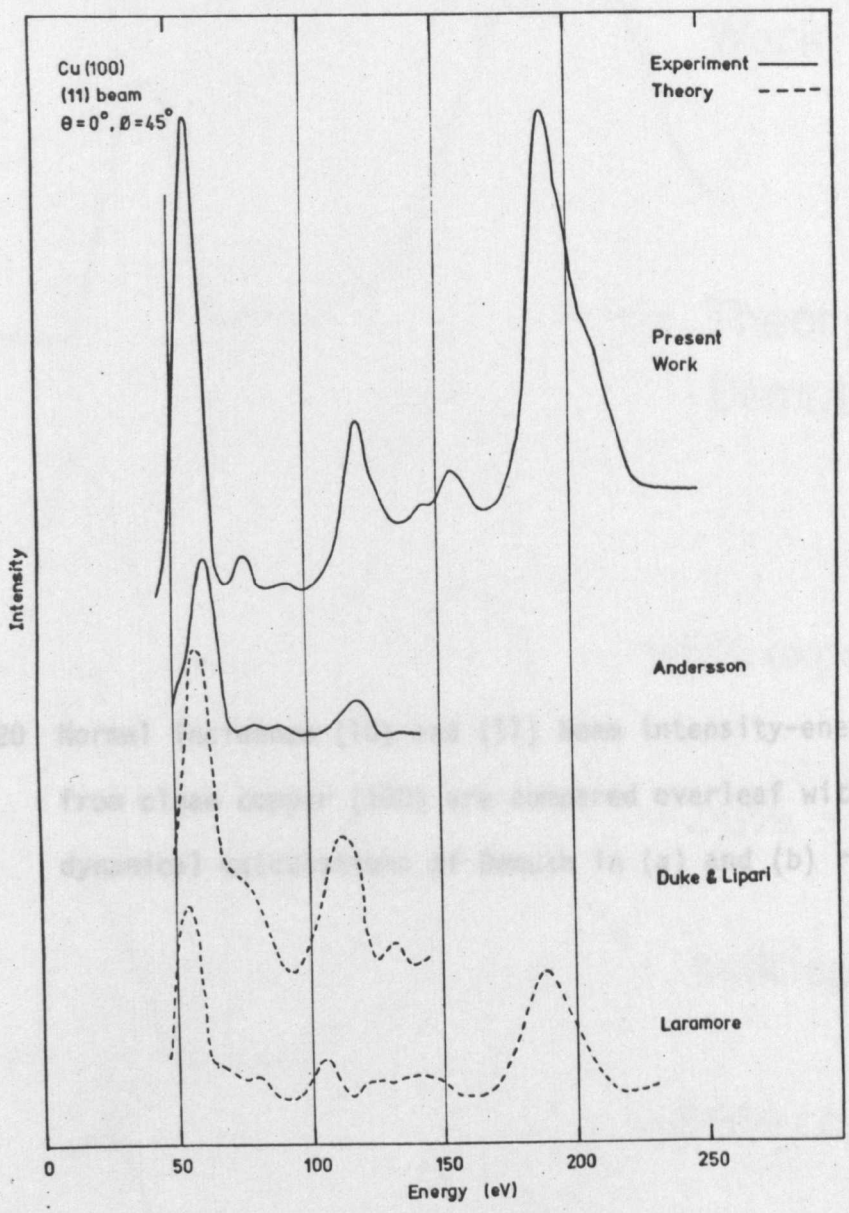

Figure 4.19 A comparison of (11) beam spectra from clean copper (100) at normal incidence.

Figure 4.20 Normal incidence (10) and (11) beam intensity-energy spectra from clean copper (100) are compared overleaf with the dynamical calculations of Demuth in (a) and (b) respectively.

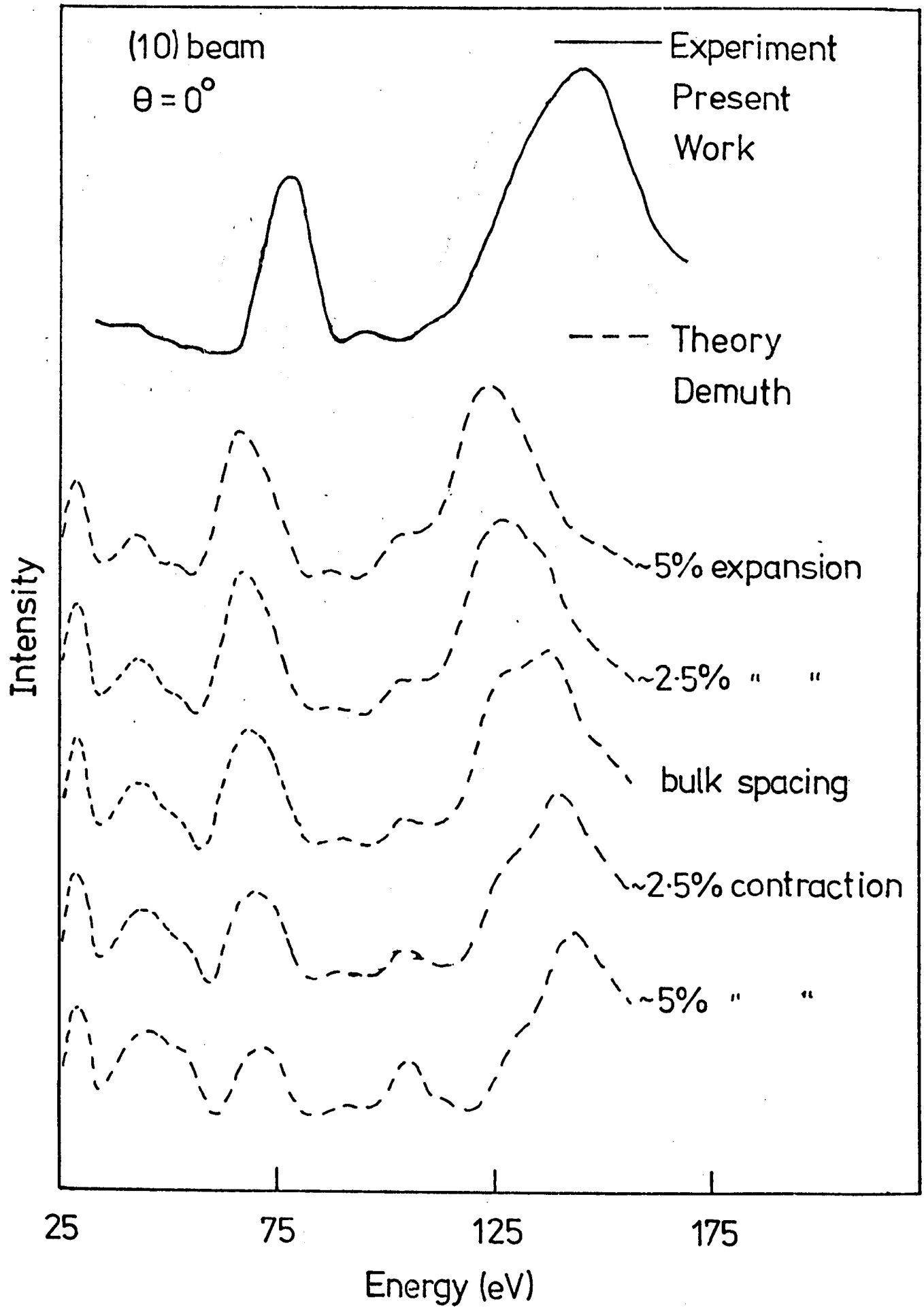
(10) beam
θ = 0°
Experiment
Present
Work
Theory
Demuth
~5% expansion
~2·5% " "
bulk spacing
~2·5% contraction
~5% " "
Intensity
25
75
125
175
Energy (eV)

(a)

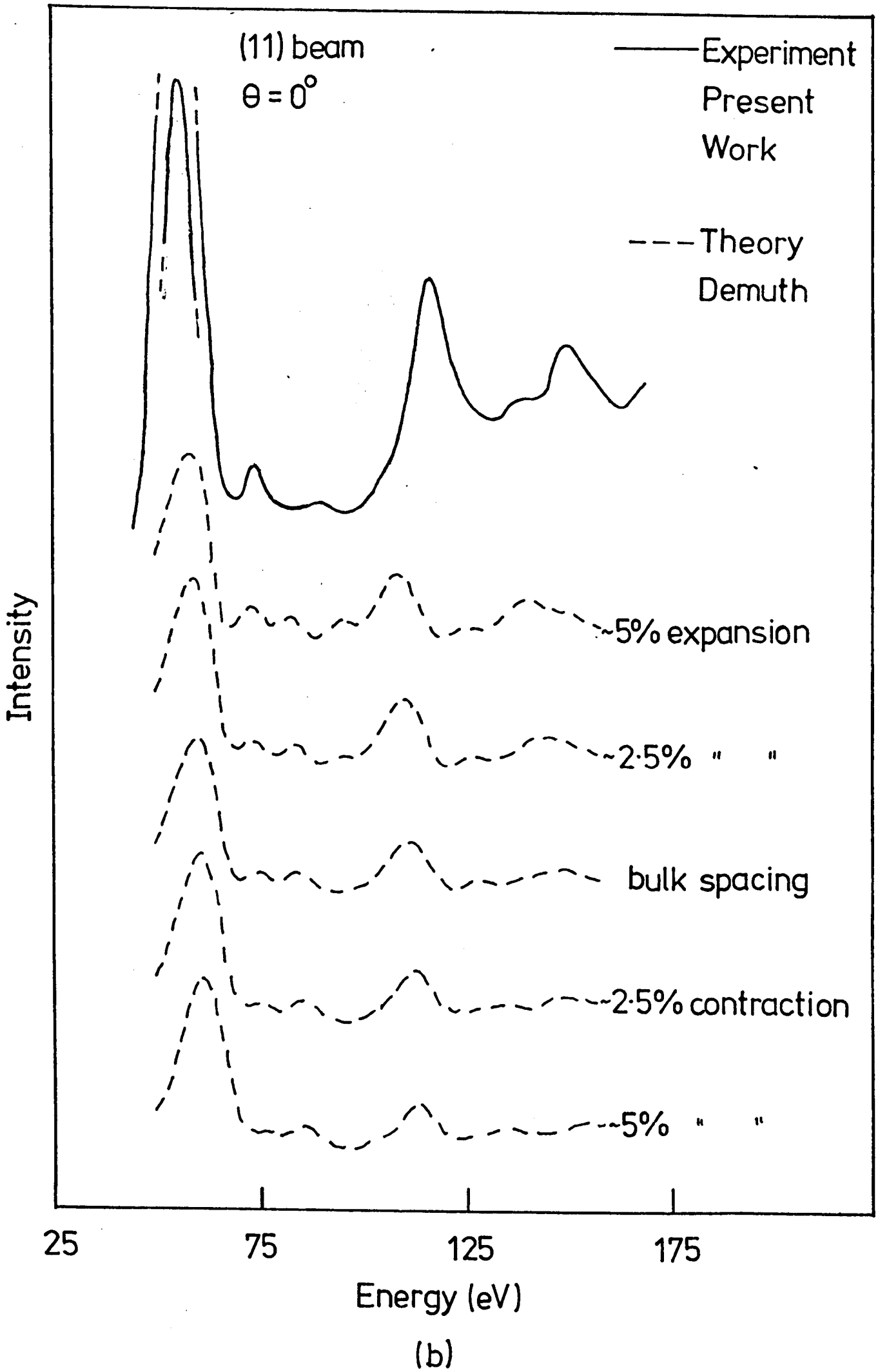
(11) beam
θ = 0°
Experiment
Present
Work
Theory
Demuth
~5% expansion
~2·5% " "
bulk spacing
~2·5% contraction
~5% " "
Intensity
25
75
125
175
Energy (eV)

(b)

except for the (10) beam where the present data exhibits severely attenuated intensities. Although the agreement with the calculations of Duke and Lipari is not as good as that for those of Laramore, they have been included here as a reference for their calculations for one of the oxygen adsorbate LEED structures reported in the next chapter. The calculated spectra of Laramore and also Duke and Lipari shown here are based on theoretical surface models that assume the bulk geometry for the top surface layer. Laramore has performed further (unpublished) calculations for a range of upper layer spacings and determined that the best fit for copper (100) experimental data was obtained with an upper layer spacing equal to the bulk value.

Normal incidence (10) and (11) beam spectra for clean copper (100) have been calculated very recently by Demuth[22] using the computational scheme of Marcus and Jepsen[23] and these are compared in figure 4.20 with the present experimental data. The agreement obtained is comparable to that of Laramore for this limited set of data. It is particularly noticeable that the agreement between theory and experiment is not as good as that achieved by Demuth _et al_[24] for nickel (100).

4.4.2 Copper (111) Surface

(00) beam spectra were obtained for a range of θ in the two high symmetry azimuths $\phi = 0^{o}$ and $\phi = 30^{o}$, as defined in figure 4.21 with respect to the LEED pattern, and are shown in figures 4.22 and 4.23 respectively. Apart from isolated (00) beam spectra obtained at a single angle of incidence (e.g. Simmons _et al_[25]), the only previously published data for the clean copper (111) surface are those of Reid.[1] However, these data are supplemented by a similarly comprehensive range of unpublished data obtained by Woodruff.[2] Both sets of data were obtained using a spot-photometer measuring technique without any AES facilities.

A comparison of some of the present results with this earlier data, which was acquired in an azimuth close to $\phi = 30^{o}$, is shown in figure 4.24

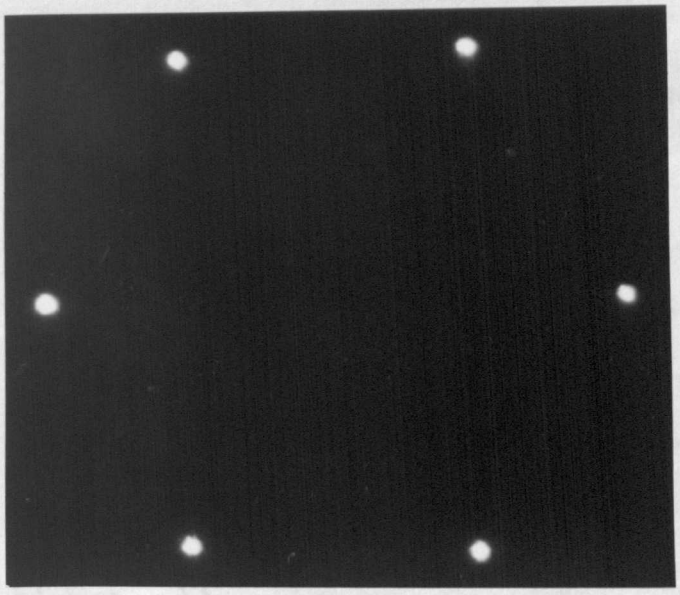

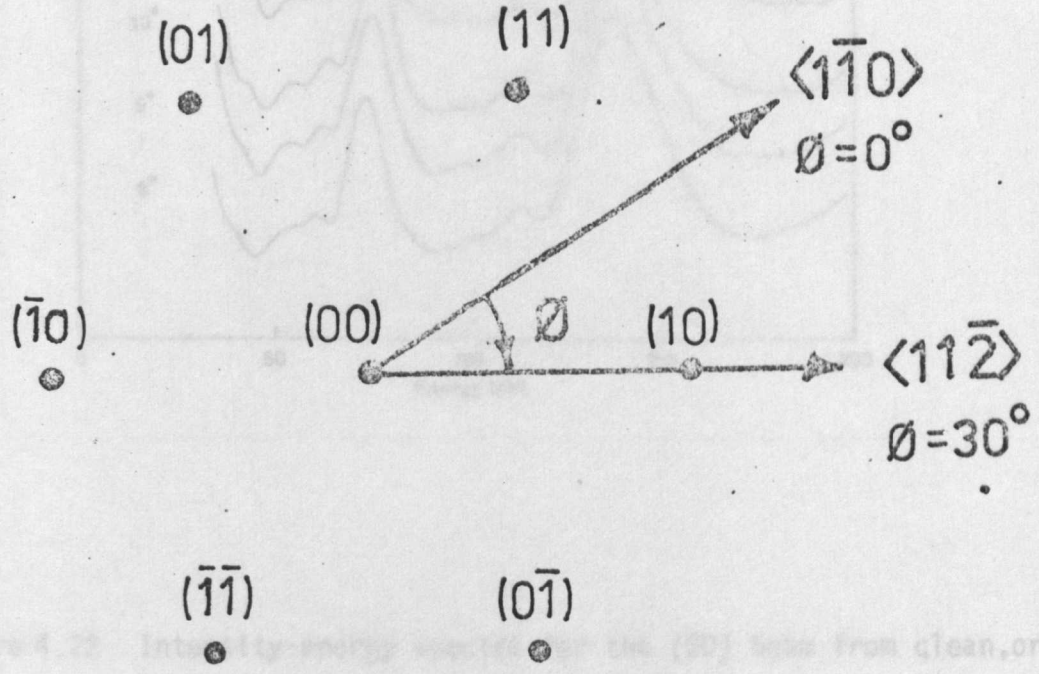

Figure 4.21 146 eV LEED pattern from clean, ordered copper (111).

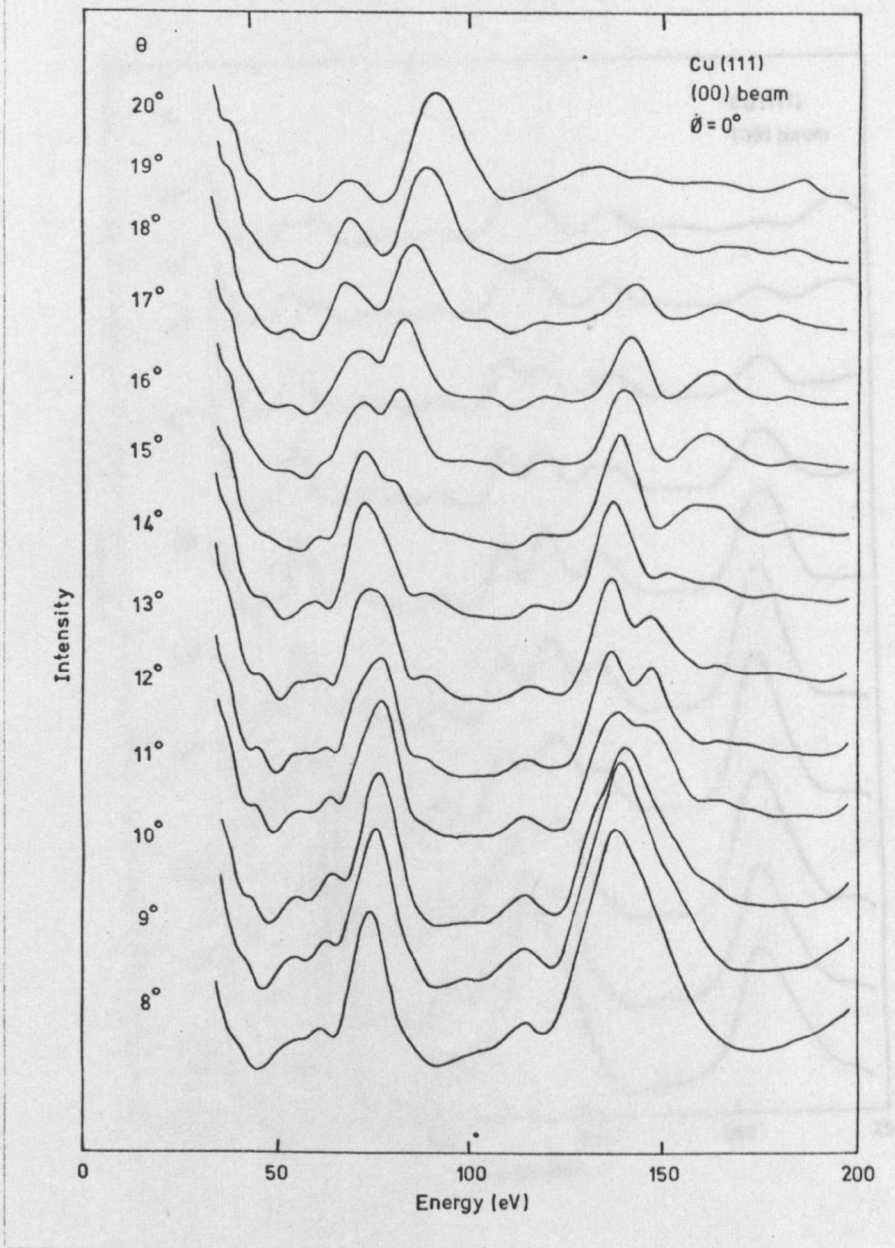

Figure 4.22 Intensity-energy spectra for the (00) beam from clean, ordered copper (111) for a range of θ at $\phi = 0^{o}$.

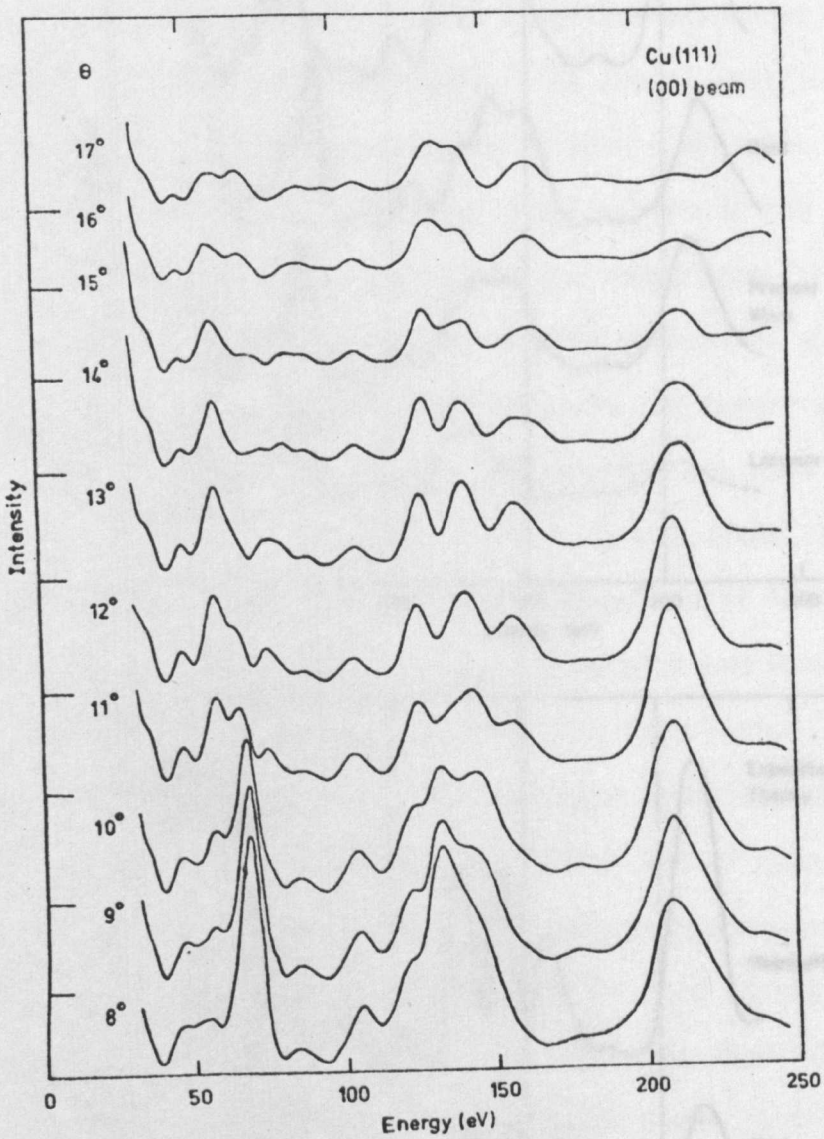

Figure 4.23 Intensity-energy spectra from clean, ordered copper (111) for a range of θ at $\phi = 30^{0}$.

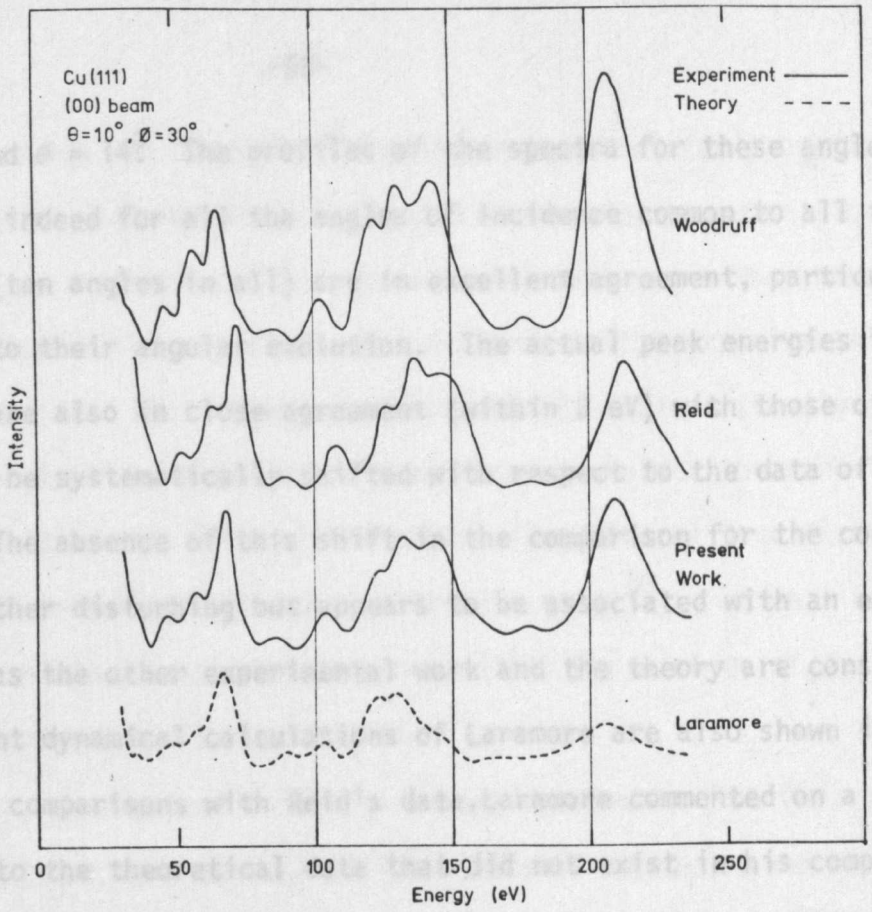

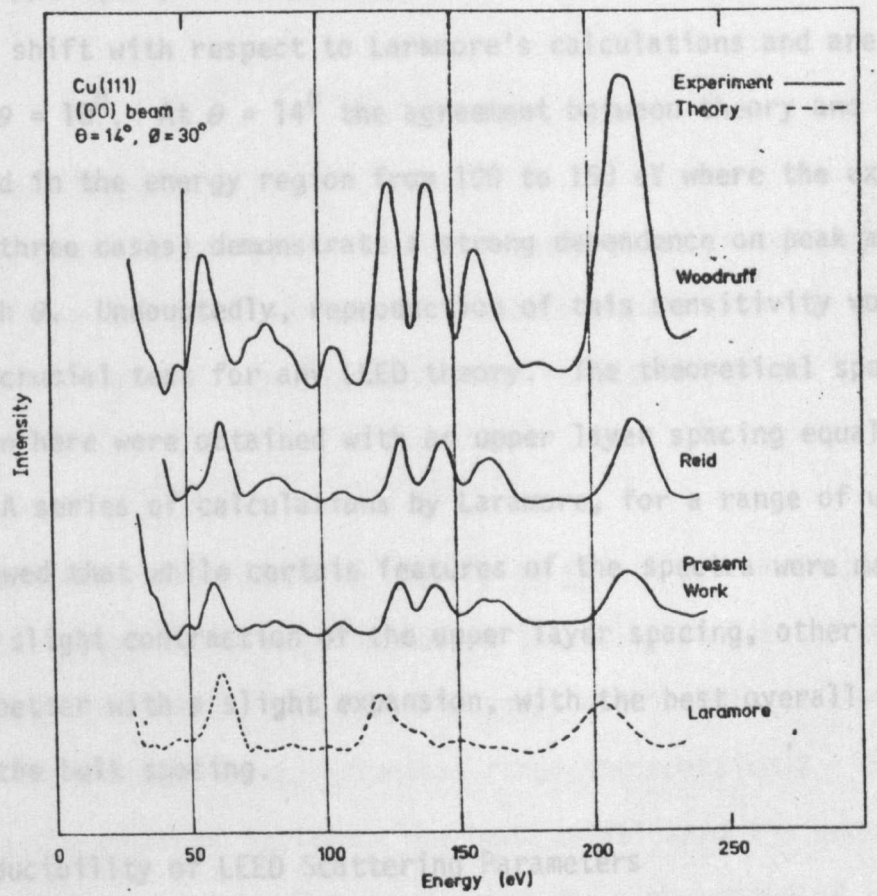

Figure 4.24 A comparison of (00) beam intensity-energy spectra from clean copper (111). Spectra for $\theta = 10^{o}$ and 14^{o} are shown for the $\phi = 30^{o}$ azimuth.

for $\theta = 10^0$ and $\theta = 14^0$. The profiles of the spectra for these angles of incidence and indeed for all the angles of incidence common to all three sets of data (ten angles in all) are in excellent agreement, particularly with respect to their angular evolution. The actual peak energies in the present data are also in close agreement (within 2 eV) with those of Woodruff, but appear to be systematically shifted with respect to the data of Reid by about 8 eV. The absence of this shift in the comparison for the copper (100) surface is rather disturbing but appears to be associated with an error in Reid's work as the other experimental work and the theory are consistent.

The recent dynamical calculations of Laramore are also shown in figure 4.24 In his comparisons with Reid's data,Laramore commented on a shift with respect to the theoretical data that did not exist in his comparisons with Reid's copper (100) data. The present results and Woodruff's results do not show a shift with respect to Laramore's calculations and are in good agreement at $\theta = 10^0$. At $\theta = 14^0$ the agreement between theory and experiment is not so good in the energy region from 100 to 150 eV where the experimental data (in all three cases) demonstrate a strong dependence on peak appearance and shape with θ. Undoubtedly, reproduction of this sensitivity would be a particularly crucial test for any LEED theory. The theoretical spectra of Laramore shown here were obtained with an upper layer spacing equal to the bulk value. A series of calculations by Laramore, for a range of upper layer spacings, showed that while certain features of the spectra were matched better with a slight contraction of the upper layer spacing, other features were matched better with a slight expansion, with the best overall fit being obtained for the bulk spacing.

4.4.3 Reproducibility of LEED Scattering Parameters

The validity of the results of surface structural analyses that are based on the correlation of experimental and theoretical LEED intensities must be determined by the confidence that can be placed in the scattering parameters that are assigned to individual intensity-energy spectra. Although

errors in the energy calibration of the spectra can be simply overcome by the application of a suitable energy shift, errors in the geometrical parameters, θ and ϕ, present a more fundamental problem as they may result in attempts to correlate non-equivalent features in the experimental and theoretical spectra. While θ and ϕ can be readily defined (section 3.4.5) the difficulty experienced in maintaining absolute values throughout an experiment is not always fully appreciated. This general problem has been highlighted by a recent publication by Lagally et al[26] in which a series of (00) beam spectra, acquired from silver (111) for a range of ϕ, failed to show a symmetry that clearly exists.

Lagally et al obtained intensity-energy spectra for the (00) beam for a range of azimuths at a nominally fixed angle of incidence and noted that the spectra exhibited six-fold symmetry:

$$I_{00}(\phi) = I_{00}(\frac{n\pi}{3} + \phi) \qquad ...4.2$$

where n is some integer.

Reciprocity has the effect of increasing the point group symmetry of the (00) beam from the (111) surface of f.c.c. crystals from the point group 3m to the point group 6mm. Consequently, the condition for the (00) beam is:

$$I_{00}(\phi) = I_{00}(\frac{n\pi}{3} \pm \phi) \qquad ...4.3,$$

a symmetry that was not observed by Lagally et al. A similar experiment to that of Lagally et al has been performed on the (111) surface of copper. Intensity-energy spectra for the (00) beam were acquired for a nominally fixed angle of incidence for an azimuthal range encompassing $\phi = 0^{o}$ and $\phi = 30^{o}$. Once the angle of incidence had been established the experiment was commenced and performed without adjusting the θ mechanism of the specimen manipulator. The symmetry anticipated was not observed. Its absence was due to small inadvertent changes in the angle of incidence caused by slight misalignment of the ϕ rotation axis.

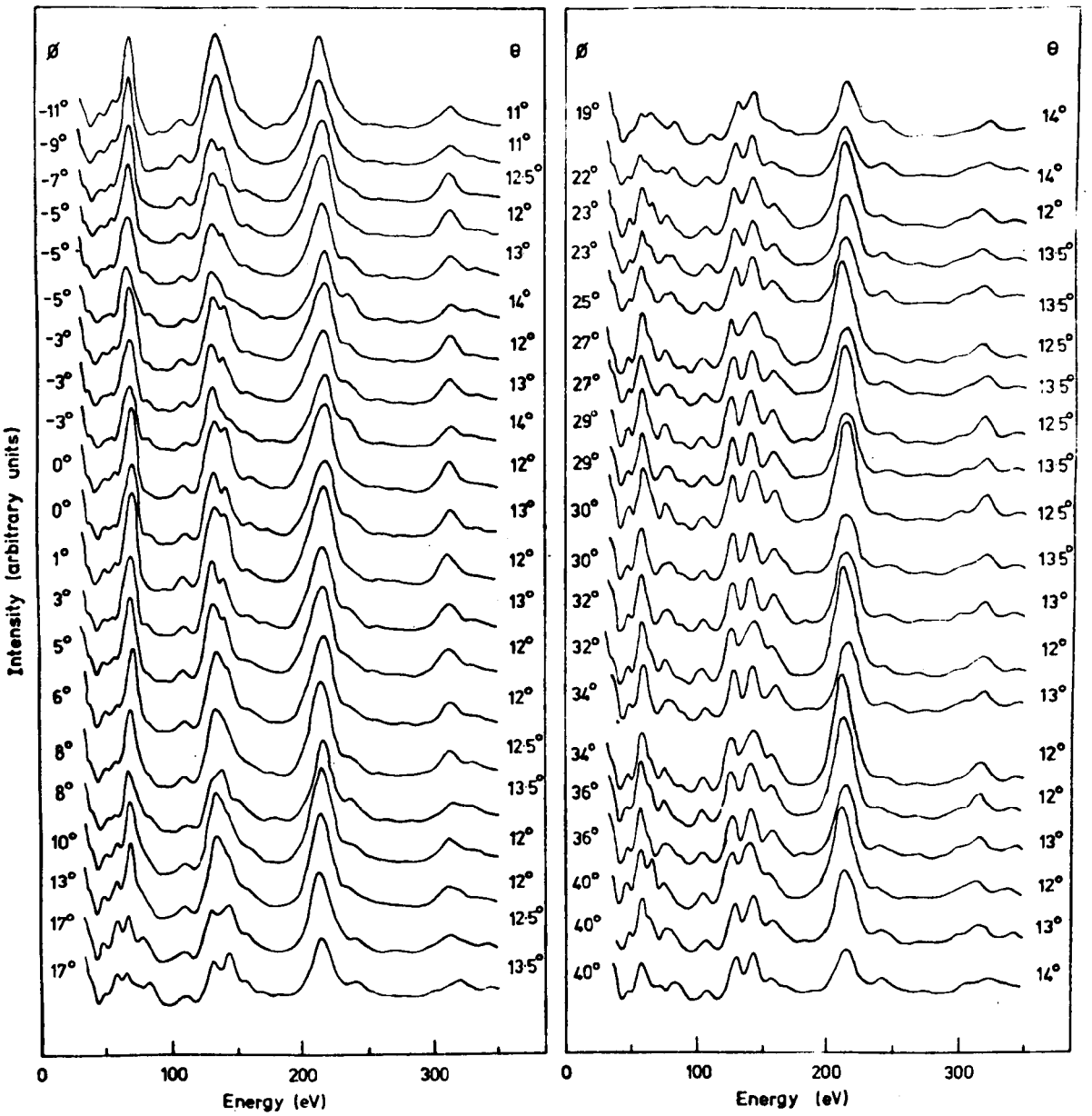

Figure 4.25 Intensity-energy spectra from a copper (111) surface for the (00) beam for a range of θ and ϕ. The measured values of θ have been corrected by comparing curves taken for incidence on either side of the surface normal.

A further experiment was performed in which intensity-energy spectra were obtained for several angles of incidence (in 1^{o} increments) on either side of the surface normal for each value of ϕ. The $+\theta$ and $-\theta$ spectra were compared for each azimuth and where necessary reciprocity was used to correct the angle of incidence (not normally by more than $1/2^{o}$). The results of this experiment are shown in figure 4.25; if the trends in the spectra that occur as ϕ is varied are studied the symmetry anticipated from equation 4.3 is evident. For example at about 140 eV the large doublet at $\phi = 0^{o}$ reverts to a single peak symmetrically as the azimuth changes in either direction. In the same region in the $\phi = 30^{o}$ azimuth the shape of the triplet observed there changes symmetrically about this azimuth as well.

*****

REFERENCES

(1) R.J.Reid, Ph.D.Thesis, University of Warwick, (1971).

(2) D.P.Woodruff, University of Warwick, unpublished data.

(3) T.W.Haas & J.T.Grant, *Appl.Phys.Lett.* 16 (1970) 172.

(4) L.H.Jenkins & M.F.Chung, *Surface Sci.* 24 (1971) 125.

(5) M.Perdereau, *Surface Sci.* 24 (1971) 239.

(6) C.Argile & G.E.Rhead, *J.Phys.C.* 7 (1974) L261.

(7) J.Pritchard,Queen Mary College,University of London,private communication. M.A.Chesters & J.Pritchard, *Surface Sci.* 28 (1971) 460.

(8) L.McDonnell,B.D.Powell & D.P.Woodruff, *Surface Sci.* 40 (1973) 669.

(9) P.J.Dobson,Imperial College, University of London, private communication.

(10) G.E.Becker & H.Hagstrum, *J.Vac.Sci.Tech.* 11 (1974) 284.

(11) J.Falconer & R.J.Madix, Stanford University,California, private communication cited by (10)

(12) F.P.Netzer & M.Prutton, to be published in *Solid State Comm.*

(13) W.A.Coghlan & R.F.Clausing, Oak Ridge National Laboratory Report ORNL-TM-3576 (1971).

(14) H.Bishop & J.C.Riviere, *J.Appl.Phys.* 40 (1969) 1740.

(15) S.Andersson & B.Kasemo, *Solid State Comm.* 8 (1970) 1885.

(16) B.D.Powell, University of Warwick, private communication.

(17) P.W.Palmberg, *Appl.Phys.Lett.* 13 (1968) 183.

(18) H.E.Farnsworth, *Phys.Rev.* 34 (1929) 679.

(19) G.E.Laramore, to be published in *Phys.Rev.B.*

(20) S.Andersson, *Surface Sci.* 18 (1969) 325.

(21) C.B.Duke & N.O.Lipari, Xerox Laboratories,Rochester,to be published.

(22) J.E.Demuth,IBM Thomas J.Watson Research Centre,New York,unpublished data.

(23) P.M.Marcus & D.W.Jepsen, *Phys.Rev.Lett.* 20 (1968) 925.

(24) J.E.Demuth,D.W.Jepsen & P.M.Marcus, to be published.

(25) G.W.Simmons,D.F.Mitchell & K.R.Lawless, *Surface Sci.* 8 (1967) 130.

(26) M.G.Lagally,T.C.Ngoc & M.B.Webb, *Surface Sci.* 25 (1971) 444.

CHAPTER FIVE. OXYGEN ADSORPTION ON (111) AND (100) SURFACES OF COPPER

5.1 Experimental Procedure for Oxygen Exposure

Clean, ordered (100) and (111) surfaces of copper were simultaneously exposed at room temperature to high purity oxygen (GradeX:B.O.C.Ltd.) for an exposure range of $1x10^{-10}$ to $1x10^{-3}$ torr-mimutes at oxygen pressures up to $1x10^{-6}$ torr. Although some workers[1] have used the Langmuir (L), where 1L is defined as $1x10^{-6}$ torr-seconds, as the unit of exposure there is not a S.I. approved unit and all the exposures quoted in this thesis are in the highly convenient experimental unit of torr-minutes.

A "dynamic" exposure technique, in which oxygen was continually leaked through the experimental chamber into the throttled ion pump was used. Residual gas analysis, using the Q7 mass spectrometer, had shown that for "static" exposures, i.e. those with the ion pump fully isolated, no oxygen was detected in the experimental chamber; only the methane series and argon was detected, possibly due to their displacement from the chamber walls by the more active oxygen. This behaviour is clearly demonstrated in figure 5.1 where the major gas species are identified in a sequence of mass spectra obtained during (a) typical UHV conditions, (b) "static" oxygen exposure and (c) "dynamic" oxygen exposure. During "dynamic" oxygen exposures the impurity content was estimated from the Q7 spectra to be less than $5x10^{-3}$ with argon (mass number 40) being the major impurity. Although the oxygen was considerably contaminated following its introduction into the experimental chamber, AES inspection of surface conditions before and after exposure did not indicate the adsorption of anything other than oxygen. All exposures were performed with the electron gun switched off and the electron beam was only re-established at base pressures of better than $5x10^{-10}$ torr and generally at $2x10^{-10}$ torr.

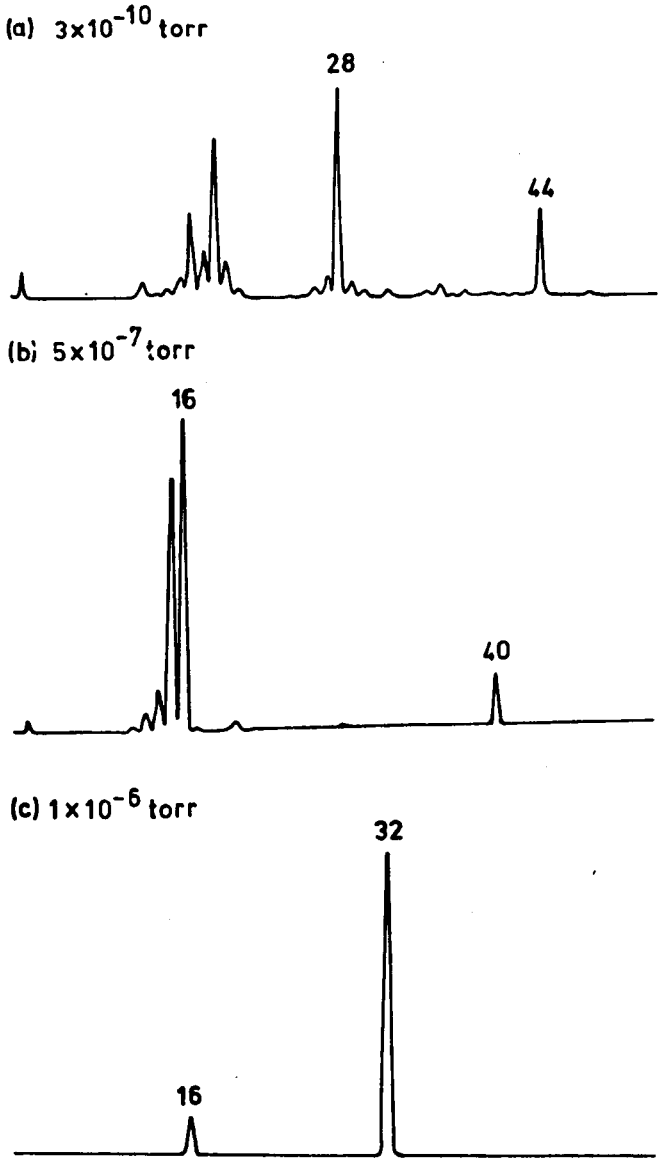

Figure 5.1 Quadrupole mass spectra for (a) typical UHV conditions,(b) "static" oxygen exposure and (c) "dynamic" oxygen exposure. The total pressures were $3x10^{-10}$ torr, $5x10^{-7}$ torr and $1x10^{-6}$ torr respectively. The major peaks are identified by mass number.

5.2 (111) Surface

5.2.1 LEED Observations during Oxygen Adsorption

Oxygen adsorbed in a disordered manner on the (111) surface of copper at room temperature for exposures up to $1x10^{-3}$ torr-minutes. A gradual increase in the background LEED intensity with exposure was observed without any indication of extra diffraction features. The results of the previous LEED studies on this particular adsorption system are summarised in table 5.1 and show that while this observation is in complete agreement with Ertl[2] and Oustry et al[4] it does not agree with the other two studies.[1,3]

Annealing the (111) surface at temperatures up to 250°C, after a range of oxygen exposures, failed to produce any ordered structures but reduced the background LEED intensity, presumably due to oxygen diffusion into the bulk. Indeed evidence of a high oxygen solubility in copper exists[5,6] and certainly there was no indication of any oxygen desorption in the Q7 mass spectra acquired during the annealing periods. The high heat of adsorption for oxygen on copper[7] of 110 Kcal $mole^{-1}$ would render thermal desorption unlikely at these temperatures.

Annealing the (111) surface at temperatures between 250 and 550°C, after oxygen exposures of $1x10^{-3}$ torr-minutes at room temperature, produced a surface structure characterised by the LEED pattern shown in figure 5.2a Careful examination of this LEED pattern showed that there were two sets of six spots centred about each of the integral order beams (i.e. the clean copper (111) beams). From the variation of the LEED pattern with energy these fractional- order beams were found to be six-fold symmetric but not symmetrically oriented with respect to the integral beams. The AES spectrum obtained from the copper (111) surface after this treatment (and also the (100) surface) is shown in figure 5.3 together with the oxygen Auger signal recorded before annealing. The very high sulphur concentration, estimated as 25 % of a monolayer, together with the lack of evidence of oxygen after annealing has resulted in the association of this structure with sulphur

TABLE 5.1

OXYGEN ADSORPTION ON COPPER (111)

REFERENCE	STRUCTURE	TREATMENT	SURFACE CHARACTERISATION
SIMMONS, MITCHELL & LAWLESS (1967) [1]	A. close packed layer rotated 30°	1×10^{-4} τ min O_2 at 25°C	Retarding Potential Measurements
	B. coincidence lattice structure	1.5×10^{-3} τ min O_2 at 25°C	
ERTL (1967) [2]	disordered	5×10^{-5} τ min O_2 at 25°C	?
TAKAHASHI, TOMITA & MOTOO (1969) [3]	(3x3)	8×10^{-3} τ min O_2 plus 2 min at 350°C	?
OUSTRY, LAFOURCADE & ESCAUT (1973) [4]	no ordered structure at room temperature		?
PRESENT WORK	disordered	1×10^{-3} τ min O_2 at 25°C	Auger Electron Spectroscopy

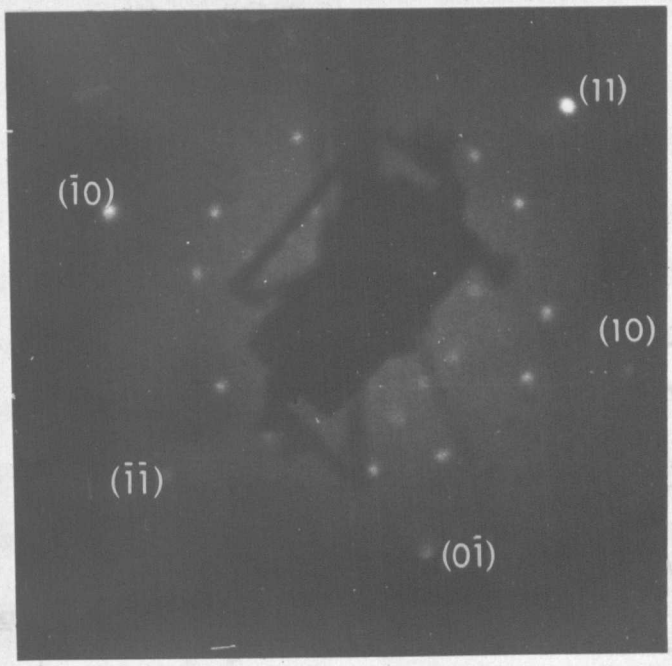

Figure 5.2a 69 eV LEED pattern for sulphur segregated copper (111) surface.

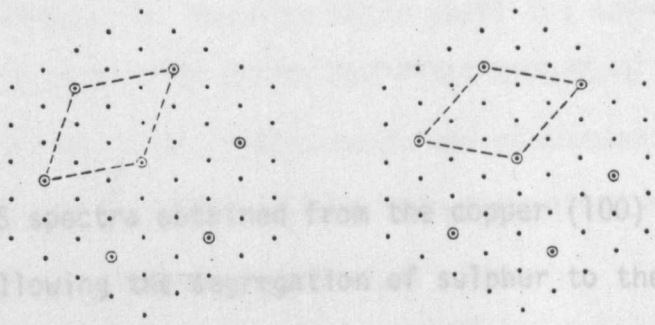

Figure 5.2b Interpretation of above LEED pattern in terms of two domains of a hexagonal surface net with net dimensions $\sqrt{7}$ times those of the clean surface net.

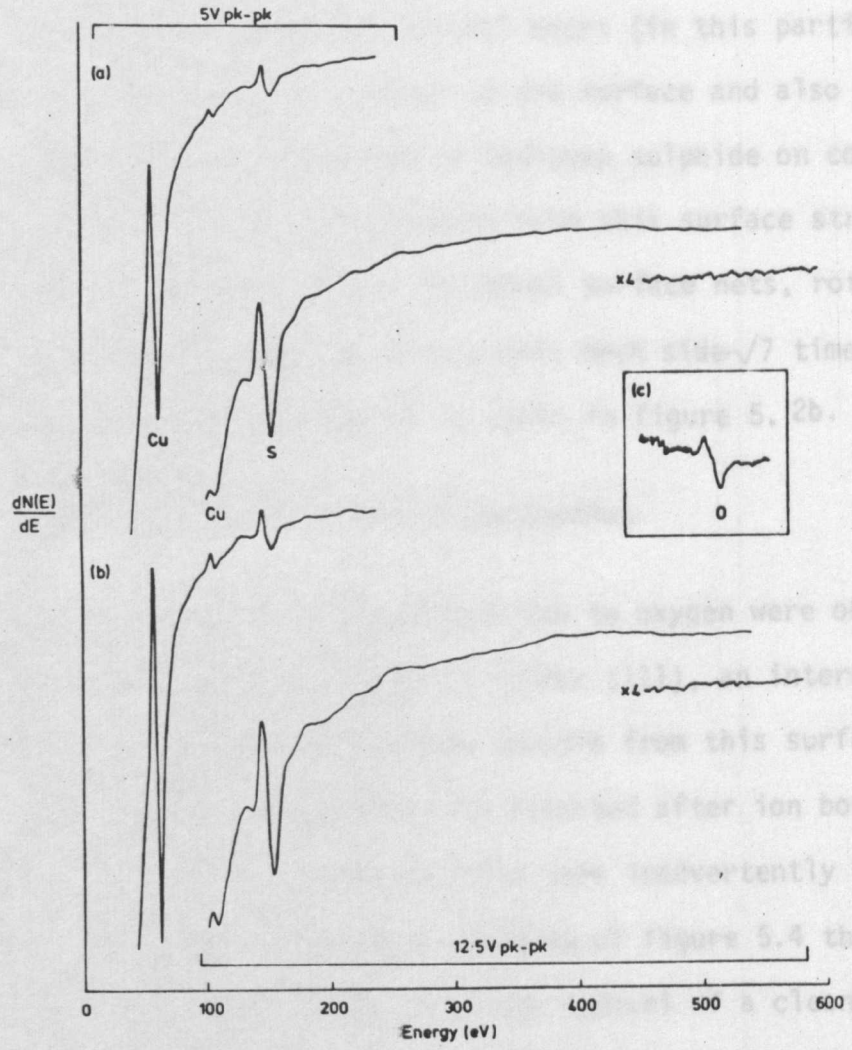

Figure 5.3 AES spectra obtained from the copper (100) and (111) surfaces following the segregation of sulphur to the surface are shown in (a) and (b) respectively. The oxygen concentration on the (111) surface prior to segregation is shown in the insert (c).

rather than oxygen. This conclusion is supported by observations of an identical structure by the author and others[8] after annealing the clean copper (111) surface at 650°C for several hours (in this particular case) in order to rapidly segregate sulphur to the surface and also by Domange and Oudar[9] following the adsorption of hydrogen sulphide on copper (111). Careful measurement of the LEED patterns from this surface structure allowed its interpretation in terms of two hexagonal surface nets, rotated with respect to each other by 38° and with a unit mesh side $\sqrt{7}$ times that of the clean surface. This interpretation is shown in figure 5. 2b.

5.2.2 AES Observations during Oxygen Adsorption

Although no ordered LEED structures due to oxygen were observed during the controlled adsorption of oxygen on copper (111), an interesting feature was observed in the secondary electron spectra from this surface. This feature, a peak at 79 eV, was initially observed after ion bombardment of the copper specimens using argon that had been inadvertently contaminated with oxygen. As shown in the upper spectrum of figure 5.4 the corresponding AES spectrum, apart from this feature, was typical of a clean, ordered copper (111) surface; no impurity Auger peaks but several TDP's were observed. A weak LEED structure, similar to the first structure reported by Simmons et al[3] in their oxygen adsorption work, was also observed. On heating to 120°C for a few minutes this surface structure disappeared immediately while the 79 eV peak was severely attenuated.

Subsequently, this peak was also observed during the progressive adsorption of oxygen onto clean copper (111) and in the lower sequence of spectra in figure 5.4 the amplitude of the 79 eV peak can be seen to maximise at an exposure of approximately 2×10^{-5} torr-minutes. At this particular exposure, the most intense oxygen Auger transition at 515 eV ($KL_{2,3}L_{2,3}$) was not detected. Indeed, the sensitivity of AES to oxygen on a copper substrate appears to be extremely low; whether this is a chemical effect or a back-scattering property of the substrate is not known. An interpretation

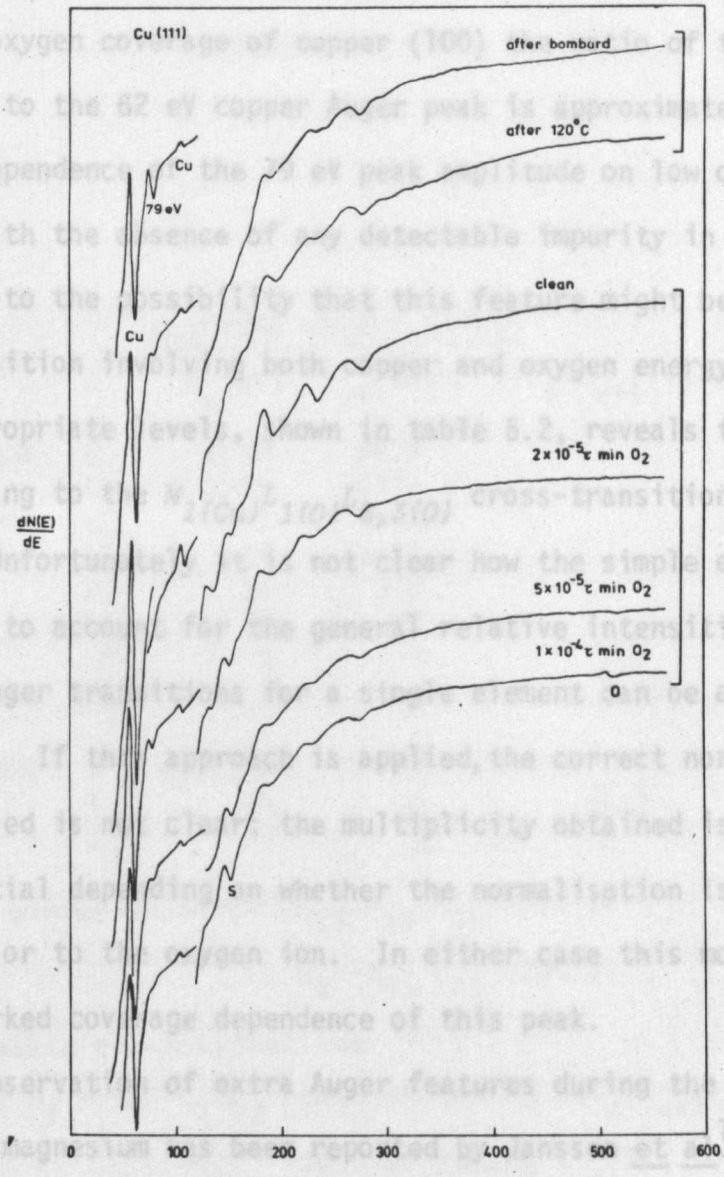

Figure 5.4 AES spectra from copper (111) showing the variation of the 79 eV peak amplitude with oxygen exposure.

of the small amplitude of the oxygen Auger peaks in terms of low oxygen coverage would appear to be incompatible with other observations. A very recent AES calibration experiment by Argile and Rhead[10] has shown that for monolayer oxygen coverage of copper (100) the ratio of the 515 eV oxygen Auger peak to the 62 eV copper Auger peak is approximately 9×10^{-3}.

The dependence of the 79 eV peak amplitude on low oxygen coverage, together with the absence of any detectable impurity in the AES spectra, gives rise to the possibility that this feature might be due to an Auger cross-transition involving both copper and oxygen energy levels. Inspection of the appropriate levels, shown in table 5.2, reveals that the energy corresponding to the $M_{1(Cu)}L_{1(O)}L_{2,3(O)}$ cross-transition is approximately correct. Unfortunately it is not clear how the simple electron multiplicity model used to account for the general relative intensities of different possible Auger transitions for a single element can be applied to a cross-transition. If this approach is applied, the correct normalisation procedure to be applied is not clear; the multiplicity obtained is either very small or substantial depending on whether the normalisation is relative to the copper ion or to the oxygen ion. In either case this model does not account for the marked coverage dependence of this peak.

The observation of extra Auger features during the oxidation of both sodium and magnesium has been reported by Janssen et al.[11] These Auger peaks, which can not be attributed to either the metal or to oxygen, exhibit an amplitude dependence with oxygen coverage that is very similar to that in figure 5.4. These peaks are termed interfacial transitions by Janssen et al who argue that the transitions involve levels in both the oxide and in the underlying metal. In their model the growth and then decay of the amplitude of the peak due to the interfacial transition are due respectively to the initial formation of the oxide layer and the subsequent movement of the oxide/metal interface to a depth that is greater than the mean escape depth of the electrons constituting the peak in question. While such a hypothesis qualitatively explains the observed behaviour of the peak observed on copper

TABLE 5.2

ELECTRON ENERGY LEVELS

		E_z(eV)	E_{z+1}(eV)	$\frac{1}{2}(E_z+E_{z+1})$(eV)
COPPER	K	8979	9659	
	L_I	1096	1194	
	L_{II}	951	1044	
	L_{III}	931	1021	
	M_I	120	137	
	M_{23}	74	87	
	M_{45}	2	9	5.5
	N_I	2.5	4	3.25
OXYGEN	K	532	686	
	L_I	24	31	27.5
	L_{23}	7	9	8

Low energy Cu peaks M_{23} M_{45} M_{45} 63 eV

M_I M_{45} M_{45} 109 eV

Possible cross-transition

(Cu) M_I - (O) L_IL_{23} 84.5 eV (using $\frac{1}{2}(E_z+E_{z+1})$)

80 eV (using E_{z+1})

it is difficult to relate this concept of a definitive oxide layer with the relatively low oxygen coverages reported here.

The formation of an extra Auger peak has also been reported during the exposure of strontium and cesium surfaces to oxygen by Helms and Spicer[12] and Desplat[13] respectively. Helms and Spicer also observed small oxygen Auger signals after substantial oxygen exposure with independent evidence of considerable adsorption. The weakness of the oxygen signal was interpreted by them as indicating that absorption rather than adsorption was ocurring at room temperature.

5.2.3 Intensity-Energy Spectra

As no ordered surface structures were observed during the room temperature adsorption of oxygen onto the (111) copper surface, detailed intensity-energy spectra were not recorded. However, limited data was acquired for the (00) beam and a range of spectra acquired in the $\phi = 30^{0}$ azimuth for different values of θ are presented in figure 5.5. On comparison with the clean surface equivalent (figure 5.5) quite significant differences have ocurred, particularly at low energies and at the higher angles of incidence.

Although the adsorbate is disordered, complete disorder must be restricted to the two dimensions parallel to the surface because the vertical displacement of the oxygen atoms relative to the top copper layer must be confined to a small range of values. The average vertical displacement of the oxygen atoms then constitutes the structure that is reflected in the observed changes in the spectra. An analysis of these differences has been made using the constant momentum transfer averaging scheme of Lagally *et al*[14] and this will be discussed in detail in chapter six.

Figure 5.5 Intensity-energy spectra for the (00) beam are shown overleaf for (a) the clean copper (111) surface and (b) the copper (111) surface after the disordered adsorption of oxygen following an exposure of 1×10^{-3} torr-minutes. Both sets of spectra were acquired for an identical range in θ in the $\phi = 30^{o}$ azimuth.

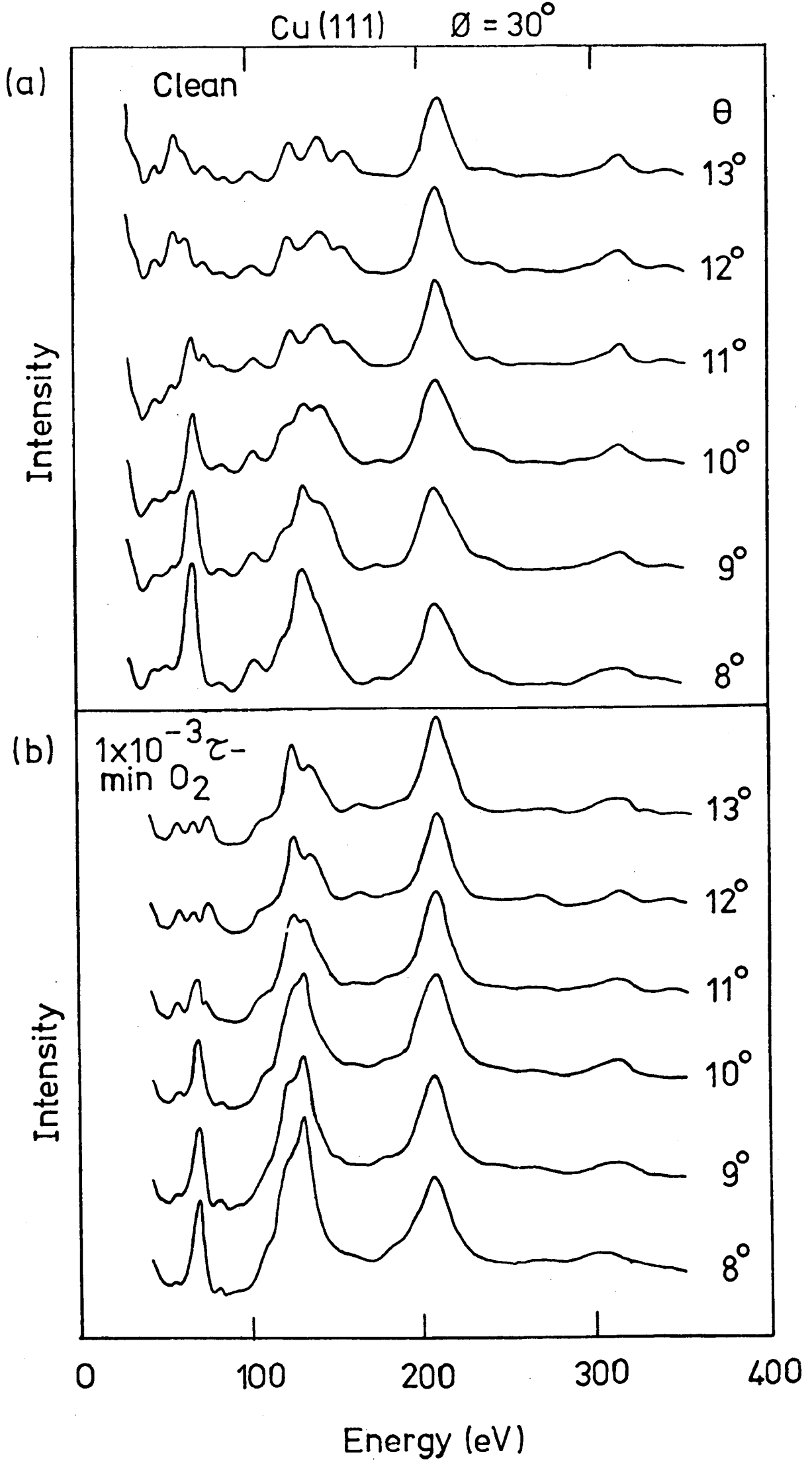
Cu (111) Ø = 30°
(a)
Clean
θ
13°
12°
11°
10°
9°
8°
Intensity
(b)
1x10⁻³ τ-min O₂
13°
12°
11°
10°
9°
8°
Intensity
0
100
200
300
400
Energy (eV)

5.3 (100) Surface

5.3.1 LEED and AES Observations during Oxygen Exposure

Oxygen exposures of $1x10^{-5}$ torr-minutes at room temperature produced a $(\sqrt{2}x\sqrt{2})R45^{o}$ LEED structure (often referred to as c(2x2) although the use of a centred square net is crystallographically incorrect as remarked in section 2.2.2). Further oxygen exposure to $1x10^{-4}$ torr-minutes at room temperature produced a (2x2) structure. Both of these structures are shown in figure 5.6 together with their corresponding surface nets. The (2x2) structure could also be produced by annealing the $(\sqrt{2}x\sqrt{2})R45^{o}$ structure at temperatures below $250^{o}C$, provided that there was sufficient disordered oxygen present on the surface following the saturation of the $(\sqrt{2}x\sqrt{2})R45^{o}$ structure. Typical AES spectra for the two structures are shown in figure 5.6c. The oxygen concentration for these structures corresponds to 0.20 monolayers for the $(\sqrt{2}x\sqrt{2})R45^{o}$ structure and 0.28 monolayers for the (2x2) structure using the calibration of Argile and Rhead. These figures can only be taken to be approximate as AES calibration experiments of this type are particularly sensitive to the energy of the primary beam which is unknown for the preliminary results of Argile and Rhead.

The results of the previous LEED studies of this particular adsorption system are summarised in table 5.3 and while the observation of the $(\sqrt{2}x\sqrt{2})$ $(\sqrt{2}x\sqrt{2})R45^{o}$ structure is in agreement with the results of Simmons *et al*[1] and also Oustry *et al*[4] the (2x2) structure reported here has not been reported previously. Although the earlier studies differ among their initial adsorption structure there has been general agreement with the second structure $(2\sqrt{2}x\sqrt{2})R45^{o}$ which was not observed in this particular study. Lee and Farnsworth[15] have shown that the $(2\sqrt{2}x\sqrt{2})R45^{o}$ structure preferentially nucleates on defect sites to the extent of bypassing their precursive "oblique" structure when oxygen adsorbs onto "as bombarded" surfaces. Thus it is certainly plausible that surface order, differences in specimen preparation, environment or the history of the specimen may account for the

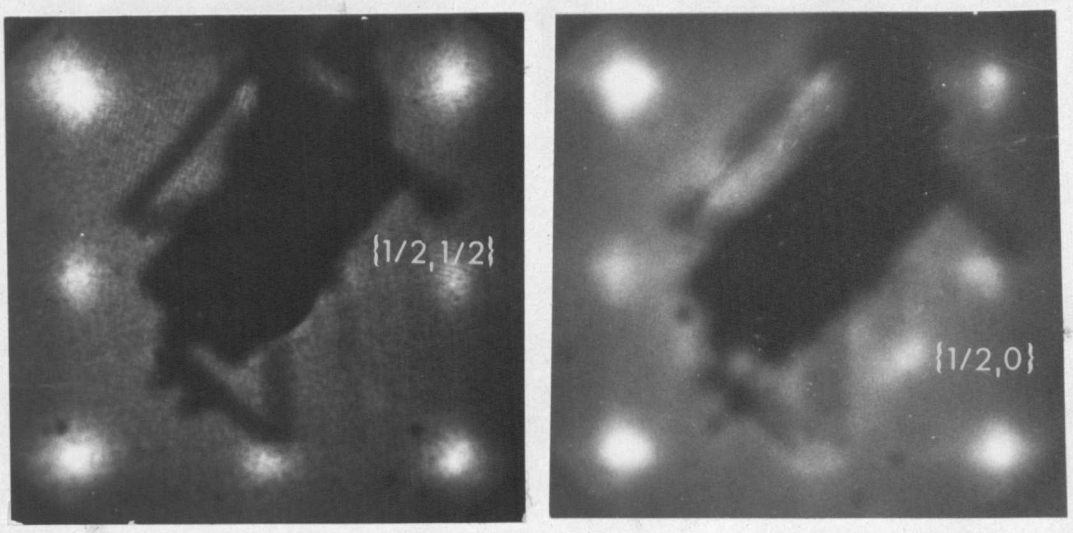

(a) (b)

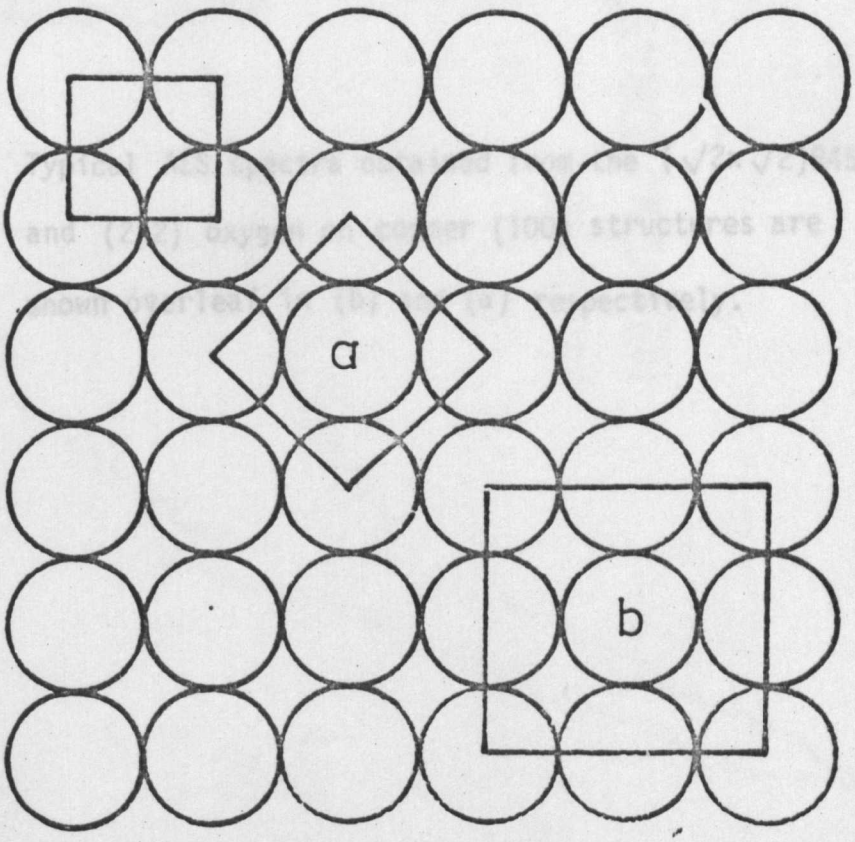

Figure 5.6 61 eV LEED patterns from ($\sqrt{2}$x $\sqrt{2}$)R45^{o} and (2x2) oxygen structures on copper (100) are shown in (a) and (b) respectively together with their respective surface nets.

Figure 5.6c Typical AES spectra obtained from the $(\sqrt{2}\times\sqrt{2})R45^{o}$ and (2x2) oxygen on copper (100) structures are shown overleaf in (b) and (a) respectively.

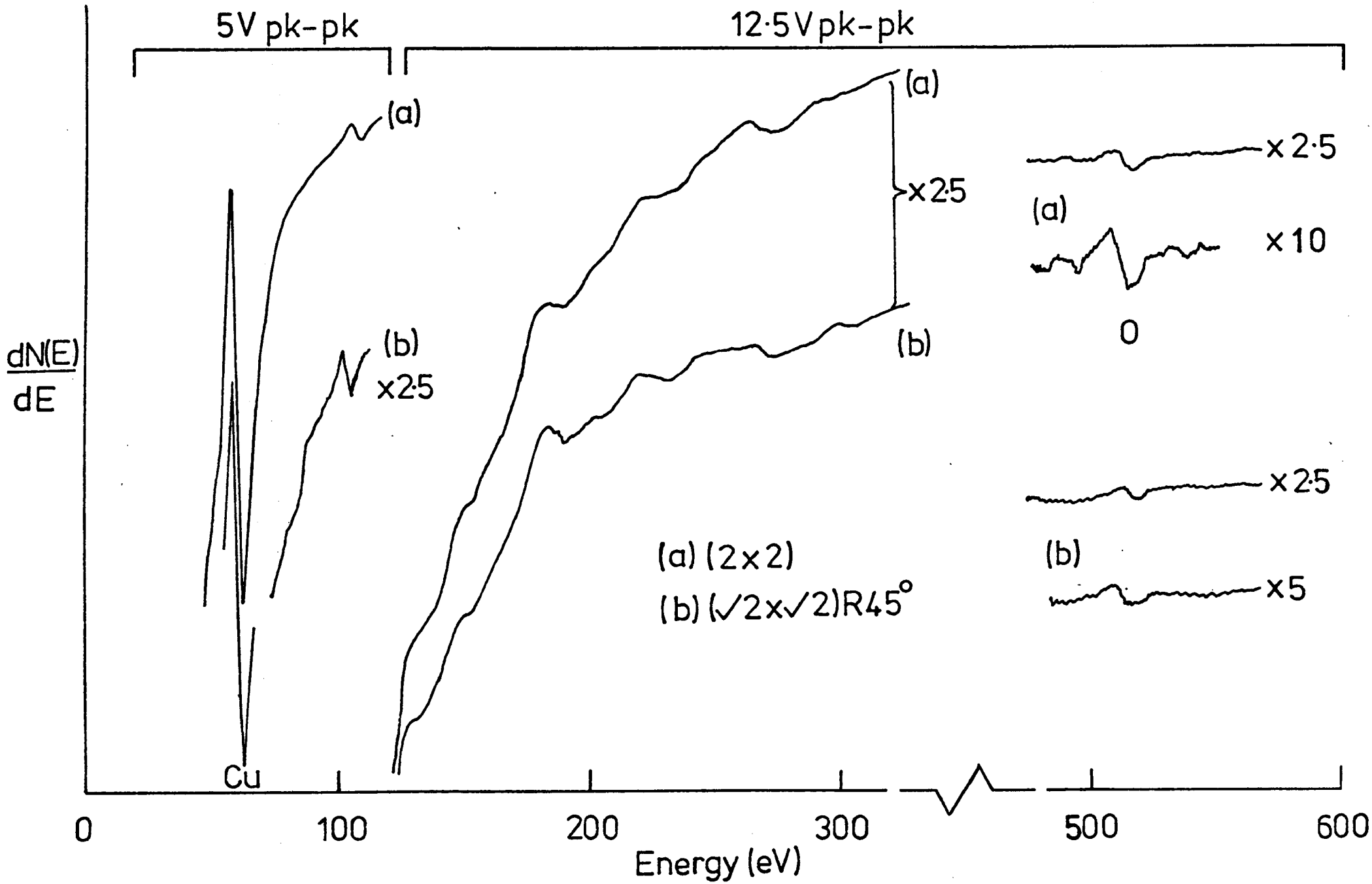
5V pk-pk
12·5V pk-pk
(a)
(b)
x2·5
x2·5
dN(E)
dE
(a)
x2·5
(a)
x10
0
(b)
x2·5
(b)
x5
(a) (2x2)
(b) (√2x√2)R45°
Cu
0
100
200
300
500
600
Energy (eV)

TABLE 5.3

OXYGEN ADSORPTION ON COPPER (100)

REFERENCE	STRUCTURE	TREATMENT	SURFACE CHARACTERISATION
LEE & FARNSWORTH [15] (1965)	A. "OBLIQUE"	1×10^{-5} τ min O_2 at 25°C	Retarding Potential Measurements
	B. $(2\sqrt{2} \times \sqrt{2})$-45°	1×10^{-4} τ min O_2 at 25°C	
SIMMONS, MITCHELL & LAWLESS (1967)[1]	A. $(\sqrt{2} \times \sqrt{2})$-45°	5×10^{-5} τ min O_2 at 25°C	Retarding Potential Measurements
	B. $(2\sqrt{2} \times \sqrt{2})$-45°	1×10^{-4} τ min O_2 at 25°C or heating A. below 250°C	
ERTL (1967) [2]	A. "OBLIQUE"	1×10^{-6} τ min O_2 at 25°C	?
	B. $(2\sqrt{2} \times \sqrt{2})$-45°	1×10^{-5} τ min O_2 at 25°C	
OUSTRY, LAFOURCADE & ESCAUT (1972) [4]	A. $(\sqrt{2} \times \sqrt{2})$-45°	1×10^{-5} τ min O_2 at 25°C	?
	B. $(2\sqrt{2} \times \sqrt{2})$-45	$>>1\times10^{-5}$ τ min O_2 or heating A. at 700°C	
PRESENT WORK	A. $(\sqrt{2} \times \sqrt{2})$-45	1×10^{-5} τ min O_2 at 25°C	Auger Electron Spectroscopy
	B. (2x2)	1×10^{-4} τ min O_2 at 25°C	

lack of observation of this particular surface structure in this study.

LEED pattern contrast for the $(\sqrt{2}x\sqrt{2})R45^{o}$ structure could be improved following room temperature adsorption by annealing at temperatures up to $250^{o}C$. Initial annealing produced a decrease in background LEED intensity with a corresponding increase in LEED beam intensities, presumably due to thermal ordering of disordered (adsorbed) oxygen. Excessive annealing times produced a decrease in the LEED beam intensities, without any increase in background intensity, and this was assumed to be associated with oxygen diffusion into the bulk. As with the (111) surface there was no evidence of any oxygen desorption. Annealing at temperatures greater than $250^{o}C$ was avoided due to the problem of sulphur segregation, which was found to occur at much lower temperatures in the presence of adsorbed oxygen than when clean.

While the formation conditions for the $(\sqrt{2}x\sqrt{2})R45^{o}$ structure were extremely reproducible, those for the (2x2) structure were found to be sensitive not only to the immediate post-adsorption anneal but to the entire thermal history of the specimen; this observation has been emphasised by Somorjai[16] as applying to chemisorption systems in general. The (2x2) structure formation conditions depended on the extent of the saturation of the $(\sqrt{2}x\sqrt{2})R45^{o}$ structure which depended in turn on the degree of annealing that the specimen had been subjected to during its entire adsorption history. However, despite these uncertainties,providing that the $(\sqrt{2}x\sqrt{2})R45^{o}$ structure saturated at some stage during its post-adsorption treatment the (2x2) structure could be produced either by annealing or by further exposure as described above.

Further oxygen exposure following the formation of the (2x2) structure was accompanied by a large increase in background intensity. With the (1/2,0) beam positions obscured by the disordered oxygen it was not possible to determine, on the basis of the LEED pattern alone,whether the structure consisted of a $(\sqrt{2}x\sqrt{2})R45^{o}$ structure plus disordered oxygen or a (2x2) structure plus disordered oxygen.

5.3.2 Thermal Faceting

A difficulty encountered with annealing was the tendency of the (100) surface to facet in the presence of oxygen. On two occasions, following the annealing at about 200°C (for several minutes) of a surface that had been exposed to 5×10^{-5} torr-minutes of oxygen, LEED patterns were observed that corresponded to the $(\sqrt{2}\times\sqrt{2})R45^{\circ}$ structure. In addition to those beams normally associated with the latter structure, a number of extra weak beams were observed which did not converge with increasing energy towards the normal (00) beam but towards another (00) beam corresponding to a plane inclined at an angle of about 18° to the normal (100) surface in a <100> direction (i.e. at $\phi = 45^{\circ}$). The restriction of faceting to only one <100> direction was presumed to indicate that the basic (100) surface was slightly misoriented.

Similar faceting behaviour, although ocurring for higher exposures and annealing temperatures, was observed by Simmons et al during oxygen adsorption on copper (100). Perdereau and Rhead[17] have shown that at room temperature vicinal surfaces decompose to (410) facets for oxygen exposures as low as 1×10^{-6} torr-minutes and that the facets are particularly well developed if the surfaces are annealed at 200°C for five minutes.

The position of the extra specular beam was measured by rotation of the LEED pattern and checked by calibrating the LEED pattern photographs. The angle of 18° observed here would indicate faceting to the (310) surface rather than the (410) surface which is inclined to the (100) surface by an angle close to 14°. Unfortunately there were not sufficient extra LEED beams discernible to determine the unit mesh of the faceted surface. The (410) surface has an oblique net whereas the (310) surface has a rectangular net.

5.3.3 The Effect of Oxygen Exposure on (00) Beam Intensity-Energy Spectra

A sequence of (00) beam spectra for $\theta = 8^{o}$ and $\phi = 45^{o}$ obtained during the progressive exposure of the copper (100) surface to oxygen is shown in figure 5.7. Examination of these spectra enables the ambiguity associated with the continued adsorption of oxygen following the formation of the (2x2) structure (section 5.3.1) to be removed. The results in figure 5.7 show that the (00) beam spectrum obtained when the exposure associated with the (2x2) structure is exceeded is extremely similar to the spectrum obtained for the $(\sqrt{2}x\sqrt{2})R45^{o}$ structure but not to that for the (2x2) structure. This is clearly indicated by the shifts in energy of the peaks near to the kinematic conditions which are shown in figure 5.7 as arrows. The apparent conclusion then is that the ordered component of this ambiguous surface structure is the $(\sqrt{2}x\sqrt{2})R45^{o}$ structure rather than the (2x2) structure and that the lack of observation of any (1/2,0) beams was due to their absence rather than due to the large background produced by the disordered oxygen.

This observation supports the general conclusion that the $(\sqrt{2}x\sqrt{2})R45^{o}$ oxygen structure is very stable and that when the latter structure is saturated further oxygen adsorption tends to be disordered with a weak tendency, at suitable coverages, to form a (2x2) oxygen structure.

5.3.4 Detailed Intensity-Energy Spectra

(a) Cu(100)-$(\sqrt{2}x\sqrt{2})R45^{o}$-O Structure

Detailed intensity-energy spectra from this structure are shown for the (00), (1/2,1/2), (10) and (11) beams in figures 5.8, 5.9, 5.10 and 5.11 respectively. As might be anticipated, the differences from the clean surface data (section 4.4.1) occur mainly at low energies (below about 50 eV at low angles of incidence). As already remarked in the previous section, the formation of the oxygen structures can be readily detected by the systematic shift in energy of peaks near to the Bragg positions in the (00)

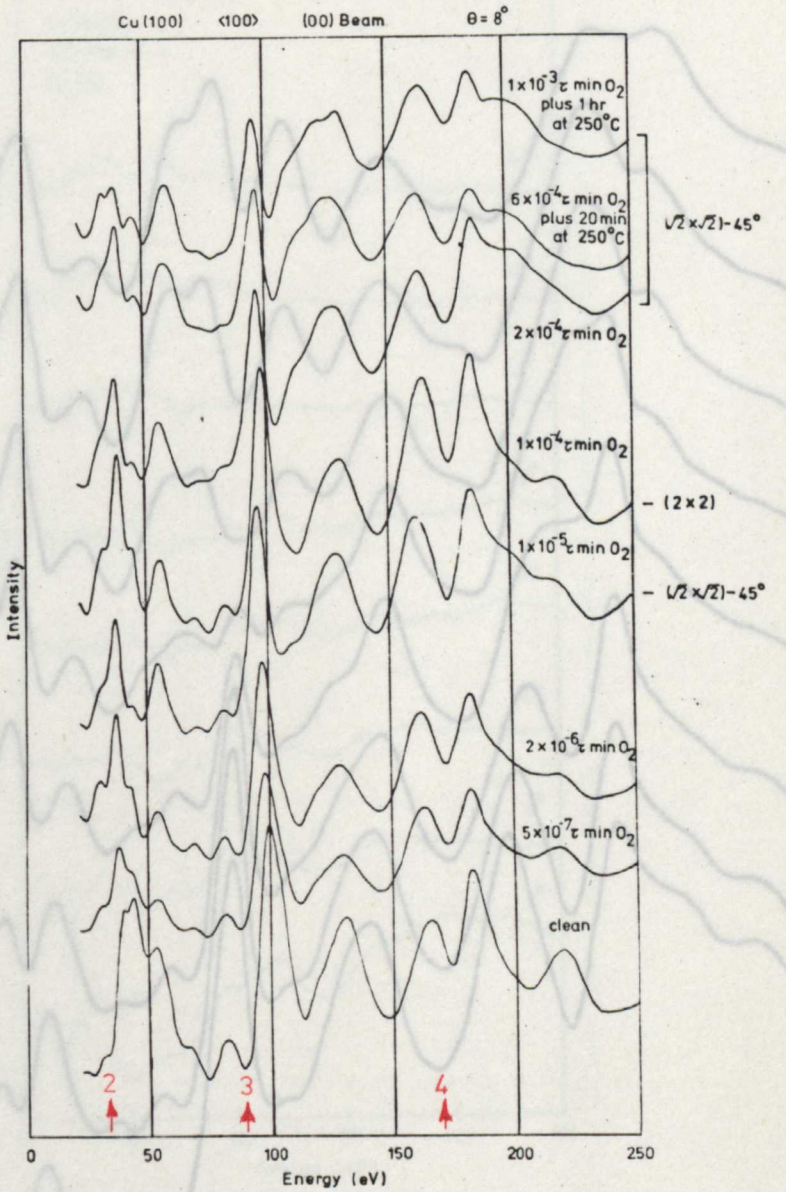

Figure 5.7 (00) beam intensity-energy spectra from copper (100) at an angle of incidence of $\theta = 8^{o}$ and an azimuth of $\phi = 45^{o}$ as a function of oxygen exposure.

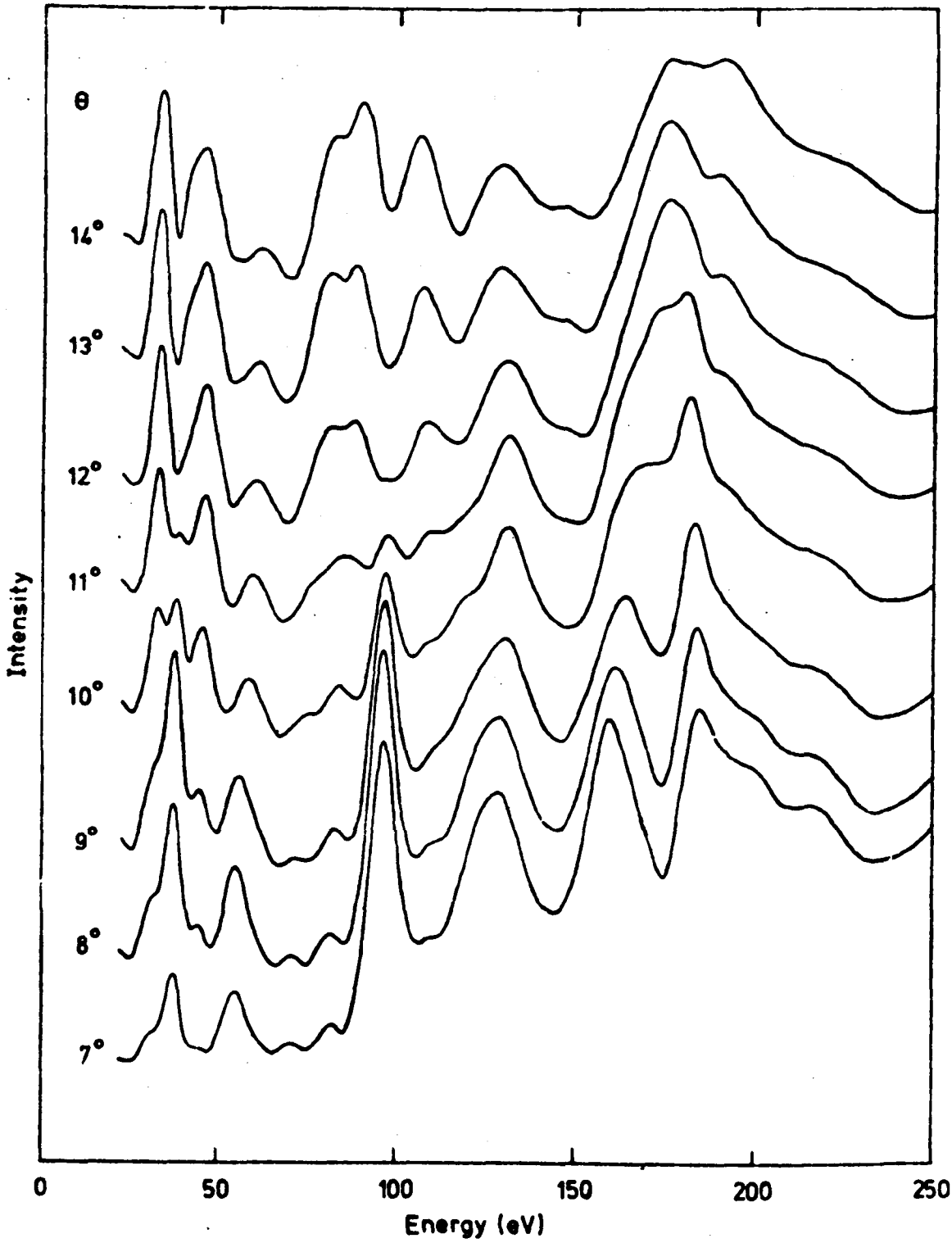

Figure 5.8 Intensity-energy spectra for the (00) beam from the Cu(100)-($\sqrt{2}$x$\sqrt{2}$)R45^{o}-O surface for a range in angle of incidence in the ϕ = 45^{o} azimuth.

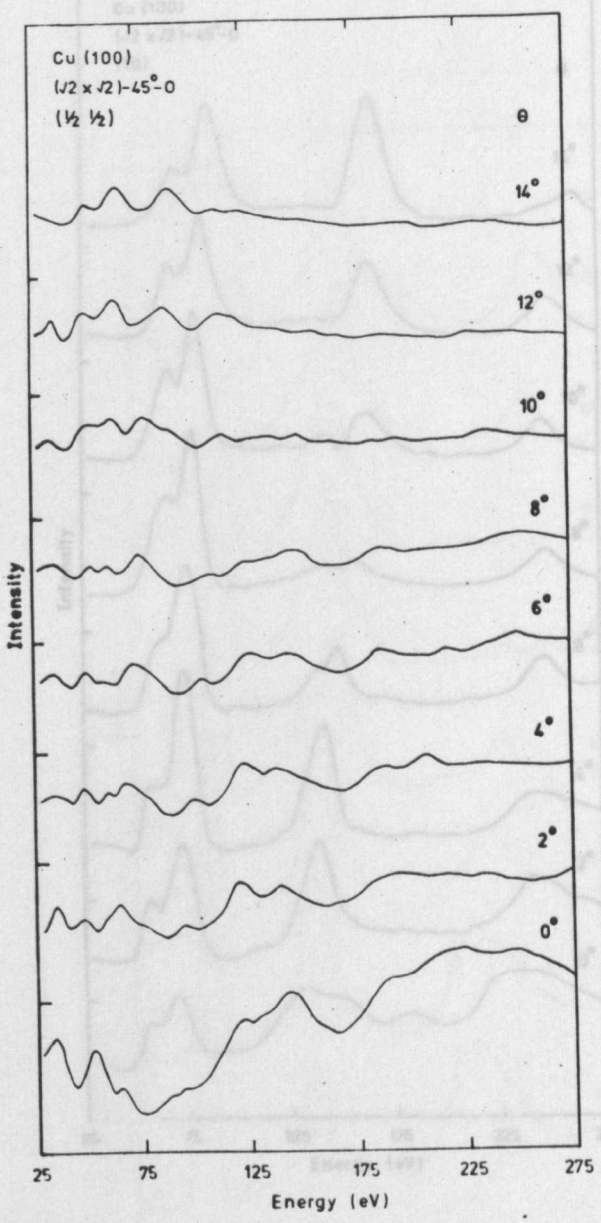

Figure 5.9 Intensity-energy spectra for the (1/2,1/2) beam from the Cu(100)-($\sqrt{2}$x $\sqrt{2}$)R45^{O}-O surface for a range in angle of incidence θ in the ϕ = 45^{O} azimuth.

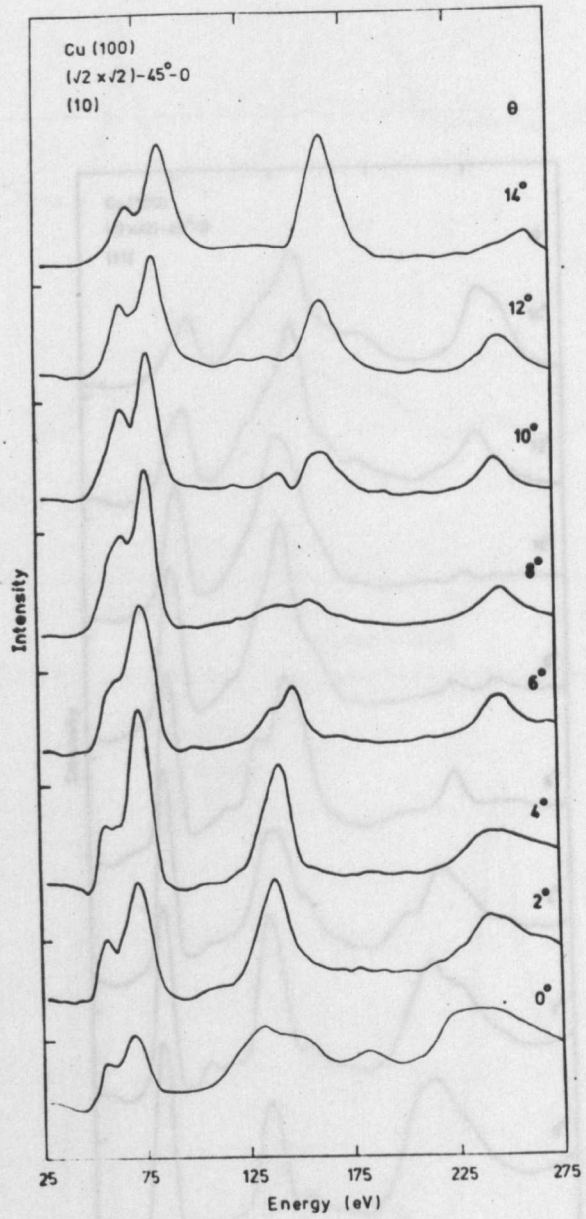

Figure 5.10 Intensity-energy spectra for the (10) beam from the Cu(100)-($\sqrt{2}$x$\sqrt{2}$)R45^{0}-O surface for a range in angle of incidence θ in the ϕ = 0^{0} azimuth.

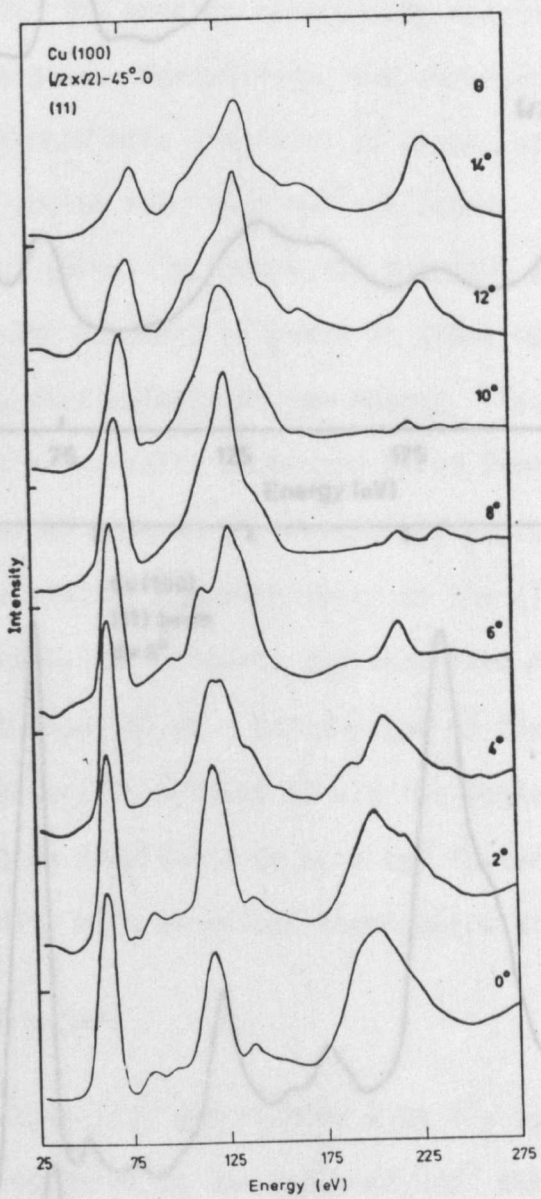

Figure 5.11 Intensity-energy spectra for the (11) beam from the Cu(100)-$(\sqrt{2}x\sqrt{2})R45^{o}$-O surface for a range in angle of incidence θ in the $\phi = 45^{o}$ azimuth.

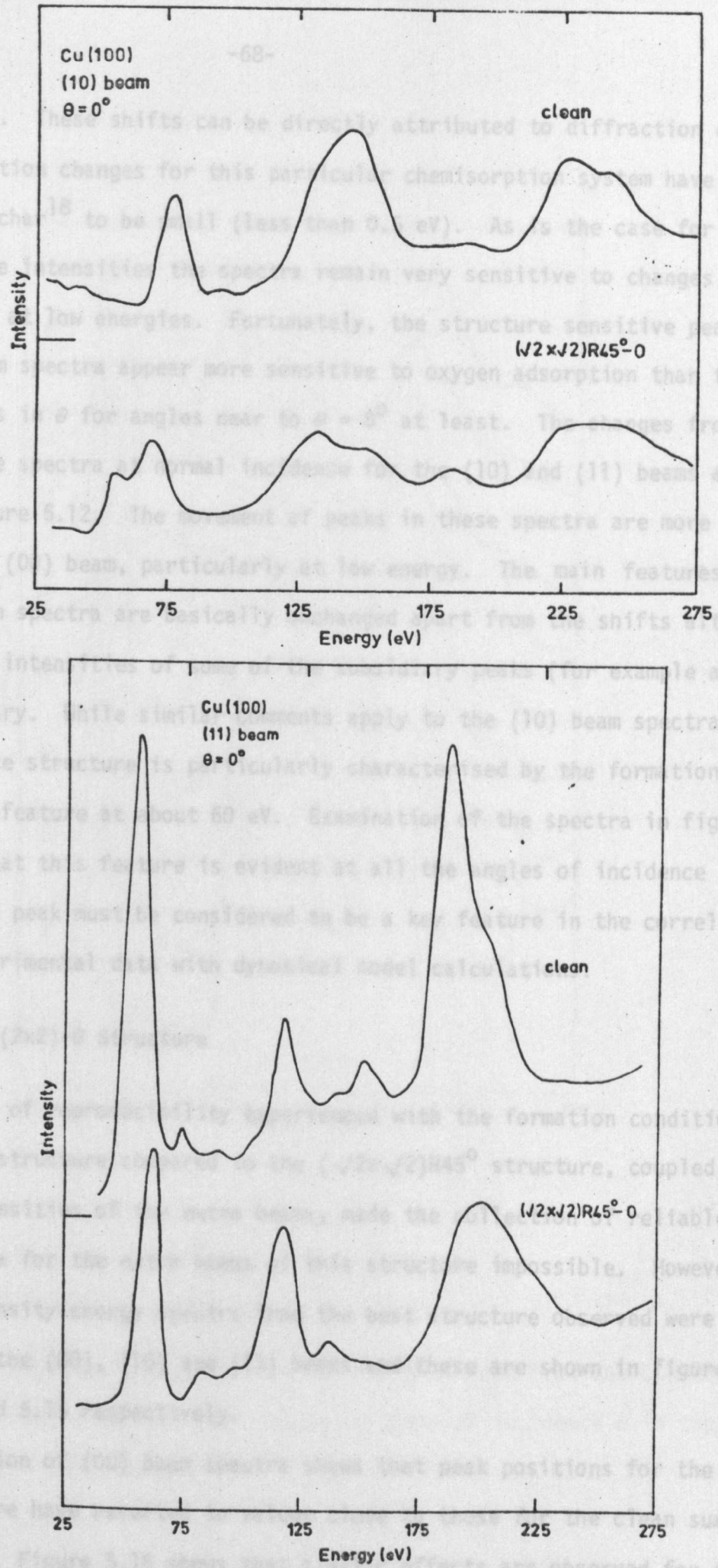

Figure 5.12 Normal incidence intensity-energy spectra are compared in (a) and (b) for the clean and Cu(100)-($\sqrt{2}$x$\sqrt{2}$)R45^{o} surfaces.

beam spectra. These shifts can be directly attributed to diffraction effects as work-function changes for this particular chemisorption system have been shown by Delchar[18] to be small (less than 0.5 eV). As is the case for the clean surface intensities the spectra remain very sensitive to changes in θ, particularly at low energies. Fortunately, the structure sensitive peaks in the (00) beam spectra appear more sensitive to oxygen adsorption than to small changes in θ for angles near to $\theta = 8^0$ at least. The changes from clean surface spectra at normal incidence for the (10) and (11) beams are shown in figure 5.12. The movement of peaks in these spectra are more marked than for the (00) beam, particularly at low energy. The main features of the (11) beam spectra are basically unchanged apart from the shifts although the relative intensities of some of the subsidiary peaks (for example around 150 eV) do vary. While similar comments apply to the (10) beam spectra this oxygen surface structure is particularly characterised by the formation of a strong extra feature at about 60 eV. Examination of the spectra in figure 5.10 shows that this feature is evident at all the angles of incidence shown. Clearly, this peak must be considered to be a key feature in the correlation of these experimental data with dynamical model calculations.

(b) Cu(100)-(2x2)-O Structure

The lack of reproducibility experienced with the formation conditions of the (2x2) structure compared to the $(\sqrt{2}x\sqrt{2})R45^0$ structure, coupled with the weak intensities of the extra beams, made the collection of reliable intensity data for the extra beams of this structure impossible. However, detailed intensity-energy spectra from the best structure observed were acquired for the (00), (10) and (11) beams and these are shown in figures 5.13, 5.14 and 5.15 respectively.

Examination of (00) beam spectra shows that peak positions for the (2x2) structure have reverted to values close to those for the clean surface (figure 5.7). Figure 5.16 shows that similar effects are observed for the non-specular beam spectra; the key feature that developed at about 60 eV in

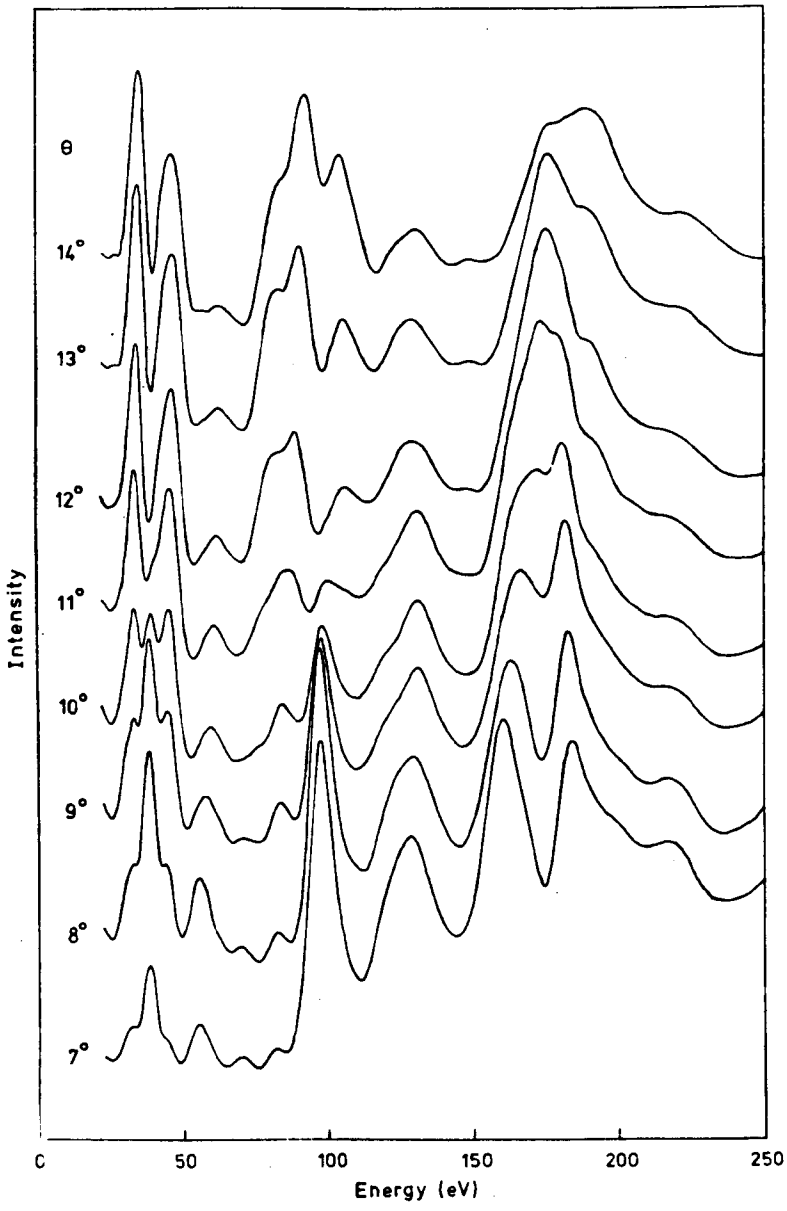

Figure 5.13 Intensity-energy spectra for the (00) beam from the Cu(100)-(2x2)-O surface for a range in angle of incidence θ in the $\phi = 45^{o}$ azimuth.

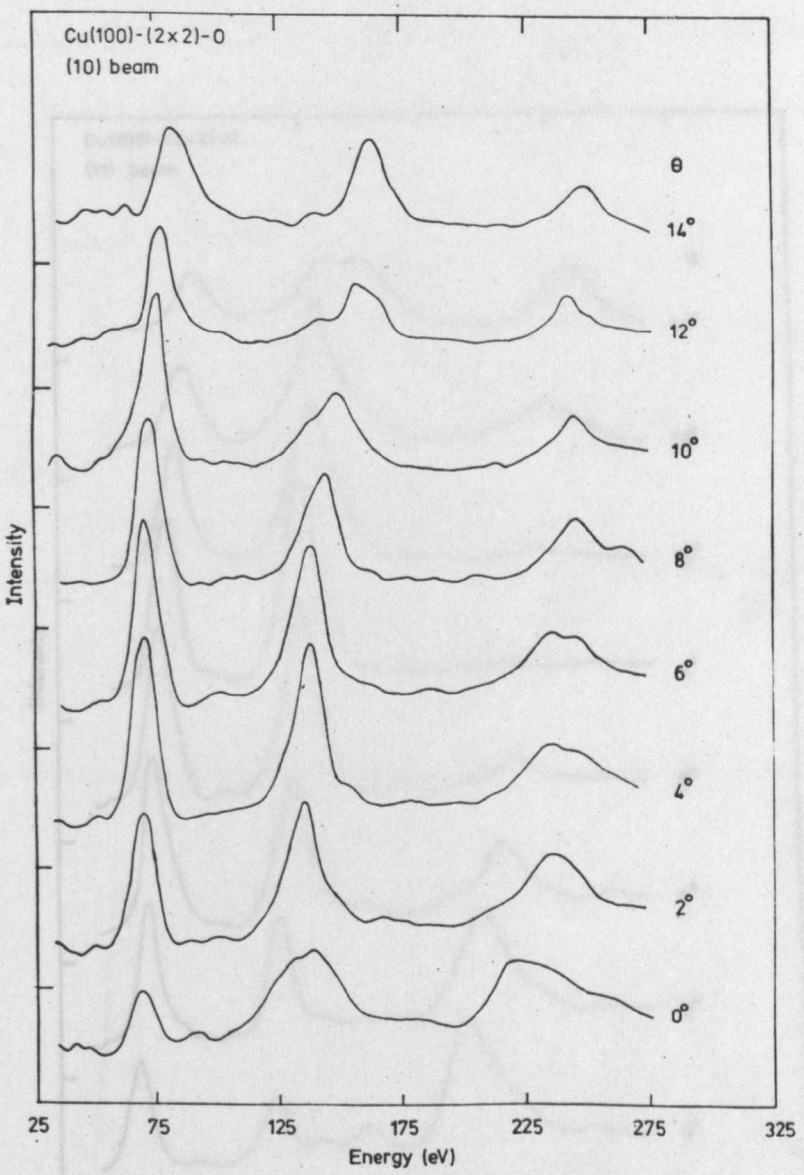

Figure 5.14 Intensity-energy spectra for the (10) beam from the Cu(100)-(2x2)-O surface for a range in angle of incidence θ in the $\phi = 0^{o}$ azimuth.

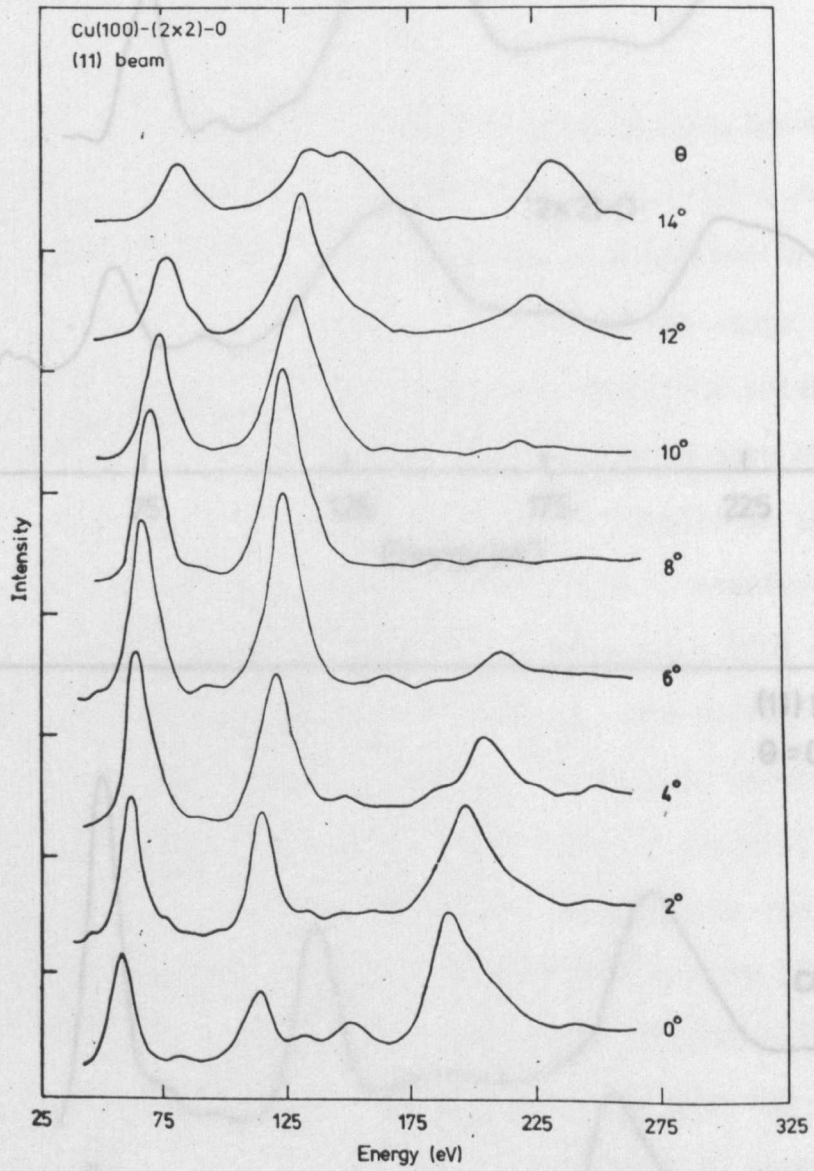

Figure 5.15 Intensity-energy spectra for the (11) beam from the Cu(100)-(2x2)-O surface for a range in angle of incidence θ in the $\phi = 45^{o}$ azimuth.

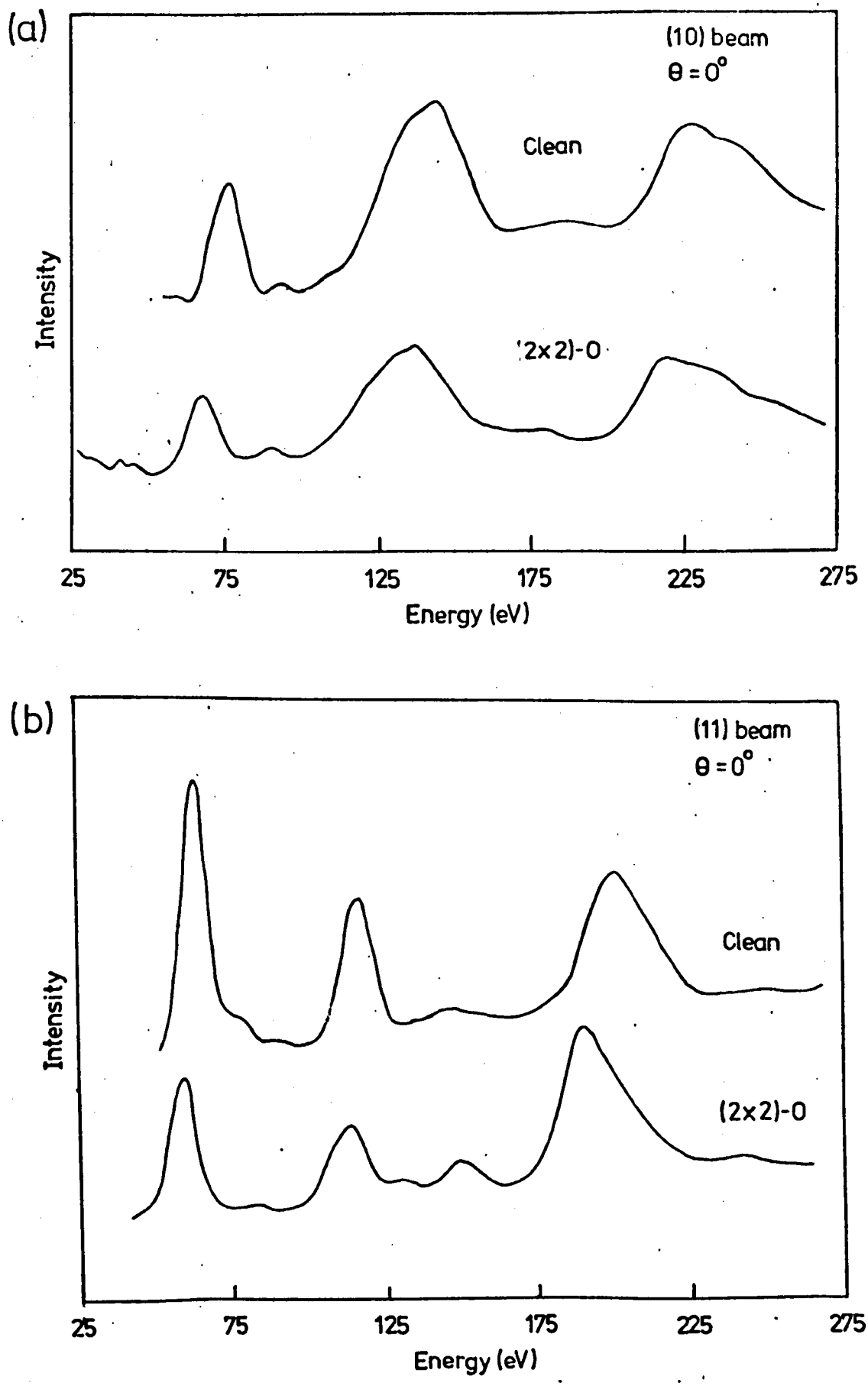

Figure 5.16 Normal incidence intensity-energy spectra are compared in (a) and (b) for the clean and Cu(100)-(2x2)-O surfaces.

the (10) beam spectra for the $(\sqrt{2}x\sqrt{2})R45^{o}$ structure is clearly missing in the normal incidence (10) beam spectrum for the (2x2) structure.

5.3.5 Correlation with Dynamical Theory

As discussed above reliable intensity-energy spectra for both substrate and adsorbate beams could only be acquired for the Cu(100)-$(\sqrt{2}x\sqrt{2})R45^{o}$-O structure and consequently only these data can be subjected to a meaningful correlation with dynamical calulations. The precursive stage to comparing experimental and theoretical intensities for an adsorbate situation must be the correlation of clean surface data. Without this we have no measure of the degree of confidence that we can place in the results of the adsorbate correlation. We have already compared in section 4.4 experimental intensities for the (00), (10) and (11) beams from the clean copper (100) substrate with three independent sets of dynamical calculations. The correlation obtained with the most extensive set (due to Laramore[19]) is good, particularly with regard to the description of the angular evolution of spectral features. Unfortunately, Laramore has not performed any calculations for this particular adsorbate structure. Consequently, we are limited here to calculations by Duke and Lipari[20] and by Demuth[21] for which only a limited range of clean surface data was available,although it is emphasised that the computational scheme used by Demuth has been considerably successful in describing experimental intensities for clean nickel.[22]

Duke and Lipari have performed dynamical calculations for various trial structures (one-fold, two-fold and four-fold coordinated oxygen atoms and also the reconstructed surface). They found the best overall fit to the present experimental data to be the reconstructed surface with a top layer spacing of 1.8 to 1.9 Å. The calculations for this structure, together with the best fits for four-fold and one-fold coordination, are shown in figures 5.17(a),(b),(c) and (d) for the (00), (1/2,1/2),(10) and (11) beams respectively (the experimental curves have been included for direct comparison).

Figure 5.17 The best fit dynamical calculations of Duke and Lipari for four Cu(100)-($\sqrt{2}$x $\sqrt{2}$)R45^{o}-O structures (one-fold, two-fold and fourfold coordinated oxygen atoms and the reconstructed surface) are shown overleaf in (a), (b), (c) and (d) for the (00), (1/2,1/2), (10) and (11) beams respectively.

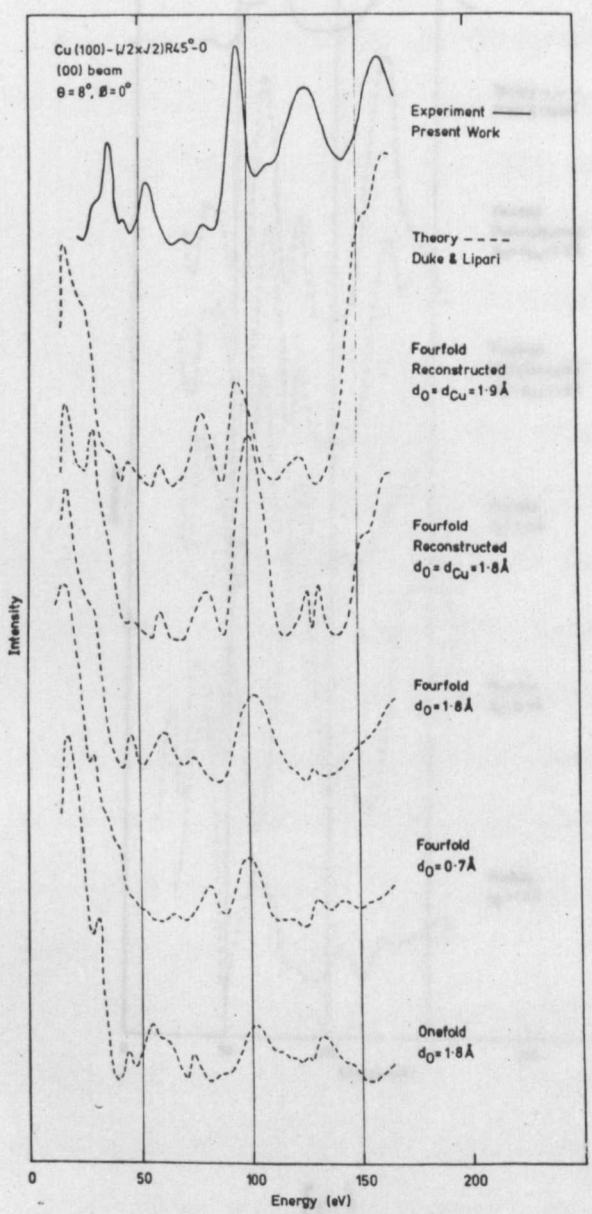
Cu (100) - (1/2 x √2) R45° - O
(00) beam
θ = 8°, Φ = 0°
Experiment
Present Work
Theory
Duke & Lipari
Fourfold
Reconstructed
$d_0 = d_{Cu} = 1{\cdot}9$ Å
Fourfold
Reconstructed
$d_0 = d_{Cu} = 1{\cdot}8$ Å
Fourfold
$d_0 = 1{\cdot}8$ Å
Fourfold
$d_0 = 0{\cdot}7$ Å
Onefold
$d_0 = 1{\cdot}8$ Å
Intensity
0
50
100
150
200
Energy (eV)

(a)

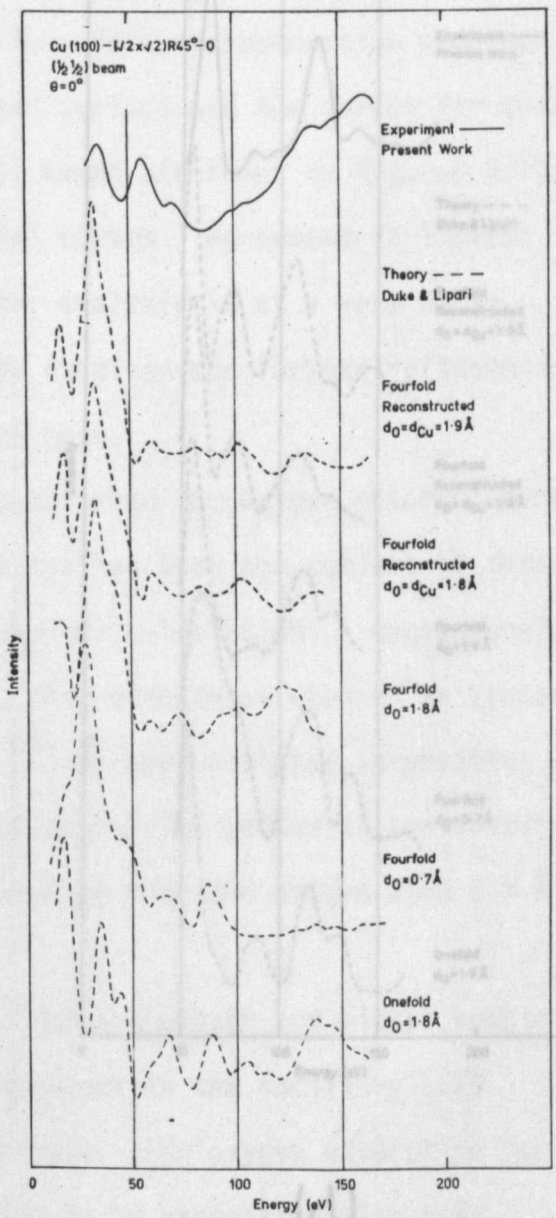
Cu (100) - (1/2 x √2) R45° - O
(½ ½) beam
θ = 0°
Experiment
Present Work
Theory
Duke & Lipari
Fourfold
Reconstructed
$d_0 = d_{Cu} = 1{\cdot}9$ Å
Fourfold
Reconstructed
$d_0 = d_{Cu} = 1{\cdot}8$ Å
Fourfold
$d_0 = 1{\cdot}8$ Å
Fourfold
$d_0 = 0{\cdot}7$ Å
Onefold
$d_0 = 1{\cdot}8$ Å
Intensity
0
50
100
150
200
Energy (eV)

(b)

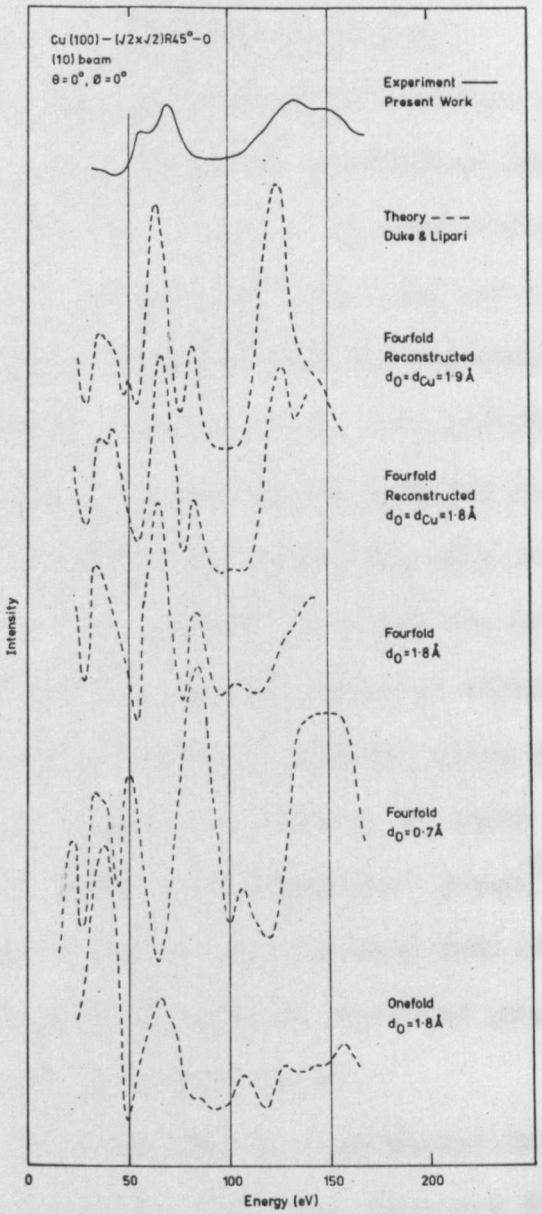
Cu (100) – (√2x√2)R45°–O
(10) beam
θ = 0°, Ø = 0°
Experiment
Present Work
Theory
Duke & Lipari
Fourfold
Reconstructed
$d_O = d_{Cu} = 1{\cdot}9$ Å
Fourfold
Reconstructed
$d_O = d_{Cu} = 1{\cdot}8$ Å
Fourfold
$d_O = 1{\cdot}8$ Å
Fourfold
$d_O = 0{\cdot}7$ Å
Onefold
$d_O = 1{\cdot}8$ Å
Intensity
0
50
100
150
200
Energy (eV)

(c)

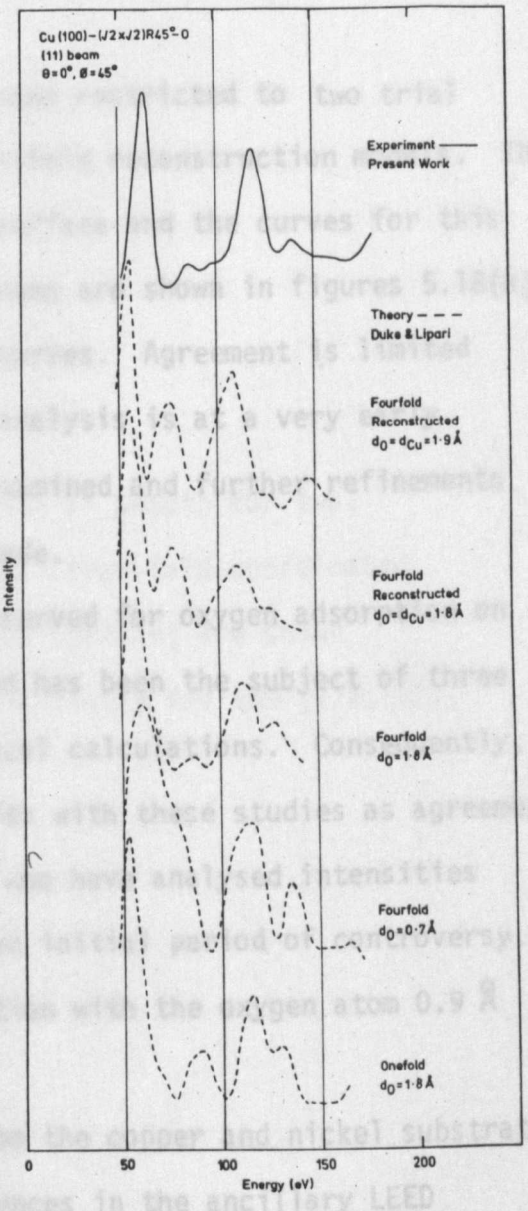
Cu (100) – (√2x√2)R45°–O
(11) beam
θ = 0°, Ø = 45°
Experiment
Present Work
Theory
Duke & Lipari
Fourfold
Reconstructed
$d_O = d_{Cu} = 1{\cdot}9$ Å
Fourfold
Reconstructed
$d_O = d_{Cu} = 1{\cdot}8$ Å
Fourfold
$d_O = 1{\cdot}8$ Å
Fourfold
$d_O = 0{\cdot}7$ Å
Onefold
$d_O = 1{\cdot}8$ Å
Intensity
0
50
100
150
200
Energy (eV)

(d)

Unfortunately, although the curves for the reconstructed surface do provide the best match of the experimental data they can not be considered to be a very good fit. This is almost certainly related to the absence of temperature from these calculations, together with the use of only four phase shifts to describe the atomic scattering.

Demuth's preliminary calculations have been restricted to two trial structures; four-fold coordination and four-fold reconstruction models. The best fit was obtained for the reconstructed surface and the curves for this structure for the (1/2,1/2), (10) and (11) beams are shown in figures 5.18(a), (b), and (c) together with the experimental curves. Agreement is limited but we would emphasise that this particular analysis is at a very early stage; several other models have yet to be examined and further refinements in the computational scheme may have to be made.

The $(\sqrt{2} \times \sqrt{2})R45^{0}$ structure has been observed for oxygen adsorption on nickel (100) by several groups of workers and has been the subject of three independent structural analyses using dynamical calculations. Consequently, it is of interest to compare the above results with these studies as agreement between independent theoretical groups[23-25] who have analysed intensities for this structure has now been made after an initial period of controversy. The accepted solution is four-fold coordination with the oxygen atom 0.9 Å above the top nickel layer.

Before comparing experimental data from the copper and nickel substrates it must be emphasised that there are differences in the ancillary LEED observations for the two adsorption situations. For oxygen adsorption on nickel (100) the $(\sqrt{2}\times\sqrt{2})R45^{0}$ net, assumed to be associated with half monolayer coverage, is preceded by a (2x2) net, thought to be associated with quarter monolayer coverage. Also, in the early stages at least the sticking factor for oxygen on nickel is quite high (about 1) which contrasts markedly with the low average sticking factor (about 10^{-3}) observed here for copper and the observation of the $(\sqrt{2}\times\sqrt{2})R45^{0}$ net before the (2x2) net. More

Figure 5.18 The best fit dynamical calculations of Demuth for two Cu(100)-($\sqrt{2}$x $\sqrt{2}$)R45^{0}-O structures (four-fold coordinated oxygen atoms and the reconstructed surface) are shown overleaf in (a), (b) and (c) respectively for the (1/2,1/2), (10) and (11) beams respectively.

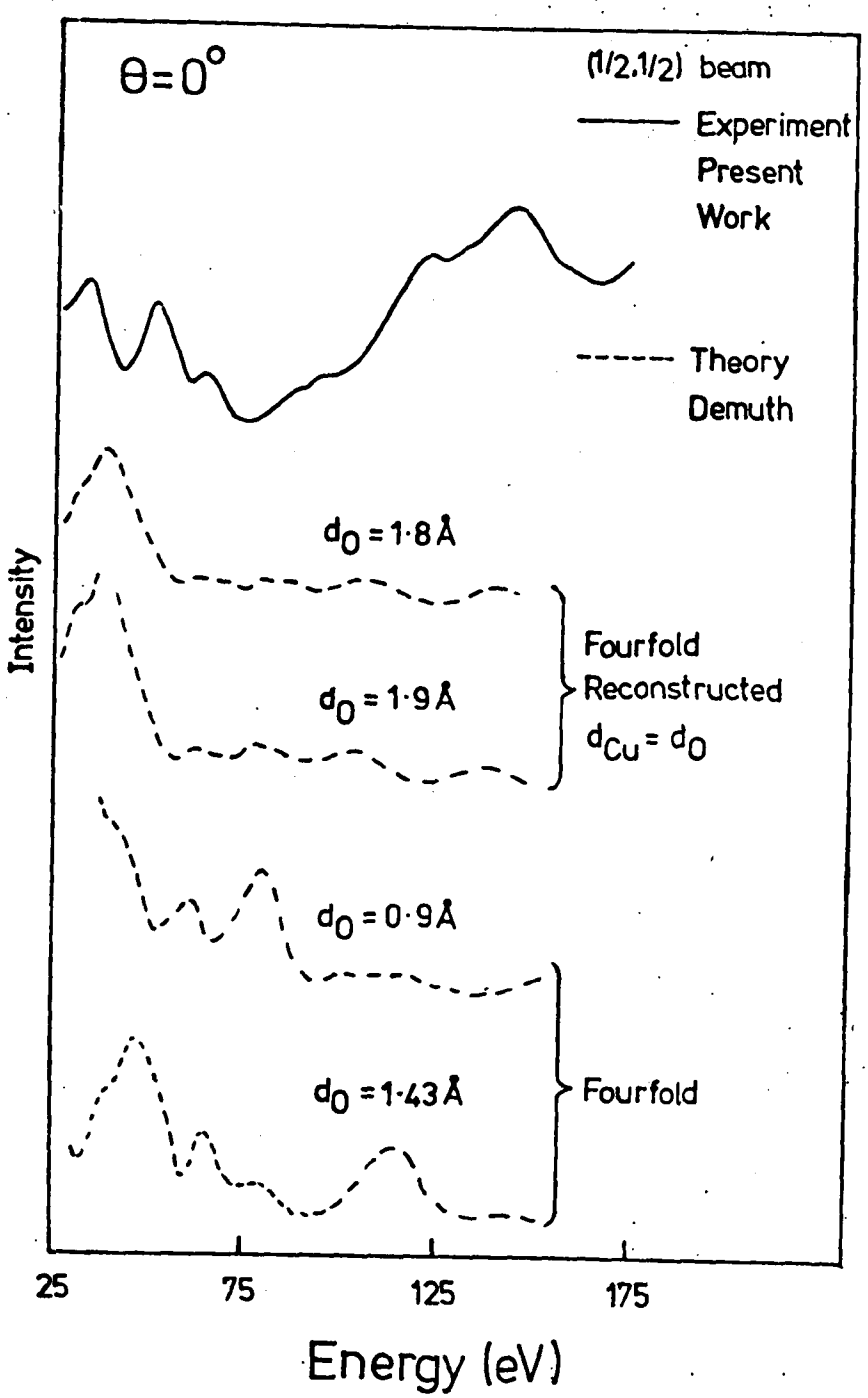
θ=0°
(1/2,1/2) beam
Experiment
Present
Work
Theory
Demuth
d_O = 1·8 Å
d_O = 1·9 Å
Fourfold
Reconstructed
$d_{Cu} = d_O$
d_O = 0·9 Å
d_O = 1·43 Å
Fourfold
Intensity
25
75
125
175
Energy (eV)

(a)

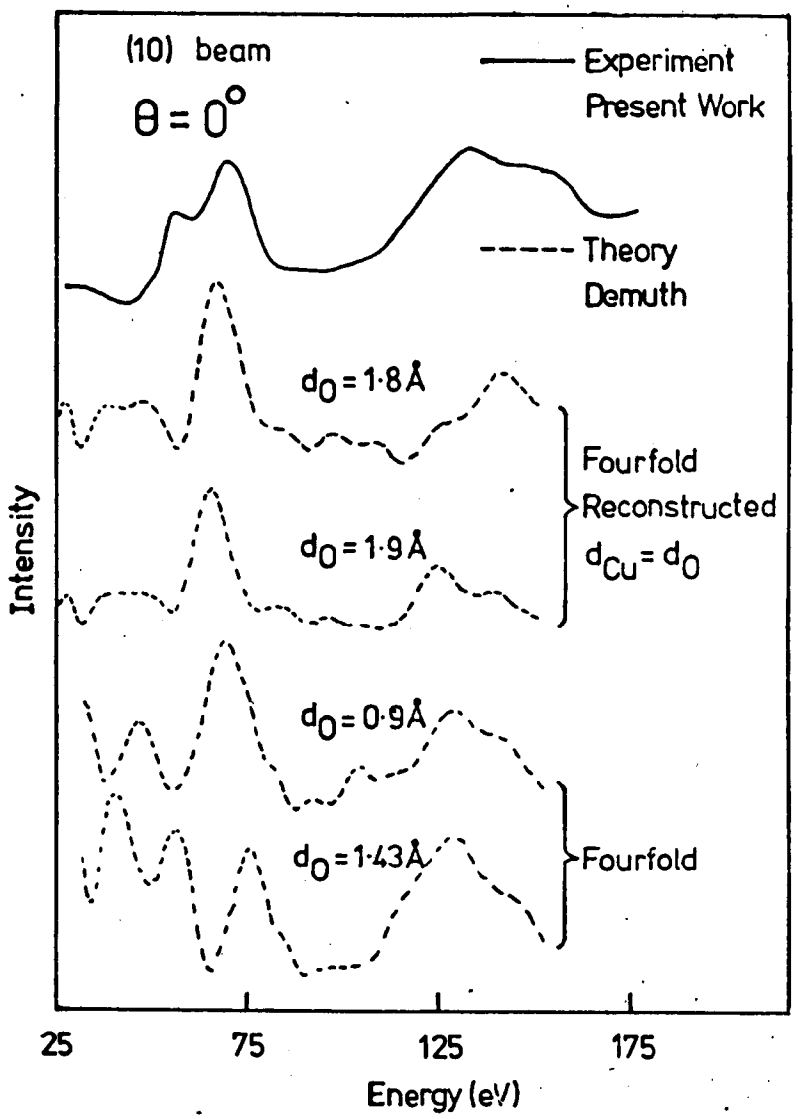
(10) beam
θ = 0°
Experiment
Present Work
Theory
Demuth
d_O = 1·8Å
d_O = 1·9Å
Fourfold
Reconstructed
$d_{Cu} = d_O$
d_O = 0·9Å
d_O = 1·43Å
Fourfold
Intensity
25
75
125
175
Energy (eV)

(b)

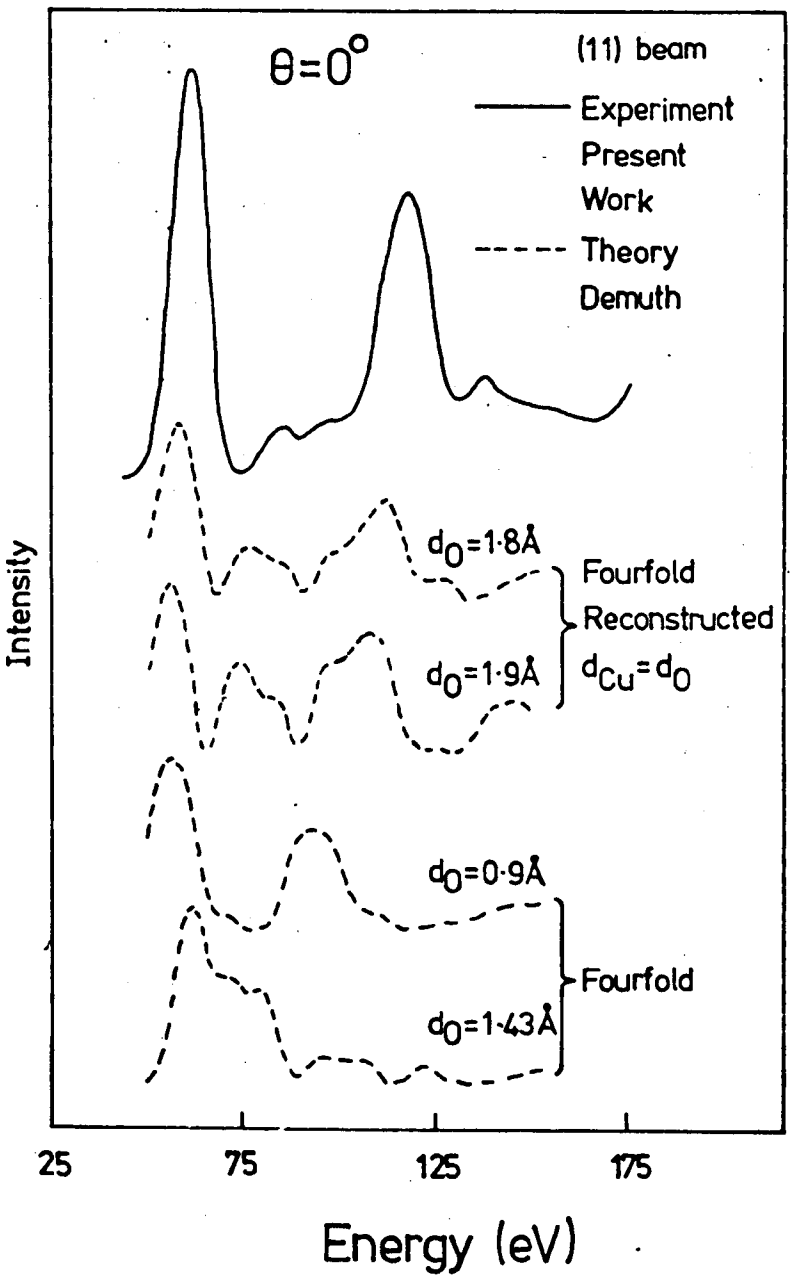
θ=0°
(11) beam
Experiment
Present
Work
Theory
Demuth
Intensity
d_O=1·8Å
d_O=1·9Å
Fourfold
Reconstructed
$d_{Cu}=d_O$
d_O=0·9Å
d_O=1·43Å
Fourfold
25
75
125
175
Energy (eV)

(c)

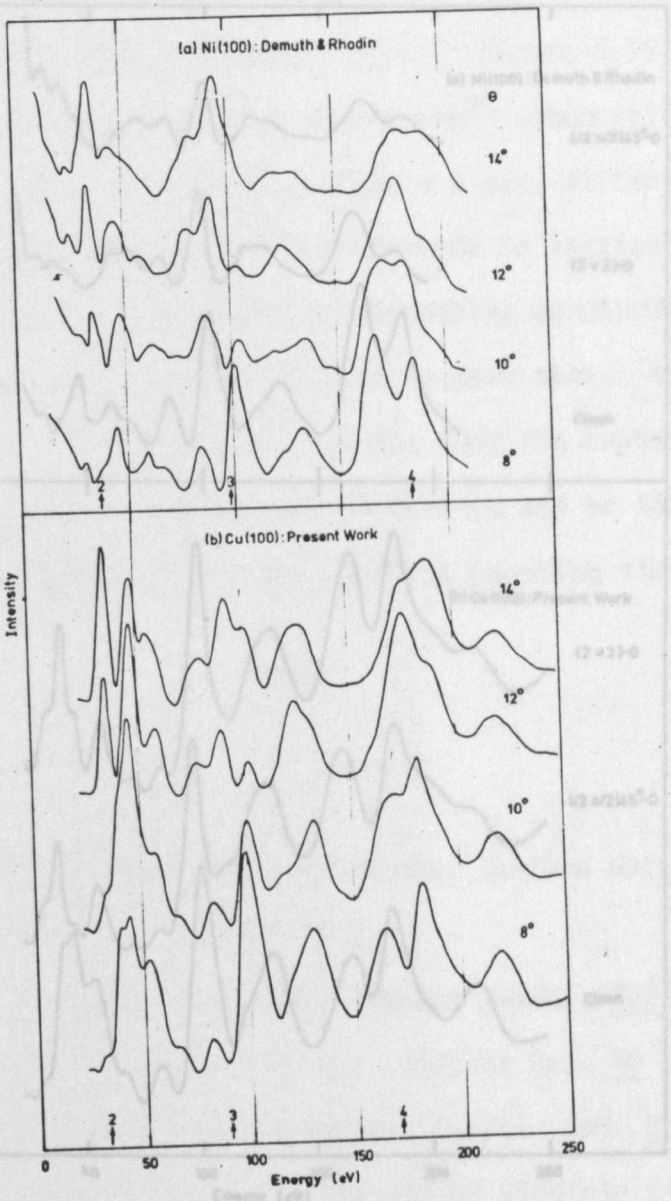

Figure 5.19 (00) beam intensity-energy spectra for the clean (100) surface of nickel and copper are shown in (a) and (b) respectively for an identical range of scattering geometry.

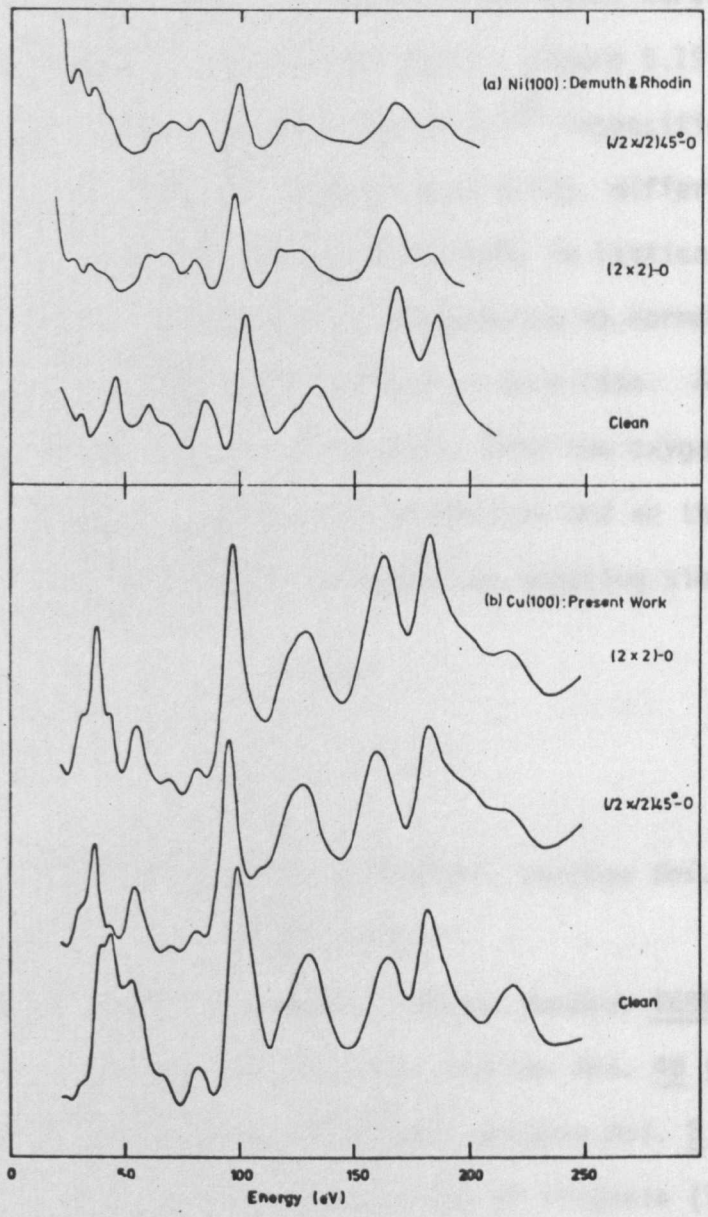

Figure 5.20 (00) beam intensity-spectra for $\theta = 8^{0}$ from the clean, $(\sqrt{2}x\sqrt{2})R45^{0}$-O and (2x2)-O surfaces are compared for nickel and copper substrates in (a) and (b) respectively.

importantly other workers have not reported the (2x2) structure at any stage of oxygen adsorption onto copper (100). Figure 5.19 and 5.20 show some relevant comparisons of copper and nickel[26] intensities. The extreme similiarity of the clean surface data (figure 5.19), differing by essentially a scaling factor associated with the difference in lattice parameter, is well known; the nominal Bragg peaks corresponding to normal incidence but including an inner potential are included in each case. Although there are still marked similarities in the spectra from the oxygen adsorbed surfaces there are also regions of significant difference and so this comparison can not provide any evidence for the two surfaces adopting similar structures.

*****

REFERENCES

(1) G.W.Simmons,D.F.Mitchell & K.R.Lawless, *Surface Sci.* 8 (1967) 130.

(2) G.Ertl, *Surface Sci.* 6 (1967) 208.

(3) N.Takahashi,H.Tomita & S.Motoo, *Comptes Rendus.* 269B (1969) 618.

(4) A.Oustry, L.Lafourcade & A.Escaut, *Surface Sci.* 40 (1973) 545.

(5) L.Trepte,Chr.Menzel-Kopp & E.Menzel, *Surface Sci.* 8 (1967) 223.

(6) D.F.Mitchell, Ph.D.Thesis, University of Virginia (1966).

(7) R.M.Dell,F.S.Stone & P.F.Tiley, *Trans.Faraday Soc.* 49 (1953) 195.

(8) L.H.Jenkins & M.F.Chung, *Surface Sci.* 24 (1971) 125.

(9) J.L.Domange & J.Oudar, *Surface Sci.* 11 (1968) 124.

(10) C.Argile & G.E.Rhead, *J.Phys.C.* 7 (1974) L261.

(11) A.P.Janssen,R.Schoonmaker,J.A.D.Matthew & A.Chambers,to be published.

(12) C.R.Helms & W.E.Spicer, *Phys.Rev.Lett.* 32 (1974) 228.

(13) J.L.Desplat, *Solid State Comm.* 13 (1973) 689.

(14) M.G.Lagally, T.C.Ngoc & M.B.Webb, *Phys.Rev. Lett.* 26 (1971) 1557.

(15) R.N.Lee & H.E.Farnsworth, *Surface Sci.* 3 (1965) 461.

(16) G.A.Somorjai, "Principles of Surface Chemistry",Prentice-Hall (1972).

(17) J.Perdereau & G.E.Rhead, *Surface Sci.* 24 (1971) 555.

(18) T.A.Delchar, *Surface Sci.* 27 (1971) 11.

(19) G.E.Laramore,to be published in *Phys.Rev.B.*

(20) C.B.Duke,N.O.Lipari and G.E.Laramore,Proceedings of CECAM colloquim on "Perspectives in the calculation of many-electron interactions in solids.", September 17-21,Taromina (1973).

(21) J.E.Demuth,IBM Thomas J.Watson Research Centre,New York,unpublished data.

(22) J.E.Demuth,D.W.Jepsen & P.M.Marcus, to be published.

(23) S.Andersson,B.Kasemo,J.B.Pendry & M.A.Van Hove, *Phys.Rev.Lett.* 31 (1973) 595.

(24) C.B.Duke,N.O.Lipari,G.E.Laramore & J.B.Theeten, *Solid State Comm.*13 (1973) 579.

(25) J.E.Demuth,D.W.Jepsen & P.M.Marcus, *Phys.Rev.Lett.* 31 (1973) 540.

(26) J.E.Demuth, Ph.D.Thesis,Cornell (1973).
J.E.Demuth & T.N.Rhodin, *Surface Sci.*42 (1974) 261; 45 (1974) 249.

CHAPTER SIX. THE CONSTANT MOMENTUM TRANSFER AVERAGING SCHEME FOR SURFACE STRUCTURE DETERMINATION BY LEED

Recent proposals to simplify surface structure determination by avoiding the use of complex and costly dynamical calculations were outlined in section 2.3.4. Of these, the method that is most applicable to the particular adsorbate surface structures described in the previous chapter is the constant momentum transfer averaging scheme of Lagally *et al*.[1,2] Tucker and Duke's energy averaging scheme[3] is best suited to those particular situations where the unit mesh of the surface is large and where there are many extra beams present. In the situations of interest here the unit mesh is small and known and the further structural information sought is the registry of the adsorbate unit mesh and the adsorbate spacing normal to the surface.

Lagally *et al*'s approach is based on the observation that whereas single scattering depends explicitly on the propagation vector $\underline{S}$, where $\underline{S}$ is defined by equation 2.22, multiple scattering events do not depend on $\underline{S}$ alone. Consequently, multiple scattering contributions might average out to a constant background leaving only the single scattering contributions for correlation with model kinematical calculations.

Lagally *et al* have shown that averaged intensities from the clean (111) surfaces of silver[1] and nickel[2] are very similar to kinematical calculations using the ideal surface structures anticipated from the bulk geometry. The resultant averages were very kinematical in appearance although very small peaks were observed at approximately two-thirds order Bragg positions. More recently, Quinto and Robertson[4] have shown that similarly extensive averages from the clean (100) surface of aluminium are not so kinematical; although well defined peaks were observed close to the integral Bragg positions, large extra peaks were observed at approximately half-order Bragg positions. Less extensive averages from the clean (111) aluminium surface were shown by Quinto and Robertson to be considerably more kinematical in appearance.

Although this averaging scheme had been considerably successful when

applied to the clean (111) surface of f.c.c. metals it had only been applied to surfaces where the structure was already known. Consequently, this technique was applied to intensity data from surfaces where the structure was not known, namely those observed for the copper-oxygen chemisorption system described in the previous chapter. In order to provide a reference with which the averaged oxygen adsorbate data could be compared and, more importantly, in order to provide a stringent test of the averaging scheme, this data reduction method was initially applied to intensity data from the clean (100) and (111) surfaces of copper.

6.1 Experimental Technique

6.1.1 Averaging of Specular Beam Intensity-Energy Spectra

The averaging contours in $\underline{K}$-space are represented schematically in figure 6.1. The specular beam intensity-energy spectra were averaged directly by using a multi-channel analyser both to compile the average and to provide the sweep control for the electron beam energy. The complete data acquisition scheme that was employed is shown schematically in figure 6.1c. In order to present the intensities to the NS544 multi-channel analyser in the form required by the constraint of maintaining constant momentum transfer during compilation of the average, a calibrated potentiometer was used to scale the channel address voltage, and hence the electron energy, by the cosine^2 of the angle of incidence θ as dictated by the following equation:

$$S = \frac{4\pi}{\lambda}\cos\theta = 4\pi\left(\frac{E}{150.4}\right)^{\frac{1}{2}}\cos\theta \quad (\text{Å})^{-1} \quad \ldots 6.1$$

where E is the electron energy in eV inside the crystal (i.e. the external electron energy E_e plus the inner potential Vo_r). By defining

$$S_o = \frac{2\pi}{d_z} \quad \ldots 6.2,$$

where d_z is the interplanar spacing perpendicular to the particular surface under consideration, the reduced scattering vector is given as:

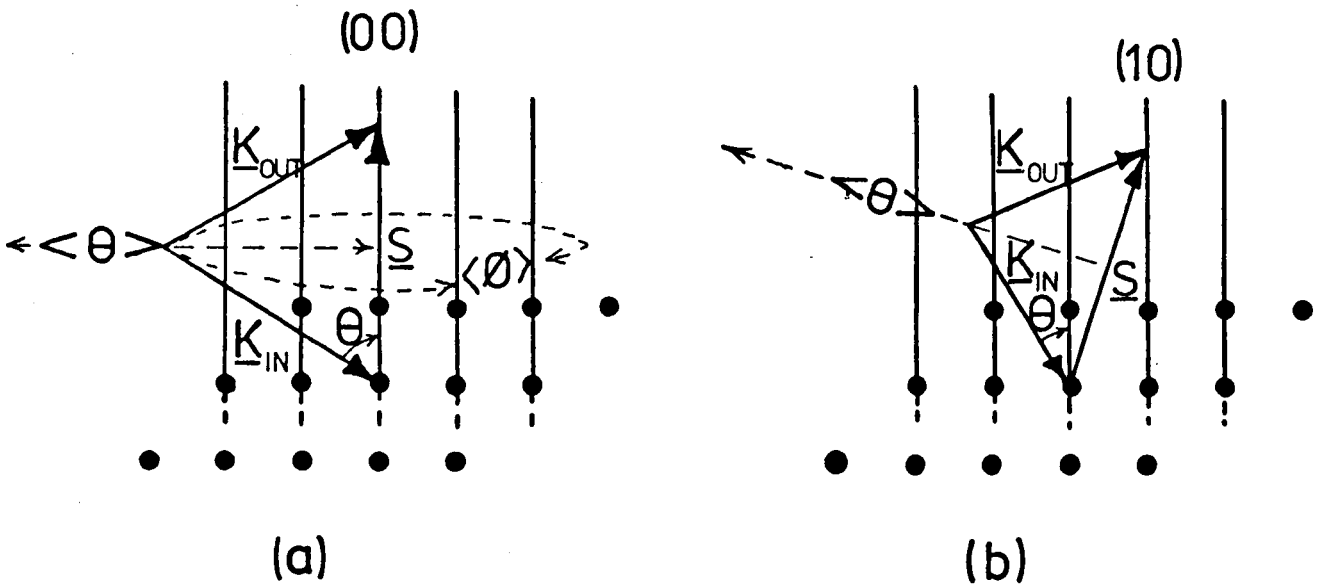

Figure 6.1(a),(b) Averaging contours in $\underline{K}$-space are represented schematically in (a) and (b) for the specular and non-specular beams respectively.

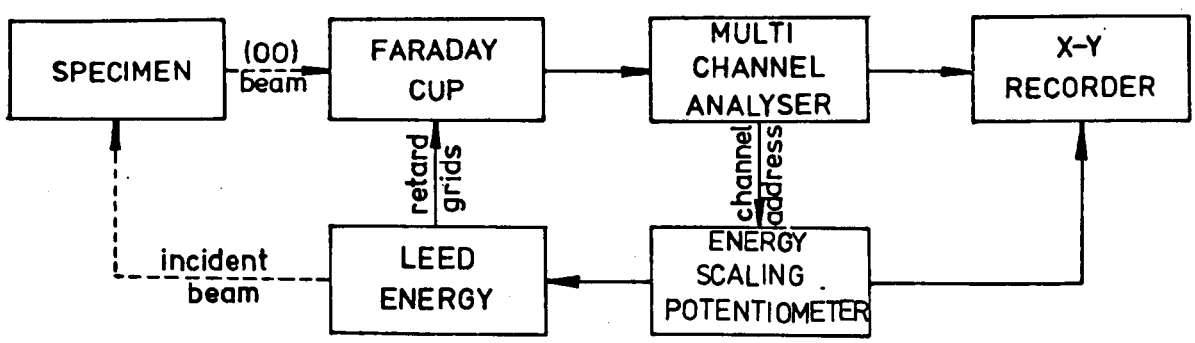

Figure 6.1(c) Schematic diagram of the data acquisition scheme used for the specular beam averaging.

$$S/S_o = 2d_z \left(\frac{E}{150.4}\right)^{\frac{1}{2}} \cos\theta \qquad \ldots 6.3$$

Thus $$(S/S_o)^2 = \frac{4d_z^2}{150.4} \cos^2\theta \; E \qquad \ldots 6.4$$

Spectra for all scattering geometries were thus generated as a function of $(S/S_o)^2$ and a simple conversion then provided a scale in terms of S/S_o. The immediate advantages of this data acquisition system were that the average could be inspected at any stage during the accumulation of the spectra and that extremely large ranges of data were relatively easy to average. As the scaling determined by equation 6.4 refers to electron energies inside the crystal the external energy E_e was swept from $-eVo_r$ which corresponds to zero energy within the crystal if a constant inner potential is assumed. Ideally Vo_r should be energy dependent (section 4.4.4) but this would have required a more sophisticated acquisition scheme than was available. As the variation with energy appears to be relatively small the corruption of the average produced by the use of a constant inner potential should be less severe than the effect of its complete omission. The inner potential was determined using $\underline{K}$-space polar diagrams of the type shown in figure 2.10 where arbitrary inner potentials are added to the external electron energies until the most kinematical plots are obtained. A 14 eV inner potential was found to give the best results for both the (100) and (111) copper surfaces.

6.1.2 Averaging of Non-Specular Beam Intensity-Energy Spectra

The data acquisition scheme developed for the specular beam averaging could not be extended to the non-specular beams merely by altering the calibration of the energy-scaling potentiometer. The individual intensity-energy spectra for these particular beams are envelopes of overlapping segments of spectra obtained for a range of Faraday cup positions (section 3.4.5). As there were no means available to automatically input the extracted envelope into the multi-channel analyser, individual spectra were acquired in

the normal manner for the non-specular beams, reduced manually to data points at 2.5 eV energy intervals and subsequently transferred to computer cards for averaging. Due to the restriction on the movement of the Faraday cup non- specular beam averages were restricted to a single azimuth.

The averaging contour in $\underline{K}$-space for the non-specular beams is shown in figure 6.1(b). Although an energy-dependent inner potential could have been readily incorporated into the computed average a constant value of 14 eV was used in order to remain consistent with the specular beam averages.

6.2 Experimental Results

6.2.1 Clean Copper (111)

Specular beam intensity-energy spectra from a clean, ordered (111) copper surface were averaged in 1^{o} steps in angle of incidence θ over the range 8^{o} to 37^{o} and in 5^{o} steps in angle of azimuth ϕ from 0^{o} to 30^{o}. The effect of averaging over θ for the $\phi = 0^{o}$ and $\phi = 30^{o}$ azimuths is shown in figures 6.2 and 6.3 respectively where progressive averages for increasing values of ϕ are shown. Even over this restricted range averaging has substantially reduced the amount of fine (multiple scattering) structure and the main spectral features are now quite clearly located close to the integral order Bragg positions although fairly weak subsidiary features exist at approximately one-third and two-thirds order Bragg positions.

The effect of averaging this particular range in θ over the non-symmetrically equivalent range in ϕ given above is shown in figure 6.4. While averaging over θ alone has been shown to be sufficient to produce quite kinematical spectra, averaging over ϕ as well can be seen from figure 6.4 to provide a further suppression of the extra features. The grand average (which is an aggregate of 210 measurements) is shown in figure 6.5 after conversion to a linear scale in reduced scattering vector and can be seen to be very kinematical with only small vestiges of multiple scattering evident. This result is in excellent agreement with the averages for the clean (111) surfaces of silver, nickel and aluminium.

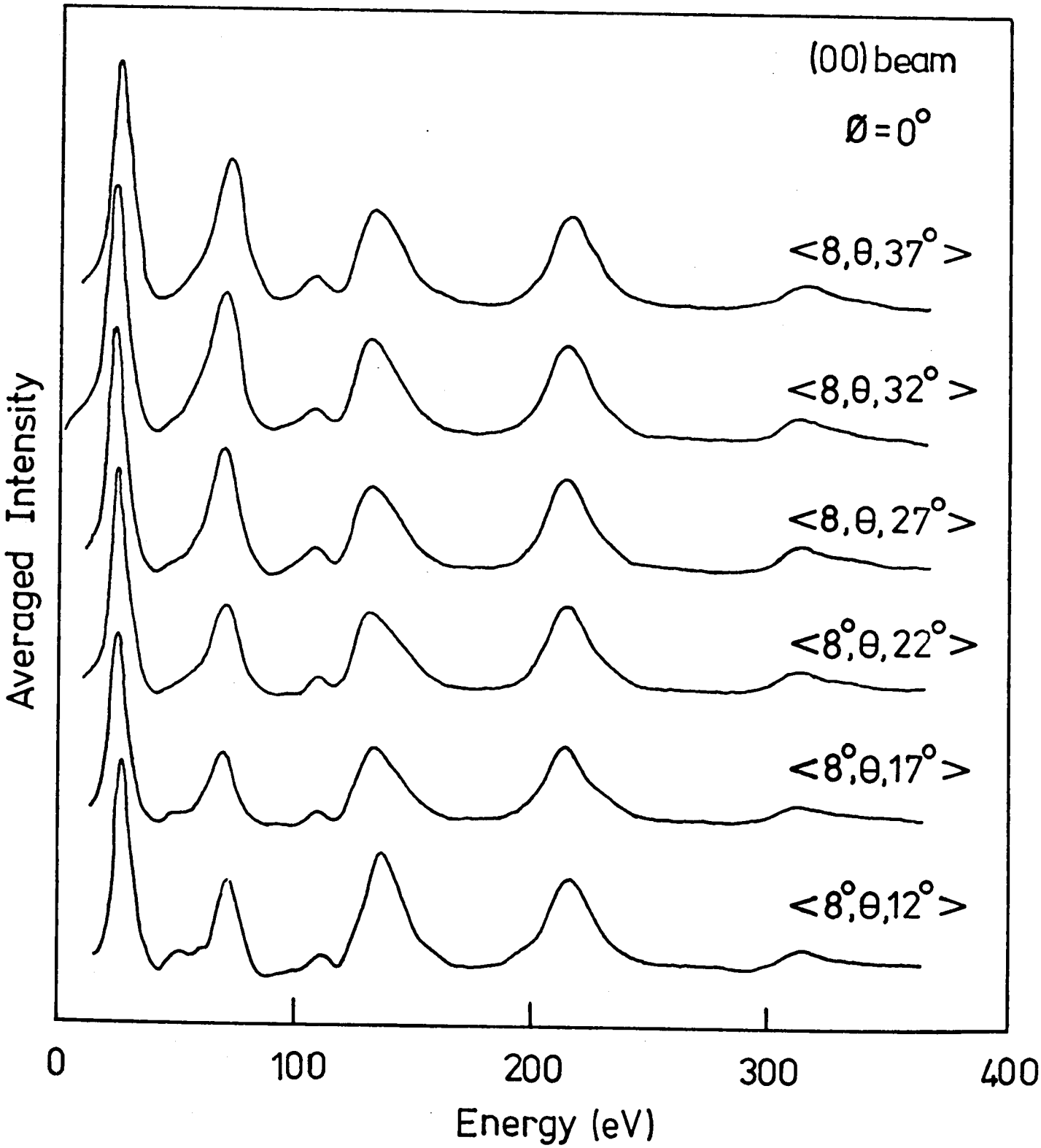

Figure 6.2 The effect of progressive θ averaging for the $\phi = 0^{o}$ azimuth from the clean copper (111) surface.

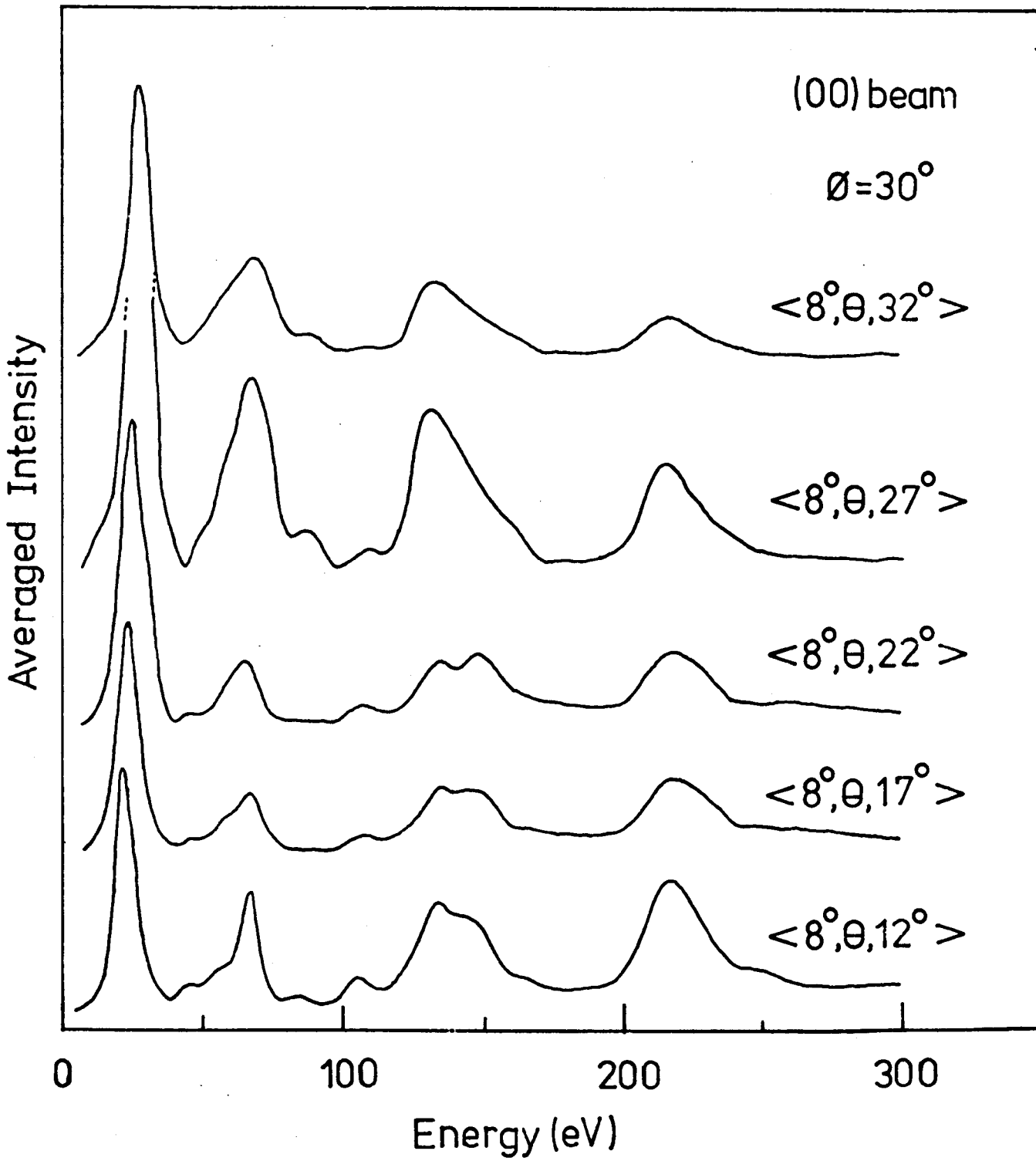

Figure 6.3 The effect of progressive averaging for the $\phi = 30^{\circ}$ azimuth from the clean copper (111) surface.

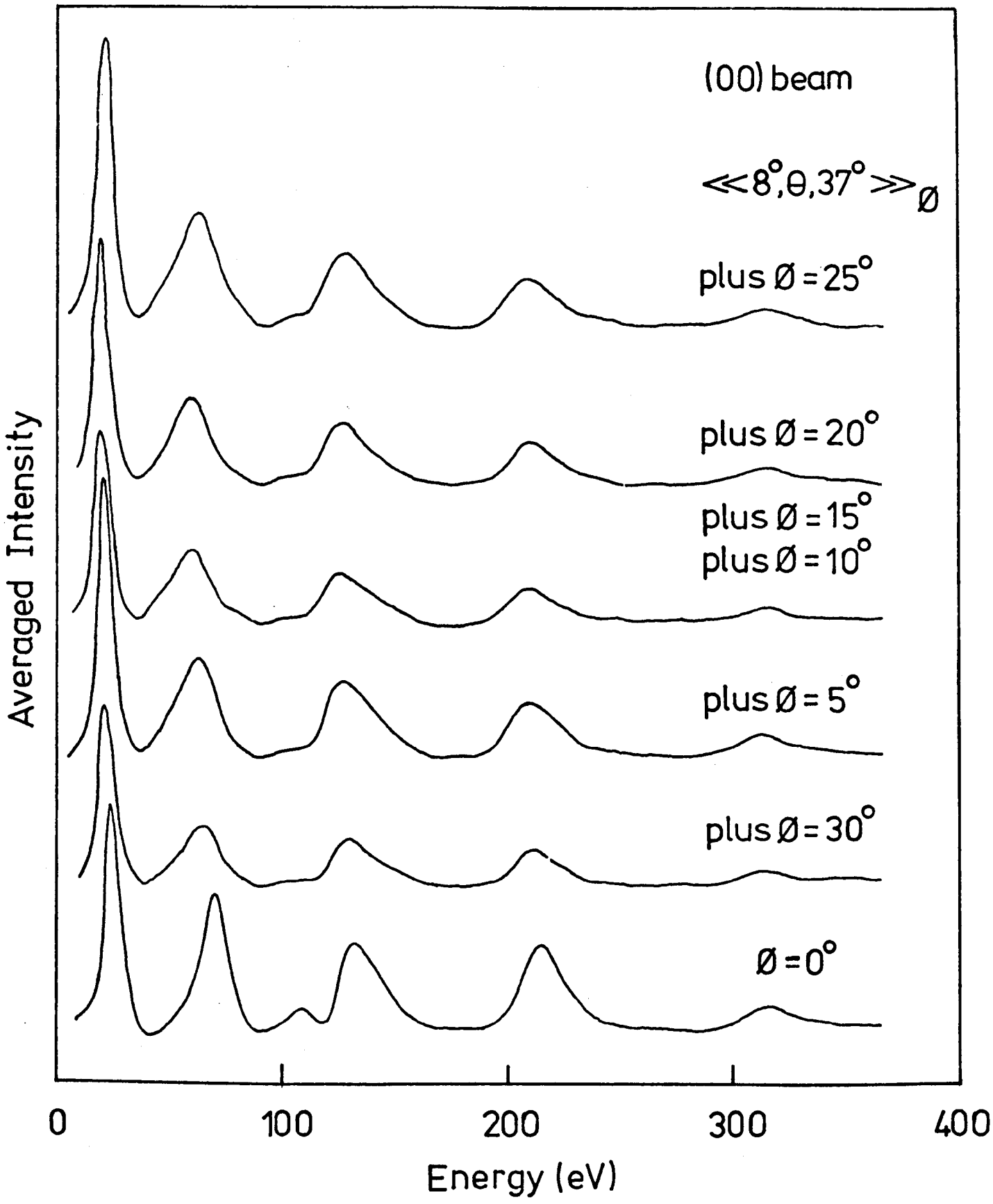

Figure 6.4 The effect of averaging θ averages over the non-symmetrically equivalent range in ϕ for the clean copper (111) surface.

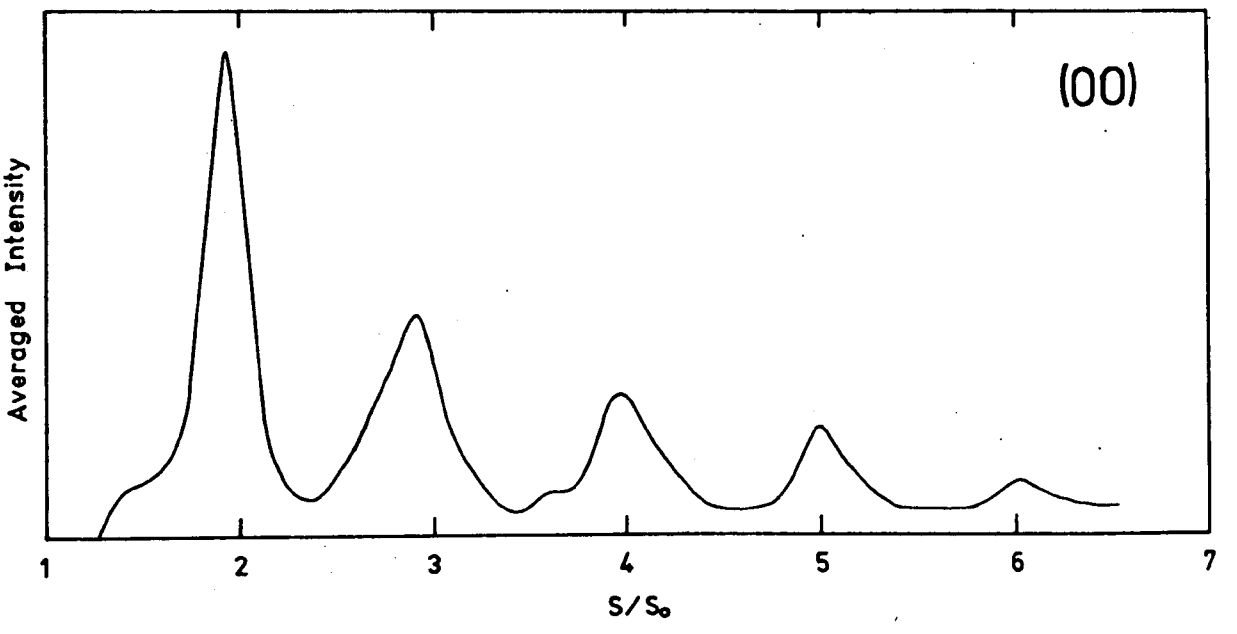

Figure 6.5 The grand average from the clean copper (111) surface.

6.2.2 Clean Copper (100)

Specular beam intensity-energy spectra from a clean, ordered copper (100) surface were averaged in 1^{o} steps in angle of incidence θ over the range 8^{o} to 37^{o} and in 5^{o} steps in angle of azimuth ϕ from 0^{o} to 45^{o}. Averaging over angle of incidence only produced spectra that were much less kinematical than those for the clean (111) copper surface; although the main peaks in the averages were located close to the integral order Bragg positions, very strong extra peaks were observed at approximately half-order positions as shown in the lowest curve in figure 6.6. The effect of progressive averaging over ϕ is also shown in figure 6.6 and the grand average is shown in figure 6.7 as a linear function of reduced scattering vector. Despite the extensive range of scattering geometries included in the grand average (the averaged intensity at a given value of S/S_{o} represents the aggregate of 330 individual measurements) it contains fairly substantial extra features at approximately half-order Bragg positions. The existence of substantial half-order features was also observed by Quinto and Robertson for averages from the clean (100) surface of aluminium.

Intensity-energy spectra for the (10) and (11) beams were averaged over angles of incidence from 0^{o} to 34^{o} and 0^{o} to 28^{o} respectively in 2^{o} steps for the single azimuths $\phi = 0^{o}$ and $\phi = 45^{o}$ respectively and the resultant averages are presented in figures 6.8 and 6.9 respectively. Although the non-specular beam averages are based on a very small number of measurements compared to the specular beam average for this surface, they are much more kinematical in appearance with very little indication of the existence of extra features. As experienced with the specular beam average, peaks in the non-specular beam averages are only approximately located at the kinematically predicted positions of integral order for the (11) beam and half order for the (10) beam.

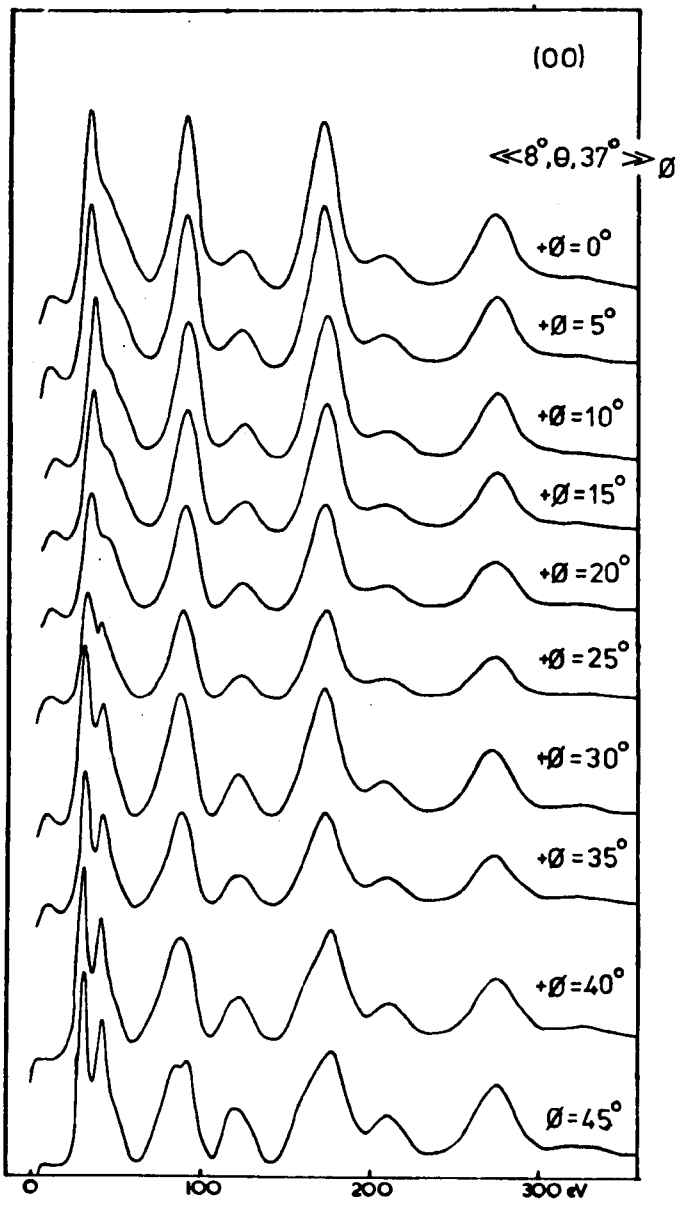

Figure 6.6 The effect of averaging θ averages over the non-symmetrically equivalent range in ϕ for the clean copper (100) surface.

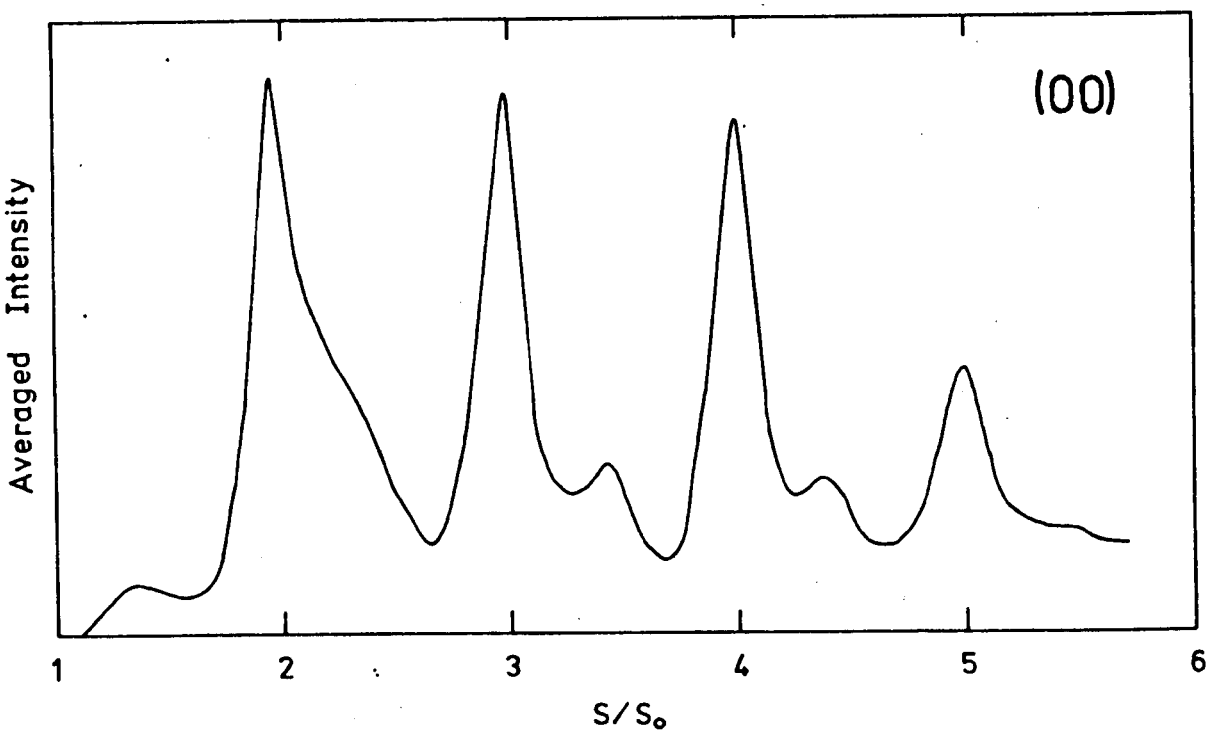

Figure 6.7 The grand average from the clean copper (100) surface.

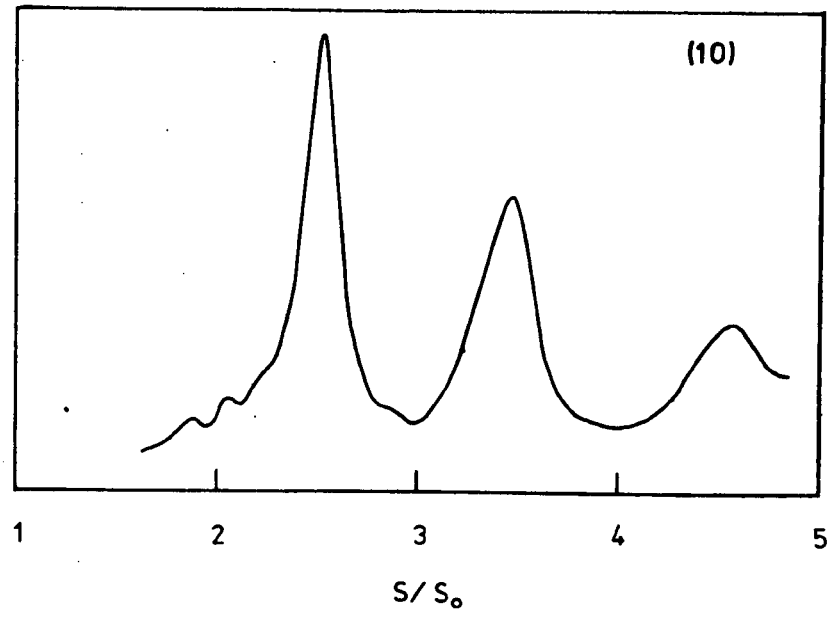

Figure 6.8 Average over θ for the (10) beam from clean copper (100)

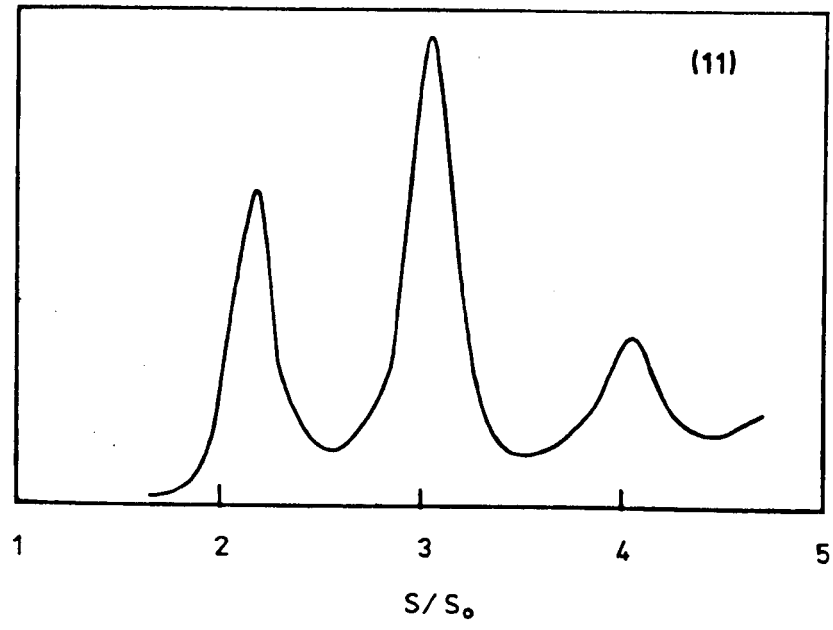

Figure 6.9 Average over θ for the (11) beam from clean copper (100)

6.2.3 Disordered Oxygen Overlayer on Copper (111)

Although no ordered oxygen structures were observed for room temperature adsorption on copper (111) intensity-energy spectra for the (00) beam were averaged over the same range of scattering geometry as for the clean surface and the resultant grand average is shown in figure 6.10. The major differences between this spectrum and that for the clean surface (figure 6.4) are the suppression of the residual features at 2.6 and 3.6 and the development of a large extra peak at 1.47. Closer comparison of the two spectra does reveal a variable shift to higher values of reduced scattering vector of peaks in the disordered oxygen adsorbate average compared with that for the clean surface. A summary of these changes is presented in table 6.1.

6.2.4 Cu(100)-($\sqrt{2}$x$\sqrt{2}$)R45^{o}-O Surface

Intensity-energy spectra for the (00), (1/2,1/2), (10) and (11) beams were averaged over the same ranges of scattering geometry as for the clean surface and the resultant averages are shown in figures 6.11 and 6.12 for the specular and non-specular beams respectively. A particularly encouraging feature of figure 6.12 is the absence of appreciable structure in the (1/2,1/2) beam average as the only structure that would be consistent with kinematical theory would be that due to the variation in the atomic scattering factor. A comparison of the averaged spectra for the (00), (10) and (11) beams with those of the clean surface reveals a variable shift to lower values of reduced scattering vector for peaks in the adsorbate averages below Bragg number 3.5 and some modification to the extra features evident in the clean surface averages. These changes are summarised for the three beams in table 6.2.

6.2.5 Cu(100)-(2x2)-O Surface

Although it was not possible to obtain sufficiently reliable intensity-energy spectra for the extra beams produced by this particular structure to enable the surface structure to be determined using dynamical model calculations, a wide range of intensity data was collected and averaged for the (00),

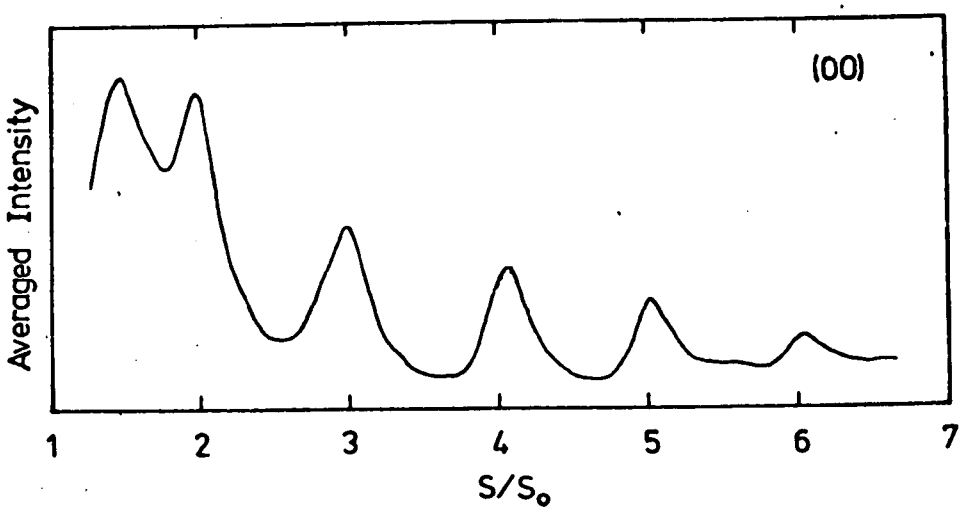

Figure 6.10 Grand average for the (00) beam from the disordered oxygen adsorbed copper (111) surface.

TABLE 6.1

Beam	Nominal Bragg Number	S/S_o Clean	S/S_o Adsorbate	Shift
(00)	2	1.94	1.98	+0.04
	3	2.91	3.00	+0.09
	4	3.98	4.04	+0.06
	5	5.00	5.02	+0.02
	6	6.03	6.06	+0.03

SUMMARY OF CHANGES IN AVERAGED SPECTRA BETWEEN THE CLEAN AND DISORDERED OXYGEN COPPER (111) SURFACES

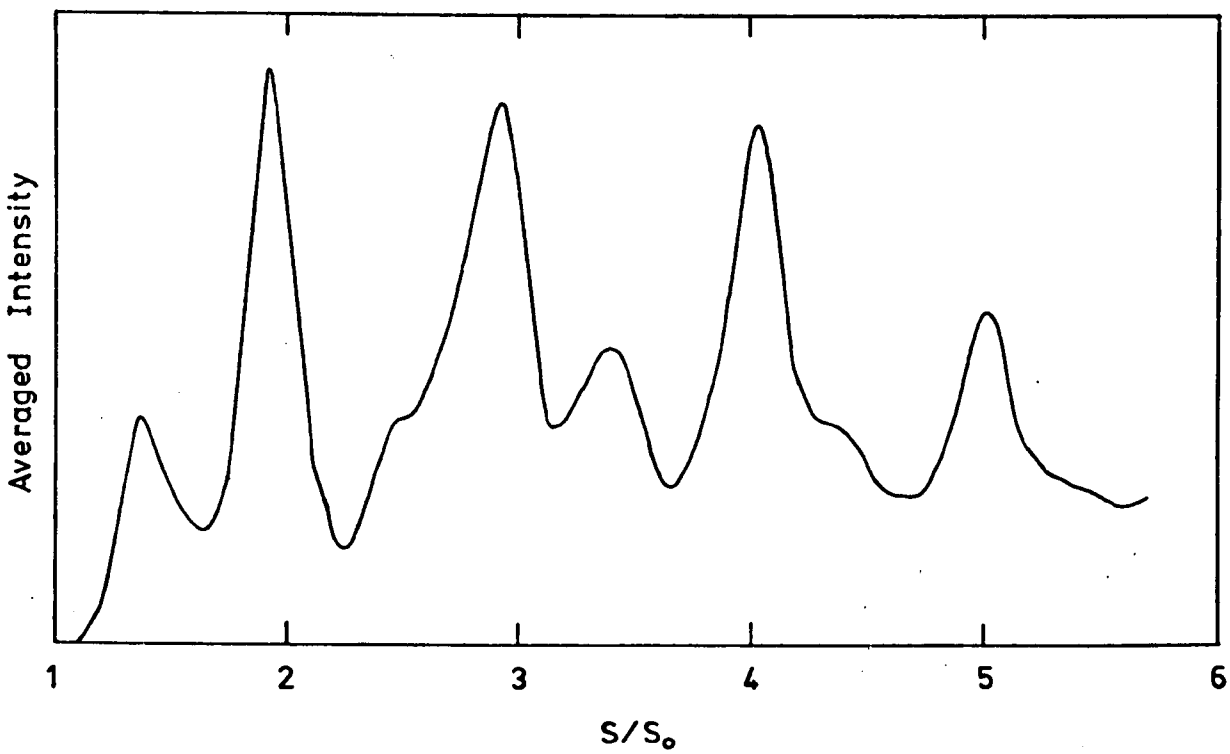

Figure 6.11 The grand average for the (00) beam from the Cu(100)-($\sqrt{2}$x $\sqrt{2}$)R45^o-O surface.

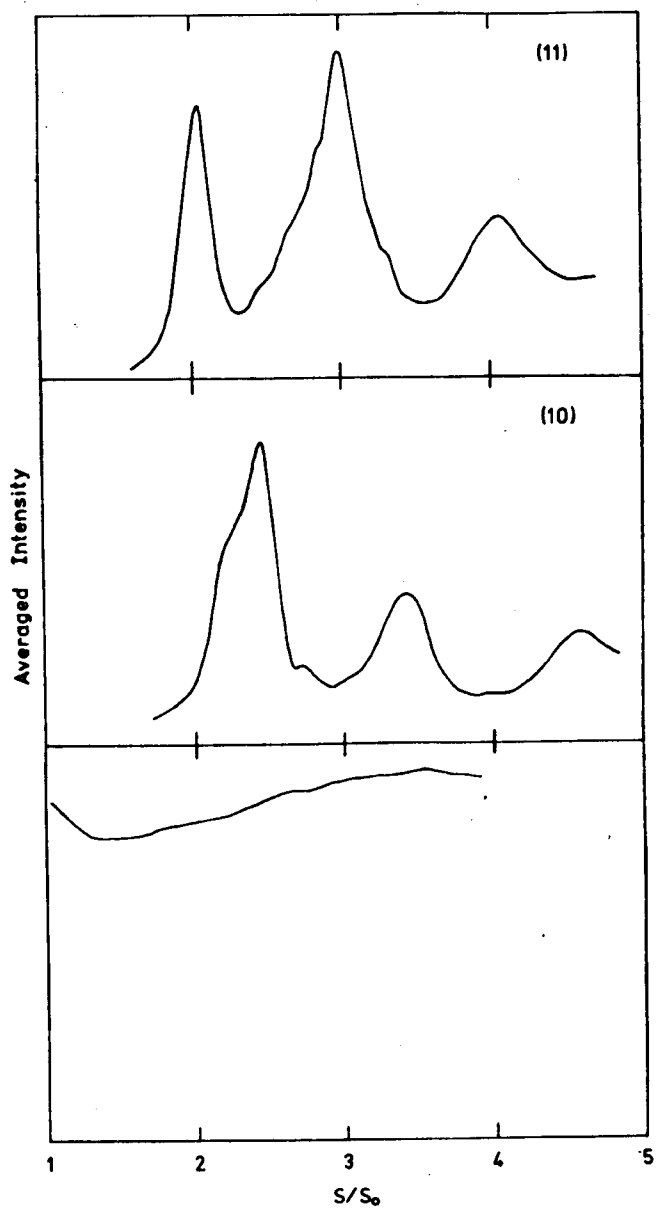

Figure 6.12 The averages for the (1/2,1/2),(10) and (11) beams from the Cu(100)-($\sqrt{2}$x$\sqrt{2}$)R45^{o}-O surface.

TABLE 6.2

Beam	Nominal Bragg Number	S/S_o Clean	S/S_o Adsorbate	Shift
(00)	2	1.96	1.93	-0.03
	3	2.98	2.93	-0.05
	4	4.00	4.05	+0.05
	5	5.00	5.02	+0.02
(10)	$2\frac{1}{2}$	2.52	2.45	-0.07
	$3\frac{1}{2}$	3.45	3.40	-0.05
	$4\frac{1}{2}$	4.57	4.62	+0.05
(11)	2	2.18	2.05	-0.13
	3	3.05	2.99	-0.06
	4	4.06	4.06	0.00

SUMMARY OF CHANGES IN AVERAGED SPECTRA BETWEEN THE CLEAN AND Cu(100)-($\sqrt{2}$x $\sqrt{2}$)R45^o-O SURFACES

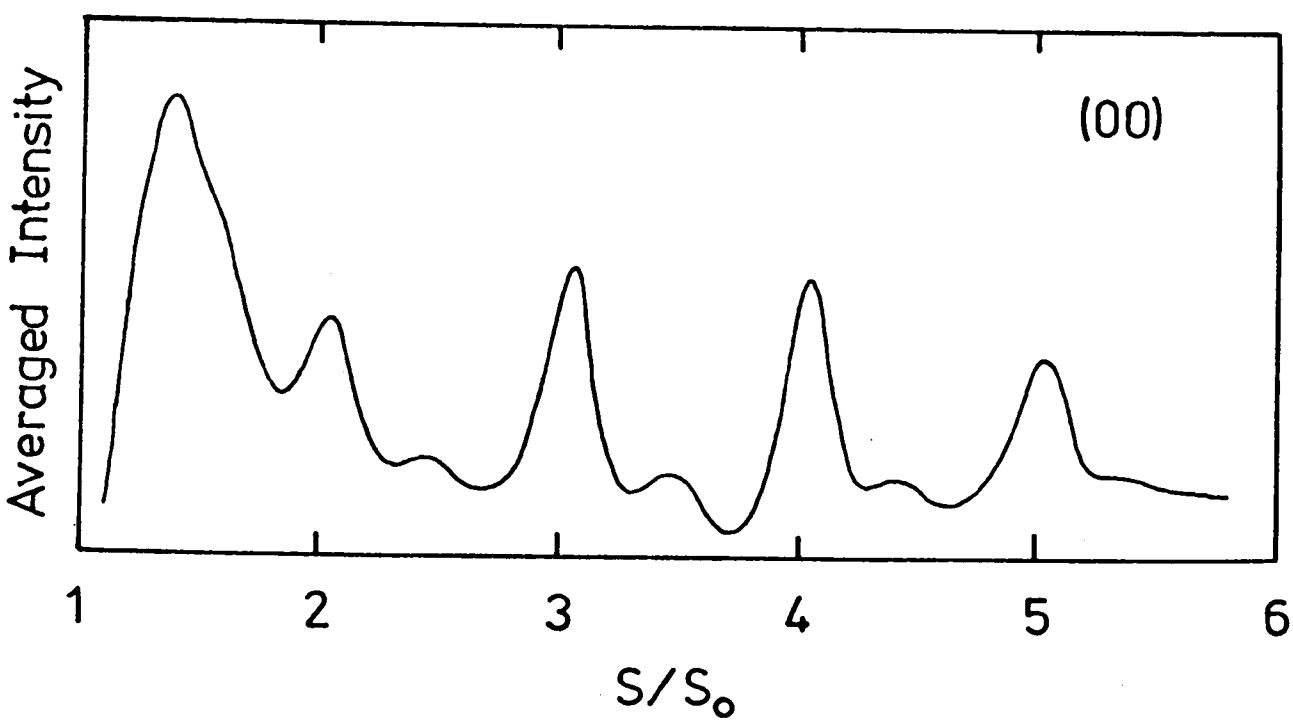

Figure 6.13 The grand average for the (00) beam from the Cu(100)-(2x2)-O surface.

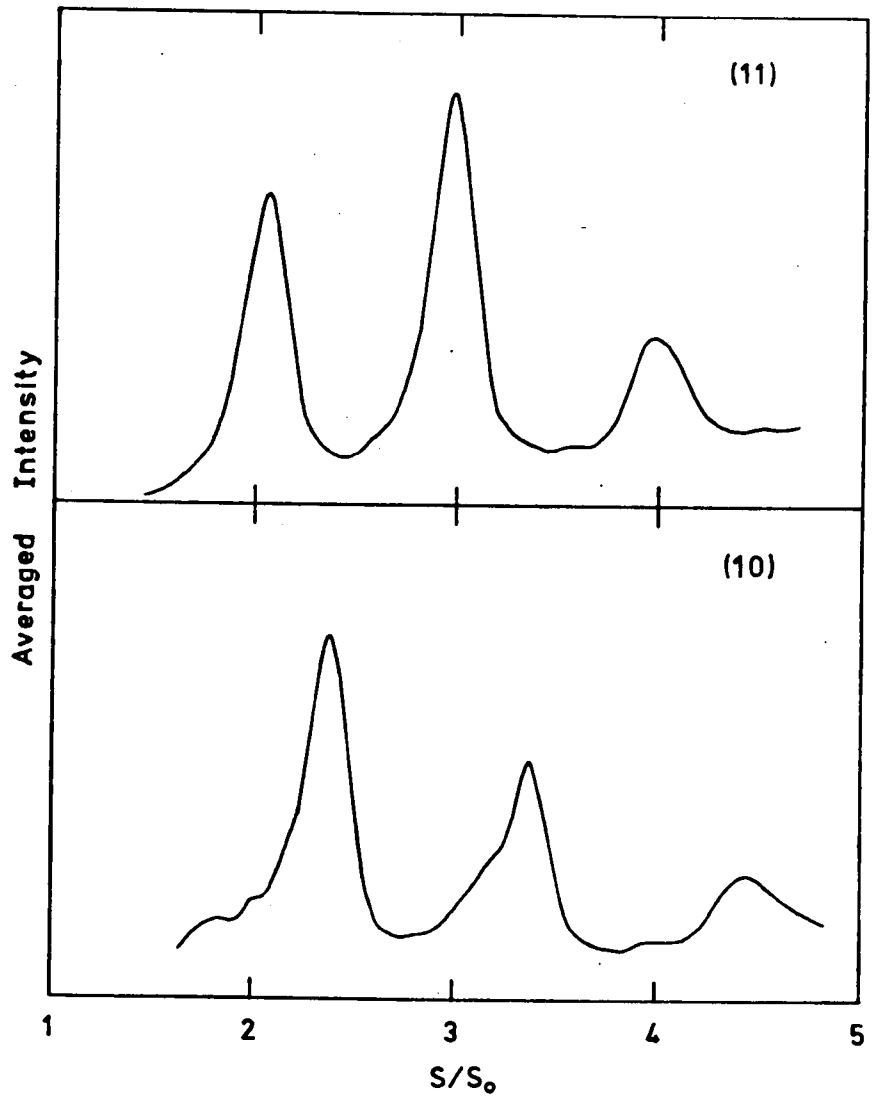

Figure 6.14 The averages for the (10) and (11) beams from the Cu(100)-(2x2)-O surface.

TABLE 6.3

Beam	Nominal Bragg Number	S/S_o Clean	S/S_o Adsorbate	Shift
(00)	2	1.96	1.93	-0.03
	3	2.98	2.93	-0.05
	4	4.00	4.05	+0.05
	5	5.00	5.02	+0.02
(10)	$2\frac{1}{2}$	2.52	2.45	-0.07
	$3\frac{1}{2}$	3.45	3.40	-0.05
	$4\frac{1}{2}$	4.57	4.62	+0.05
(11)	2	2.18	2.05	-0.13
	3	3.05	2.99	-0.06
	4	4.06	4.06	0.00

SUMMARY OF CHANGES IN AVERAGED SPECTRA BETWEEN THE CLEAN AND Cu(100)-(2x2)-O SURFACES

(10) and (11) beams for this structure over the same range of scattering geometries used for the clean surface averages. The resultant averages are shown in figures 6.13 and 6.14 for the specular and non-specular beams respectively and a summary of the changes observed in these spectra relative to the clean surface averages is given in table 6.3. The peaks in the (00) beam average have been shifted to higher values whereas the peaks in both the (10) and (11) beam averages have been shifted to lower values of the reduced scattering vector.

6.3 Correlation with Kinematical Calculations

6.3.1 Kinematical Calculations

The kinematical calculations used in the following structural analyses were performed using a computational scheme based on the pseudo-kinematical theory of Pendry.[5] The theory was formulated and compiled as a Fortran computer program by Mitchell[6] for operation on the University of Warwick 4130 computer. Electron scattering at the ion-cores was described in the usual manner in terms of phase shifts using the calculations up to $l = 6$ by Zimmer[7] from a computational scheme similar to Pendry.[8] Inelastic scattering was introduced using an imaginary potential derived from the observed peak widths in the (00) beam averages from the clean (100) and (111) surface of copper. The peak width ΔE is simply related to the imaginary potential Vo_i by:[9]

$$\Delta E = 2Vo_i . \qquad \ldots 6.5$$

The variation of experimental (average) peak width, and hence imaginary potential, is shown in figure 6.15 for the (00) beam for the two clean surfaces.

In order to obtain realistic relative intensities in the theoretical spectra a constant Debye-Waller factor, derived from a rather approximate Debye temperature of 300 K, was included. The intrinsic variation of the atomic scattering factor with scattering anglewas overcome by averaging

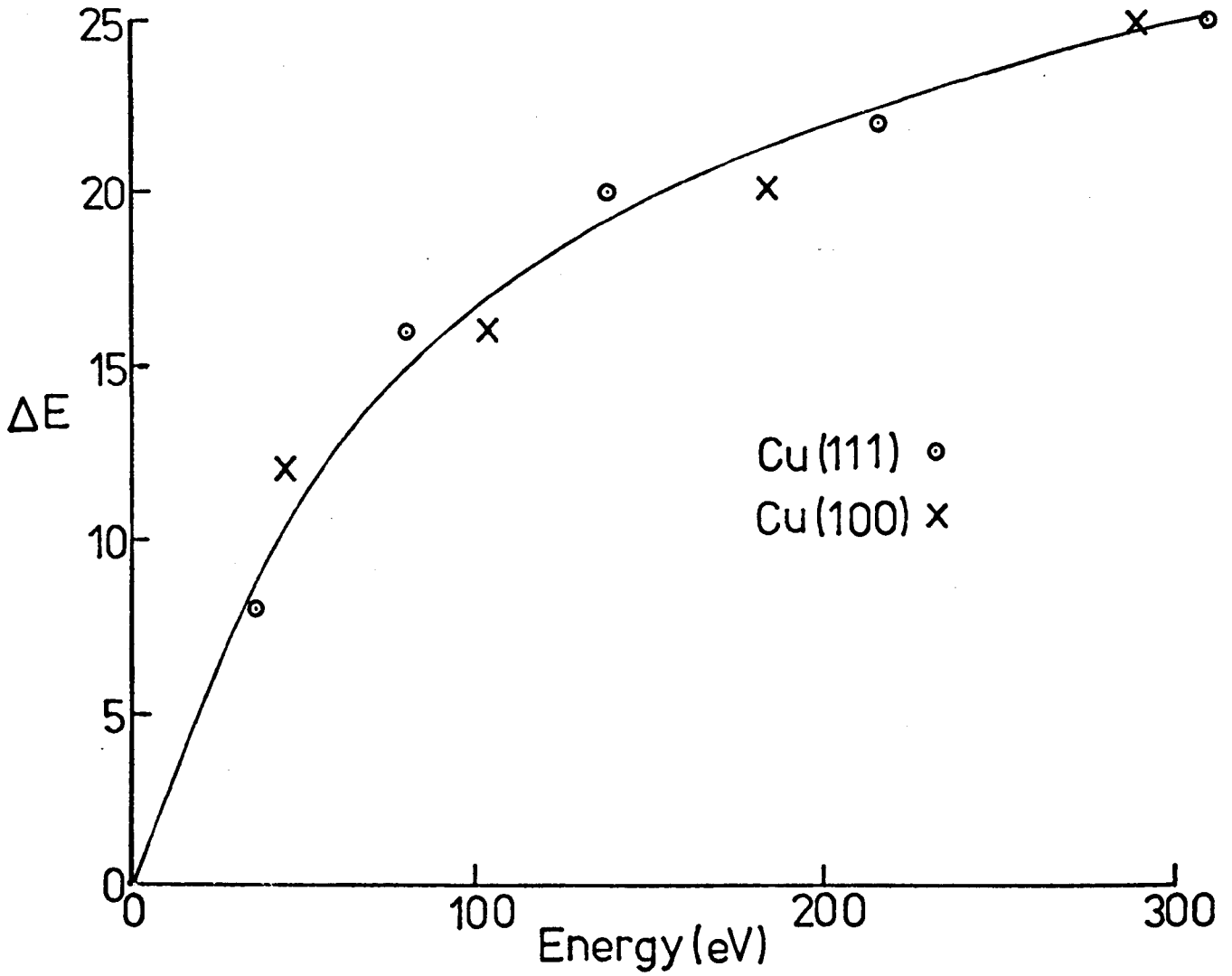

Figure 6.15 The variation of experimental peak widths derived from the (00) beam averages for the clean (100) and (111) copper surfaces.

the theoretical calculations over the identical range of angle of incidence used experimentally. The azimuthal range did not have to be considered as kinematical calculations are independent of azimuth.

6.3.2 Criteria for Correlation

The inherent difficulty in the correlation of experimental averages with model calculations is determining which of the observed differences between the clean and the adsorbate averages relate to structural effects. Three types of features can be considered:

(a) Absolute peak positions.

(b) Shifts in peak positions in the unknown surface structure relative to the averaged data for the clean surface.

(c) The existence of extra peaks or shoulders.

While absolute peak positions will be influenced by surface structure they are not unique indicators of structural change as they are also influenced by the inner potential for which the energy dependence is difficult to characterise at present. Consequently, attention has been focussed in the correlations presented here on the shifts in the adsorbate peak positions relative to those for the clean surface. This presupposes that the inner potential does not vary between the clean surface and the adsorbate surface and although this is assumed in dynamical correlations as well, there are indications that a change in inner potential between the substrate and the adsorbate can have a marked effect.[10] The observed shifts in the experimental peak positions relative to the model calculations for the clean surface have been assumed to be associated with deficiencies in the model, such as the use of an approximate inner potential, which are assumed not to change for the adsorbate structure.

Because extra features, that are not predicted by kinematical theory, are observed in averages for the clean surface there is no guarantee that the modification of such features in the corresponding adsorbate structure averages are not due to variations in multiple scattering rather than due

to structural effects. Any interpretation of the existence, shifting, amplification or suppression of these features must therefore be made with due caution. Consequently, the criteria adopted here for dealing with these extra features are:

(a) Model calculations need not necessarily predict extra features for the adsorbate structure average where equivalent extra features appear in the experimental average for the clean surface.

(b) Model calculations should not predict extra features where none exist in the experimental average from the absorbate surface.

In the correlations presented here the data used has been restricted to features between Bragg numbers 1.5 and 3.5 as this represents an energy range up to about 150 to 200 eV over which LEED is considered to have its maximum surface sensitivity. The correlation of experimental data with theory is presented in the next three sections using the graphical form suggested by Andersson et al[11] for dynamical correlations.

6.3.3 Cu(100)-($\sqrt{2}$x$\sqrt{2}$)R45°-O Surface Structure

Having restricted the structural analysis to features between Bragg numbers 1.5 and 3.5 the features to be considered for this structure are shown in table 6.4. Several theoretical models were examined for this structure and these are shown schematically in figure 6.16. Four atomic oxygen structures, with a coverage of one oxygen atom per unit adsorbate mesh (corresponding to half monolayer coverage with respect to the substrate mesh) and three molecular structures of higher coverages were considered. The molecular models will be discussed first.

Two models involving the adsorption of the O_2 species were investigated where the diatomic moiety was bonded to either the nearest neighbour copper atoms (M2a) or to the next nearest neighbours (M2b). Both of these structures correspond to a coverage of two oxygen atoms per unit adsorbate mesh. In the theoretical calculations of these models it was necessary that two symmetrically equivalent domains were included. The final molecular model

TABLE 6.4

Beam	Nominal Bragg Number	S/S_o Clean	S/S_o Adsorbate	Shift	Extra Features (Shoulders)
(00)	2	1.96	1.93	-0.03	2.5
	3	2.98	2.93	-0.05	
(10)	$2\frac{1}{2}$	2.52	2.45	-0.07	2.25
(11)	2	2.18	2.05	-0.13	2.65
	3	3.05	2.99	-0.06	

EXPERIMENTAL DATA USED IN THE CORRELATION WITH THEORY FOR THE Cu(100)-($\sqrt{2}$x $\sqrt{2}$)R45^{o}-O SURFACE

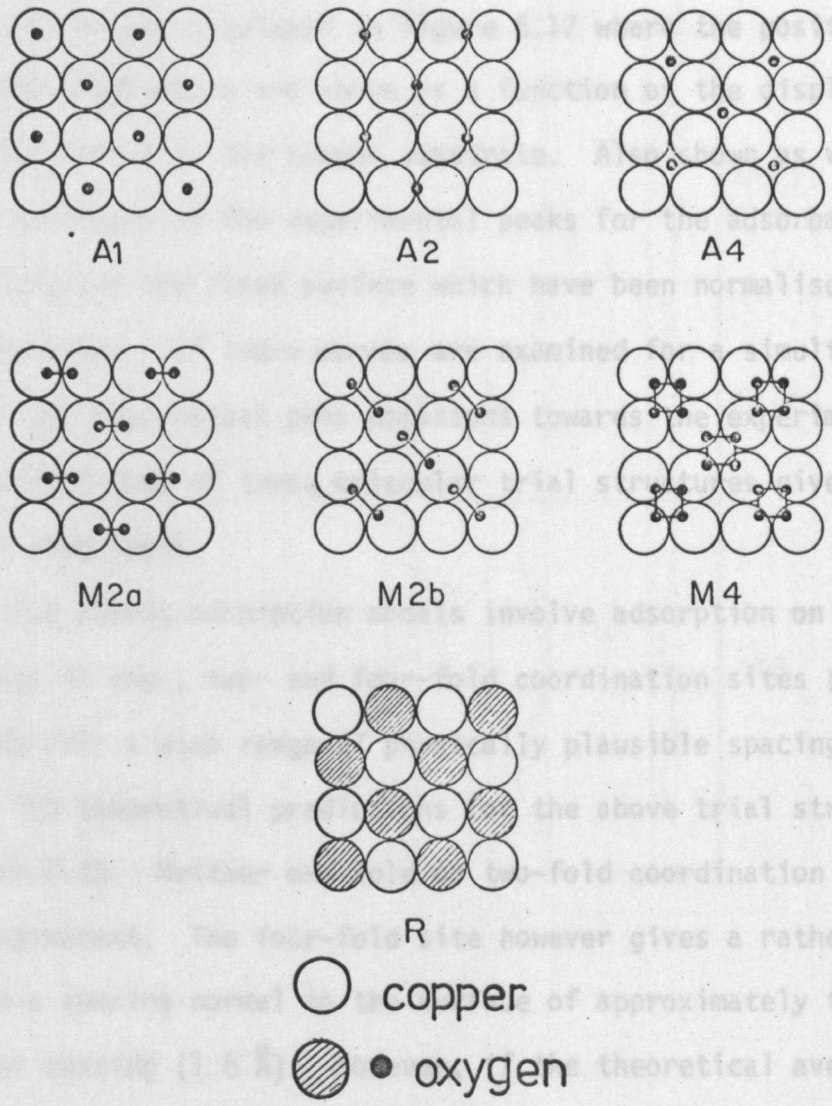

Figure 6.16 Schematic diagram of the theoretical models used in the correlation of experiment and theory for the Cu(100)-($\sqrt{2}$x$\sqrt{2}$)R45^{o}-O surface.

considered consisted of the O_4 species adsorbed in a nearest neighbour configuration on the unreconstructed surface (M4) which corresponded to a coverage of four oxygen atoms per unit adsorbate mesh. The O-O distance used in the molecular calculations was taken as 1.48 Å which is close to the value in hydrogen peroxide. The theoretical results for the above molecular structures are displayed in figure 6.17 where the positions of the five peaks under examination are shown as a function of the displacement of the oxygen layer normal to the copper substrate. Also shown as vertical lines are the positions of the experimental peaks for the adsorbate structure relative to those for the clean surface which have been normalised to the theoretical positions. If these curves are examined for a simultaneous convergence of the theoretical peak positions towards the experimental values it is apparent that none of these molecular trial structures gives good agreement with experiment.

Three of the atomic adsorption models involve adsorption on top of the copper substrate in one-, two- and four-fold coordination sites (A1, A2 and A4 respectively) for a wide range of physically plausible spacings normal to the surface. The theoretical predictions for the above trial structures are shown in figure 6.18. Neither one-fold or two-fold coordination sites produce good agreement. The four-fold site however gives a rather good agreement with a spacing normal to the surface of approximately the copper substrate layer spacing (1.8 Å). However, if the theoretical averaged spectra for this particular structure are examined(figure 6.19) the shapes are in poor agreement with the experiment. There is no evidence of the observed shoulders and the second order Bragg peak for the (00) beam is almost completely annihilated by the rapidly sloping background. In view of this discrepancy, agreement with experiment can not be considered satisfactory despite the realistic peak shifts computed. Also, the Cu-O bond length of about 4.1 Å that is implied by this structure is unreasonably large being approximately twice that of known Cu-O bond distances.[12,13]

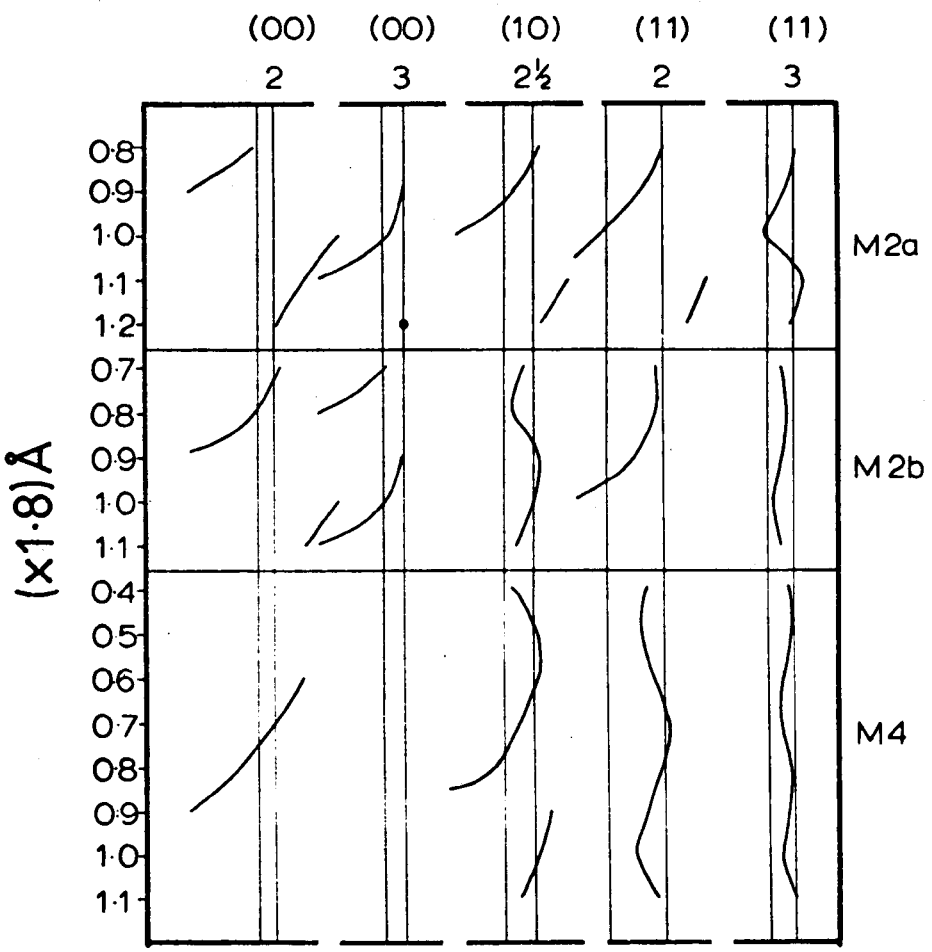

Figure 6.17 Theoretical peak positions as a function of trial structure for various molecular adsorption models. The black dot indicates a peak that does not appear to fit the trends shown.

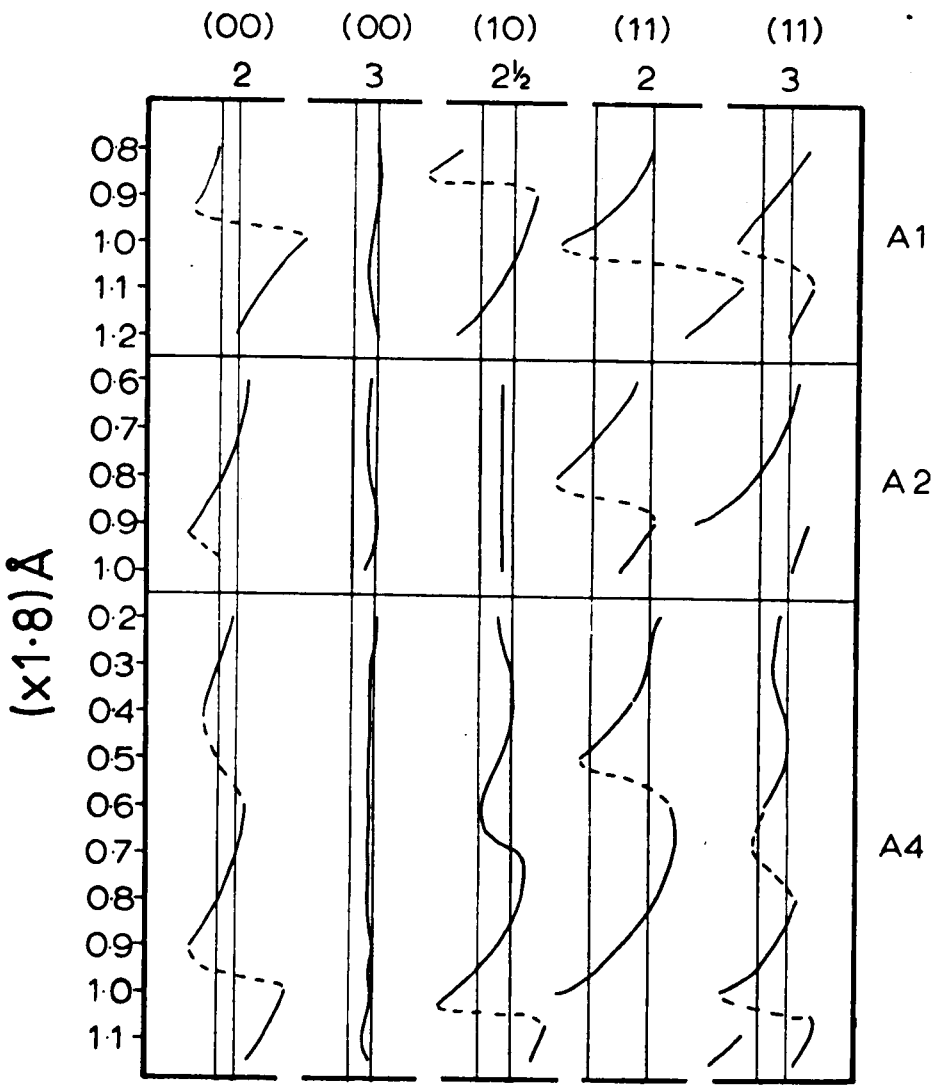

Figure 6.18 Theoretical peak positions as a function of trial structure for the one-fold, two-fold and four-fold atomic adsorption models. The dashed lines indicate peaks with greatly suppressed intensities.

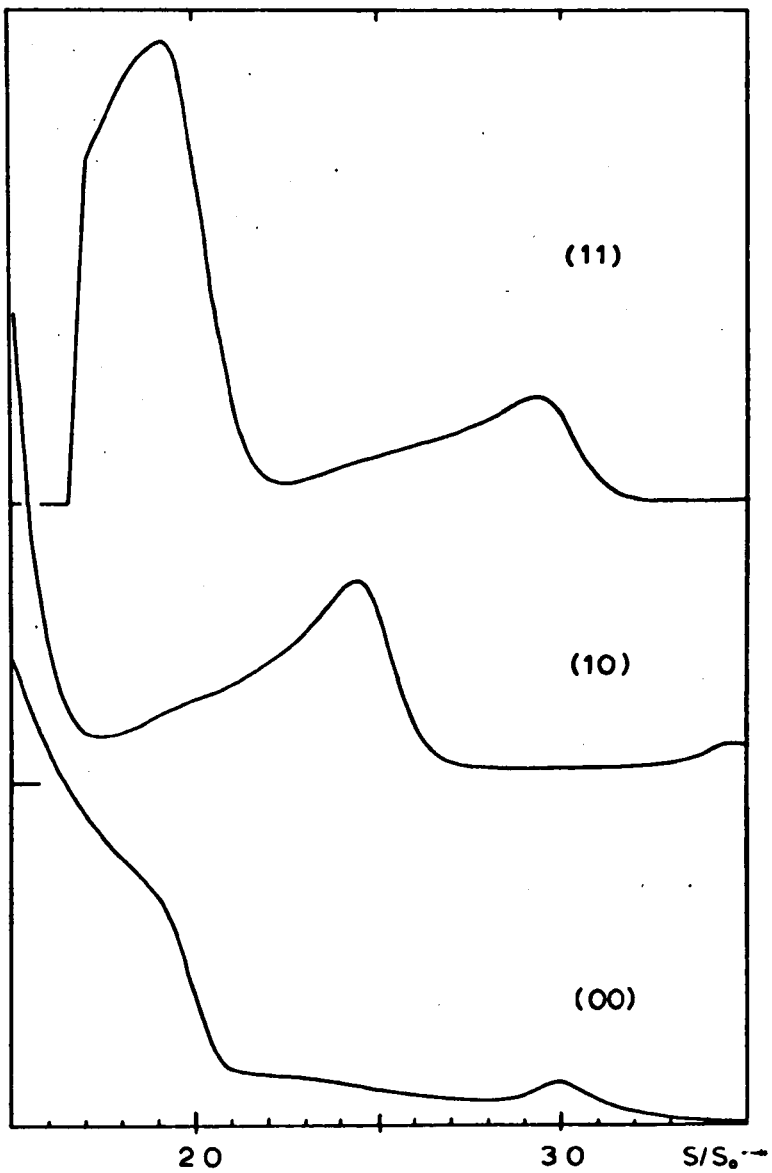

Figure 6.19 Theoretical averaged intensity spectra for the A4 structure with a spacing of the oxygen layer above the top substrate layer of 1.7 Å.

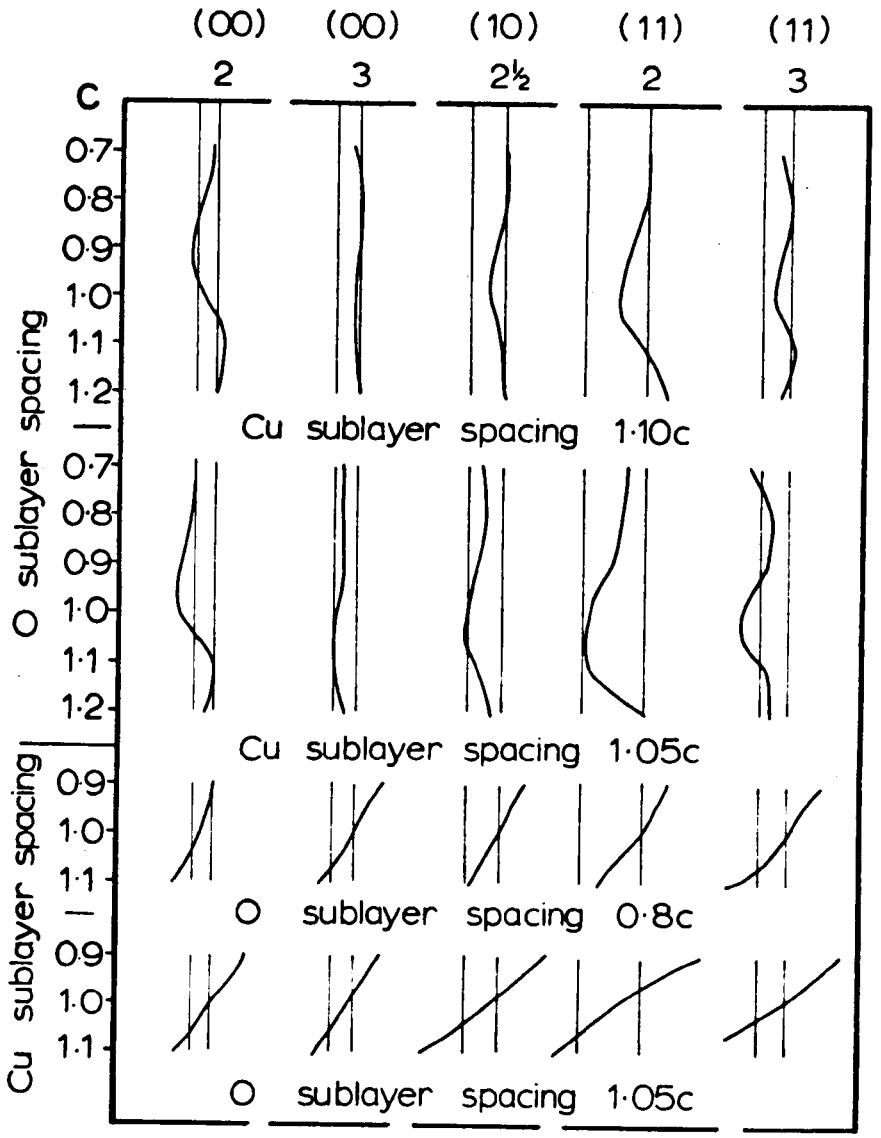

Figure 6.20 Theoretical peak positions as a function of trial structure for the reconstructed surface R where c is the substrate layer spacing (1.8 Å).

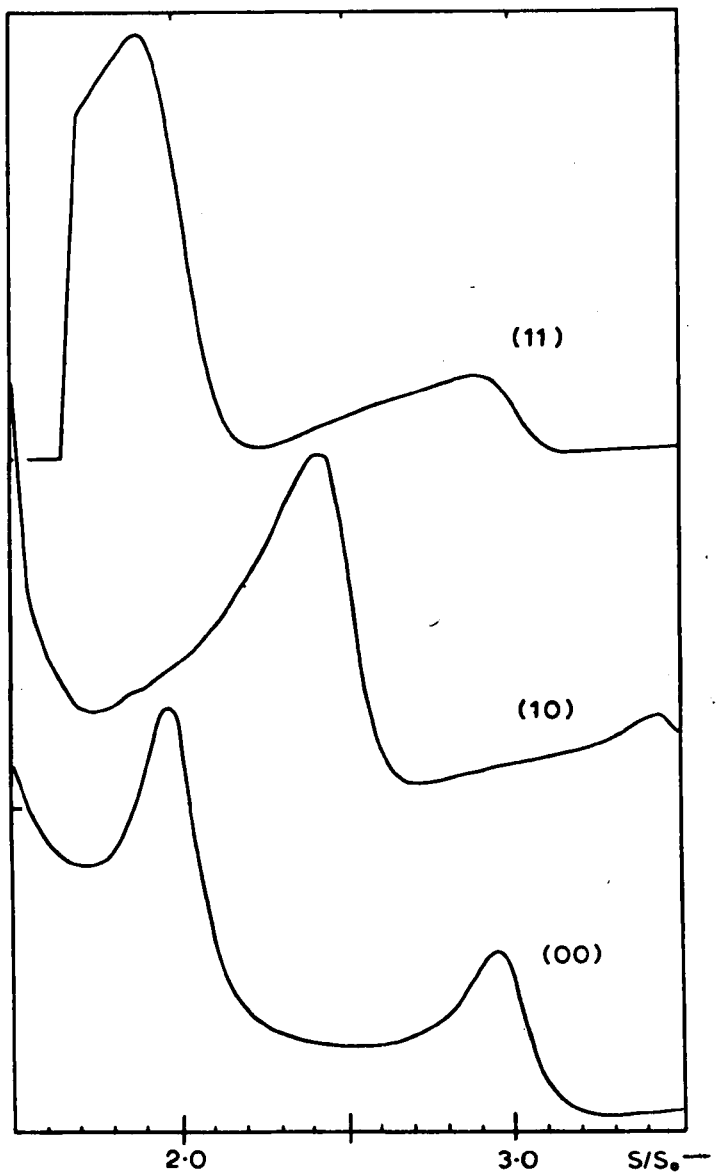

Figure 6.21 Theoretical averaged spectra for the reconstructed surface with copper and oxygen sublayer spacings of 1.05 times the substrate layer spacing.

The dependence of theoretical peak position for the reconstructed surface (R), where alternate atoms in the top layer are now oxygen instead of copper, is shown in figure 6.20 as a function of the oxygen sublayer spacing for two different copper sublayer spacings and as a function of copper sublayer spacing for one oxygen sublayer spacing. It is apparent from this figure that the dependence of peak position on copper spacing is both stronger and more systematic than on oxygen location. Good agreement is obtained for copper spacings in the range 1.05 to 1.10 times the copper substrate layer spacing. The optimum oxygen spacing appears to be approximately coplanar with the reconstructed copper atoms. The averaged spectra for a trial structure in this optimum range, namely with oxygen and copper sublayer spacings of 1.05 times the copper substrate spacing, are shown in figure 6.21. The peak positions are much better than those for the four-fold structure in figure 6.19, the shapes are now quite satisfactory and, although small, shoulders are evident in approximately the correct positions. Satisfactory convergence to a reconstructed structure within the above range appears to have been obtained.

6.3.4 Cu(100)-(2x2)-O Surface Structure

The features considered in the structural analysis for this particular adsorbate are shown in table 6.5. Several theoretical models were examined for this surface structure and these are shown schematically in figure 6.22. Four atomic oxygen adsorption structures, two possible coverages of either one or three oxygen atoms per unit adsorbate mesh (corresponding to one-quarter and three-quarter monolayer coverage with respect to the substrate mesh) and two types of substrate (clean copper and the half-monolayer reconstructed surface) were considered. No adsorption structures involving molecular oxygen were considered for this structure. For the case of two-fold and "four-fold" adsorption on the reconstructed substrate (A2R,A4R) alternate adsorption sites are no longer equivalent and consequently two symmetrically equivalent domains of this structure were averaged together theoretically.

TABLE 6.5

Beam	Nominal Bragg Number	S/S_o Clean	S/S_o Adsorbate	Shift
(00)	2	1.96	1.93	-0.03
	3	2.98	2.93	-0.05
(10)	2½	2.52	2.45	-0.07
(11)	2	2.18	2.05	-0.13
	3	3.05	2.99	-0.06

EXPERIMENTAL DATA USED IN THE CORRELATION WITH THEORY FOR THE Cu(100)-(2x2)-O SURFACE

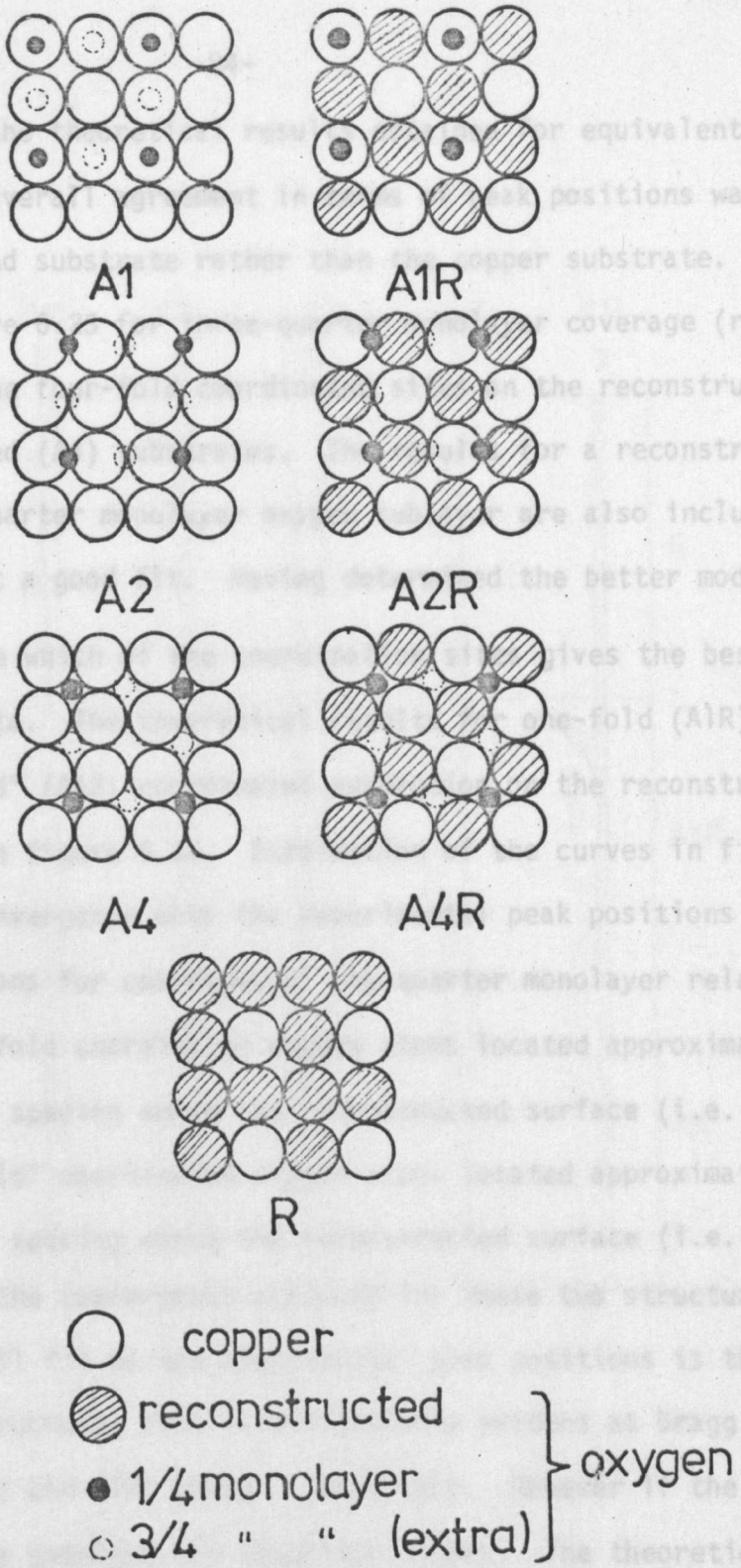

Figure 6.22 Schematic diagram of the theoretical models used in the correlation of experiment and theory for the Cu(100)-(2x2)-O surface.

Comparison of the theoretical results obtained for equivalent coordination showed that closer overall agreement in terms of peak positions was obtained for the reconstructed substrate rather than the copper substrate. This is illustrated in figure 6.23 for three-quarter monolayer coverage (relative to the substrate) in the four-fold coordinated sites on the reconstructed (A4R) and non-reconstructed (A4) substrates. The results for a reconstructed surface involving a three-quarter monolayer oxygen sublayer are also included in figure 6.23 (R) but are not a good fit. Having determined the better model substrate it remains to decide which of the coordination sites gives the best fit with the experimental data. The theoretical results for one-fold (A1R), two-fold (A2R) and "four-fold" (A4R) coordinated adsorption on the reconstructed surface are shown in figure 6.24. Examination of the curves in figure 6.24 for simultaneous convergence onto the experimental peak positions reveals two possible solutions for coverages of one-quarter monolayer relative to the substrate: one-fold coordinated oxygen atoms located approximately 1.2 times the substrate spacing above the reconstructed surface (i.e. at 2.1 to 2.2 Å) and "four-fold" coordinated oxygen atoms located approximately 0.6 times the substrate spacing above the reconstructed surface (i.e. at 1.1 Å).

Comparison of the convergence achieved for these two structures shows that the best overall fit to the experimental peak positions is the "four-fold" adsorption structure; this is particularly evident at Bragg numbers 2.3 and 2.5 for the (11) and (10) beams respectively. However if the computed averaged spectra are examined the situation alters. The theoretical averages for the (00), (10) and (11) beams are shown in figures 6.25 and 6.26 for the one-fold and "four-fold" solutions. The shapes of the curves are quite different with the second order Bragg peak in the (00) beam spectra for the "four-fold" coordinated structure being markedly suppressed relative to its equivalent in the one-fold spectra. Thus as in the previous structural analysis final selection was determined by peak shapes and the one-fold structure was selected as being the most satisfactory overall. The existence of an extra feature at approximately Bragg number 2.4 in the (00) beam theoretical spectra for the one-fold structure can not be used as evidence

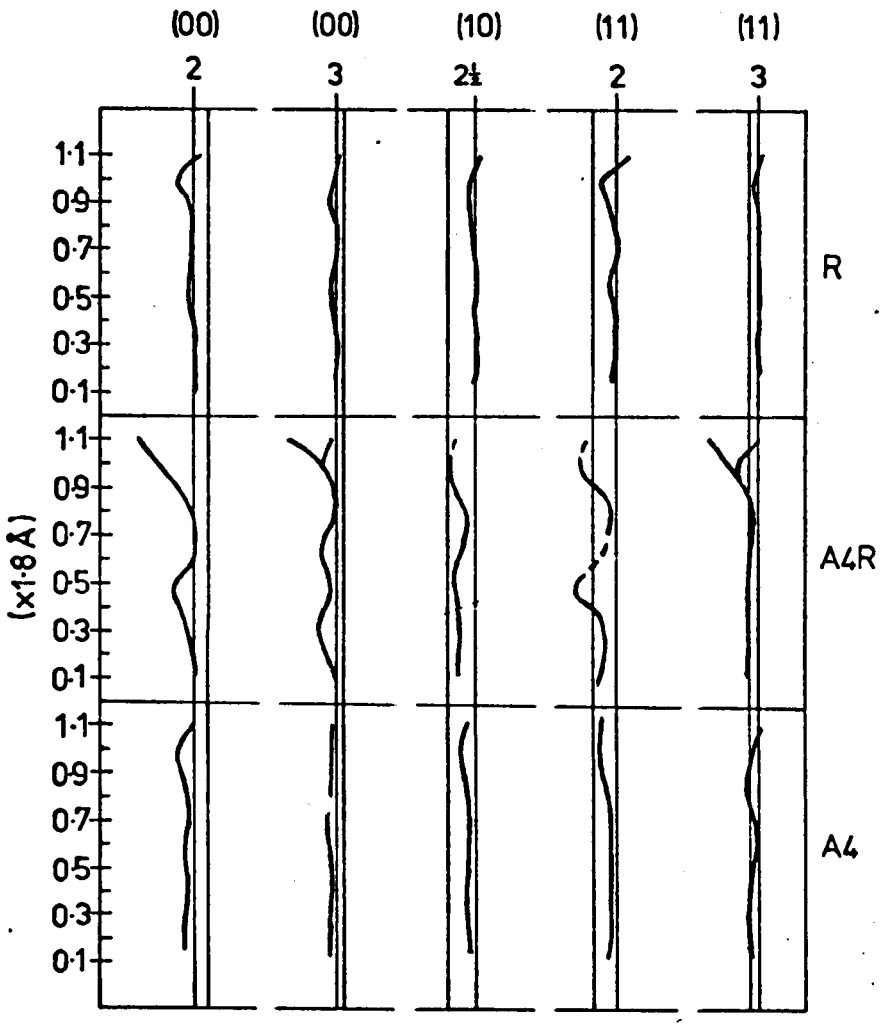

Figure 6.23 Theoretical peak positions as a function of trial structure for the four-fold coordinated adsorption sites on the reconstructed (A4R) and non-reconstructed (A4) substrates and for the reconstructed surface (R).

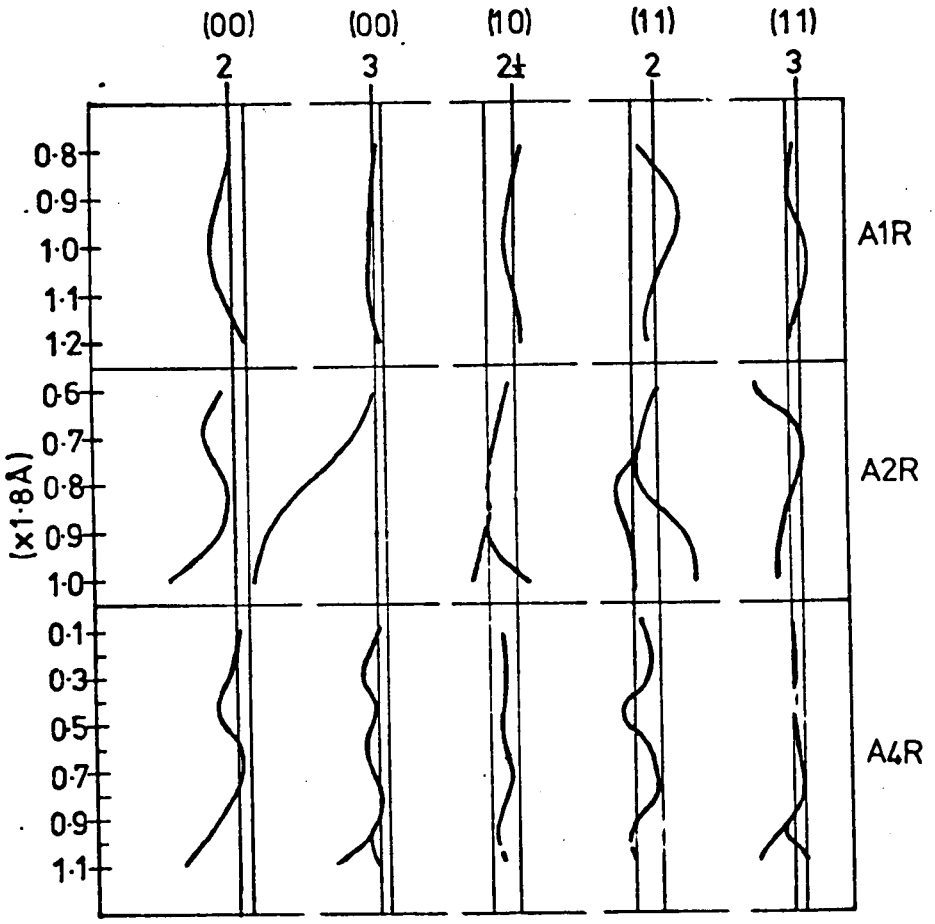

Figure 6.24 Theoretical peak positions as a function of trial structure for one-fold, two-fold and "four-fold" coordinated adsorption onto the reconstructed surface.

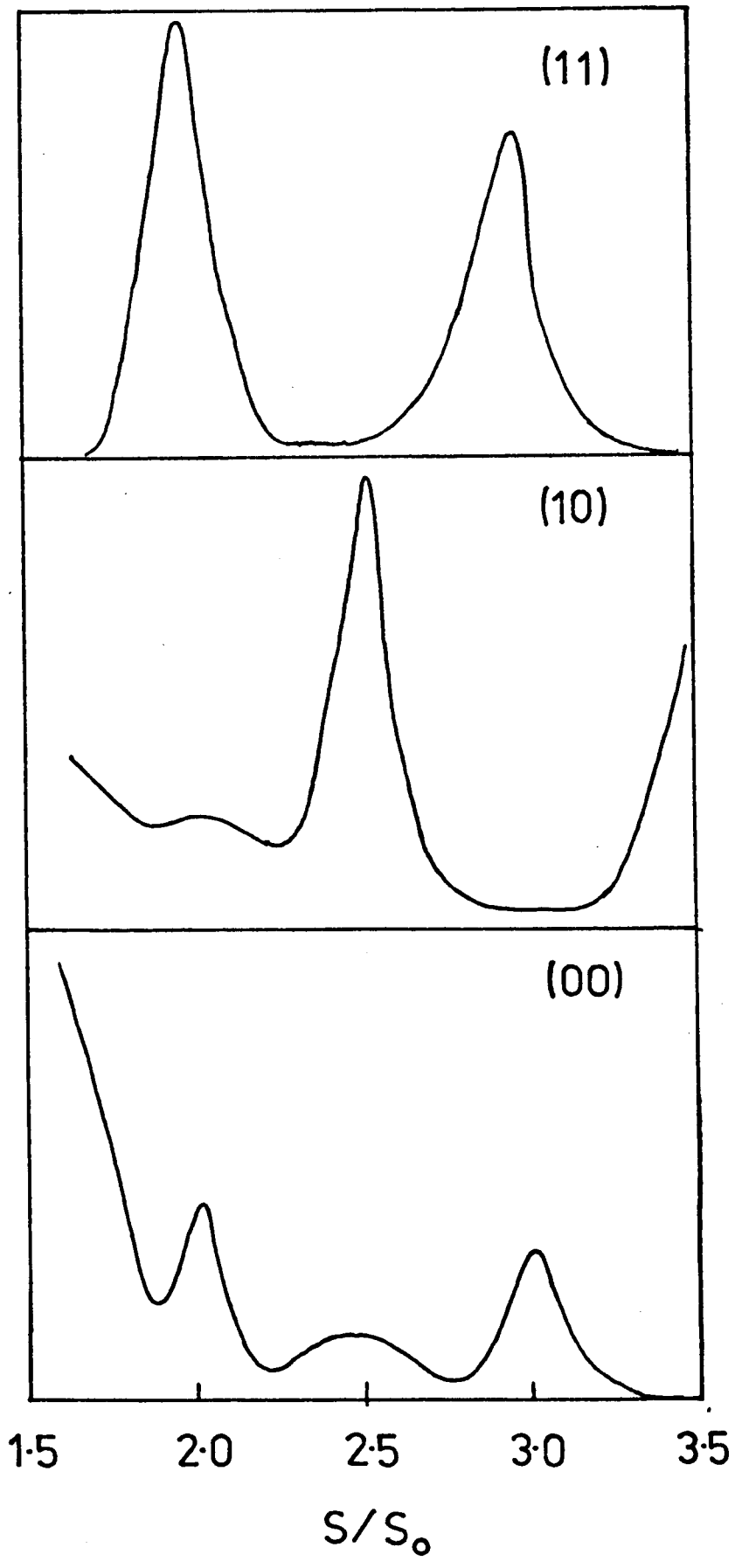

Figure 6.25 Theoretical averaged spectra for AlR structure with a spacing of the oxygen layer of 2.1 to 2.2 Å above the top substrate layer.

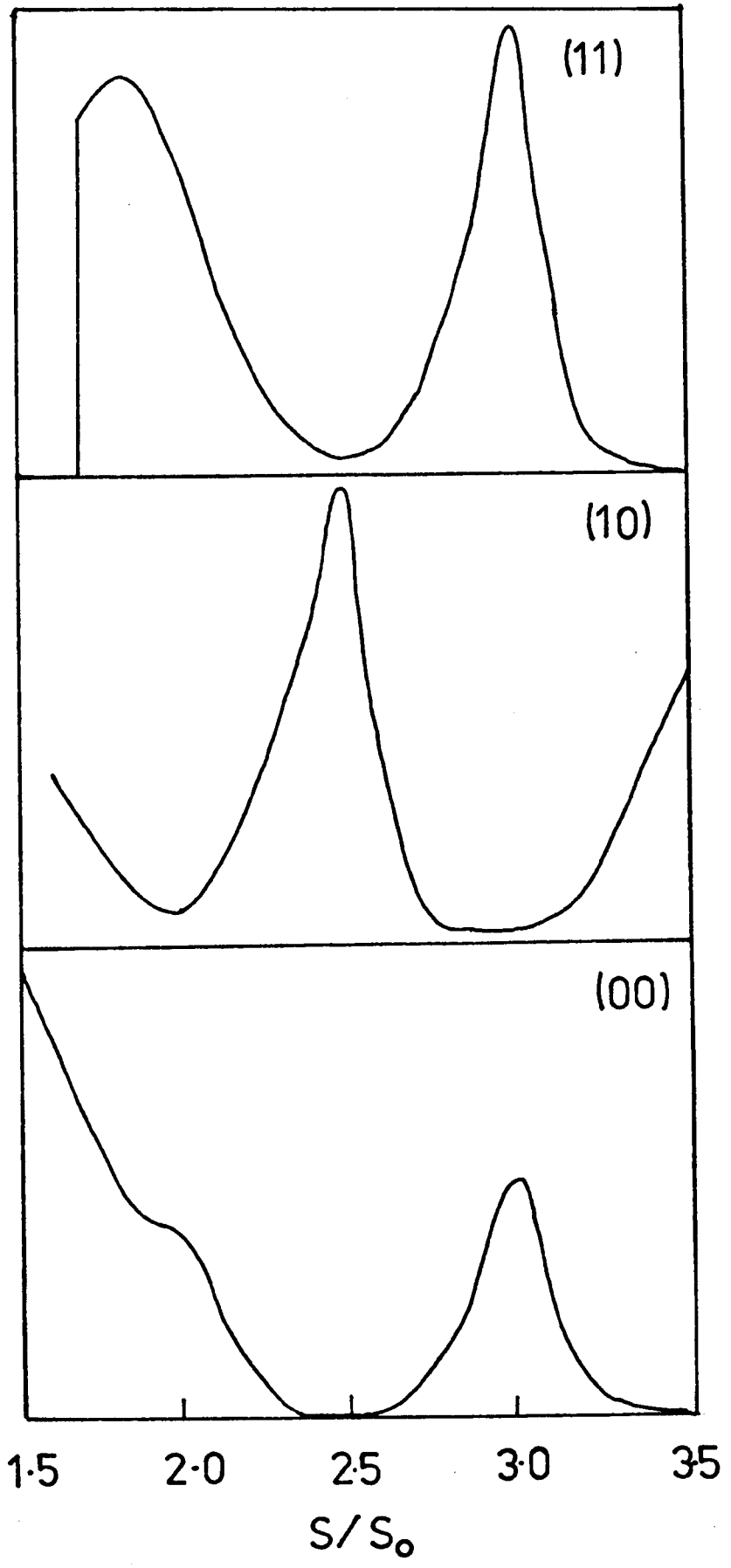

Figure 6.26 Theoretical averaged spectra for A4R structure with a spacing of the oxygen layer of 1.1 Å above the top substrate layer.

to support or indeed to counter this conclusion; as an extra feature due to multiple scattering exists in the clean surface experimental spectrum for the (00) beam it can not be determined whether the existence of an extra feature in the experimental adsorbate spectra at the same position is indicative of multiple scattering, structural changes or indeed a combination of the two effects. We conclude therefore that a structure consisting of a quarter monolayer of oxygen located between 2.1 and 2.2 Å above a reconstructed layer with the oxygen atoms positioned directly above the copper atoms is the optimum solution of this analysis. Examination of the effect of varying the vertical spacing of the reconstructed layer used as the substrate for this particular solution yielded an optimum spacing of 1.0 to 1.05 times the normal substrate spacing. While increasing the oxygen coverage to three-quarter monolayer relative to the substrate did not seriously affect the peak positions peak shapes were altered severely relative to the results for quarter monolayer coverage.

6.3.5 Disordered Oxygen on Copper (111)

For disordered adsorption, structural analyses are limited to the (00) beam and the two features to be considered here are shown in table 6.6. The theoretical (00) beam spectra were computed by Woodruff[14] using a suitably modified version of Mitchell's computational scheme. Spectra were calculated for coverages of one, two and three monolayers of oxygen and for a range of physically plausible spacings normal to the surface. Also the average "thickness" of the oxygen layer (the model used is shown schematically in figure 6.27) at a particular mean vertical spacing could be altered. While the shape of the vertical distribution of oxygen atoms used here was rather artificial it was felt that more refined distributions were not justified within the structural resolution of this technique. The theoretical results are presented in the usual manner in figure 6.28 as a function of the mean vertical displacement of the oxygen layer, the

TABLE 6.6

Beam	Nominal Bragg Number	S/S_o Clean	S/S_o Adsorbate	Shift
(00)	2	1.94	1.98	+0.04
	3	2.91	3.00	+0.09

EXPERIMENTAL DATA USED IN THE CORRELATIONS WITH THEORY FOR THE DISORDERED OXYGEN COPPER (111) SURFACE

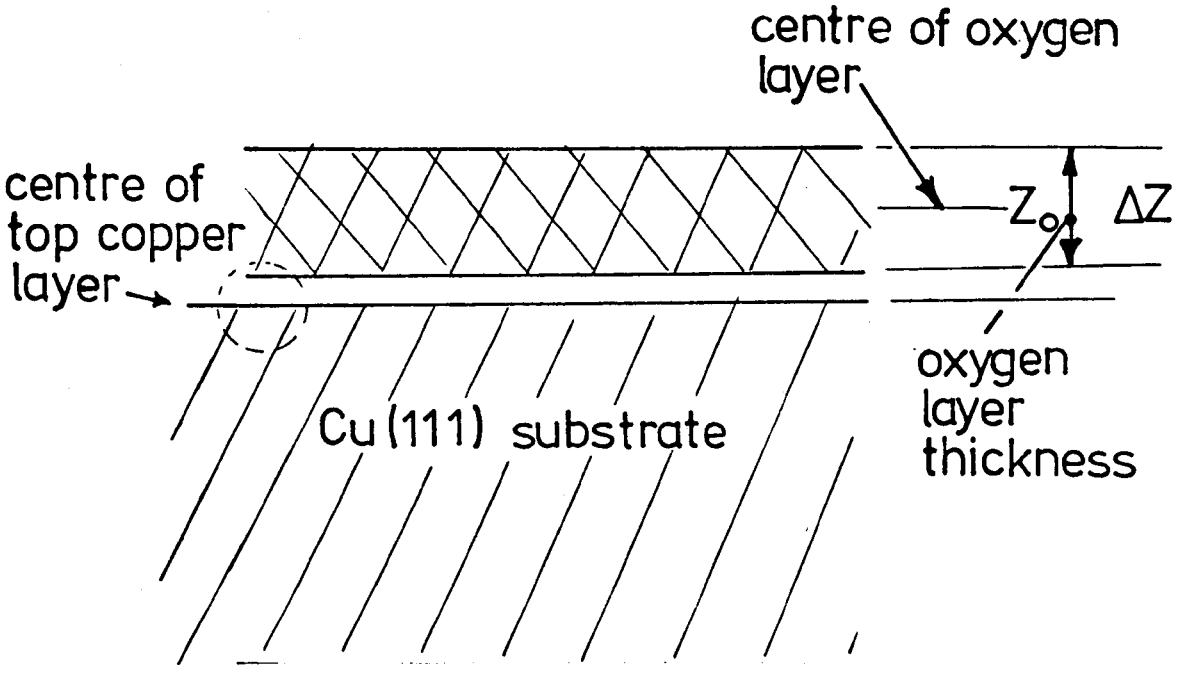

Figure 6.27 Schematic diagram of the theoretical model for the disordered adsorption of oxygen onto the copper (111) surface.

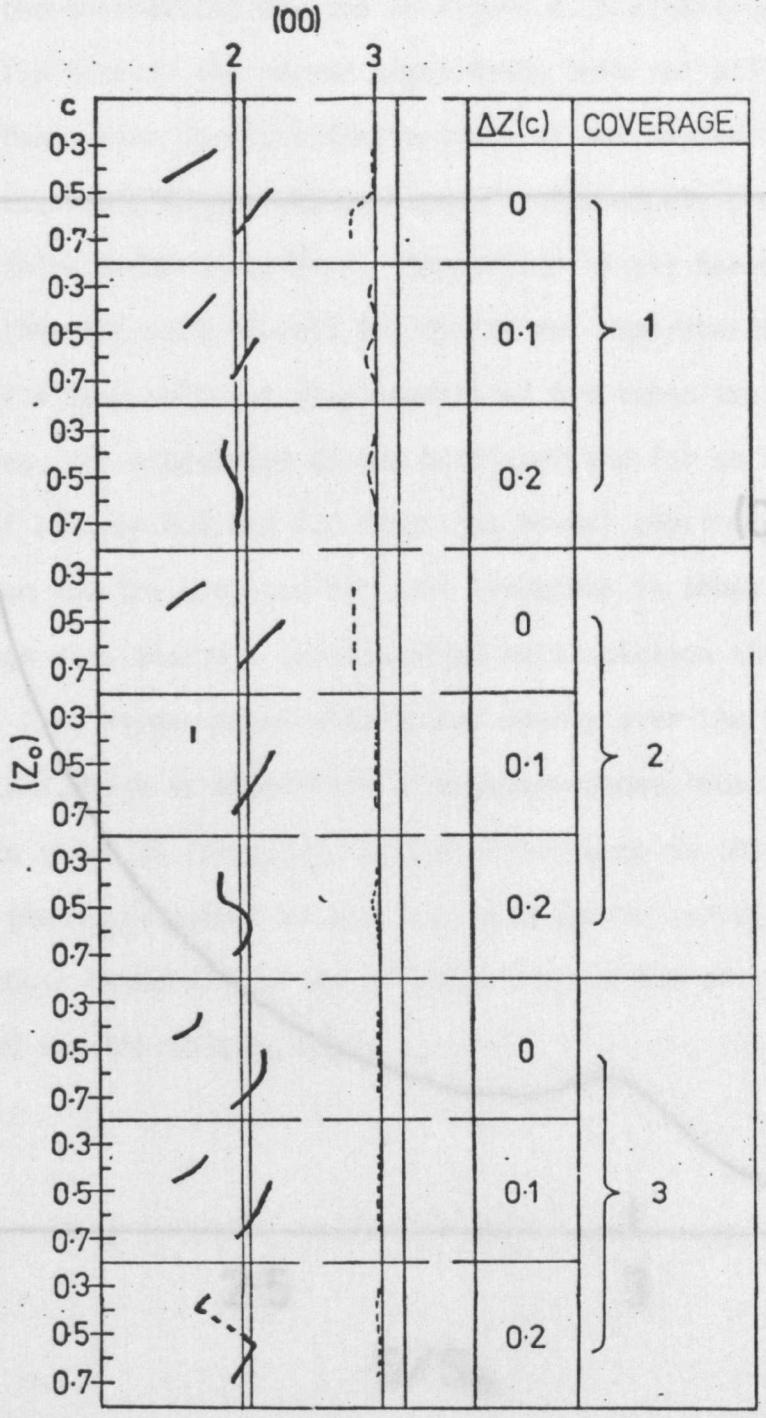

Figure 6.28. Theoretical peak positions as a function of trial structure for the disordered oxygen structures on the copper (111) surface.

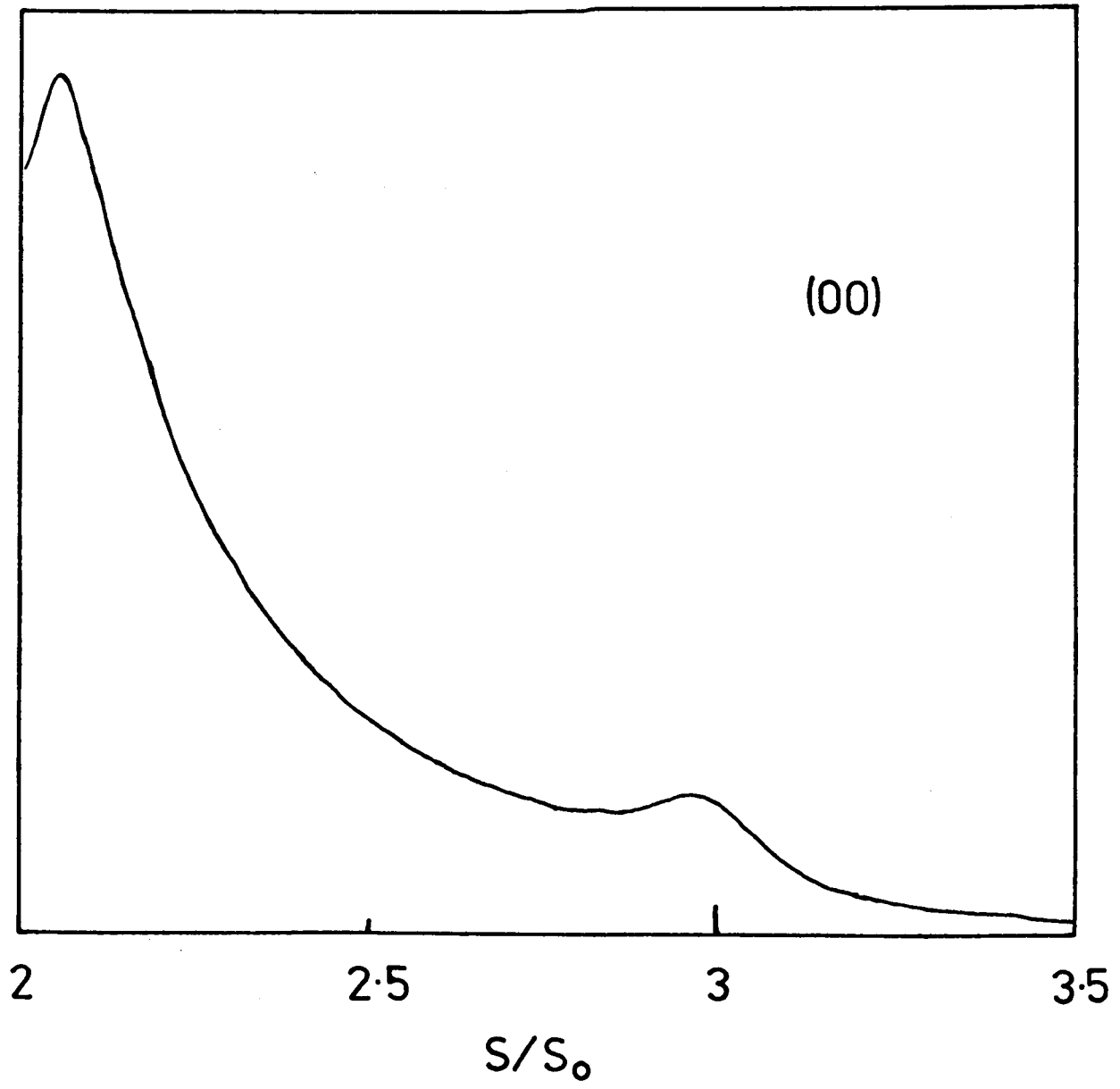

Figure 6.29 Theoretical (00) beam averaged spectra for one monolayer of disordered oxygen located at a mean vertical displacement of 0.6 times the normal substrate spacing and a mean thickness of 0.1 times the normal substrate spacing.

coverage and also the average thickness of the oxygen layer.

While the theoretical spectra in figure 6.28 clearly converge quite satisfactorily towards the second order Bragg peak for all the model structures for a mean vertical displacement of the oxygen layer of 0.6 times the normal substrate layer spacing none of these models provides as good a fit to the third order Bragg peak. Comparison of all the curves in figure 6.28 shows that the best overall fit to the two experimental peaks is obtained for a mean vertical displacement of 0.6 times the normal substrate layer spacing, for a coverage of one monolayer and for an average layer thickness of between 0.1 and 0.2 times the normal substrate layer spacing. The (00) beam spectra computed for this structure is shown in figure 6.29.

Although this analysis has converged on a solution that is physically reasonable, i.e. oxygen atoms distributed evenly over the vertical range, 1.0 Å to 1.4 Å,which is compatible with oxygen atoms located in three-fold coordination sites on the (111) surface, confidence in this solution is limited by the small number of features used in the correlation, the poor fit to one of those features and the relative suppression of its intensity in the averaged spectra (figure 6.29).

6.4 Discussion

In the structural correlations presented here only those features of the data which should be primarily associated with structural changes have been considered; i.e. peak shifts and to a secondary extent the weaker extra features that occur. Confidence in any structural solution will depend on the accuracy with which experimental averages can be performed and the sensitivity of the experimental spectra to parameters, such as the inner potential, which we have assumed to remain constant between the clean and the adsorbate experimental averages. The intrinsic accuracy of the averaging technique is demonstrated in figure 6.30 where independently derived intensity-energy spectra for the (11) beam from clean copper (100) were averaged and found to agree to within 0.005 for the peaks at Bragg numbers 2, 3 and 4. The variation in relative intensities between the two curves was due to the operation of the electron gun at different focussing conditions for the two sets of data. The effect of varying the inner potential was examined when the non-specular beam averages were computed: it was found that the value of inner potential used did not critically affect the widths of the peaks and the shifts induced were such that providing that the same inner potential was used for both the clean and adsorbate averages relative peak shifts were not affected. Measurements of the work function change associated with oxygen adsorption on copper (100) by Delchar[15] showed a change of less than 0.4 eV which would produce a change in S/S_o of less than 0.005 within the range considered and consequently is of no importance in these correlations.

The fundamental concept of the averaging scheme for structural determination assumes that the location of features in individual intensity-energy spectra is determined solely by the structure of the surface and the scheme extracts those features having a kinematical dependence on the angle of incidence. While this is a reasonable assumption when the atomic scattering factors are real the atomic scattering factors in LEED are complex. Thus the phase relationship between scattering from different atoms in LEED is determined not only by the position of the atom but also by their scattering factors.

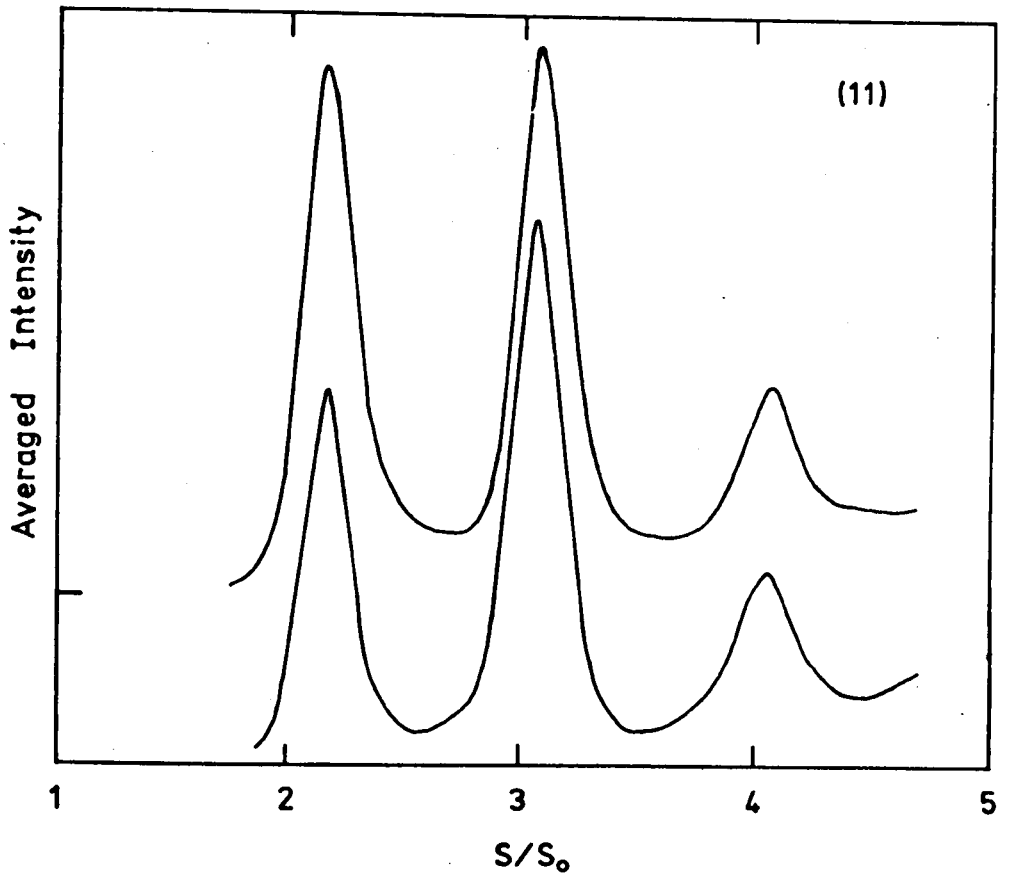

Figure 6.30 Two independent averages performed over identical ranges of scattering geometry for the (11) beam from clean copper (100) surfaces.

The scattering factors are functions of scattering angle and hence angle of incidence and consequently, on averaging, features in individual spectra which are attributable to adsorbate and substrate scattering interference will not add as expected. The extent of this problem will of course depend on the particular atomic scattering factors involved. Although the method adopted here,of averaging theoretical spectra over an identical range in scattering geometry to that of the experiment,will ensure that the proper comparison is made there is a danger that this effect will greatly reduce the sensitivity of this technique.

The application of this techique is complicated further by the existence of multiple scattering effects in the experimental averages. This is particularly so for the copper (100) surface and consequently it is a cause for concern that unidentified multiple scattering features in adsorbate averages may be inadvertently associated with structural changes. However, by comparing data from both clean and adsorbate surfaces it is possible to anticipate those regions in which spurious effects might occur.

Although difficulties of this nature must limit the potential of this averaging scheme for determining surface structures the three analyses presented here have all indicated plausible structural solutions. However, this may be entirely fortuitous and it remains to be seen whether dynamical theory calculations will confirm these results.

*****

REFERENCES

(1) M.G.Lagally,T.C.Ngoc & M.B.Webb, *Phys.Rev.Lett.* 26 (1971) 1557.

(2) M.G.Lagally,T.C.Ngoc & M.B.Webb, *J.Vac.Sci.Tech.* 9 (1972) 645.

(3) C.W.Tucker,Jr. & C.B.Duke, *Surface Sci.* 23 (1970) 411;29 (1972) 237.

(4) D.T.Quinto & W.D.Robertson, *Surface Sci.* 34 (1973) 501.

(5) J.B.Pendry, *J.Phys.C.* 5 (1972) 2567.

(6) K.A.R.Mitchell, University of British Columbia, private communication.

(7) R.S.Zimmer, University of Warwick, private communication.

(8) J.B.Pendry, *J.Phys.C.* 4 (1971) 2514.

(9) J.B.Pendry, *J.Phys.C.* 2 (1969) 2283.

(10) F.Forstman,European Physical Society Meeting on Metal Surfaces, Hindas, Sweden, August (1973).

(11) S.Andersson,B.Kasemo,J.B.Pendry & M.A.Van Hove, *Phys.Rev.Lett.* 31 (1973) 595.

(12) "Tables of Interatomic Distances and Configurations in Molecules and Ions", Chemical Society, London, Special Publication No.11, (1958).

(13) A.F.Wells, "Structural Inorganic Chemistry", Oxford University Press (1962)

(14) D.P.Woodruff, University of Warwick, private communication.

(15) T.A.Delchar, *Surface Sci.* 27 (1971) 11.

CHAPTER SEVEN. ANGULAR DEPENDENCE OF AUGER ELECTRON EMISSION FROM COPPER SURFACES

Although Auger electron spectroscopy is now widely used in surface studies, it has yet to be established as a truly quantitative technique. While specific calibration experiments have enabled quantitative assessments to be made with a high degree of accuracy, these measurements are based on the net Auger emission emanating from within the mean electron escape depth. Consequently, the further refinement of quantification requires both a knowledge of the in-depth distribution of the emitting element(s) and of the relative importance of emission from different layers within the escape depth. Allowances will also have to be made for any angular dependence that may exist in the emission of the Auger electrons. Although consideration of the latter effect will not be so essential for analysers employing large collection angles or for samples which are sufficiently polycrystalline within the detected volume, the present trends towards analysers with reduced collection angles (e.g. the cylindrical mirror analyser compared to the LEED optics) and smaller electron beam probes will accentuate this effect.

Harris[1] has studied the angular dependence of Auger electron emission from a polycrystalline molybdenum surface, contaminated with sulphur and carbon, and interpreted his results as distinguishing between true surface and more bulk emitting atoms. Such an experiment averages out all crystallographic effects and also any effects associated with an inherent angular dependence of the emission at the ion. Harris's experiments were not extended to the single crystal surface and despite his promising demonstration of coarse in-depth resolution for the polycrystalline surface no further experiments of this type were reported.

In this chapter the results of a study of the angular dependence of Auger electron emission from clean and adsorbate covered (100) and (111) surfaces of copper are reported.

7.1 Experimental Technique

The electronic detection scheme used to perform AES with the Faraday cup is identical to that used in conjunction with the LEED optics (section 3.3.3) and is shown schematically in figure 7.1. Profiles of the angular dependence of Auger electron emission were obtained by manually stepping the Faraday cup at 2.5^{o} increments and then recording the $N'(E)$ spectra over the required energy range at each angular position. The peak to peak amplitudes of the Auger transitions were obtained from the $N'(E)$ spectra and taken to be a measure of the intensity of the Auger emission. Although all the Auger transitions studied here were superimposed on a positively sloping background (particularly steep for the 62 eV copper Auger transition), which has the effect of modifying the true height of the differentiated feature, the slope was found to remain constant over the complete range of emission angles studied and consequently no corrections were made for this effect.

The first reported observation of an anisotropy in the angular emission of Auger electrons from a single crystal surface was made by the author for the 62 eV copper Auger emission from copper (111) using the prototype Faraday cup with a single retard grid in an arbitrary azimuth (figure 7.2). Although an extremely poor signal to noise ratio existed for these particular measurements it is clear from the figure that an anisotropy exists. Much improved signal to noise ratios were obtained with the modified Faraday cup which incorporated two retard grids and all the results presented in the following sections were obtained using it. Angular profiles were obtained using both the LEG2 and the SE3K/5U electron guns for which different experimental procedures were employed.

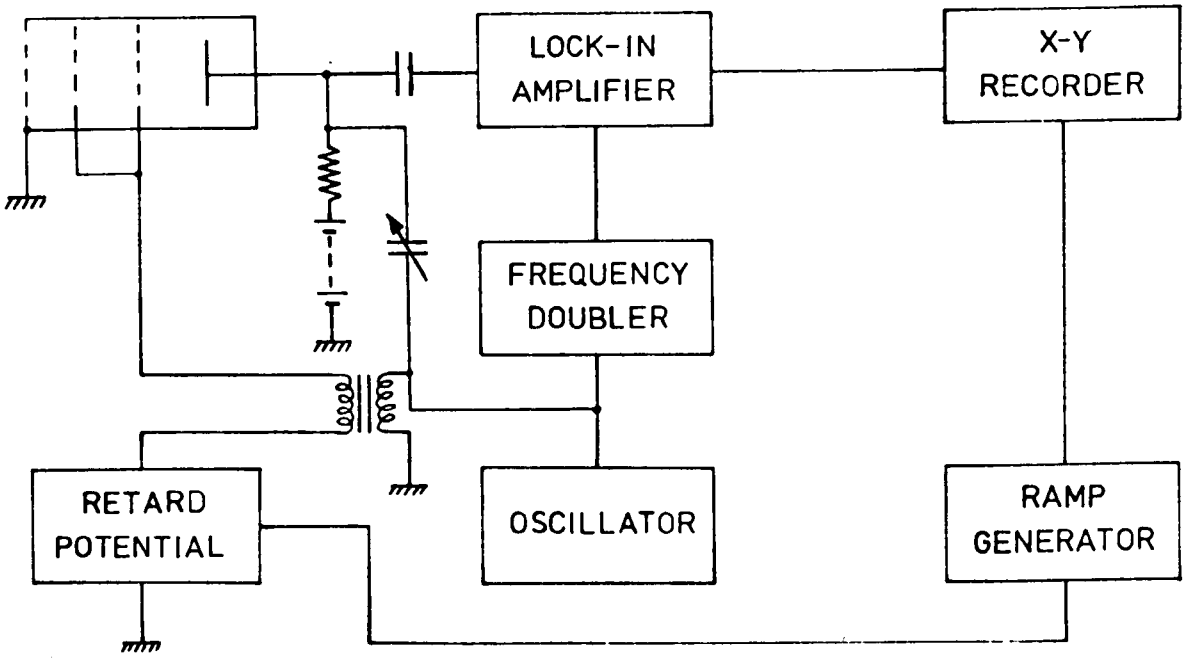

Figure 7.1 Schematic diagram of the electronic detection scheme used to perform AES with the Faraday cup.

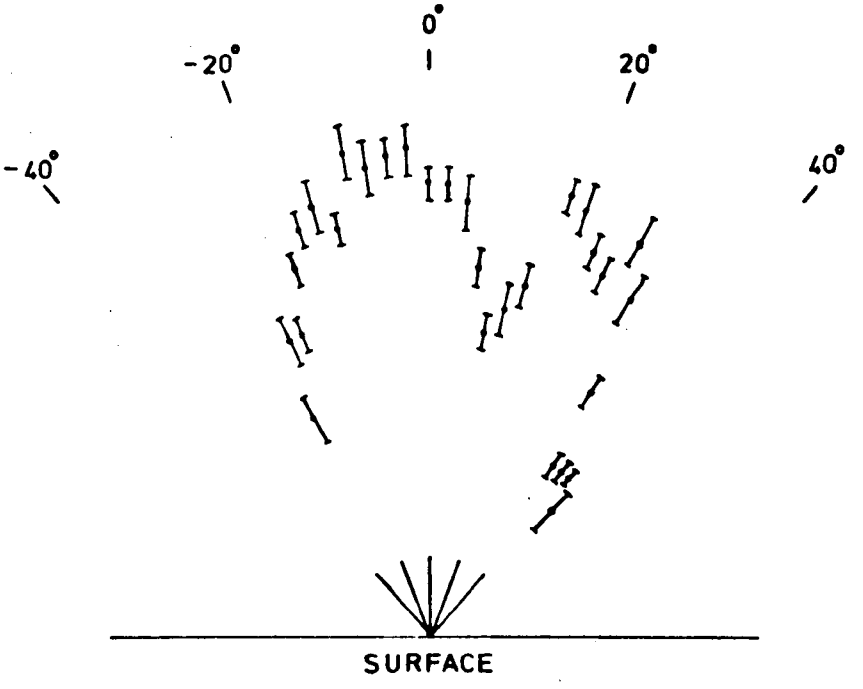

Figure 7.2 The intensity of the 62 eV copper Auger emission from the clean copper (111) surface as a function of collection angle for an azimuth of $\phi = 4^{o}$ using the single retard grid Faraday cup.

7.1.1 Measurements using the LEG2 Electron Gun

The preliminary investigation of the angular dependence of Auger electron emission was performed, in the absence of an electron gun with a higher beam current, using the LEG2 electron gun incorporated in the LEED optics. Although primarily a LEED electron gun, the LEG2 could be used at primary electron energies of 1.5 KeV where the spot diameter was of the order of 1 mm at the specimen although its low beam current (of the order of 3 uA) is a severe limitation to its use in AES.

The experimental geometry used to acquire the angular profile is shown in figure 7.3 where the angle of incidence of the exciting electron beam θ and the Faraday cup collection angle Ψ are defined with respect to the external surface normal $\underline{n}$. The intrusion of the drift tube (A4) of the LEG2 into the collection circle of the Faraday cup was considerably disadvantageous as a 28^{o} sector was lost from each angular profile. Fortunately as will be shown in section 7.3.1 the profiles proved invariant to the angle of incidence of the electron beam, thereby enabling the missing sector of any profile to be recovered simply by repeating the particular profile for a suitably different value of θ.

The major experimental difficulty encountered was the definition of the position of the external surface normal in terms of the position of the Faraday cup. A satisfactory scheme was adopted for this as follows:

(a) The LEED display was used to check the inter-alignment of the rotary drive axes of the specimen manipulator and the Faraday cup (section 3.4.1), to establish the crystal azimuth ϕ and to determine normal incidence (section 3.4.2).

(b) Following a rotation of the specimen by Ω^{o} with respect to the position for normal incidence, the specular beam was located using the Faraday cup. The Faraday cup was then known to be Ω^{o} from the surface normal.

While reliable angular profiles could be obtained using the LEG2 electron gun, for example all the results presented in sections 7.3.1 and 7.3.2 were

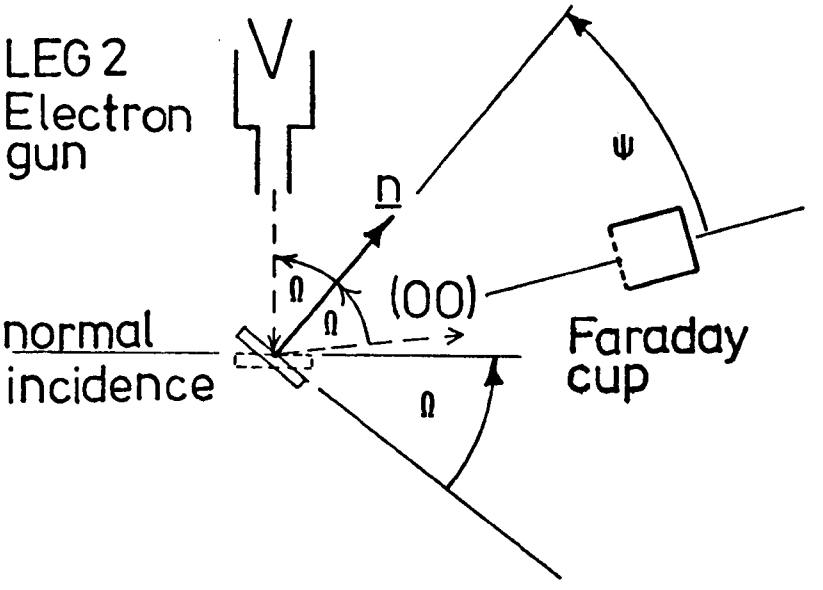

Figure 7.3 The experimental geometry used to acquire angular profiles using the LEG2 electron gun.

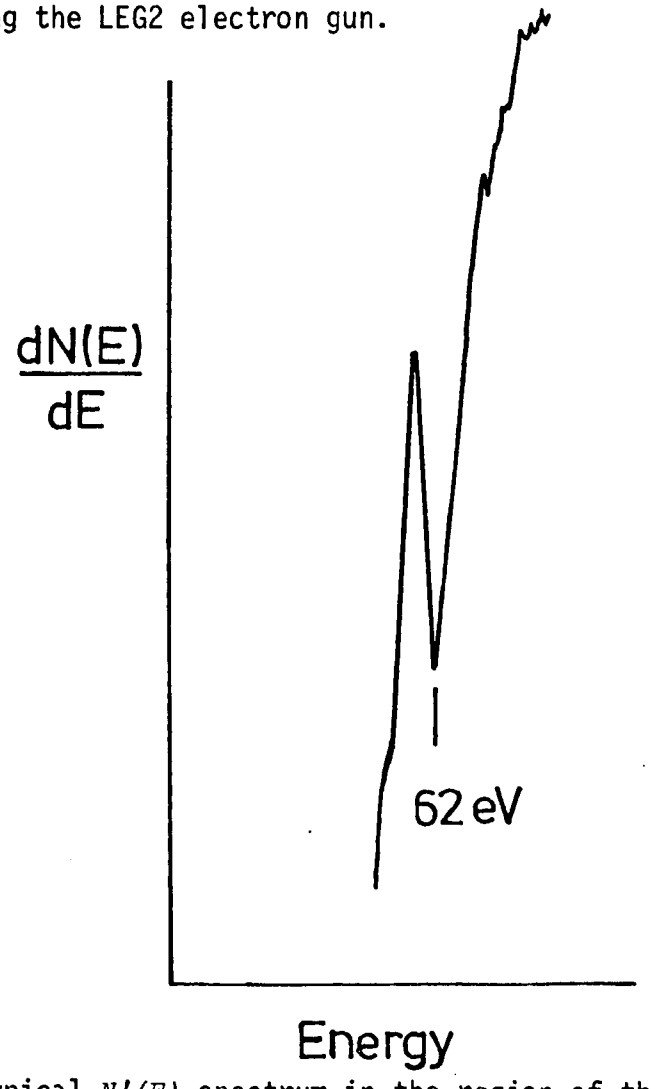

Figure 7.4 A typical $N'(E)$ spectrum in the region of the 62 eV copper Auger peak obtained with the LEG2 electron gun.

acquired using this gun, the low incident electron beam available restricted the measurements to the most intense $M_{2,3}M_{4,5}M_{4,5}$ Auger transition from copper ocurring at 62 eV (actually an unresolved doublet). Indeed, even for this transition the signal to noise ratios were such that the results of several profiles had to be averaged together to yield acceptable error bars; usually an average of three profiles was sufficient for this purpose. A typical $N'(E)$ spectrum in the vicinity of the 62 eV copper Auger emission is shown in figure 7.4 where the noise levels present can be readily appreciated at higher energies away from the differentiated peak; the very steep slope in the region of the 62 eV peak is deceptive in appearing to smooth out the noise.

7.1.2 Measurements using the SE3K/5U Electron Gun

The SE3K/5U electron gun delivered a beam current of up to 60 uA at 1.5 KeV with a beam diameter at the specimen of less than 0.5 mm. The greatly improved signal to noise ratio obtained with this gun can be seen in figure 7.5 where the $N'(E)$ spectrum from a sulphur contaminated copper (100) surface is shown together with the equivalent spectrum obtained with the three grid LEED optics. In addition to the 62 eV copper Auger peak, the 109 eV copper Auger peak and the 150 eV sulphur Auger peak can clearly be seen using a primary beam current of 35 uA.

The experimental geometry used to acquire the angular profile with this electron gun is shown in figure 7.6. With this gun there is no physical obstruction of the movement of the Faraday cup and the sector lost from any profile is only determined by the physical cut off of the electron beam by the Faraday cup which amounts to about 10^{o}. The scheme adopted for defining the angle of incidence of the primary beam and also the surface normal is as follows:

(a) The LEED display was used to check the inter-alignment of the rotary drives, to establish the crystal azimuth and to determine normal incidence.

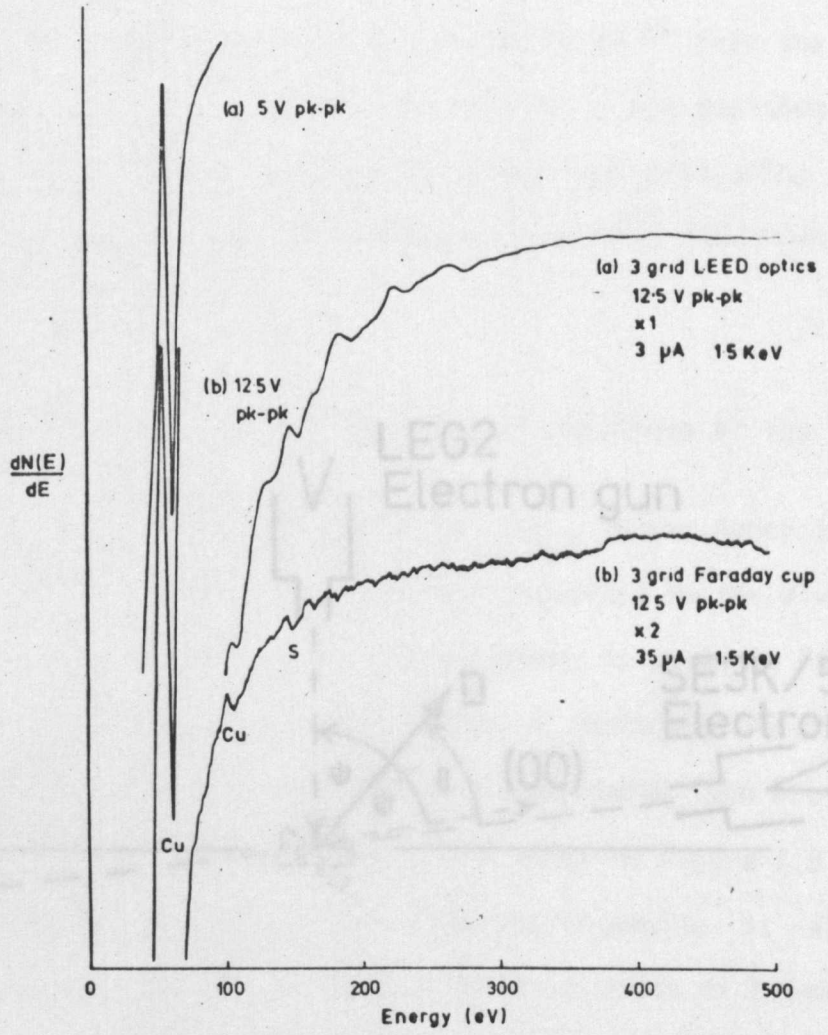

Figure 7.5 A comparison of $N'(E)$ spectra obtained from the identical sulphur contaminated copper (100) surface using (a) the LEED optics and integral LEG2 electron gun and (b) the double retard grid Faraday cup and SE3K/5U electron gun.

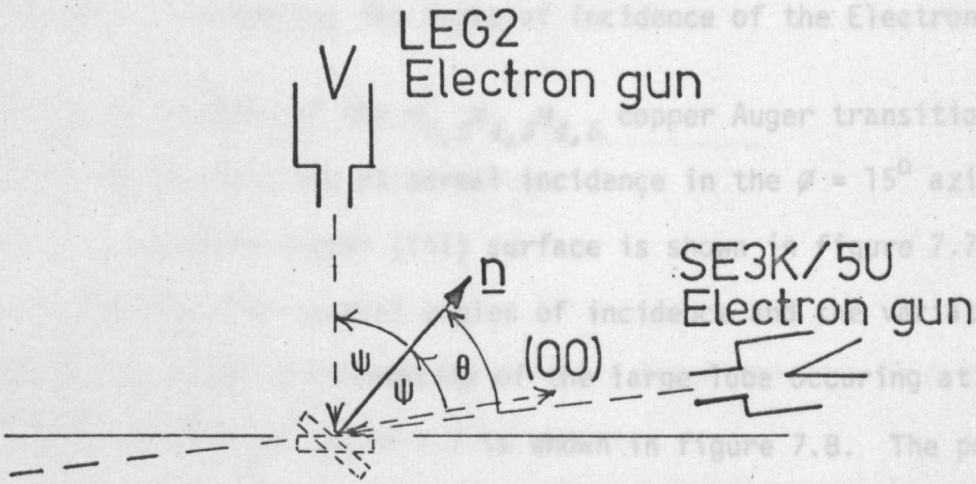

Figure 7.6 The experimental geometry used to acquire angular profiles using the SE3K/5U electron gun.

(b) Following a rotation of the specimen by Ψ^{o} with respect to the position for normal incidence, the specular beam was located with the Faraday cup. The Faraday cup was then known to be Ψ^{o} from the surface normal.

(c) After translating the specimen vertically the position of the incident beam from the SE3K/5U electron gun was measured using the Faraday cup from which the angle of incidence θ was then determined.

7.2 Experimental Results

7.2.1 The Effect of Varying the Angle of Incidence of the Electron Beam

The angular profile of the $M_{2,3}M_{4,5}M_{4,5}$ copper Auger transition that occurs at 62 eV was obtained at normal incidence in the $\phi = 15^{o}$ azimuth from the clean, ordered copper (111) surface is shown in figure 7.7. This profile was repeated for several angles of incidence and the variation with θ of both the position and intensity of the large lobe occuring at 33^{o} in the angular profile of figure 7.7 is shown in figure 7.8. The position of this lobe is invariant with θ while the intensity is approximately proportional to secθ in agreement with the results of Palmberg.[2] The independence of peak position with θ enabled the missing sector of each angular profile to be recovered from a profile obtained at a different θ. In the following section the profiles presented have been prepared in this manner; the normal incidence profile is shown using open circles while the section of glancing incidence profile that has been superimposed is marked in full circles. In each case the glancing incidence profile was normalised using the secθ relationship and found to agree with the overlapping normal incidence profile within the error limits displayed.

7.2.2 The Effect of Varying the Azimuthal Angle of Collection

Angular profiles of the 62 eV copper Auger transition from the clean, ordered copper (111) surface are shown in figures 7.9(a), (b), (c) and (d) for the azimuths $\phi = 0^{o}$, $\phi = 8^{o}$, $\phi = 13^{o}$ and $\phi = 30^{o}$ respectively. The basic

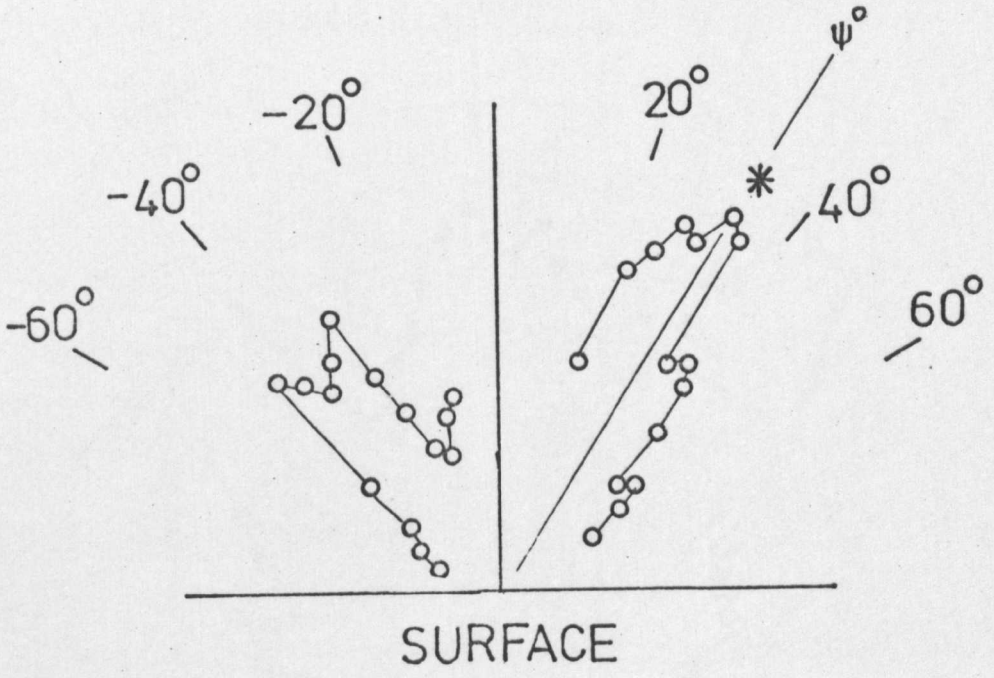

Figure 7.7 Angular profile of the 62 eV copper Auger emission from clean copper (111) in the $\phi = 15^{\circ}$ azimuth.

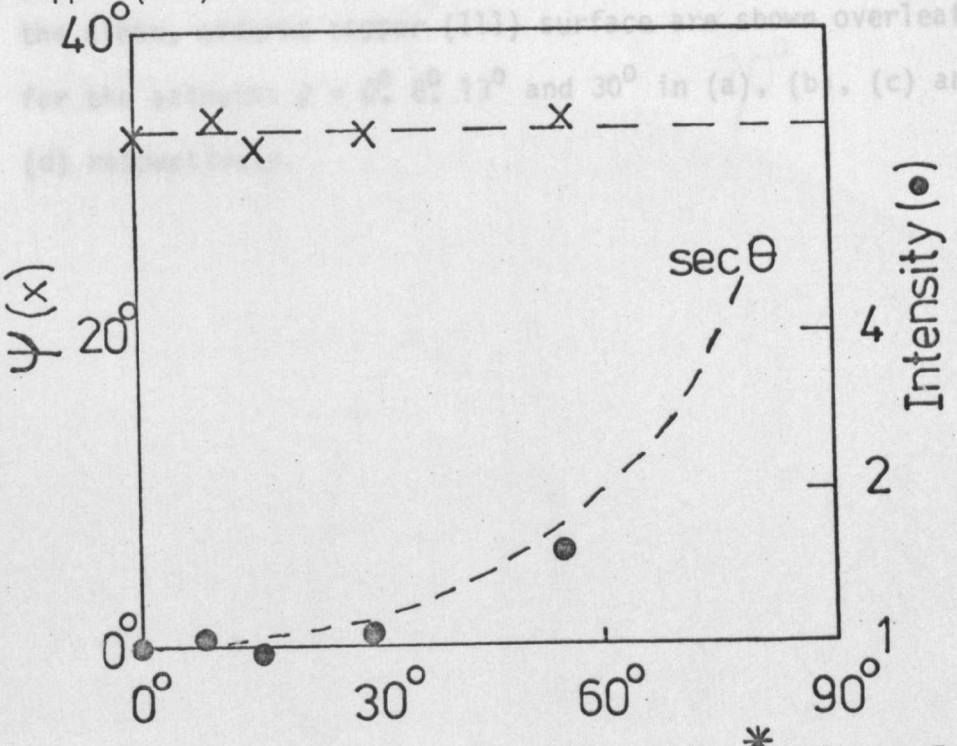

Figure 7.8 The position and intensity of the large lobe* in figure 7.7 are plotted as a function of the angle of incidence of the exciting electron beam.

Figure 7.9 The angular profiles of the 62 eV copper Auger emission from the clean, ordered copper (111) surface are shown overleaf for the azimuths ϕ = 0^{o}, 8^{o}, 13^{o} and 30^{o} in (a), (b), (c) and (d) respectively.

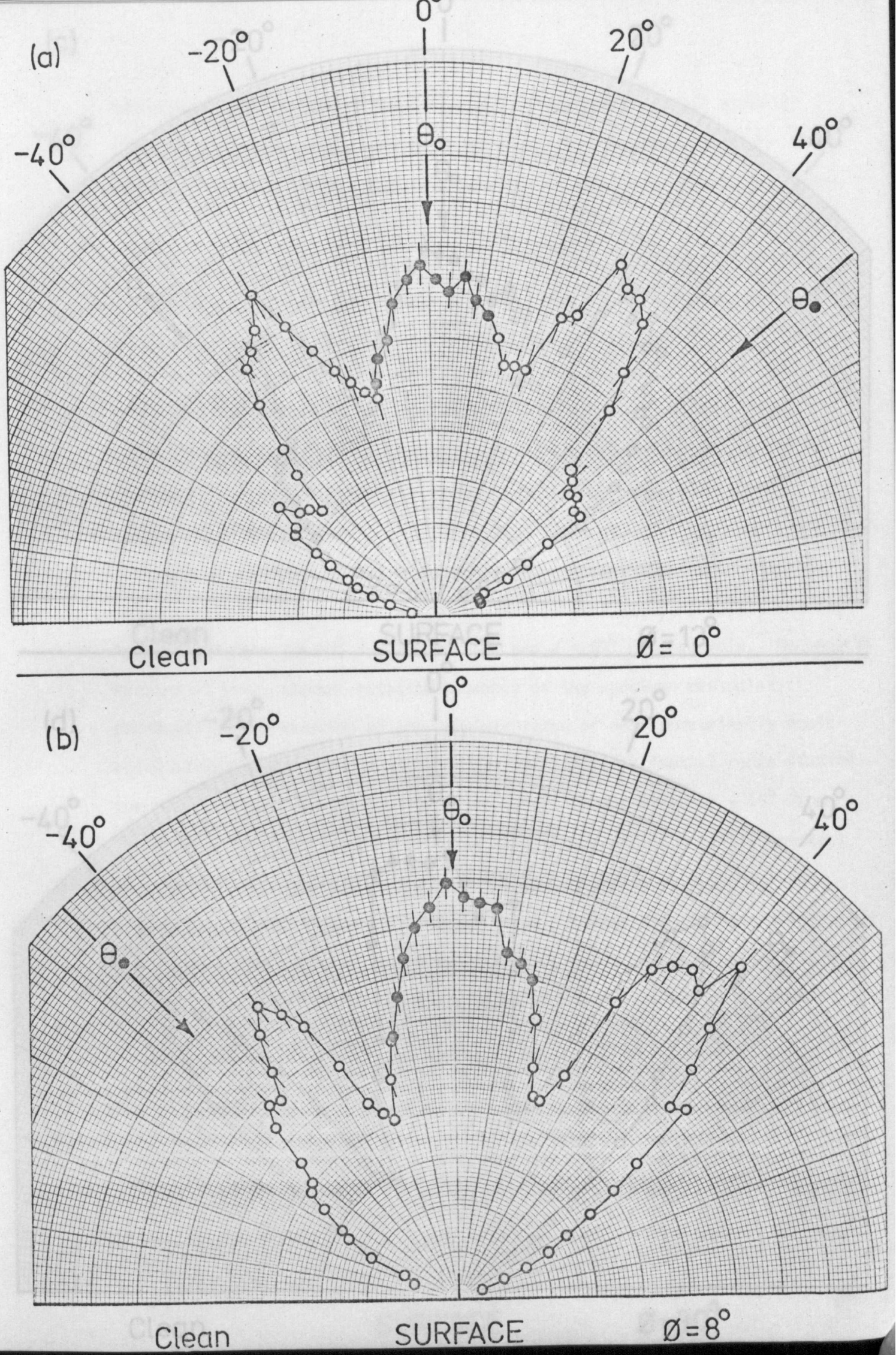
(a)
0°
-20°
20°
-40°
40°
θ₀
θ
Clean SURFACE Ø= 0°
(b)
0°
-20°
20°
-40°
40°
θ₀
θ
Clean SURFACE Ø=8°

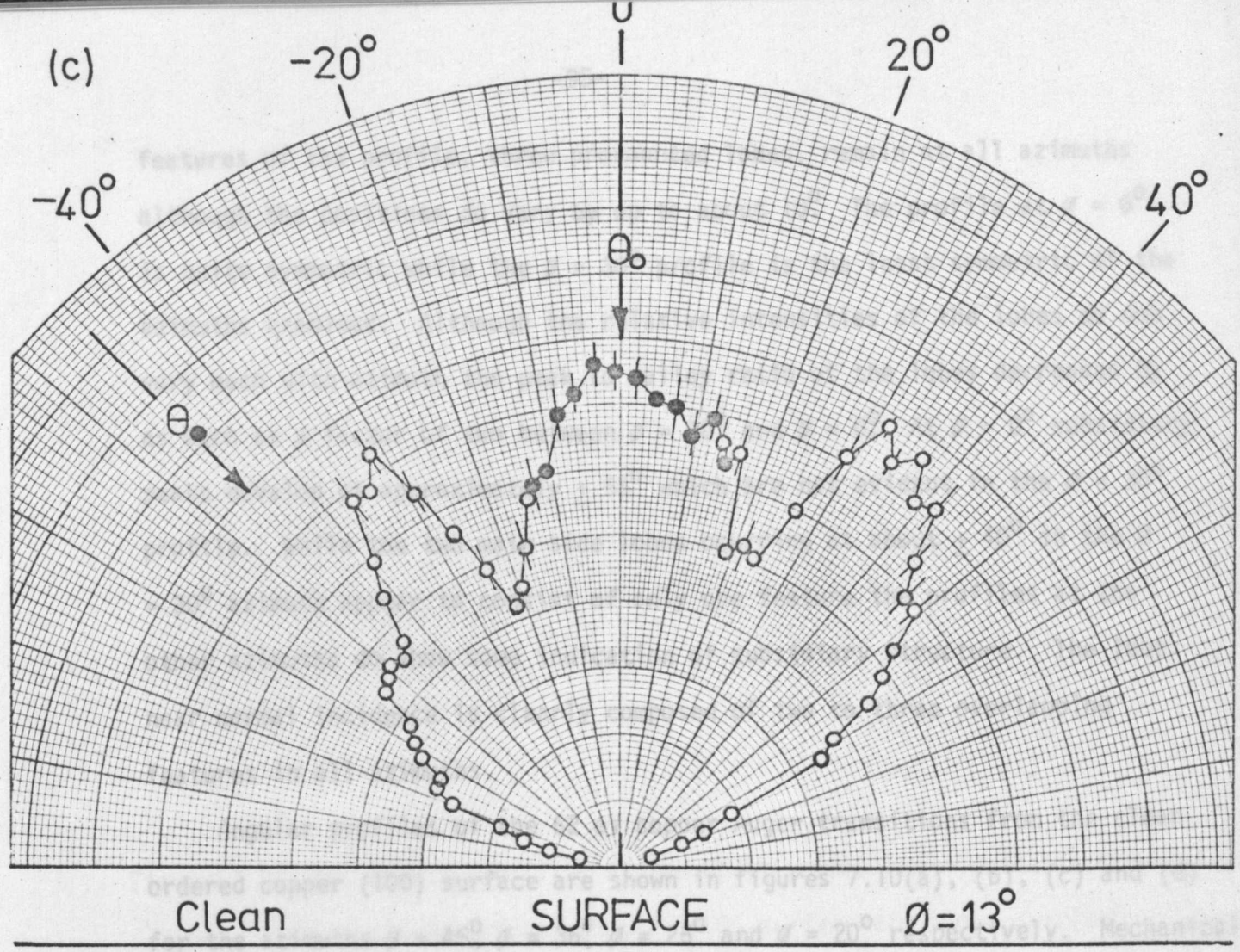
(c)
0°
-20°
20°
-40°
40°
θ₀
θ
Clean SURFACE Ø=13°

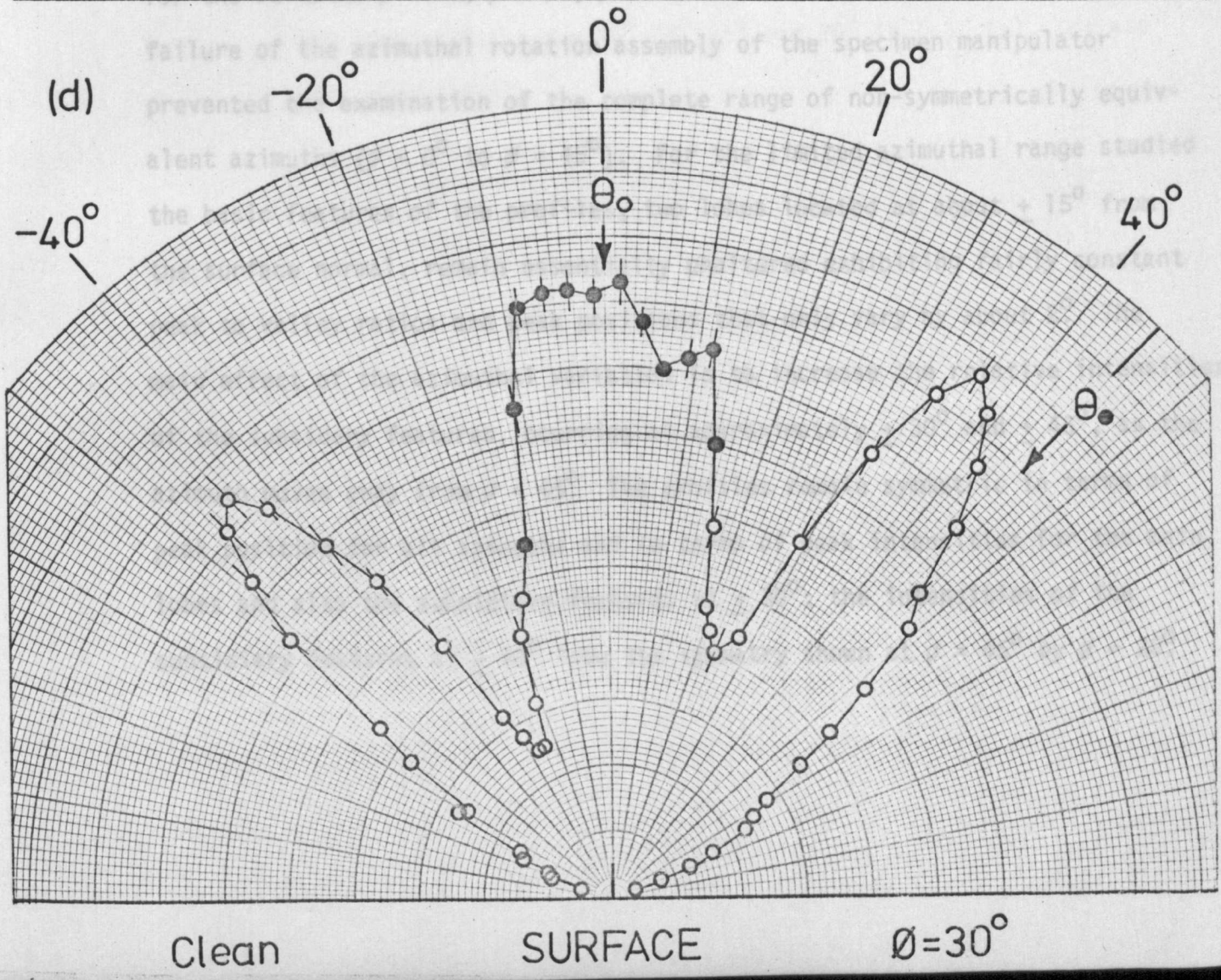
(d)
0°
-20°
20°
-40°
40°
θ₀
θ
Clean SURFACE Ø=30°

features of the profile, three pronounced lobes, remain at all azimuths although the positions do vary by up to about 10^{o}. The profile at $\phi = 0^{o}$ is quite symmetric while the $\phi = 30^{o}$ profile is the least symmetric of the azimuths examined. Although the relative intensities of the lobes do not vary much with azimuth the peak to valley ratio of the lobes decreases by as much as a factor of two between $\phi = 30^{o}$ and $\phi = 0^{o}$. At $\phi = 0^{o}$ subsidiary peaks develop at approximately $\pm 55^{o}$ which are not evident in the $\phi = 30^{o}$ profile. While the two main side lobes ocurring at about $\pm 40^{o}$ in the $\phi = 30^{o}$ azimuth appear to consist of only one feature the profiles at the other azimuths do show some indication of subsidiary structure. The lobe near normal incidence is clearly composed of two to three overlapping features in all azimuths.

Angular profiles of the 62 eV copper Auger transitions from the clean ordered copper (100) surface are shown in figures 7.10(a), (b), (c) and (d) for the azimuths $\phi = 45^{o}$, $\phi = 36^{o}$, $\phi = 25^{o}$ and $\phi = 20^{o}$ respectively. Mechanical failure of the azimuthal rotation assembly of the specimen manipulator prevented the examination of the complete range of non-symmetrically equivalent azimuths ($\phi = 0^{o}$ to $\phi = 45^{o}$). For the limited azimuthal range studied the basic features of the profiles, two lobes located at about $\pm 15^{o}$ from the surface normal, remain essentially unaltered exhibiting fairly constant peak to valley ratios and peak positions that only vary by about 2^{o}. The main effect of the azimuthal variation is to increase the relative intensities of the subsidary features, ocurring at approximately $\pm 30^{o}$ and $\pm 45^{o}$, as the azimuth moves away from $\phi = 45^{o}$. The profiles remain symmetric in terms of peak position for all azimuths and in terms of peak intensities for the main lobes and also the subsidiary features at $\pm 30^{o}$; the intensities of the subsidiary features at $\pm 45^{o}$ lose the symmetry shown at $\phi = 45^{o}$ by $\phi = 20^{o}$.

Figure 7.10 The angular profiles of the 62 eV copper Auger emission from the clean, ordered copper (100) surface are shown overleaf for the azimuths ϕ = 45^{o}, 36^{o}, 25^{o} and 20^{o} in (a), (b), (c) and (d) respectively.

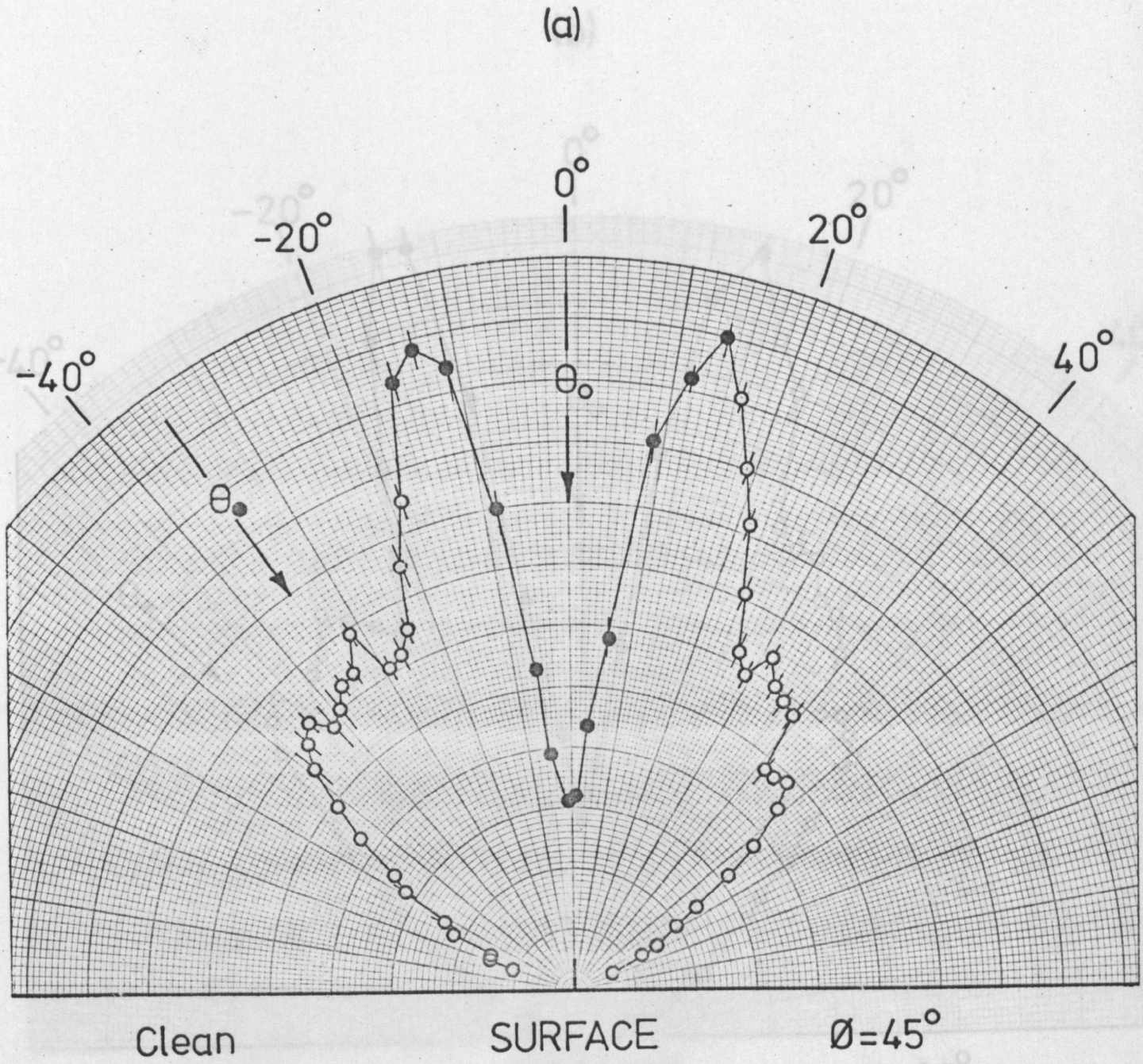
(a)
0°
-20°
20°
-40°
40°
θ
θo
Clean
SURFACE
Ø=45°

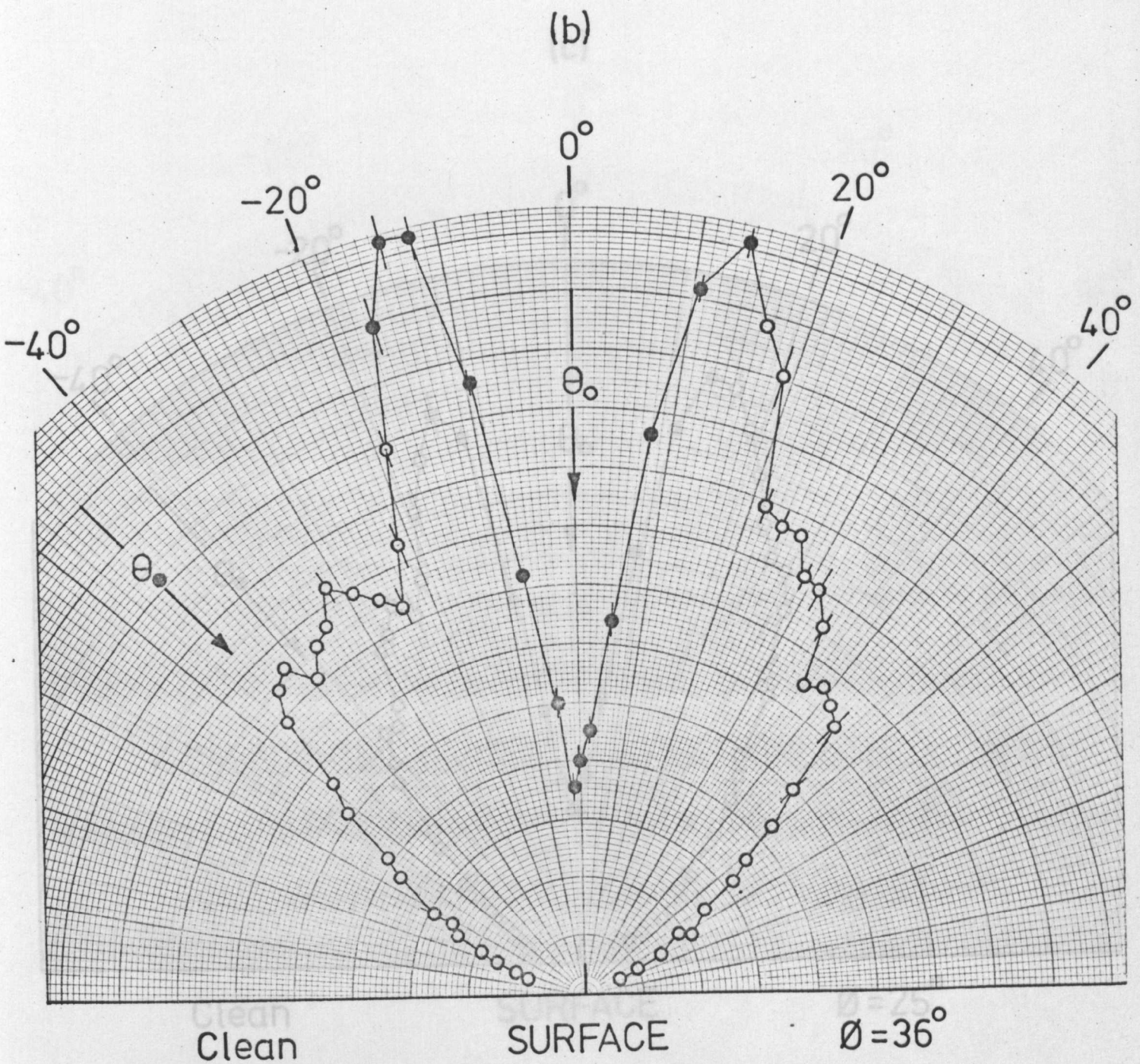
(b)
0°
-20°
20°
-40°
40°
θo
θ
Clean
SURFACE
Ø=36°

(c)

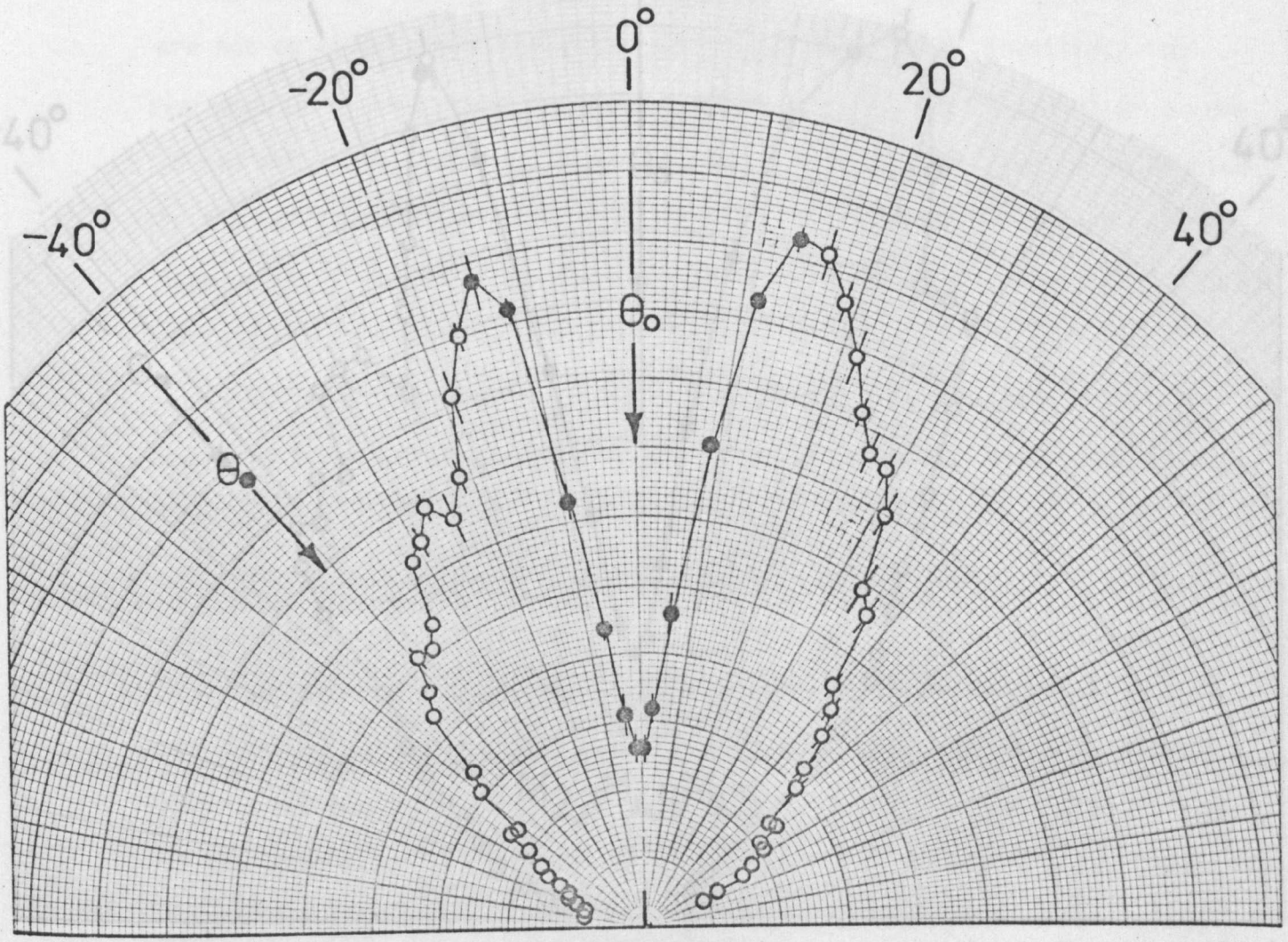

Clean SURFACE Ø = 25°

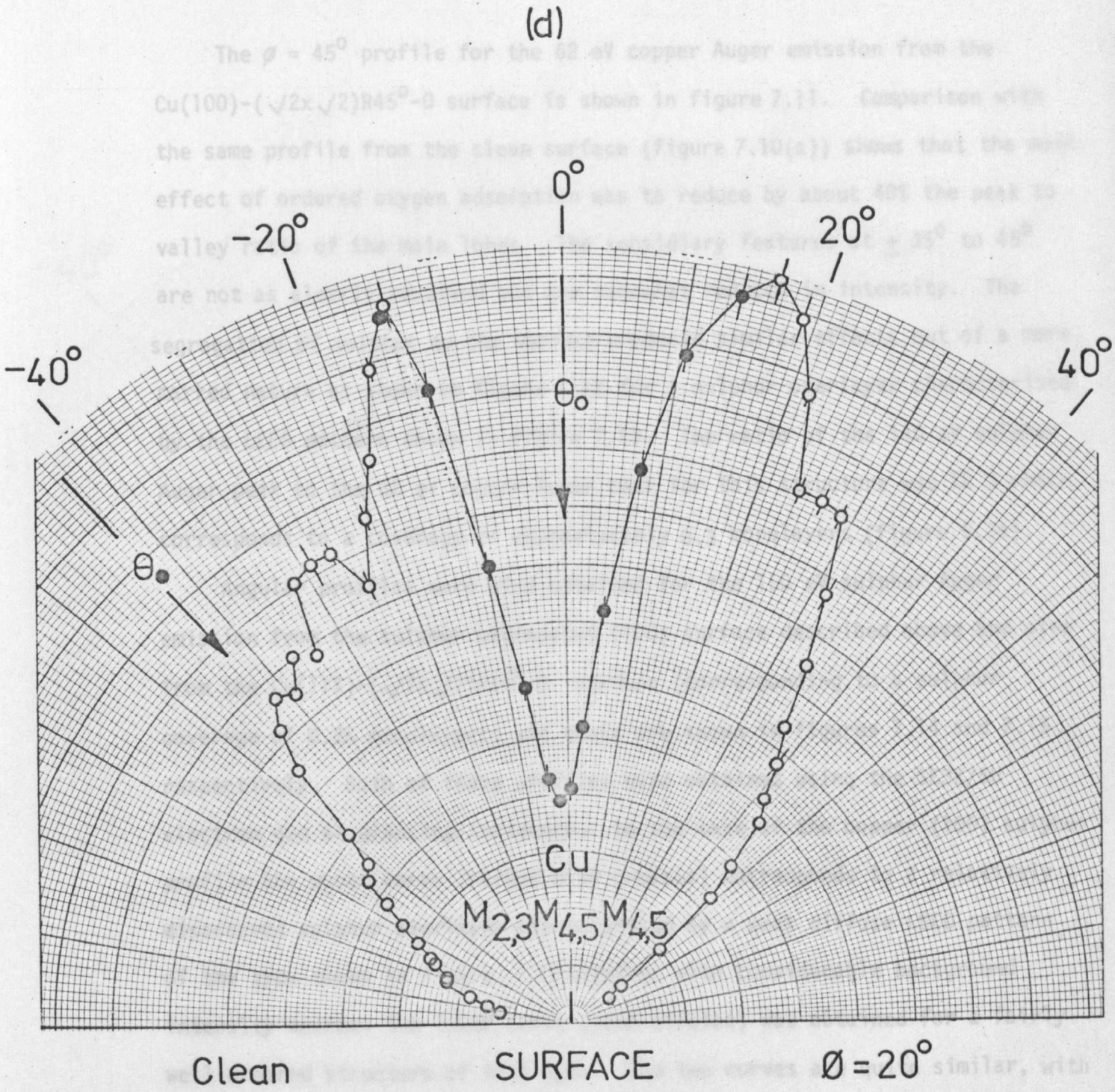
(d)
0°
-20°
20°
-40°
40°
θo
θ
Cu
M2,3M4,5M4,5
Clean
SURFACE
Ø = 20°

7.2.3 The Effect of Adsorption

The $\phi = 45^0$ profile for the 62 eV copper Auger emission from the Cu(100)-($\sqrt{2}x\sqrt{2}$)R45^0-O surface is shown in figure 7.11. Comparison with the same profile from the clean surface (figure 7.10(a)) shows that the main effect of ordered oxygen adsorption was to reduce by about 40% the peak to valley ratio of the main lobes. The subsidiary features at $\pm$ 35^0 to 45^0 are not as clearly resolved and are somewhat reduced in intensity. The segregation of sulphur to the surface produced similar effects but of a more marked nature as shown in figure 7.12 for a sulphur overlayer characterised by the LEED pattern shown in figure 7.13. The ratio of the 150 eV sulphur Auger peak to the 62 eV copper Auger peak for this structure was 12 % which corresponds to a coverage of approximately 0.3 monolayers (figure 5.3a).

Angular profiles were also obtained for the 150 eV sulphur Auger emission from the sulphur segregated (100) surface described above and also from the Cu(111)-($\sqrt{7}x\sqrt{7}$)R19^0-S surface (corresponding to a sulphur coverage of 0.25 monolayers) and these are shown in figures 7.14 and 7.15 respectively. Both of these profiles were obtained using the SE3K/5U electron gun at glancing incidence. In the case of the copper (100) sulphur profile the upper curve (marked with crosses) corresponds to a relatively disordered sulphur overlayer characterised by a weak diffuse LEED pattern of the type shown in figure 7.13 together with considerable background intensity whereas the lower curve (open circles) was obtained for a fairly well ordered structure of this type. The two curves are quite similar, with that corresponding to the more ordered sulphur structure exhibiting more fine structure. The sulphur profiles from the two copper substrates are characterised by differences in the basic shape of the profile; the (100) profile exhibits greatest intensity along the surface normal while the (111) profile has a slight minimum there. Considerable fine structure is superimposed on the broad structure of the profiles from both surfaces.

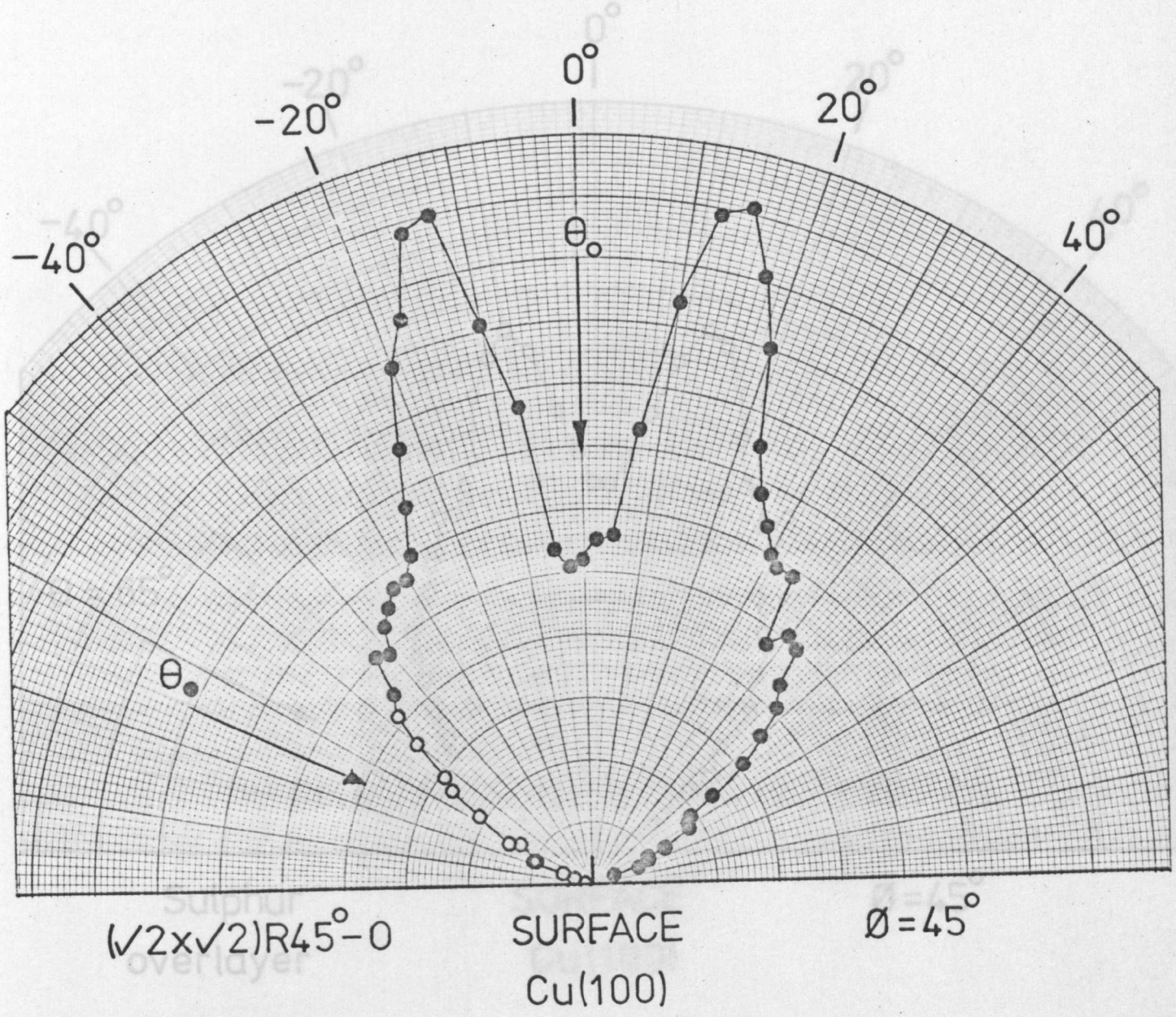

Figure 7.11 Angular profile of the 62 eV copper Auger emission from the Cu(100)-($\sqrt{2}$x $\sqrt{2}$)R45°-O surface.

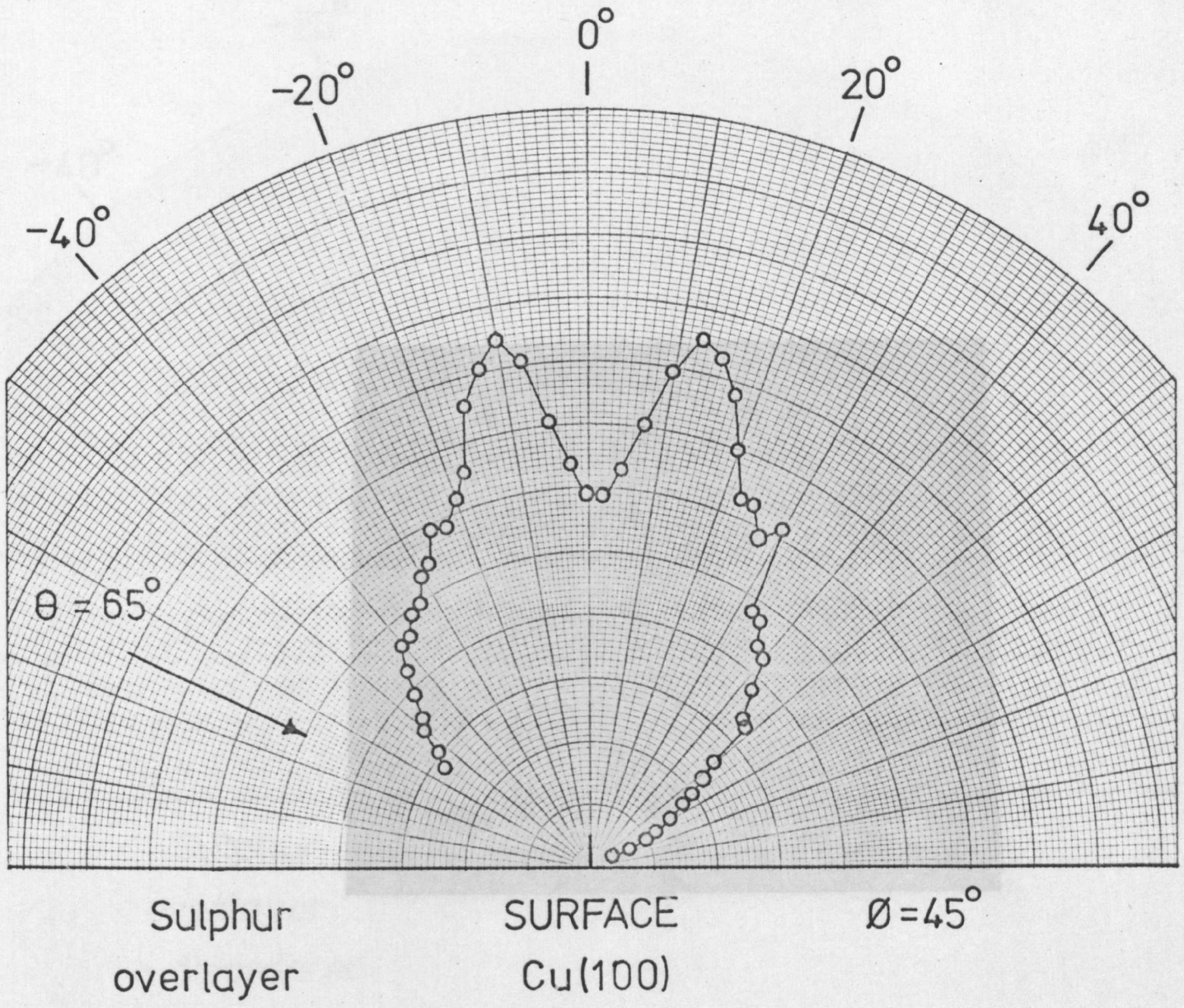

Figure 7.12 Angular profile of the 62 eV copper Auger emission from a sulphur segregated copper (100) surface characterised by the LEED pattern in figure 7.13.

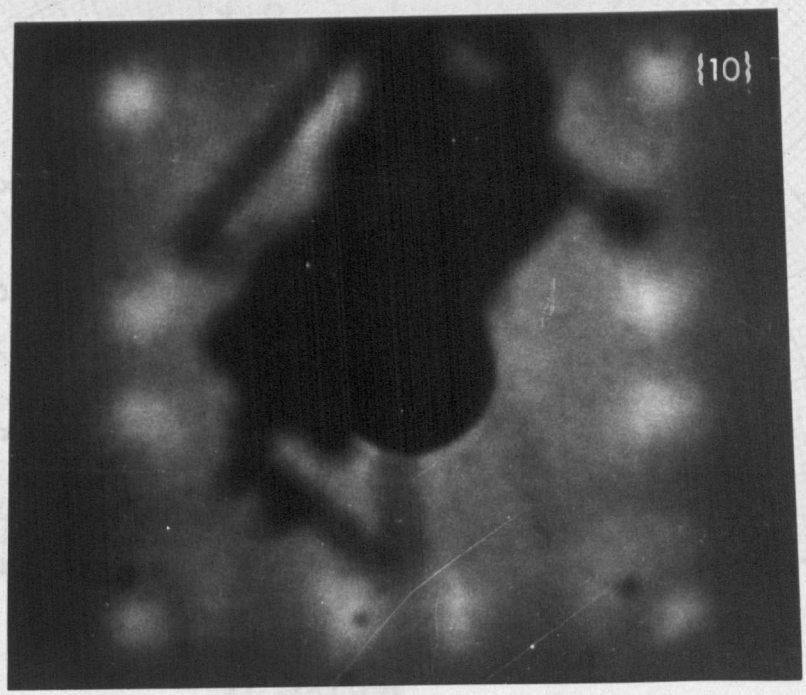

Figure 7.13 LEED pattern from the well ordered sulphur segregated copper (100) surface.

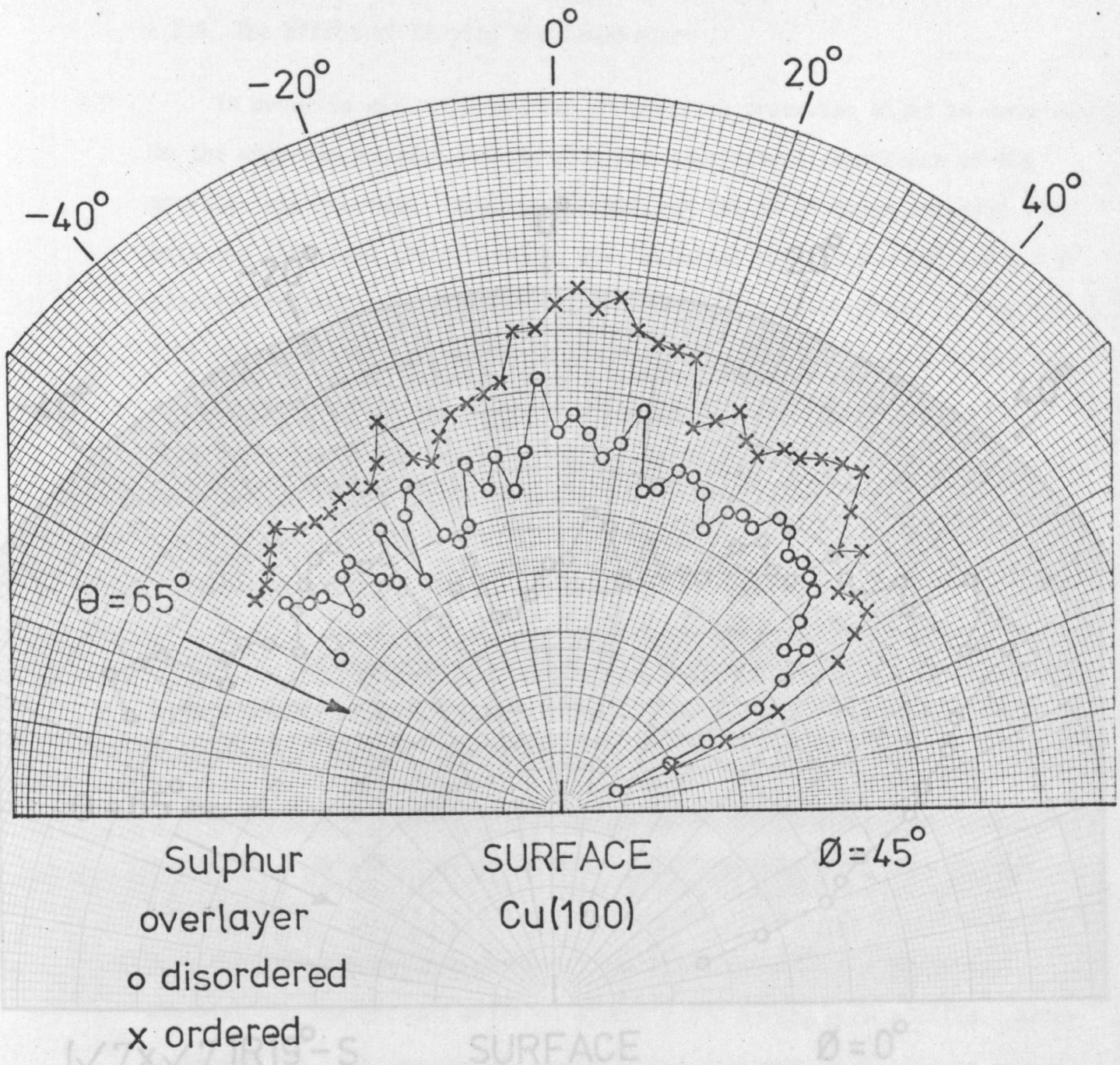

Figure 7.14 Angular profile of the 150 eV sulphur Auger emission from a sulphur segregated copper (100) surface characterised by the LEED pattern in figure 7.13. The upper curve (crosses) corresponds to a weak diffuse LEED pattern exhibiting high background intensities while the lower curve (open circles) corresponds to a well-contrasted LEED pattern.

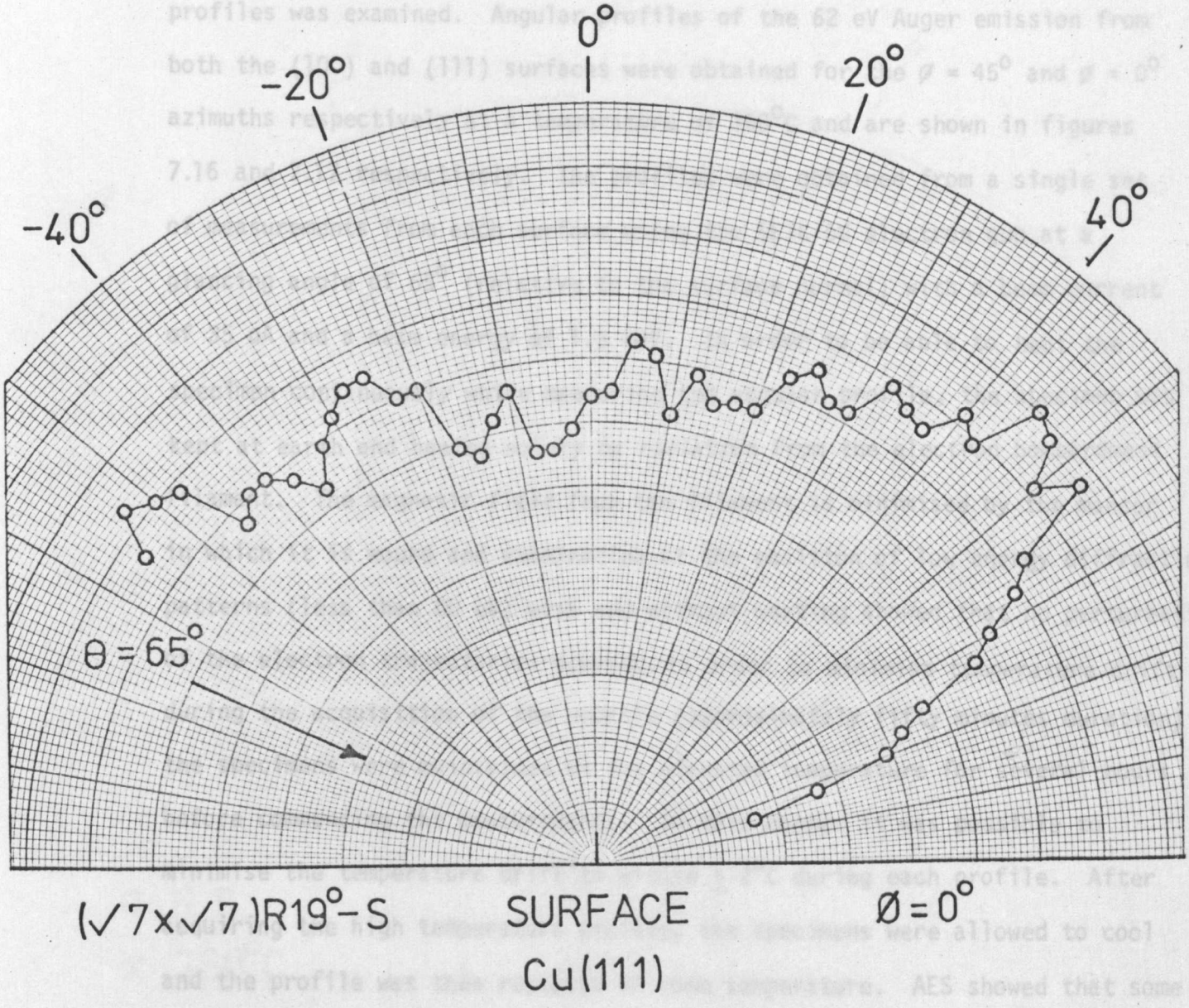

Figure 7.15 Angular profile of the 150 eV sulphur Auger emission from the Cu(111)-($\sqrt{7}$x$\sqrt{7}$)R19°-S surface.

7.2.4 The Effect of Varying the Temperature

In order to determine whether diffraction processes might be contributing to the observed angular anisotropies the temperature dependence of the profiles was examined. Angular profiles of the 62 eV Auger emission from both the (100) and (111) surfaces were obtained for the $\phi = 45^{o}$ and $\phi = 0^{o}$ azimuths respectively at a temperature of $360^{o}C$ and are shown in figures 7.16 and 7.17 respectively. The profiles were obtained from a single set of measurements from each surface using the SE3K/5U electron gun at a glancing angle of 65^{o} (relative to the surface normal) with a beam current of 35 uA and a beam energy of 1.5 KeV. In order to be able to heat the specimen continuously while measuring the angular profile, the specimen was kept at earth and heated solely by radiation from the electron bombardment filament. The magnetic field from the filament is minimised by the manner in which it is wound and examination of the position of low energy diffraction patterns (less than 60 eV) with and without heating showed that no perturbation of the electron trajectories ocurred. In order to minimise temperature drift during the acquisition of the profile (approximately fifty minutes duration) the specimens were maintained at the elevated temperature for several hours before commencing the measurements. In this manner it was possible to minimise the temperature drift to within $\pm 2^{o}C$ during each profile. After acquiring the high temperature profile, the specimens were allowed to cool and the profile was then repeated at room temperature. AES showed that some sulphur segregation had ocurred during the temperature stabilisation period. However, the level of contamination was not high (less than 5% of a monolayer) and more importantly there was little difference between the levels of contamination for the elevated temperature and the room temperature profiles.

Examination of the profiles for the two surfaces shows that in both cases the effect of temperature is quite small. The basic structure of the profiles remains unaltered with the main effect being a reduction of peak to valley ratios by about 15 to 20% for both surfaces.

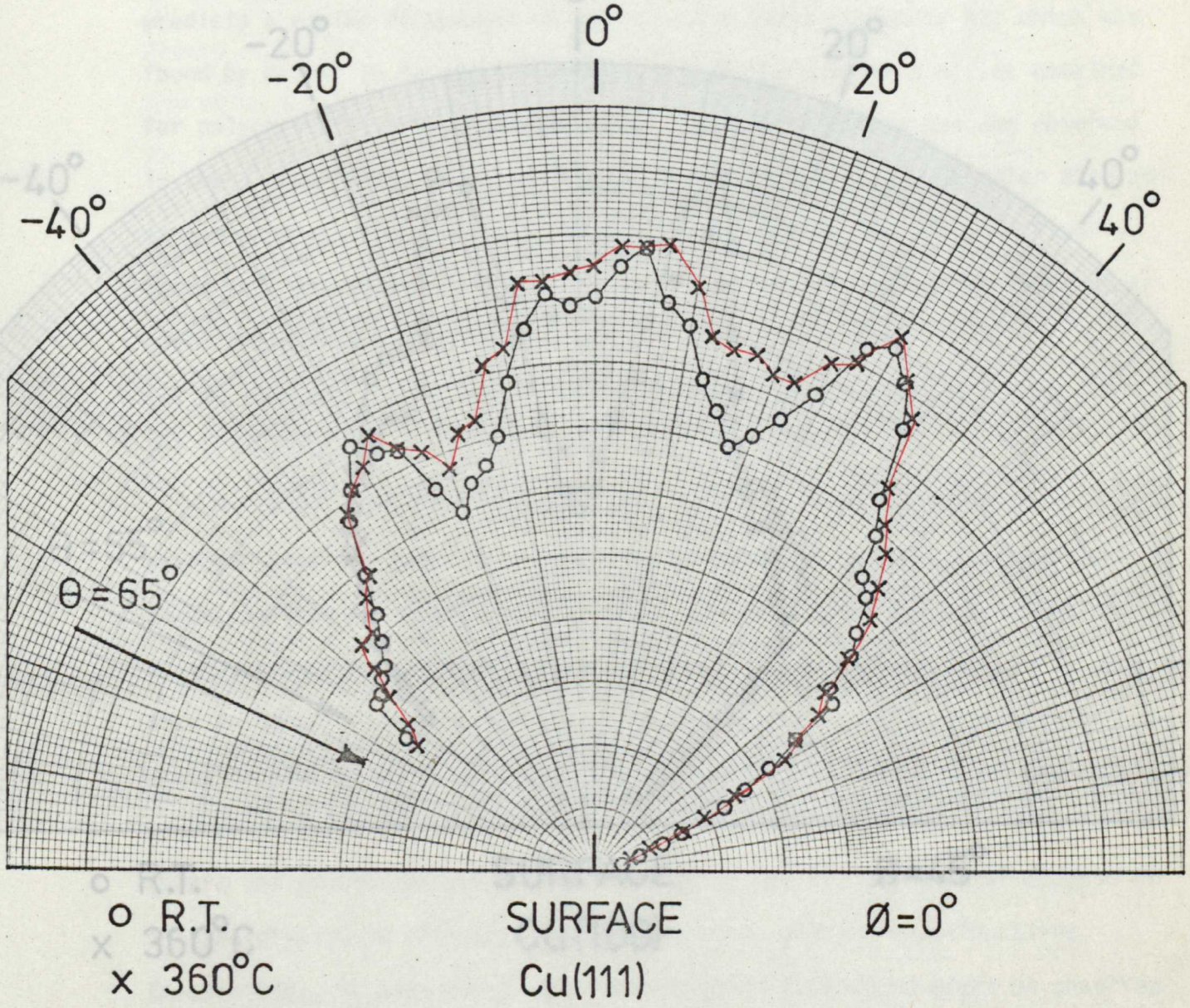

Figure 7.16 Angular profiles of the 62 eV copper Auger emission from the copper (100) surface in the $\phi = 45^{\circ}$ azimuth obtained at room temperature and at 360°C.

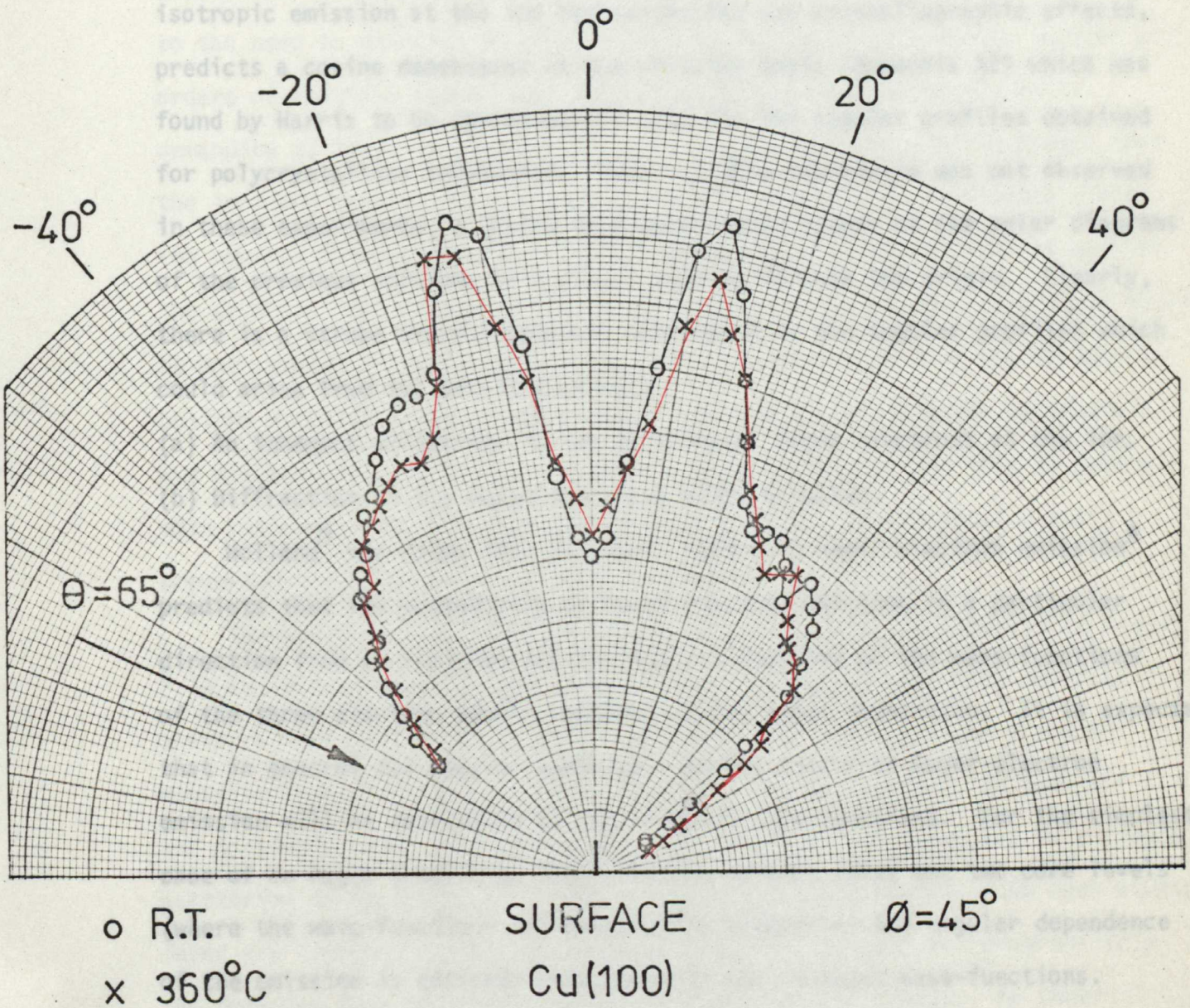

Figure 7.17 Angular profiles of the 62 eV copper Auger emission from the copper (111) surface in the $\phi = 0^{o}$ azimuth obtained at room temperature and at 360°C.

7.3 Discussion

The simplest model of Auger electron emission from a solid, assuming isotropic emission at the ion and neglecting any crystallographic effects, predicts a cosine dependence on the emission angle (Appendix A2) which was found by Harris to be approximately true for the angular profiles obtained for polycrystalline molybdenum. Such a simple dependence was not observed in these experiments; a cosine dependence would appear on the polar diagrams of the previous sections as a circle passing through the origin. Clearly, there is a strong crystallographic dependence in the angular profiles which could arise from two possible effects:

(a) An inherent anisotropy in the emission of Auger electrons at the ion.

(b) Diffraction of the Auger electrons after emission.

Holland[3] has shown that the basic theory of Auger electron emission[4] predicts that the probability of Auger electron emission in a particular direction from an isolated ion is simply a function of the wave-functions of the three electron levels involved in the Auger transition. It is expected that in general the angular dependence at the source of Auger electron emission will be determined by the relevant wave-functions. For the simplest case of an Auger transition involving one valence level and two core levels (where the wave-functions are spherically symmetric) the angular dependence of the emission is entirely determined by the relevant wave-functions. Consequently, in situations where this angular dependence might be observed the study of Auger transitions that involve only valence electrons becomes a useful means of testing model wave-functions for the valence electrons in the surface region. For a gas the inherent angular dependence of the emission would be averaged out but there is no reason to believe that the angular dependence would be lost for a crystalline solid although it might be expected to be considerably weakened. Scattering of the Auger electron after emission by neighbouring ion cores would also have to be incorporated into model calculations.

Since low energy electrons are strongly scattered by ion cores the observed angular dependence may well arise from diffraction of the emitted electrons. An exact calculation of this effect is extremely difficult due to the need to describe accurately the ion core potential and to include all orders of multiple scattering. The calculations will obviously be as demanding as those of LEED as the scattering problem is similar except that the incident wave is now an outgoing spherical wave that originates within the crystal whereas in LEED it is an ingoing plane wave originating outside the crystal. Although it might be expected that the angular dependence would be much weaker than in LEED because the observed effect is a sum of contributions over all incident directions, preliminary calculations by Woodruff and Holland[5] that include only single scattering events are able to predict with reasonable accuracy the basic features of the experimental results presented here for the clean copper surfaces.

The model used by Woodruff and Holland is shown schematically in figure 7.18 and was originally suggested by Matsudaira et al[6] who have recently observed very similar effects in the angular profiles of Auger electron emission from clean and adsorbate covered surfaces of iron. In Woodruff and Holland's model isotropic emission at the ion is assumed and only single scattering is included. The single scattering contributions from each atomic layer are combined using an imaginary potential to damp out progressively the emission from subsequently deeper layers in the crystal. An inner potential is included to correct the observed Auger kinetic energy to that inside the crystal and also to refract the outgoing electrons at the crystal/vacuum boundary. The calculated profiles for the 62 eV copper Auger emission from both the clean (100) and (111) surfaces of copper are shown in figure 7.19 for the $\phi = 45^{o}$ and the $\phi = 0^{o}$ azimuths respectively. Although the real and imaginary potentials were used in these calculations as variable parameters (within realistic limits) the best fit with experiment was achieved using identical parameters for both surfaces. Comparison with the experimental data shows that the basic features for both surfaces are

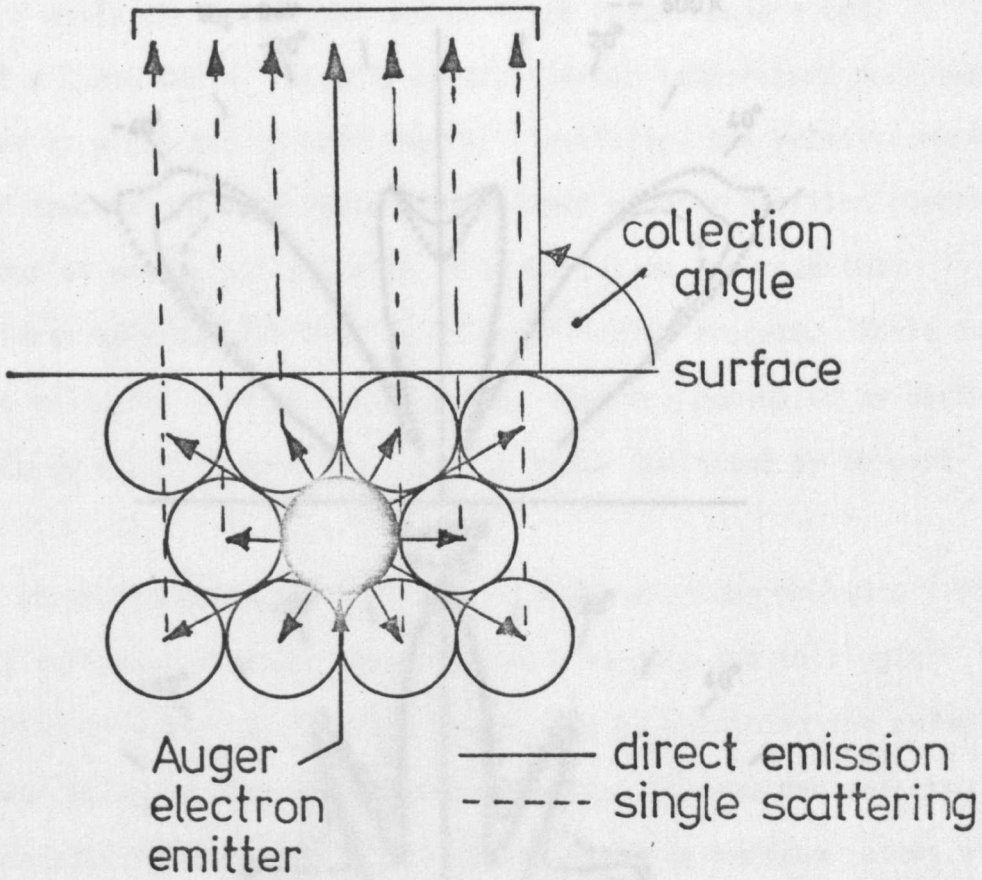

Figure 7.18 Schematic diagram of the diffraction model used by Woodruff and Holland. The particular case illustrated is emission along the surface normal.

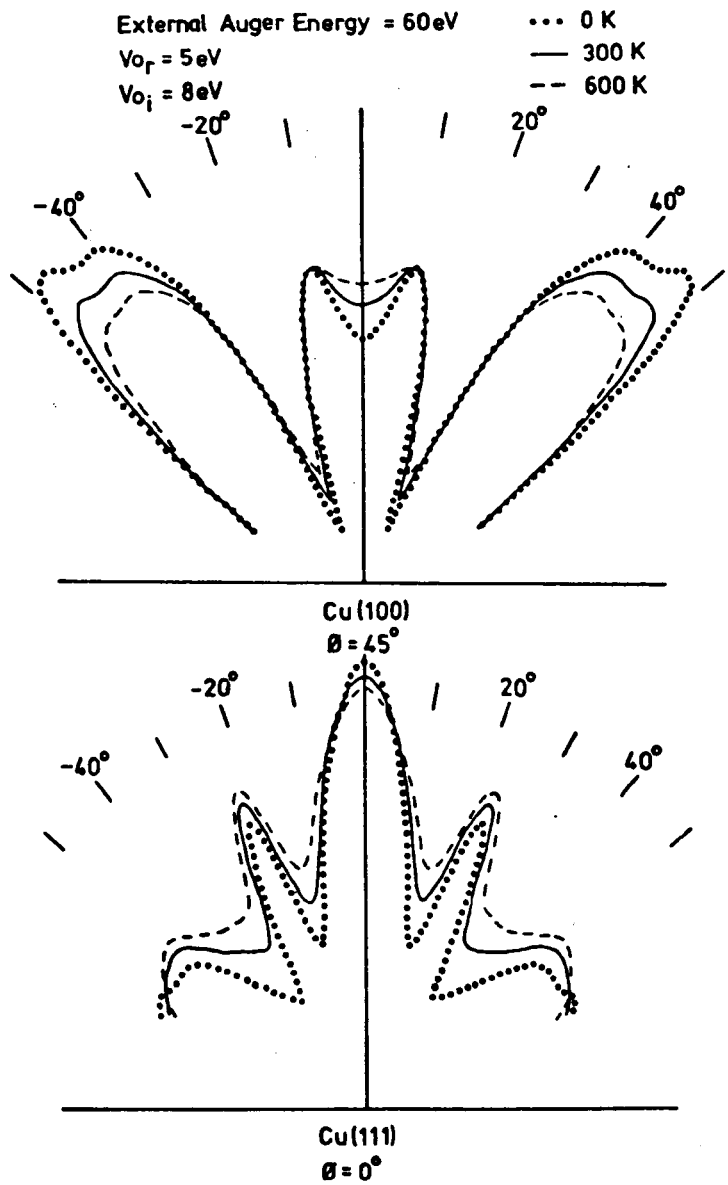

Figure 7.19 Angular profiles of the 62 eV copper Auger emission from the (100) and (111) surfaces of copper for the $\phi = 45^{o}$ and $\phi = 0^{o}$ azimuths calculated by Woodruff and Holland for 0 K, 300 K and 600 K.

well described. The effect of varying the temperature for the theoretical calculations is also shown in figure 7.19 where the solid line corresponds to room temperature while the dotted and dashed lines refer respectively to temperatures of 0 K and 600 K. Clearly a very similar temperature dependence to that observed is predicted by this theory. Initially, the relative weakness of the observed temperature dependence of the Auger angular profiles compared to LEED behaviour at equivalent energies was thought to indicate that diffraction effects were not dominant in this particular process. While such a conclusion is valid for diffraction processes that are dominated by back-scattering (such as LEED) it does not apply to those dominated by forward-scattering.

Thus the strong anisotropies observed in Auger electron emission from (100) and (111) surfaces of copper appear to be primarily due to single forward scattering effects. It is anticipated that by examining the anisotropy of Auger electron emission from an impurity atom that information relating to its in-depth distribution and also to its coordination to surface atoms will be obtained. Whether a single scattering theory will be sufficiently accurate to enable such interpretations to be made will not be established until more refined calculations that include higher orders of multiple scattering have been performed and their significance assessed.

*****

REFERENCES

(1) L.A.Harris, *Surface Sci.* 15 (1969) 77.

(2) P.W.Palmberg, *Appl.Phys.Lett.* 13 (1968) 183.

(3) B.W.Holland,L.McDonnell & D.P.Woodruff, *Solid State Commun.* 11 (1972) 991.

(4) E.H.S.Burhop, "The Auger Effect",Cambridge University Press (1952).

(5) D.P.Woodruff & B.W.Holland, University of Warwick,private communication.

(6) T.Matsudaira,M.Watanabe & M.Onchi, Sixth International Conference on Solid Surfaces, Kyoto, Japan, March (1974).

CHAPTER EIGHT. CONCLUSION

A commercial LEED optics has been successfully combined with an energy-analysing Faraday cup to provide a very versatile LEED experimental system where the condition of the surface can be continually monitored using the LEED pattern while measuring individual LEED beam intensities with the Faraday cup. As well as enabling accurate LEED intensities to be measured for much larger ranges of experimental parameters the time taken to acquire such data has been sustantially reduced by comparison with the more traditional techniques.

Detailed intensity-energy spectra from several diffraction beams have been obtained for a wide range of energies and scattering geometries from both the clean, ordered (100) and (111) surfaces of copper. These data represent the most extensive data base currently available for clean copper surfaces and compare very favourably with the less extensive data available from earlier studies.

While particularly good agreement has been obtained between three independent experimental studies of LEED behaviour from the clean copper (111) surface for the (00) beam in a rather sensitive region of scattering geometry, the difficulties encountered in achieving good reproducibility have been discussed and illustrated with reference to some published data for the (00) beam from silver (111) which failed to show a symmetry that clearly exists. Such considerations emphasise the importance in comparing experimental and theoretical data of correlating "trends" in intensity-energy spectra that occur with changing scattering geometry rather than merely examining isolated spectra. Comparison of the present intensity data from clean copper (100) and (111) surfaces with the limited dynamical calculations that are currently available have shown that good agreement is achieved using model calculations that assume the bulk geometry for both surfaces. A particularly encouraging feature of the comparisons with theory of the experimental intensity-energy spectra, for both copper surfaces, has been the good description of the angular evolution

of the (00) beam spectra with changes in scattering geometry. It is noticeable though that, despite the generally good agreement obtained in such comparisons, the overall correlation is not as extensive as that achieved at present for the low index surfaces of nickel.

Although the segregation of sulphur to both the (100) and (111) surfaces of copper was rather troublesome clean, ordered surfaces could be readily obtained providing that the post-bombardment annealing temperature was kept below about 500^{o}C. AES was used to examine the surfaces at frequent intervals during the acquisition of LEED intensities and an extremely useful feature of the experimental system was the ability to change rapidly between the LEED and AES modes of operation. AES analysis of the copper (100) and (111) surfaces revealed that extra features were present in the secondary electron spectra from ordered surfaces. These features were characterised by a unique temperature dependence and have consequently been termed TDP's (Temperature Dependent Peaks). These features have caused considerable confusion in the interpretation of AES spectra and it transpires that they have been observed on materials other than copper. TDP's appear to be due to diffraction of outgoing secondary electrons and appear to be of little intrinsic interest although their presence is specifically indicative of surface order, but not cleanliness, which may prove of value in AES studies which lack LEED facilities. Fortunately, their marked temperature dependence allows their presence to be detected simply by raising or lowering the specimen temperature.

Although the adsorption of oxygen on copper has been studied using LEED by by several workers most of the work has been restricted to interpreting the LEED patterns in terms of the reciprocal nets of the various oxygen structures observed. There is considerable disagreement over some of the observed structures which has been complicated by the general absence of an *in situ* technique for chemically analysing the surface region. The clean, ordered (100) and (111) surfaces of copper were exposed in this study at room

temperature to a range of oxygen exposures up to $1x10^{-3}$ torr-minutes. No ordered oxygen structures were observed on the copper (111) surface although a new Auger peak, associated with low oxygen coverages, was observed at 79 eV and attributed to a cross-transition involving oxygen and copper energy levels. On the copper (100) surface two oxygen surface structures were observed: a $(\sqrt{2}x\sqrt{2})R45^{o}$ structure following oxygen exposures of $1x10^{-5}$ torr-minutes and a (2x2) structure following oxygen exposures of $1x10^{-4}$ torr-minutes. The first structure was very stable and has been observed in several earlier studies for identical conditions although it was usually preceded by various structures that were not observed in this partciular study. Similarly, the (2x2) oxygen structure reported here has not been reported previously. Sulphur segregation was more severe on oxygen adsorbed surfaces and annealing after room temperature adsorption (performed to improve LEED pattern contrast) had to be limited to temperatures of about $250^{o}C$. As well as inducing sulphur segregation excessive annealing temperatures were avoided due to the removal of adsorbed oxygen by dissolution in the bulk crystal.

Detailed intensity-energy spectra for the Cu(100)-$(\sqrt{2}x\sqrt{2})R45^{o}$-O and the Cu(100)-(2x2)-O surfaces have been acquired and represent the most extensive data base currently available from oxygen adsorbate structures on copper (100). Indeed this data base is one of the few available for adsorbate structures in general; similarly extensive data bases for oxygen and sulphur adsorbate structures on nickel (100) have only become available recently. Due to the absence of intensity data for the extra beams for the (2x2) oxygen structure only the $(\sqrt{2}x\sqrt{2})R45^{o}$ oxygen structure data is sufficiently extensive to provide a rigorous test for dynamical model calculations. The limited dynamical calculations that have been performed for the Cu(100)-$(\sqrt{2}x\sqrt{2})R45^{o}$-O structure have been compared to the experimental data from this study and indicate that the solution for this structure appears to be a reconstructed co-planar surface consisting of a half-monolayer each of copper and oxygen with a vertical spacing of approximately that of the clean substrate.

The recently proposed data reduction technique for surface structure determination, that is based on averaging LEED intensity-energy spectra while maintaining constant momentum transfer in order to extract the kinematical contributions to the spectra and hence the structure, has been applied to both clean and oxygen adsorbed copper surfaces. Although averaged spectra from the clean copper (111) surface is extremely kinematical, in agreement with other studies of (111) surfaces of f.c.c. metals, similarly extensive averages from the copper (100) surface are not so kinematical and exhibit strong extra features due to multiple scattering at approximately half-order Bragg conditions. Similar averages have been perfomed for the two ordered oxygen structures observed on the copper (100) surface and also for the disordered oxygen "structure" on copper (111) and the differences in the spectra relative to the averages from the clean surfaces, mainly shifts in peak positions, have been interpreted using pseudo-kinematical model calculations. The results of the three analyses, which are the first structural analyses performed on unknown surface structures using this technique, have all been physically reasonable solutions: for the Cu(100)-($\sqrt{2}$x$\sqrt{2}$)R45^{o}-O structure the best fit was found for a coplanar reconstructed surface with oxygen and copper sub-layer spacings in the range 1.05 to 1.10 times the normal substrate spacing; for the Cu(100)-(2x2)-O structure the best fit was found for a quarter monolayer of oxygen located between 2.1 and 2.2 Å above a reconstructed layer with the oxygen atoms positioned directly above the copper sub-layer atoms; for disordered oxygen adsorption on the copper (111) surface the best fit was found for oxygen atoms distributed evenly over the range 1.0 Å to 1.4 Å above the copper top layer. Although the interpretation of the Cu(100)-($\sqrt{2}$x$\sqrt{2}$)R45^{o}-O structure using the limited dynamical calculations that are presently available is in agreement with the analysis using this data reduction scheme, suitably extensive dynamical calculations will have to be performed before any confidence can be expressed in the conclusions of this technique.

By using the energy-analysing facility of the Faraday cup, the first observation of anisotropies in the angular distribution of Auger electron emission from single crystal surfaces has been made. Anisotropies in the emission of both copper and sulphur Auger electrons from clean and sulphur segregated copper (100) and (111) surfaces have been examined. The differences observed between the copper Auger emission at 62 eV from the (100) and (111) surfaces is clearly crystallographically associated. The general behaviour of the angular profiles for the 62 eV copper Auger emission can be described in terms of interference between the emitted Auger electrons and singly-scattered Auger electrons. Preliminary investigations indicate that the angular anisotropies of Auger electron emission from an adsorbate for example will be a function of its surface coordination and also its in-depth distribution through the surface region. Consequently, this technique may prove to be extremely valuable in determining the surface structure information that is presently sought using LEED.

*****

SUGGESTIONS FOR FUTURE WORK

The controversy over the different structures that are observed when oxygen adsorbs at room temperature onto the clean (100) and (111) surfaces of copper remains unresolved and indeed has been further complicated by this work with the observation of a structure that hitherto was unreported. While the previous studies have not had the benefit of Auger electron spectroscopy it would be unwise to assume that the differences in the structures were due simply to differences in surface cleanliness. Consequently, this chemisorption system requires further examination to determine exactly what factors are producing the different adsorption characteristics. However, despite these difficulties the data base for the Cu(100)-($\sqrt{2}$x$\sqrt{2}$)R45^{o}-O surface was acquired for well characterised surface conditions and correlation with future model calculations will be of interest, particularly as a test for the proposed solution using the data reduction technique.

The results of the study of the angular dependence of Auger electron emission are particularly interesting as a possible source of structural information. The present experimental arrangement is limited to the most intense Auger emissions and an extension of this study to surface impurities of low concentrations requires a sensitivity that is not available with the present technique. The author is presently engaged on a Science Research Council research project to study angular dependences of Auger electron emission and in order to obtain a high sensitivity with good energy and angular resolution a rotatable hemi-spherical electron energy analyser has been constructed.

*****

APPENDIX ONE. AES Calibration for Sulphur on Copper

The results of a specific AES calibration for sulphur on a copper (100) substrate has been published very recently by Argile and Rhead[1] who obtained a ratio of the 150 eV sulphur Auger peak to the 62 eV copper Auger peak of 0.28 ± 0.03 for monolayer coverage which is in excellent agreement with the unpublished results of Domange who used a radiochemical calibration (0.30 ± 0.05).[2]

The results of these calibrations were not available during the course of this study and instead the author used an approximate calibration deduced from the radiochemical calibration of Perdereau[3] for sulphur on a nickel substrate; the ratio of the 150 eV sulphur Auger peak to the 60 eV nickel Auger peak for monolayer coverage (assuming simple close packing of the sulphur) was:

$$\frac{I(S)}{I(Ni)} = 0.43 \pm 0.05$$

Now, we know from Palmberg et al[4] that for the $M_{2,3}M_{4,5}M_{4,5}$ Auger transition we have:

$$\frac{I(Cu)}{I(Ni)} = 1.13$$

Thus

$$\frac{I(S)}{I(Cu)} = 0.40 \pm 0.05$$

Although the method used to deduce this value is subject to several criticisms the result is in reasonable agreement with the values from the direct calibration. This ratio has been used throughout this work as representing a reasonable upper limit to the sulphur concentration. While the direct calibrations indicate lower concentrations the calibration technique is susceptible to differences in the excitation and collection geometry and also in the primary electron beam energy.

*****

(1) C.Argile & G.E.Rhead, *J.Phys.C.* 7 (1974) L261.

(2) J.L.Domange, cited as a private communication in (1).

(3) M.Perdereau, *Surface Sci.* 24 (1971) 239.

(4) P.W.Palmberg, "Handbook of Auger Spectra", Physical Electronic Industries, Minnesota (1971).

APPENDIX TWO. Simple Theory for the Angular Dependence of Auger Electron Emission

Let us consider Auger electron emission from an element of unit area at a depth between x and $x+dx$ below the surface:

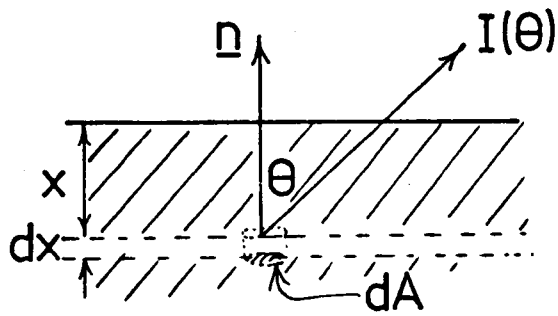

For unit area dA the Auger current emitted from the volume element $dAdx$ in a direction θ from the surface normal $\underline{n}$ is:

$$dI(\theta) = j \exp(-l/\lambda)$$

where j is the Auger current emitted isotropically per unit solid angle and where the number of Auger electrons is assumed to decrease exponentially with path length l for which λ is the mean free path. Rewriting l as $x\cos\theta$ the total Auger current emitted in the direction θ can be derived as:

$$I(\theta) = \int_0^\infty j \exp(-x\cos\theta/\lambda)dx$$

$$= j\left[-\cos\theta \exp(-x\cos\theta/\lambda)\right]_0^\infty$$

Thus $$I(\theta) = j\frac{\cos\theta}{\lambda}$$

If we normalise to the total current emitted in the direction of the surface normal given by $I(0)$ then:

$$\frac{I(\theta)}{I(0)} = \cos\theta$$